University of Science and Technology of China

Université Pierre et Marie Curie

Thèse de doctorat

Discipline : Physique des particules

présentée par

Kun Liu

Observation du boson de Higgs dans sa désintégration en $\gamma\gamma$ et recherche de sa désintégration en $Z\gamma$ avec le détecteur ATLAS

---

dirigée par Yanwen Liu et Giovanni Marchiori

Soutenue le 24 juin 2014 devant le jury composé de :

M. Matteo Cacciari	LPTHE	président
M. Sergei Ganjour	SPP-IRFU/CEA	rapporteur
M. Aleandro Nisati	INFN	rapporteur
M. Fabrice Hubaut	CPPM-IN2P3/CNRS	examinateur
M. Zhengguo Zhao	USTC	examinateur
M. Yanwen Liu	USTC	directeur
M. Giovanni Marchiori	LPNHE-IN2P3/CNRS	directeur

Laboratoire de Physique Nucléaire et de Hautes Energies(LPNHE)
Barre 12-22, 1er étage - 4 place Jussieu
75 252 Paris

Université Pierre et Marie Curie
École Doctorale de Sciences
LPNHE
4 place Jussieu
75252 Paris Cedex 05

Acknowledgements

During the last five years, as I went from knowing nothing at all to having at least a little grasp of particle physics, I got a great amount of help from my supervisors, colleagues and friends. I could not have finished this thesis without them.

I would like to express my special appreciation and thanks to my supervisor in the University of Science and Technology of China, M. LIU Yanwen. He guided my first steps into the world of particle physics and gave me my grounding in high energy physics. Without his understanding and support, I would not have been able to stay in Paris for three years, nor to concentrate my attention on my thesis program. He always encouraged me when doing analysis or making a presentation.

I would also like to express my special appreciation and thanks to my supervisor in the Laboratoire de Physique Nucléaire et de Hautes Energies, M. MARCHIORI Giovanni. Without his assistance and dedicated involvement at every step throughout the process, this thesis would have never been completed. He guided my progress with his great knowledge and outstanding research work. I must also thank him for his great efforts to improve my English, for daily help with life in Paris, and for sharing interesting things with me.

I would like to express my gratitude to my colleagues in LPNHE : Lydia Roos, Bertrand Laforge, Sandro De Cecco, Sandrine Laplace, Giovanni Calderini, Jose Ocariz, Irena Nikolic, Herberth Torres, Olivier Davignon, Camilla Rangel, Liwen Yao and Marco Bomben. I was happy to work with you all over the last three years in Paris !

I would like to express my gratitude to my colleagues in USTC : Zhengguo Zhao, Liang Han, Yi Jiang, Haiping Peng, Jianbei Liu, Yingchun Zhu and Minghui Liu. I would like to give special thanks to Minghui Liu. He help me a lot, answering my questions even when they were very naive.

I would like to thank my friends within ATLAS group, including Kerstin Tackman, Fabrice Hubaut, Marco Delmastro, Andrea Bocci, Marcos Jimenez, Elisabeth Petit and Fuquan Wang. Discussions with them both in ATLAS official meetings and in our leisure time always brought me fresh ideas.

Thanks to the guys who shared their happiness with me over the past years, especially to Jun Gao, Mei Hao, Changqiao Li, Ruiqi Zhang and Ziyu Guo. I would like to give special thanks to Changqiao Li. He helped me a lot in doing administrative stuff for the university.

I would like to give special thanks to my parents, brother and sisters. They always give me selfless love and support. They encouraged and supported me, enabling me to overcome many difficulties.

Last but not at least, I would like to thank my friends who supported me while writing this thesis and helped me strive towards this goal.

Observation du boson de Higgs dans sa désintégration en $\gamma\gamma$ et recherche de sa désintégration en $Z\gamma$ avec le détecteur ATLAS

Résumé

Ce travail de thèse concerne la recherche du boson de Higgs à l'aide de canaux de désintégration contenant des photons dans l'état final, basée sur les données enregistrées par le détecteur ATLAS en 2011 et 2012, à une énergie dans le centre de masse des collisions proton-proton $\sqrt{s} = 7$ et 8 TeV. La sélection des évévenements, les principaux bruits de fond, les propriétés du signal, la discrimination statistique entre signal et bruits de fond, ainsi que l'interprétation des résultats en terme de boson de Higgs du modèle standard sont discutés. Dans le canal de désintégration $H \to \gamma\gamma$, un excès par rapport au niveau de bruit de fond est clairement visible à une masse $m_H = 126,8 \pm 0,2(stat) \pm 0,7(syst)$ GeV et avec une significativité locale de $7,4\sigma$. En revanche, dans le canal de désintégration rare $H \to Z\gamma$, aucun excès n'est observé dans la fenêtre de masse allant de 120 à 150 GeV. Ce résultat est interprété comme une limite égale à 11 fois la valeur de la section efficace de production $pp \to H \to Z\gamma$ prédite par le modèle standard pour une masse du boson de Higgs de $m_H = 125,5$ GeV, proche de celle mesurée dans les canaux en $\gamma\gamma$ et en quatre leptons. Une reconstruction et une identification efficace des photons, ainsi qu'une connaissance précise des performances du système de déclenchement et de l'algorithme d'identification, sont des aspects importants de ces mesures. Une grande partie de ce manuscrit est ainsi consacrée à la description de l'optimisation de ces performances et des activités de mesures que j'ai réalisées pendant ces trois années.

Mots-clefs

Expérience ATLAS, boson de Higgs, désintégration rare, déclenchement photon, identification des photons.

Observation of the Higgs particle in $\gamma\gamma$ events and search for the Higgs particle in $Z\gamma$ events at ATLAS

Abstract

This thesis focuses on the searches for the Higgs boson in events with photons in the final states, using the full proton-proton collision data collected by ATLAS at $\sqrt{s} = 7$ and 8 TeV in 2011 and 2012. Higgs boson decays to photon pairs or to a photon and a Z boson decaying to di-electrons or di-muons are investigated. The event selection, the main backgrounds, the signal properties, and the statistical discrimination between the signal and background in data and the interpretation of the results in terms of a Standard Model Higgs boson are discussed. In the $H \to \gamma\gamma$ channel a clear excess over the background is seen at a mass of $m_H = 126.8 \pm 0.2(stat) \pm 0.7(syst)$ GeV, with a local significance of 7.4σ. In the rare decay channel $H \to Z\gamma$ no evidence of excess over the background is observed in the mass range 120-150 GeV, and, for a Higgs boson mass near the one obtained from the combined mass measurement in the $\gamma\gamma$ and 4-lepton final states, $m_H = 125.5GeV$, an upper limit of 11 times the SM prediction, at 95% confidence level, is set on the production cross section times the $H \to Z\gamma$ cross section. One of the most important ingredient for these measurements is the efficient reconstruction and identification of photons, and a precise knowledge of the trigger and identification performance. A significant part of the document is thus devoted to the photon performance optimisation and measurement activities that I carried on in the past three years.

Keywords

ATLAS experiment, the Higgs boson, rare decay, photon trigger, photon identification.

Contents

Introduction

The Standard Model (SM) of elementary particles and their interactions was built in the second half of the century, based on the three foundations of relativity, quantum mechanics and gauge invariance. Several experimental results have confirmed the validity of the Standard Model predictions in the explored energy range, and all new discoveries have been accommodated by the SM. However, the Standard Model missed one last piece when the ATLAS experiment at the Large Hadron Collider (LHC) started taking data in 2010: the elementary particles of the SM cannot have a non-vanishing mass without violating the SM gauge invariance. This is the case unless there exists a scalar field, called the Higgs field, which spontaneously breaks the gauge symmetry through the Brout-Englert-Higgs (BEH) mechanism, thus giving mass to the elementary particles and leading to the existence of a neutral scalar particle, the Higgs boson. When the work described in this document started, the existence of such a Higgs boson was still unknown: this particle had been searched for without success by various experiments over the world in the past decades, and only limits on its possible mass had been set.

One of the main purposes of the ATLAS and CMS experiences at the LHC at CERN was indeed the search for the Higgs boson, as well as the tests of possible new physics beyond the SM at unprecedented energy scales. In the SM, the Higgs boson is an unstable particle. Among its decay modes, the $H \to \gamma\gamma$ channel is one of the most sensitive channels. It plays an important role in determining the Higgs boson mass, spin and parity. At the same time, since the $H \to \gamma\gamma$ channel is mediated by loops of charged particles, it also acts as a sensitive probe to new physics. Another decay mode, tightly associated to the decay of $H \to \gamma\gamma$, is the decay $H \to Z\gamma$. In the SM, the branching ratio of the decay $H \to Z\gamma$ is about two thirds of that for the $H \to \gamma\gamma$ decay. Moreover, since new particles affecting the $H \to \gamma\gamma$ can also contribute the $H \to Z\gamma$, the two decay channels should be correlated. Therefore, studying them in a joint way can reveal more details about the underlying physics.

In the frame of my doctoral studies, I worked on the Higgs boson searches in the $H \to \gamma\gamma$ and $H \to Z\gamma$ decay channels. This thesis describes my contributions to these two analysis, as well as the photon performance studies that I have performed during the same years in order to improve the accuracy and the reach of these searches. The document is organized as follows.

A brief review of the phenomenology of the Standard Model is presented in Chapter 1. The text focuses on the electroweak theory and the BEH mechanism, followed by a short explanation of the constraints on the Higgs boson mass. Higgs boson decays to a photon pair or a Z boson and a photon are reviewed at the end of this chapter.

Chapter 2 briefly describes the LHC machine and the ATLAS detector. The LHC accelerator complex and the ATLAS sub-detectors are reviewed. Their design and running parameters are summarized. In the second part of the chapter, the reconstruction of various final-state objects (photon, electron, muon, jet and missing transverse energy) and

their performance in the ATLAS experiment are described.

Chapter 3 describes my work on the photon trigger performance and photon identification efficiency measurements. The proposal and optimization of some new photon triggers for 2012 and for the future LHC run is discussed. The photon trigger efficiency measurement using photons from radiative Z decays is illustrated in detail. In the photon identification efficiency measurements, my contributions to two of the three data-driven measurements are presented. The combination of the various photon efficiency measurements and their impact on the $H \to \gamma\gamma$ search is given at the end of the chapter.

Chapter 4 presents the search for a Higgs boson in $H \to Z\gamma \to \ell\ell\gamma$ using the full ATLAS pp collision data collected in 2011 and 2012. The event selection, the main backgrounds, the signal properties, and the statistical discrimination between the signal and background in data and the interpretation of the results in terms of a Standard Model Higgs boson are discussed. The compatibility between data and background only hypothesis is tested. 95% $C.L.$ limits on the Higgs boson production cross section times $H \to Z\gamma$ branching ratio are set as a function of the Higgs mass between 120 GeV and 150 GeV. My personal contributions include the optimization of the classification of the selected events in categories with different signal-to-background ratio, signal and background modelling, the evaluation of the experimental systematic uncertainties and the statistical extraction of the final results by means of a profile likelihood ratio technique.

Chapter 5 recalls the observation of the Higgs boson in the $H \to \gamma\gamma$ channel using the same pp collision data used in the $H \to Z\gamma$ search. An excess over background is observed with a local significance of 7.4 σ at a mass of 126.5 GeV. The measured Higgs boson mass (m_H) is $126.8 \pm 0.2(stat) \pm 0.7(syst)$. The signal strength parameters for different Higgs boson production modes are determined. My contributions to this analysis includes photon trigger and identification efficiency measurements, background composition studies and some background suppression studies to improve the signal purity in the VH associated production mode.

Chapter 1

Phenomenology

What are the elementary constituents of matter? What are the fundamental laws of the universe? Studies to answer these questions have been carried out along mankind's history. The result is a theory named the Standard Model (SM), that asserts that matter in the universe is composed of elementary fermions of spin-1/2, which interact with each other through fields propagated by elementary bosons of integral spin. There are three types of interactions in the SM : the electromagnetic, weak, and strong forces. The quanta of these forces are the photon (γ), the $W^{\pm}/Z^0$ bosons and the eight gluons (g). The gravity is not yet included in the SM. An additional scalar particle, the Higgs boson, is responsible for the masses of the elementary particles and for the differences between the electromagnetic and the weak forces. The elementary fermions are of two kinds, depending on their interactions: leptons and quarks. Leptons do not carry a "color" charge and thus are not affected by the strong force, while quarks are sensitive to all the fundamental interactions. For both leptons and quarks there are three replicas or "generations", consisting of two particles: an up-type (charge $q = 2/3$) and a down-type ($q = -1/3$) quark, or a charged lepton ($q = -1$) and a neutrino ($q = 0$). Their charges are in unit of absolute value of electron charge ($|e|$). The elementary particles included in the Standard Model with their properties (mass, charge and spin) are illustrated in Fig. 1.1.

In this chapter, the phenomenology of the Standard Model theory is briefly reviewed. The contents mainly focus on the electroweak theory and the Higgs boson physics, followed by a short explanation of the constraints from collider experiments prior to LHC and early LHC data. Higgs boson decays to di-photons or a Z boson and a photon are briefly reviewed at the end of this chapter.

1.1 The Gauge Principle

The Standard Model is built on the "gauge principle", *i.e.* the idea that the interactions between the elementary particles correspond to (and arise from) symmetries of the Lagrangian under a group of local transformations. To find them, one can start from the invariances of the free Lagrangian under a global transform and to extend them to a local symmetry. As an example, consider the Dirac Lagrangian density which describes a free electron (or positron):

$$\mathcal{L}_{free} = \bar{\psi}_e(i\gamma^\mu\partial_\mu - m_e)\psi_e = i\bar{\psi}_e\gamma^\mu\partial_\mu\psi_e - m_e\bar{\psi}_e\psi_e \tag{1.1}$$

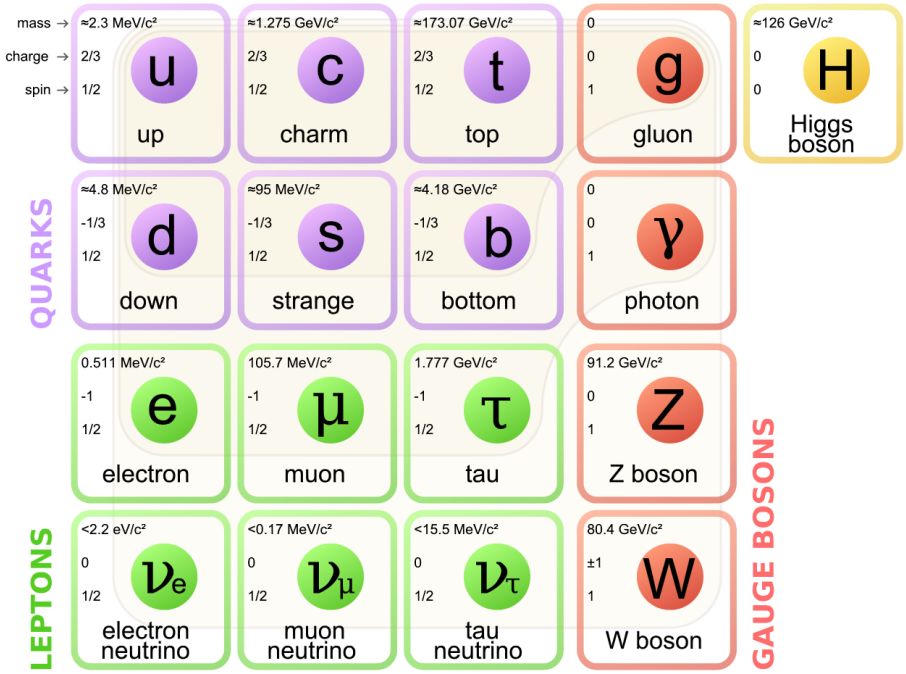

Figure 1.1 – Elementary particles included in the Standard Model. The elementary fermions making up matter are in purple color (quarks) and in green color (leptons). The four gauge bosons are in red color. The Higgs boson predicted for giving mass to the other particles is in the top-right corner.

where ψ_e is the electron field, and m_e is the electron mass. γ^μ are the gamma matrices (also called Dirac matrices):

$$\gamma^0 = \begin{pmatrix} 0 & 1 \\ 1 & 0 \end{pmatrix}, \gamma^i = \begin{pmatrix} 0 & \tau^i \\ -\tau^i & 0 \end{pmatrix} \tag{1.2}$$

where τ^i are the Pauli matrices:

$$\tau_1 = \begin{pmatrix} 0 & 1 \\ 1 & 0 \end{pmatrix}, \tau_2 = \begin{pmatrix} 0 & -i \\ i & 0 \end{pmatrix}, \tau_3 = \begin{pmatrix} 1 & 0 \\ 0 & -1 \end{pmatrix} \tag{1.3}$$

The first term of Eq. 1.1 is the kinetic density, while the second one is the mass term. This Lagrangian is invariant under global $U(1)$ phase transformations of the kind:

$$\psi_e \rightarrow \psi'_e = e^{iq\theta}\psi_e, \tag{1.4}$$

where q is the electron charge and θ is an arbitrary space-time independent parameter. However, when considering local gauge $U(1)$ phase transformations:

$$\psi_e \rightarrow \psi'_e = e^{iq\theta(x)}\psi_e \tag{1.5}$$

the Lagrangian is not invariant, since:

$$\begin{aligned} \mathcal{L}_{free} \rightarrow \mathcal{L} &= (e^{-iq\theta(x)}\bar{\psi}_e)(i\gamma^\mu\partial_\mu - m)(e^{iq\theta(x)}\psi_e) \\ &= \mathcal{L}_{free} - q\partial_\mu\theta(x)\bar{\psi}_e\gamma^\mu\psi_e \end{aligned} \tag{1.6}$$

Its invariance under the local gauge $U(1)$ symmetry can be restored by introducing an additional vector field A_μ, replacing

$$\partial_\mu \rightarrow D_\mu = \partial_\mu + iqA_\mu \tag{1.7}$$

in (1.1), and requiring that under this $U(1)$ symmetry A_μ transforms as:

$$A_\mu \rightarrow A'_\mu = A_\mu - \partial_\mu \theta(x) \tag{1.8}$$

The new Lagrangian density becomes:

$$\begin{aligned} \mathcal{L} &= \bar{\psi}_e i\gamma^\mu D_\mu \psi_e \\ &\equiv \mathcal{L}_{free} - qJ^\mu A_\mu \end{aligned} \tag{1.9}$$

and one can recognize in the last term the interaction between the electromagnetic current $J^\mu \equiv \bar{\psi}_e \gamma^\mu \psi_e$ and a vector field A_μ which can be identified with the photon. Imposing the invariance of the free electron Lagrangian under the local gauge $U(1)$ transformation thus leads to the introduction of a vector boson (γ) and its interaction with the electron.

1.2 The Electroweak Unification

The electron Lagrangian density (1.9) can be expressed in terms of the left-handed ($\psi_{e,L}$) and right-handed ($\psi_{e,R}$) components of the electron field ψ_e:

$$\mathcal{L} = i\bar{\psi}_{e,R}\gamma^\mu \partial_\mu \psi_{e,R} + i\bar{\psi}_{e,L}\gamma^\mu \partial_\mu \psi_{e,L} - qA_\mu(\bar{\psi}_{e,R}\gamma^\mu \psi_{e,R} + \bar{\psi}_{e,L}\gamma^\mu \psi_{e,L}) - m(\bar{\psi}_{e,R}\psi_{e,L} + \bar{\psi}_{e,L}\psi_{e,R}) \tag{1.10}$$

The mass term mixes the left-handed and right-handed fields, while kinetic and the interaction terms do not. For the massless electron neutrino, its Lagrangian density only includes the kinetic terms of left-handed component, since $m_\nu = 0, q_\nu = 0$.

At the beginning of the 1960s, charged-current weak interactions of leptons had been observed and it was established that they couple left-handed electrons and neutrinos together. To describe their interaction, a gauge group with at least two generators was searched for. The idea of Bludman in 1958 was to use $SU(2)$ as symmetry group. The left-handed electron ($\psi_{e,L}$) and neutrino ($\psi_{\nu_e,L}$) were put in a common multiplet on which the gauge group acts:

$$\psi_L = \begin{pmatrix} \psi_{\nu_e,L} \\ \psi_{e,L} \end{pmatrix} \tag{1.11}$$

while the right-handed electron field is treated as a singlet: $\psi_R = \psi_{e,R}$, since no right-handed neutrino was observed. Neglecting the lepton masses, the Lagrangian density for the first family of leptons can be written as:

$$\mathcal{L} = i\bar{\psi}_L \gamma^\mu \partial_\mu \psi_L + i\bar{\psi}_{e,R}\gamma^\mu \partial_\mu \psi_{e,R} \tag{1.12}$$

Under $SU(2)_L$ transformations, the lepton fields transform as:

$$\begin{aligned} \psi_L &\rightarrow \psi'_L = e^{i\hat{\theta}.\hat{\tau}}\psi_L \\ \psi_{e,R} &\rightarrow \psi'_{e,R} = \psi_{e,R} \end{aligned} \tag{1.13}$$

where $\hat{\theta} = (\theta_1, \theta_2, \theta_3)$ and $\hat{\tau}(\tau_1, \tau_2, \tau_3)$ are the Pauli matrices. The invariance of the Lagrangian density (1.12) under local transformations is obtained by replacing

$$\partial_\mu \rightarrow D_\mu = \partial_\mu - ig\frac{\hat{\tau}}{2}\hat{W}_\mu \tag{1.14}$$

for the left handed fermions, where $\hat{W}_\mu = W^1_\mu, W^2_\mu, W^3_\mu$ are a massless isovector triplet.

The derivatives of left-handed and right-handed fields become:

$$\begin{aligned} \partial_\mu \psi_L \to D_\mu \psi'_L &= (\partial_\mu - ig\frac{\tau_i}{2}W^i_\mu)e^{i\hat{W}.\hat{T}}\psi_L \\ \partial_\mu \psi_{e,R} \to \partial_\mu \psi'_{e,R} &= \partial_\mu \psi_{e,R} \end{aligned} \tag{1.15}$$

The new Lagrangian density becomes:

$$\begin{aligned} \mathcal{L} &= i\bar{\psi}_L \gamma^\mu D_\mu \psi_L + i\bar{\psi}_{e,R}\gamma^\mu \partial_\mu \psi_{e,R} \\ &= \frac{g}{\sqrt{2}}(J^{+,\mu}W^+_\mu + J^{-,\mu}W^-_\mu) + g(-\bar{\psi}_{e,L}\gamma^\mu \psi_{e,L} + \bar{\psi}_{\nu_e,L}\gamma^\mu \psi_{\nu_e,L})W^3_\mu \end{aligned} \tag{1.16}$$

where $J^{\pm,\mu}$ are the charged leptonic currents defined as:

$$J^{+,\mu} = (J^{-,\mu})^\dagger = \bar{\psi}_{\nu_e,L}\gamma^\mu \psi_{e,L} \tag{1.17}$$

and

$$W^\pm_\mu = \frac{1}{\sqrt{2}}(W^1_\mu \mp iW^2_\mu) \tag{1.18}$$

The requirement of the $SU(2)_L$ gauge invariance thus gives rise to 3 bosons: W^+, W^- and W^3. The $W^\pm$ mediate the charged weak interactions. W^3_μ is a neutral boson but the current it couples to cannot be identified with the electromagnetic one. In order to incorporate electromagnetic interactions, a different symmetry group therefore is needed.

In 1961 Sheldon Glashow proposed the group $SU(2)_L \otimes U(1)$ as gauge group for the electromagnetic and weak interactions [1]. In order to be invariant under local $SU(2)_L \otimes U(1)$ transformations, the Lagrangian density (1.12) is extended by introducing $\hat{W}_\mu(W^1_\mu, W^2_\mu, W^3_\mu)$ and B_μ fields with the following transform laws:

$$\psi_L \to \psi'_L = e^{i\hat{\theta}.\hat{\tau}+i\alpha Y}\psi_L \tag{1.19}$$

$$\psi_{e,R} \to \psi'_{e,R} = e^{i\alpha Y}\psi_{e,R} \tag{1.20}$$

$$\partial_\mu \to D_\mu = \partial_\mu - ig\frac{\tau_i}{2}W^i_\mu - ig'\frac{Y}{2}B_\mu \tag{1.21}$$

where the weak hypercharge (Y) is $Y = -1$ for the left-handed doublet and $Y = -2$ for the right-handed singlet.

The interaction between the left-handed fields is thus:

$$i\bar{\psi}_L\gamma^\mu(-ig\frac{\tau_i}{2}W^i_\mu + ig'\frac{1}{2}B_\mu)\psi_L = \frac{g}{\sqrt{2}}(J^{+,\mu}W^+_\mu + J^{-,\mu}W^-_\mu) + g\bar{\psi}_L\gamma^\mu\frac{\tau_3}{2}W^3_\mu\psi_L - g'\bar{\psi}_L\gamma^\mu\frac{B_\mu}{2}\psi_L \tag{1.22}$$

Including also the right-handed component, the Lagrangian density for the interactions becomes:

$$\mathcal{L}_{\text{int}} = \frac{g}{\sqrt{2}}(J^{+,\mu}W^+_\mu + J^{-,\mu}W^-_\mu) + g(\bar{\psi}_L\gamma^\mu\frac{\tau_3}{2}\psi_L)W^3_\mu + g'(-\bar{\psi}_L\gamma^\mu\frac{1}{2}\psi_L - \bar{\psi}_{e,R}\gamma^\mu\psi_{e,R})B_\mu \tag{1.23}$$

Defining the lepton weak isospin (as $J^{3,\mu}$) and weak hypercharge (as $J^{Y,\mu}$) currents as:

$$J^{3,\mu} = \bar{\psi}_L\gamma^\mu\frac{\tau_3}{2}\psi_L \tag{1.24}$$

and

$$J^{Y,\mu} = -\frac{1}{2}\bar{\psi}_L\gamma^\mu\psi_L - \bar{\psi}_{e,R}\gamma^\mu\psi_{e,R}, \tag{1.25}$$

the neutral-current interactions can be written as:

$$\mathcal{L}^{(neutral)} = gJ^{3,\mu}W_\mu^3 + g'J^{Y,\mu}B_\mu \tag{1.26}$$

The electromagnetic interaction can be recovered by means of a rotation of the neutral vector boson fields, definining $Z_\mu \equiv W_\mu^3 cos\theta_w - B_\mu sin\theta_w$, $A_\mu \equiv W_\mu^3 sin\theta_w + B_\mu cos\theta_w$, where the weak mixing angle (or Weinberg angle) θ_w is fixed by:

$$g \sin\theta_w = g' \cos\theta_w. \tag{1.27}$$

This yields:

$$\mathcal{L}^{(neutral)} = gJ^{3,\mu}(cos\theta_w Z_\mu + sin\theta_w A_\mu) + g'J^{Y,\mu}(-sin\theta_w Z_\mu + cos\theta_w A_\mu) \tag{1.28}$$

In particular, the neutral-current interaction mediated by A_μ is given by:

$$\begin{aligned}\mathcal{L}^{(A_\mu)} &= gsin\theta_w A_\mu (J^{3,\mu} + J^{Y,\mu}) \\ &= gsin\theta_w A_\mu [-(\bar{\psi}_{e,L}\gamma^\mu \psi_{e,L} + \bar{\psi}_{e,R}\gamma^\mu \psi_{e,R})] \\ &= gsin\theta_w A_\mu J^{e.m.,\mu}\end{aligned} \tag{1.29}$$

where $J^{e.m.,\mu}$ is the electromagnetic current defined as:

$$J^{e.m.,\mu} = -(\bar{\psi}_{e,L}\gamma^\mu \psi_{e,L} + \bar{\psi}_{e,R}\gamma^\mu \psi_{e,R}) \tag{1.30}$$

Comparing with (1.24) and (1.25), one can see that:

$$J^{3,\mu} + J^{Y,\mu} = J^{e.m.,\mu} \tag{1.31}$$

The full interaction terms in the Lagrangian (1.23) can be rewritten as:

$$\begin{aligned}\mathcal{L}_{\text{int}} &= \frac{g}{\sqrt{2}}(J^{+,\mu}W_\mu^+ + J^{-,\mu}W_\mu^-) + gJ^{3,\mu}W_\mu^3 + g'J^{Y,\mu}B_\mu \\ &= \frac{g}{\sqrt{2}}(J^{+,\mu}W_\mu^+ + J^{-,\mu}W_\mu^-) + (gW_\mu^3 - g'B_\mu)J^{3,\mu} + g'B_\mu J^{e.m.,\mu} \\ &= \frac{g}{\sqrt{2}}(J^{+,\mu}W_\mu^+ + J^{-,\mu}W_\mu^-) + \frac{g}{cos\theta_w}(J^{3,\mu} - sin^2\theta_w J^{e.m.,\mu})Z_\mu + gsin\theta_w J^{e.m.,\mu}A_\mu\end{aligned} \tag{1.32}$$

It includes the weak charge currents, a neutral current mediated by a Z boson and the electromagnetic current coupled to the photon. The electron mass term can not be included in the Lagrangian since it breaks the gauge symmetry. In the following sections it will be shown how the Higgs mechanism provides a way to gives mass to particles while keeping the Lagrangian invariant under $SU(2)_L \otimes U(1)$ transformation.

1.3 Spontaneous Symmetry Breaking

The Higgs mechanism is based on the idea of spontaneous symmetry breaking: the Lagrangian is invariant under the full group $SU(2) \otimes U(1)$, but the vacuum is not and thus the gauge symmetry is broken. As a consequence, when expanding the lagrangian around the vacuum, $SU(2)_L \times U(1)$-violating mass terms for the particles appear.

The idea can be illustrated with a simplified scenario. Consider a complex scaler field $\phi = (\phi_1 + i\phi_2)/\sqrt{2}$ with the following Lagrangian:

$$\mathcal{L} = \partial_\mu \phi^* \partial^\mu \phi - V(\phi) \tag{1.33}$$

in which the potential energy density has the form :

$$V(\phi) = \mu^2\phi^*\phi + \lambda(\phi^*\phi)^2. \tag{1.34}$$

This Lagrangian obeys the global symmetry:

$$\phi(x) \to \phi'(x) = e^{iq\theta} * \phi(x) \tag{1.35}$$

For $\mu^2 > 0, \lambda > 0$, the minimum of the potential energy density corresponds to the state $\phi_1 = \phi_2 = 0$.

In the case of $\mu^2 < 0, \lambda > 0$, $V(\phi)$ takes the "mexican-hat" shape of Fig. 1.2, and has a continuous set of minima for:

$$\sqrt{\phi_1^2 + \phi_2^2} = \sqrt{\frac{-\mu^2}{\lambda}} \equiv v, \tag{1.36}$$

In this case, the particle spectrum of the theory is obtained by expanding the Lagrangian under small oscillations around the vacuum. We choose as vacuum state the following:

$$\phi_1 = v, \ \phi_2 = 0, \tag{1.37}$$

which is clearly not invariant under the symmetry (1.35), and define new fields as the perturbations from vacuum state:

$$\eta = \phi_1 - v, \ \xi = \phi_2 \tag{1.38}$$

Then, the Lagrangian (1.33) becomes:

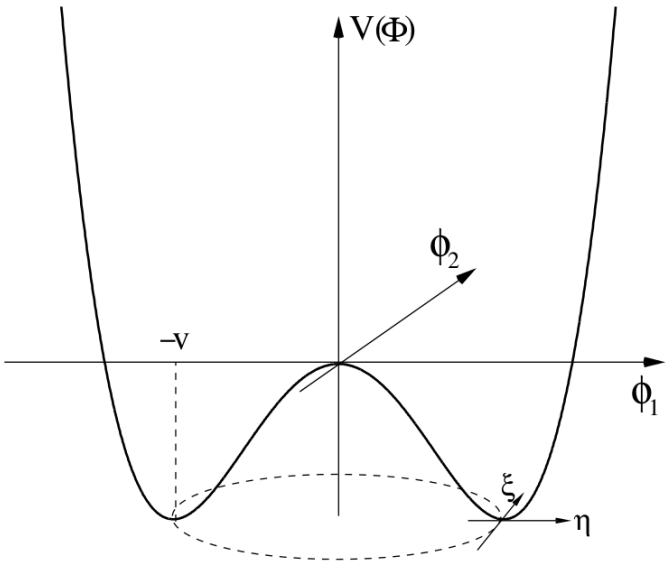

Figure 1.2 – The potential $V(\phi)$ [Eq.(1.34)] as a function of ϕ_1 and ϕ_2 for $\mu^2 < 0$.

$$\begin{aligned}
\mathcal{L} &= \partial_\mu(\eta+v)\partial^\mu(\eta+v) + \frac{(\partial_\mu\xi)^2}{2} - \mu^2\frac{[(\eta+v)^2+\xi^2]}{2} - \frac{\lambda[(\eta+v)^2+\xi^2]}{4} \\
&= \frac{1}{2}(\partial_\mu\eta)^2 + \frac{1}{2}(\partial_\mu\xi)^2 - \frac{1}{4}\lambda v^4 + \lambda v^2\eta^2 + \lambda v\eta^3 + \frac{1}{4}\lambda\eta^4 + \frac{1}{4}\lambda\xi^4 + \lambda v\eta\xi^2 + \frac{1}{2}\lambda\eta^2\xi^2 \\
&= \underbrace{\frac{1}{2}(\partial_\mu\eta)^2 - (\lambda v^2)\eta^2}_{\text{massive scalar particle } \eta} + \underbrace{\frac{1}{2}(\partial_\mu\xi)^2 + 0 * \xi^2}_{\text{massless scalar particle } \xi} + \underbrace{\cdots}_{\text{higher order terms}}
\end{aligned} \tag{1.39}$$

As a consequence of the spontaneous symmetry breaking, one massless particle (ξ) and one massive particle (η) are generated. The mass of the particle η is:

$$m_\eta = \sqrt{2\lambda v^2} = \sqrt{-2\mu^2} \tag{1.40}$$

1.4 The Higgs Mechanism

The Higgs mechanism is essentially the spontaneous breaking of a local gauge symmetry. Let's consider again a complex scalar field ϕ with potential $V(\phi)$ as in (1.34) and a local $U(1)$ symmetry, of the form:

$$\phi(x) \to \phi'(x) = e^{iq\theta(x)} * \phi(x) \tag{1.41}$$

To keep the Lagrangian (1.33) invariant under this symmetry, a massless gauge field(A_μ) transforming as:

$$A_{\mu(x)} \to A'_\mu(x) = A_\mu(x) - \frac{1}{q}\partial_\mu\theta(x) \tag{1.42}$$

is needed. At the same time, the derivative operator should be replaced by the 'covariant derivative' D_μ:

$$\partial_\mu \to D_\mu = \partial_\mu + iqA_\mu \tag{1.43}$$

The invariant Lagrangian density under the local gauge $U(1)$ phase transformation is thus:

$$\mathcal{L} = D_\mu\phi^* D^\mu\phi - \frac{1}{4}F_{\mu\nu}F^{\mu\nu} - V(\phi) \tag{1.44}$$

where $F_{\mu\nu} = \partial_\mu A_\nu - \partial_\nu A_\mu$ is the field strength for the field A_μ.

Again, in the case of $\mu^2 < 0, \lambda > 0$, the vacuum is not invariant under the initial symmetry. Let's choose as vacuum the state ($\phi_1 = v, \phi_2 = 0$), and expand (1.44) around the vacuum, introducing $h = \phi_1 - v, \xi = \phi_2$. We also use (1.41) to redefine ϕ such that ϕ_2 is always 0:

$$\phi = \frac{1}{\sqrt{2}}(v + h) \tag{1.45}$$

The Lagrangian near the vacuum state then becomes:

$$\begin{aligned}
\mathcal{L}_{scalar} &= (D^\mu\phi)^\dagger(D_\mu\phi) - V(\phi) \\
&= (\partial^\mu + ieA^\mu)\frac{1}{\sqrt{2}}(v+h)(\partial_\mu - ieA_\mu)\frac{1}{\sqrt{2}}(v+h) - \mu^2(v+h)^2 - \lambda(v+h)^4 \\
&= \underbrace{\frac{1}{2}(\partial_\mu h)^2 - \lambda v^2 h^2}_{\text{massive scalar particle h}} + \underbrace{\frac{1}{2}e^2v^2A_\mu^2}_{\text{gauge field with mass}} + \underbrace{e^2vA_\mu^2 h + \frac{1}{2}e^2A_\mu^2h^2}_{\text{Higgs and gauge fields interaction}} \\
&- \underbrace{\lambda v h^3 - \frac{1}{4}\lambda h^4}_{\text{Higgs self-interactions}}
\end{aligned} \tag{1.46}$$

The spontaneous $U(1)$ local symmetry breaking mechanism gives rise to a mass for the gauge boson A_μ and introduces a new real scalar field (h). Furthermore, it also gives a mass term for the field h, the interaction terms between the gauge boson and h, and the self-interaction terms of the h field.

In the case of electroweak interactions, where the symmetry group is $SU(2)_L \otimes U(1)_Y$, we can introduce a doublet of complex scalar fields:

$$\phi = \begin{pmatrix} \phi^\dagger \\ \phi^0 \end{pmatrix} = \frac{1}{\sqrt{2}} \begin{pmatrix} \phi_1 + i\phi_2 \\ \phi_3 + i\phi_4 \end{pmatrix} \tag{1.47}$$

obeying the following transformation law:

$$\begin{aligned} U(1)_Y : \phi \to \phi' &= e^{-iI.\theta(x)}\phi \\ SU(2)_L : \phi \to \phi' &= e^{-i\hat{\tau}.\hat{\theta}(x)/2}\phi \end{aligned} \tag{1.48}$$

where $\theta(x)$ and $\hat{\theta}(x)$ are independent variables. The Lagrangian density is thus extended by including the kinetic and potential terms for the fields ϕ:

$$\mathcal{L} = (D^\mu\phi)^\dagger(D_\mu\phi) - V(\phi^\dagger\phi) \tag{1.49}$$

This Lagrangian has an infinite set of ground states. Let's choose as vacuum state the one corresponding to $\phi_1 = \phi_2 = \phi_4 = 0$ and $\phi_3 = v$, and exploit the $SU(2)_L \otimes U(1)_Y$ invariance to write a perturbation around the vacuum as:

$$\phi = \frac{1}{\sqrt{2}} \begin{pmatrix} 0 \\ v + h \end{pmatrix} \tag{1.50}$$

where h is the scalar Higgs field. The derivative of ϕ is thus:

$$\begin{aligned} D_\mu\phi &= [\partial_\mu + \frac{ig}{2}\hat{\tau}\hat{W}_\mu + \frac{ig'}{2}\hat{B}_\mu]\frac{1}{\sqrt{2}} \begin{pmatrix} 0 \\ v + h \end{pmatrix} \\ &= \frac{1}{\sqrt{2}}\partial_\mu h + \frac{i(v+h)}{\sqrt{8}} \begin{pmatrix} g(W_\mu^1 - iW_\mu^2) \\ -gW_\mu^3 + g'B_\mu \end{pmatrix} \end{aligned} \tag{1.51}$$

Similarly, its conjugate is:

$$(D^\mu\phi)^\dagger = \frac{1}{\sqrt{2}}\partial^\mu h - \frac{i(v+h)}{\sqrt{8}} \begin{pmatrix} g(W_\mu^1 + iW_\mu^2), -gW_\mu^3 + g'B_\mu \end{pmatrix} \tag{1.52}$$

The product $(D^\mu\phi)^\dagger D_\mu\phi$ in the Lagrangian thus gives (considering only the mass terms for the W and B fields):

$$\begin{aligned} (D^\mu\phi)^\dagger D_\mu\phi &= \frac{v^2}{8} \begin{pmatrix} g(W_\mu^1 + iW_\mu^2), -gW_\mu^3 + g'B_\mu \end{pmatrix} * \begin{pmatrix} g(W_\mu^1 - iW_\mu^2) \\ -gW_\mu^3 + g'B_\mu \end{pmatrix} \\ &= \frac{v^2}{g^2}[(W_\mu^1)^2 + (W_\mu^2)^2] + (gW_\mu^3 - g'B_\mu)^2 \\ &= \frac{v^2}{8}[g^2(W^+)^2 + g^2(W^-)^2 + (g^2 + g'^2)Z_\mu^2 + 0 * A_\mu^2] \end{aligned} \tag{1.53}$$

where

$$\begin{aligned} W_\mu^+ &= \frac{1}{\sqrt{2}}(W_\mu^1 - iW_\mu^2) \\ W_\mu^- &= \frac{1}{\sqrt{2}}(W_\mu^1 + iW_\mu^2) \\ Z_\mu &= \frac{1}{\sqrt{g^2 + g'^2}}(gW_\mu^3 - g'B_\mu) \\ A_\mu &= \frac{1}{\sqrt{g^2 + g'^2}}(g'W_\mu^3 + gB_\mu) \end{aligned} \tag{1.54}$$

There are thus three massive gauge bosons ($W^{\pm}$, Z) and one massless boson (γ) with masses:

$$\begin{aligned} M_{W^+} &= M_{W^-} = \frac{1}{2}vg \\ M_Z &= \frac{v}{2}\sqrt{g^2+g'^2} \\ M_\gamma &= 0 \end{aligned} \tag{1.55}$$

The masses of the $W^{\pm}$ and Z bosons are related by:

$$\frac{M_W}{M_Z} = \frac{g'}{\sqrt{g^2+g'^2}} \equiv cos(\theta_w) \tag{1.56}$$

g and g' are free parameters in the Standard Model theory, but related to G_F, M_W and e. We know from latest experimental measurements that the W boson mass is 80.385 ± 0.015 GeV [2] and the Z boson mass is 91.1876 ± 0.0021 GeV [2], and their ratio is in agreement with the relation (1.56).

By looking at (1.46), the mass of the quantum of the Higgs field, the Higgs boson, can be identified with:

$$m_h = \sqrt{2\lambda v^2} \tag{1.57}$$

The value of the Higgs vacuum expectation value (v) is around 246 GeV, as measured via muon decay [3]:

$$v = \sqrt{\frac{1}{\sqrt{2}G_F}} \tag{1.58}$$

where G_F is the Fermi coupling constant, $G_F = 1.166 \times 10^{-5}$ GeV^{-2}. Since λ is a free parameter of the theory, the Standard Model does not predict the Higgs boson mass.

The electron mass term can also be generated through spontaneous symmetry breaking by noticing that the original Lagrangian density can be extended by including a $SU(2)_L \otimes U(1)_Y$-invariant coupling between the Higgs doublet and the fermion field:

$$\mathcal{L}_{mass} = -\lambda_f[\bar{\psi}_L \phi \psi_R + \bar{\psi}_R \bar{\phi} \psi_R] \tag{1.59}$$

After spontaneous symmetry breaking, this term becomes:

$$\begin{aligned} \mathcal{L}_{mass} &= -\lambda_e \frac{1}{\sqrt{2}}[\begin{pmatrix} \bar{\psi}_{\nu_e,L}, \bar{\psi}_{e,L} \end{pmatrix}_L \begin{pmatrix} 0 \\ v+h \end{pmatrix} \psi_{e,R} + \bar{\psi}_{e,R} \begin{pmatrix} 0, v+h \end{pmatrix} \begin{pmatrix} \psi_{\nu_e,L} \\ \psi_{e,L} \end{pmatrix}] \\ &= \frac{-\lambda_e(v+h)}{\sqrt{2}}(\bar{\psi}_{e,L}\psi_{e,R} + \bar{\psi}_{e,R}\psi_{e,L}) \\ &= \underbrace{-\frac{\lambda_e v}{\sqrt{2}}\bar{\psi}_e\psi_e}_{\text{electron mass term}} \quad \underbrace{-\frac{\lambda_e}{\sqrt{2}}h\bar{\psi}_e\psi_e}_{\text{electron-higgs coupling term}} \end{aligned} \tag{1.60}$$

As a consequence of spontaneous symmetry breaking, the electron acquires a mass $m_e = \frac{\lambda_e v}{\sqrt{2}}$, and its coupling to the Higgs boson, $\frac{\lambda_e}{\sqrt{2}} = \frac{m_e}{v}$, is proportional to its mass.

1.5 Constraints on the Standard Model Higgs Boson Mass

The Higgs boson mass is not predicted by the Standard Model, since the parameter λ in the Higgs mass term (1.57) is free. However, some constraints can be set on the Higgs

boson mass. In absence of the Higgs field, the elastic scattering cross section of longitudinally polarised massive gauge bosons (e.g. $W_L^+W_L^- \to W_L^+W_L^-$) diverges quadratically with increasing centre-of-mass energy in perturbation theory. In the Standard Model, the existence of the Higgs boson leads to the cancellation of the ultraviolet divergences, provided the Higgs boson mass is not too heavy [4, 5]:

$$m_H < \sqrt{\frac{4\pi\sqrt{2}}{3G_F}} \sim 700 \text{ GeV} \tag{1.61}$$

Experimentally, constraints on the Higgs boson mass have been set through direct searches, performed over several decades by the LEP, Tevatron and LHC experiments in various Higgs boson decay channels. In June 2012 the limits obtained on the Higgs boson cross section times branching ratio normalized to the SM expectation (shown in Fig. 1.3) excluded a SM Higgs boson with mass $m_H < 117.5$ GeV, $m_H > 128$ GeV and m_H in [118.5,122.5] at 95% confidence level. In July 2012 a new particle consistent with the SM Higgs boson was discovered by ATLAS [6] and CMS [7]. Its mass was measured to be $126.0 \pm 0.4(stat) \pm 0.4(sys)$ GeV ($125.3 \pm 0.4(stat) \pm 0.5(sys)$ GeV) in the ATLAS (CMS) experiment.

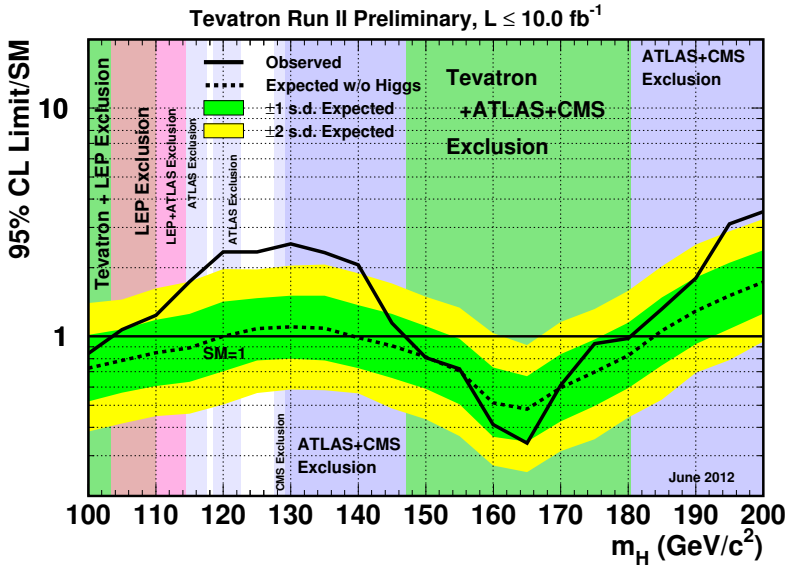

Figure 1.3 – Observed and expected (median, for the background only hypothesis) 95 % C.L. upper limits on the ratios of Higgs event rate to the SM prediction, as functions of the Higgs boson mass for the combined CDF and D0 analyses. The limits are set scanning the assumed Higgs mass in step of 5 GeV for which both experiments have performed dedicated searches in different channels. Adjacent point are connected with straight lines for better readability. The bands indicate the confidence intervals at 68% and 95% C.L. for the expected limits, in the absence of signal. The limits are obtained with a Bayesian approach [8].

Besides the direct limits, the Higgs boson mass can also be constrained by a global fit of the electroweak parameters using as inputs several measurements, such as those of the W, Z, top masses and widths, and of various cross sections. The most recent fit, shown in Fig. 1.4 [9], yields $m_H = 94^{+25}_{-22}$ GeV, which is consistent within 1.3 σ with the latest value of the mass measured by ATLAS [6] and CMS [7]. Figure 1.5 shows the comparisons between

the W boson mass (M_W) and top mass (m_t) determined with direct measurements (green bands and data points) and from the fit to electroweak data excluding the measurements of M_W, m_t and m_H (gray contour areas) or the fit results using all data except the M_W and m_t measurements (blue contour areas). Their agreement demonstrates the impressive consistency of the Standard Model.

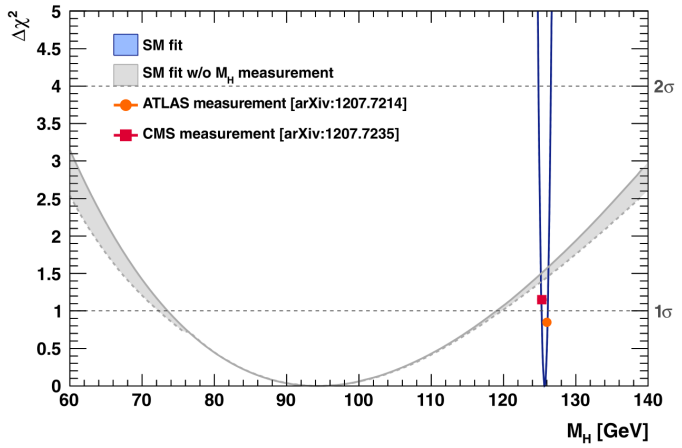

Figure 1.4 – $\Delta\chi^2$ profiles as a function of the Higgs mass. The gray band shows the result when excluding the new M_H measurements from the fit, while the blue line shows the result when including the new M_H measurements in the fit [9].

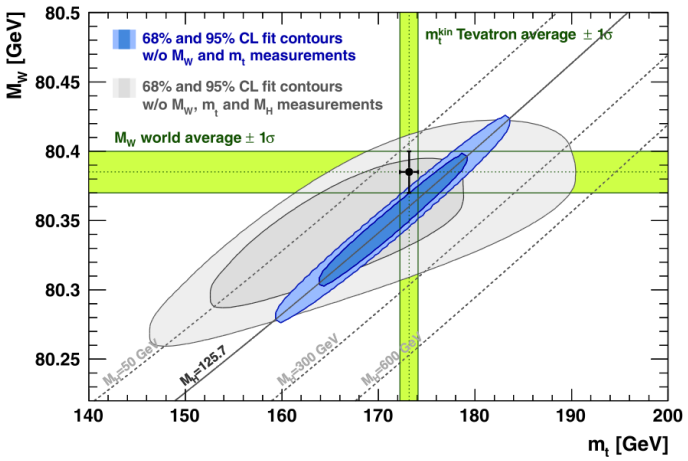

Figure 1.5 – 2-dimensional contours, at 68% and 95% CL, for M_W and m_t. The blue (gray) areas illustrate the fit results when including (excluding) the new M_W measurements. The direct measurements of M_W and m_t are always excluded in the fit. The vertical and horizontal bands (green) indicate the 1σ regions of the direct measurements(Color figure online) [9].

The decay width is also an important property of the Higgs boson. In the SM the Higgs boson width grows rapidly with the Higgs mass, as shown in Fig. 1.6. For a light Higgs boson, its width (few MeV) is negligible compared to the experimental resolution on the invariant mass distribution of its decay products. On the other hand, a heavy Higgs boson would show up as a broad resonance, with a width similar to its mass for $m_H \approx 1.7$ TeV. Theoretically, this situation is very challenging, since the production processes and decay

modes do not factorize anymore from each other. More details about this issue and its ongoing investigations, can be found in Refs. [10, 11, 12, 13]. The latest upper limit on the Higgs boson width, set by the CMS experiment using the interference between $H \to ZZ$ and non-resonant electroweak ZZ production in events in which where either $ZZ \to 4\ell$ or $ZZ \to 2\ell 2\nu$, is $\Gamma_H < 4.2 \times \Gamma_H^{SM}$ at the 95% confidence level, where $\Gamma_H^{SM} = 4.15$ MeV [14] for m_H near 125 GeV.

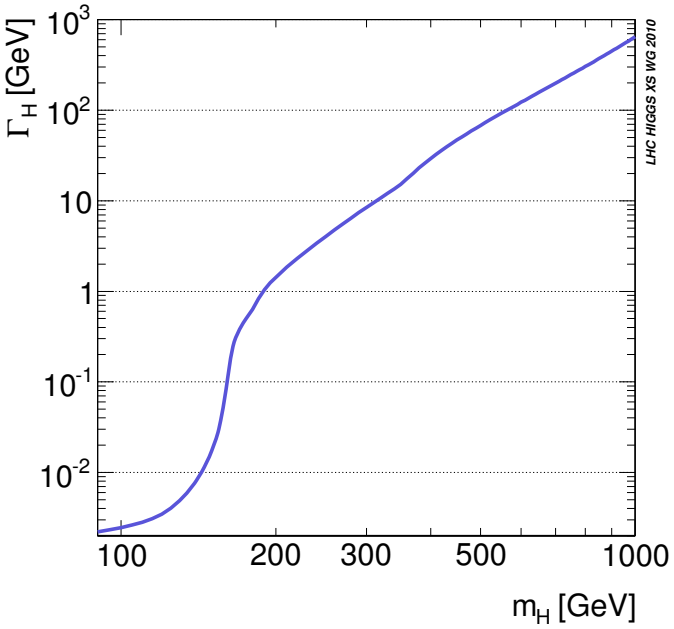

Figure 1.6 – The SM Higgs boson total decay width as a function of Higgs boson mass.

1.6 Higgs Boson Production and Decay

In this section, we describe the main Higgs boson production mechanisms and decay modes at the LHC. The five processes with the largest cross sections are:

— gluon-gluon fusion ($gg \to H$)
— vector boson fusion ($qq \to Hqq$ via $W^+W^-, ZZ \to H$)
— associated production with either a W or a Z boson ($q\bar{q} \to VH, V = W, Z$)
— associated production with $t\bar{t}$ events ($gg, q\bar{q} \to t\bar{t}H$)

The lowest-order Feynman diagrams of those five processes are shown in Fig. 1.7.

The production cross sections of these five processes as a function of the Higgs boson mass are shown in Fig. 1.8. The dominant production mechanism is gluon-gluon fusion, while vector boson fusion is the sub-dominant one. Contributions from associate production with W, Z or $t\bar{t}$ are small ($< 5\%$ in total).

The SM Higgs boson is unstable and decays at tree level into massive particle–anti-particle pairs. The partial decay widths to fermion or weak boson pairs are proportional to the coupling of the Higgs boson to fermions ($g_{Hf\bar{f}}$) or to weak bosons (g_{HVV}), given by:

$$g_{Hf\bar{f}} = \frac{m_f}{v} = (\sqrt{2}G_F)^{1/2} m_f \tag{1.62}$$

$$g_{HVV} = \frac{2m_V^2}{v} = 2(\sqrt{2}G_F)^{1/2} M_V^2 \tag{1.63}$$

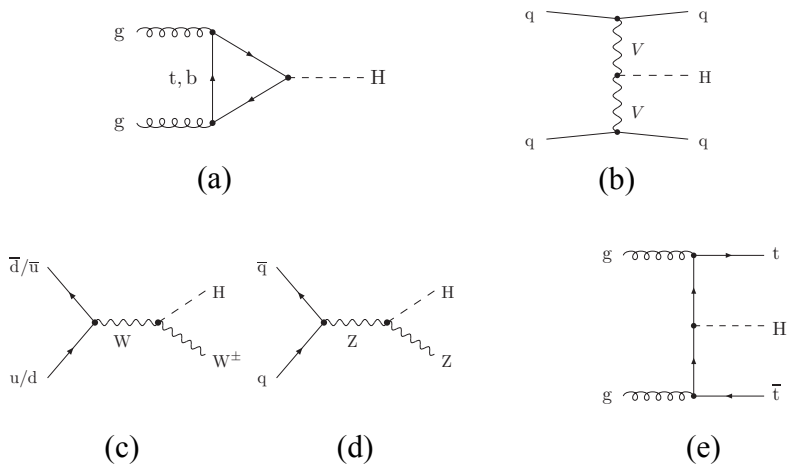

Figure 1.7 – Lowest order Feynman diagrams for the different Higgs boson production processes: gluon-gluon fusion (a), vector-boson fusion (b), associated production with a W (c) or Z (d) vector boson, and associated production with a $t\bar{t}$ pair (e).

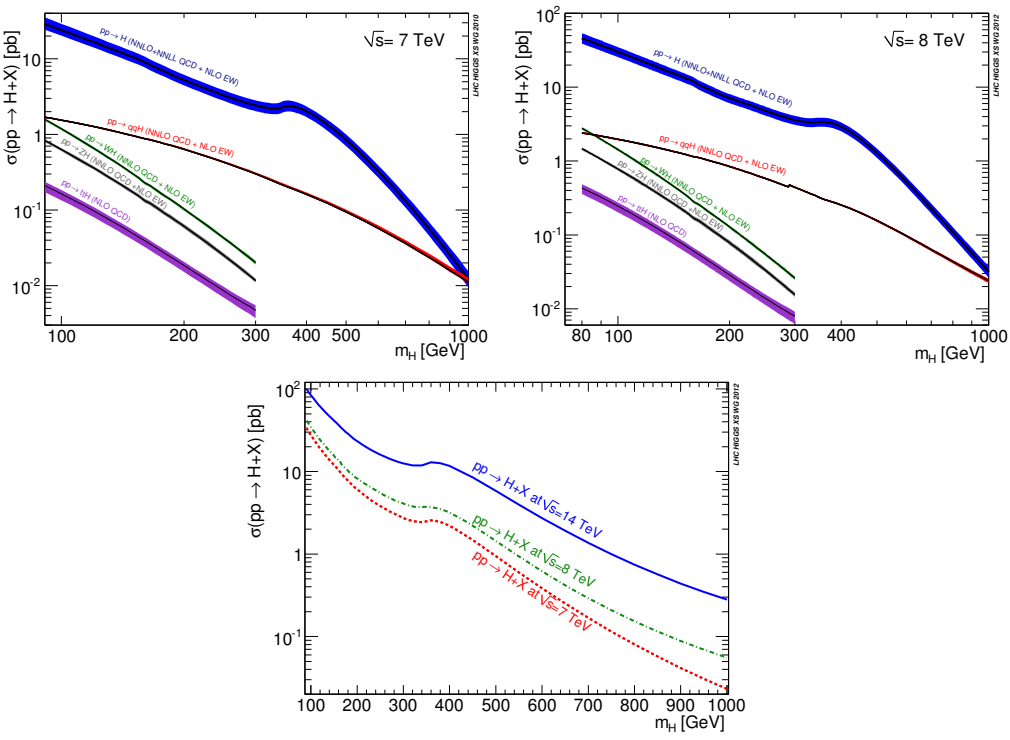

Figure 1.8 – Standard Model Higgs boson production cross sections as a function of the Higgs boson mass, for different production processes, in pp collisions at $\sqrt{s} = 7$ TeV (top-left) and at $\sqrt{s} = 8$ TeV (top-right). The total cross sections at $\sqrt{s} = 7, 8$ and 14 TeV are compared in the bottom plot.

Decays to the final states of $\gamma\gamma, gg, Z\gamma$ are induced at loop-level and are thus usually suppressed. The decay widths of the most important decay modes at the LHC are the following:

- $H \to f\bar{f}$: the leading-order Feynman diagram is shown in Fig. 1.9, on the left plot. Its leading-order decay width is:

$$\Gamma(H \to f\bar{f}) = N_C \frac{G_F m_f^2 m_H}{4\pi\sqrt{2}} \left(1 - \frac{4m_f^2}{m_H^2}\right)^{\frac{3}{2}} \tag{1.64}$$

  where N_C is a colour multiplicity factor: $N_C = 3$ for quarks and $N_C = 1$ for leptons. In the case of decays to light quarks, one has to include gluon exchange and gluon emission in the final state. QCD corrections becomes very important for $H \to b\bar{b}$ and $H \to c\bar{c}$ [15].

- $H \to ZZ$ or WW: the leading-order Feynman diagram is shown in Fig. 1.9, on the right plot. The corresponding decay width is:

$$\begin{aligned}
\Gamma(H \to W^+W^-) &= \frac{G_F m_H^3}{8\pi\sqrt{2}} \left(1 - \frac{4M_W^2}{m_H^2}\right)^{\frac{1}{2}} \left(1 - \frac{4M_W^2}{m_H^2} + \frac{12M_W^4}{m_H^4}\right) \\
\Gamma(H \to ZZ) &= \frac{G_F m_H^3 M_W^2}{16\pi\sqrt{2}M_Z^2} \left(1 - \frac{4M_Z^2}{m_H^2}\right)^{\frac{1}{2}} \left(1 - \frac{4M_Z^2}{m_H^2} + \frac{12M_Z^4}{m_H^4}\right)
\end{aligned} \tag{1.65}$$

- Loop induced decays into $\gamma\gamma, Z\gamma$ and gg: the $H\gamma\gamma$, $HZ\gamma$ and Hgg couplings are generated by loops via massive particles, e.g. W boson and quarks. The leading-order Feynman diagrams for these three processes are shown in Fig. 1.10. Only fermion loops contribute to $H \to gg$, while both fermion and W loops contribute to $H \to \gamma\gamma$ and $H \to Z\gamma$. Among fermions, the top quark gives the largest contribution, since the Yukawa coupling (1.62) between the Higgs boson and the quarks is proportional to the fermion mass. In the $H \to \gamma\gamma$ and $H \to Z\gamma$ decay, the contribution from the W loop diagram dominates over the contribution due to fermion loops. Their leading-order decay widths for $H \to \gamma\gamma$ and $H \to gg$ are:

$$\begin{aligned}
\Gamma(H \to \gamma\gamma) &= \frac{G_\mu \alpha^2 m_H^2}{128\sqrt{2}\pi^3} \left|\sum_f N_C Q^2 f I_f(x) + I_W(x)\right|^2 \\
\Gamma(H \to gg) &= \frac{G_\mu \alpha_s^2 M_H^2}{36\sqrt{2}\pi^3} \left|\frac{3}{4}\sum_Q I_Q(x)\right|
\end{aligned} \tag{1.66}$$

  where $x = \frac{m_H^2}{4M_W^2}$, $\frac{m_H^2}{4m_f^2}$ or $\frac{m_H^2}{4m_Q^2}$. I_f and I_W are dimensionless functions given by:

$$\begin{aligned}
I_f(x)(\ or\ I_Q(x)) &= 2[x + (x-1)F(x)]x^{-2} \\
I_W(x) &= -[2x^2 + 3x + 3(2x-1)F(x)]x^{-2}
\end{aligned} \tag{1.67}$$

  In case of $x \leq 1$:

$$F(x) = arcsin^2\sqrt{x} \tag{1.68}$$

  while in case of $x > 1$:

$$F(x) = -\frac{1}{4}[log\frac{1+\sqrt{1-x^{-1}}}{1-\sqrt{1-x^{-1}}} - i\pi]^2 \tag{1.69}$$

  For $H \to Z\gamma$, the decay width is given by a formula similar to $H \to \gamma\gamma$, but more complicated. Its full expression is given in Ref. [16].

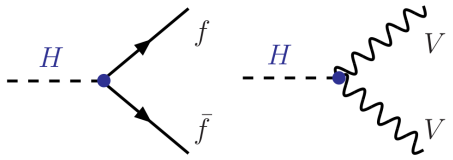

Figure 1.9 – Leading-order Feynman diagram of the Higgs boson decays to fermion-antifermion (left) or weak bosons pairs (right).

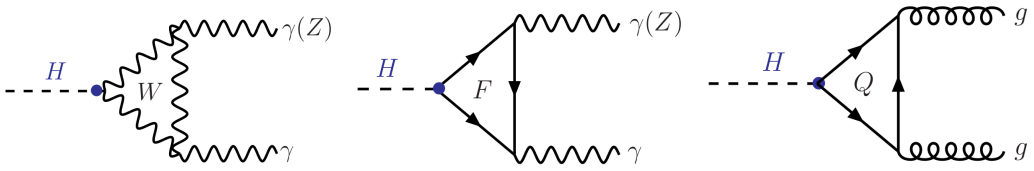

Figure 1.10 – Leading-order Feynman diagram of the Higgs boson decays to $\gamma\gamma$ ($Z\gamma$) (left two pictures) or gg (right picture).

The predicted branching ratios of various final states depend on the Higgs boson mass, as shown in Fig. 1.11, and thus also the sensitivity of each channel in searches for the Higgs boson. A light Higgs boson ($m_H < 135$ GeV) decays mostly into fermions, in particular into a $b\bar{b}$ pair. In the intermediate mass region (GeV $135 < m_H < 160$ GeV), the Higgs boson decays preferentially into WW^*, ZZ^*, where one W or Z boson is produced off-shell (and is thus denoted with a $*$, open up and their branching ratios increase with m_H. In the high mass region ($m_H > 160$ GeV), the Higgs boson decays to two real bosons, WW and ZZ, are dominating. The sensitivity depends also on the signal selection efficiency and purity of the selected sample. For a light Higgs boson, the decays into $b\bar{b}$ final states, though the most abundant, have the worse signal-to-background ratio because of the large QCD background, and the modest di-jet invariant mass resolution. On the other hand, rare decay channels like $H \to \gamma\gamma$ and $H \to ZZ \to \ell\ell\ell\ell$ have very clean final states and significantly better invariant mass resolution, and as a consequence they provide the highest sensitivity to a light Higgs boson signal.

1.7 The $H \to \gamma\gamma$ and $H \to Z\gamma$ Decays

In this thesis, the observation of the Higgs boson via its $H \to \gamma\gamma$ decay and the search for the rare decay $H \to Z\gamma \to \ell\ell\gamma$ in the ATLAS experiment will be discussed. For a Higgs boson mass of 125 GeV, the cross section times branching ratio of the Higgs boson decays into $\gamma\gamma$ is 40 (50) fb at $\sqrt{s} = 7$ TeV (8 TeV), while in the $H \to Z\gamma$ channel it is 27 (34) fb. The expected signal rate is thus quite small. However, in these two channels, all final state particles can be reconstructed in the ATLAS detector with high efficiency and excellent energy resolution, and their invariant mass provides a powerful way to separate the signal (Higgs boson decay) from background. The reconstructed Higgs mass distribution is expected to exhibit a narrow peak with the width dominated by detector resolution, while the background distribution is relatively flat. The backgrounds can be classified into two parts: irreducible background, due to other processes producing the same final states as the Higgs boson decay (*i.e.* $\gamma\gamma$ or $Z\gamma$ continuum production), and reducible background, caused by jets misidentified as photons (*i.e.* γ+jet or Z+jet

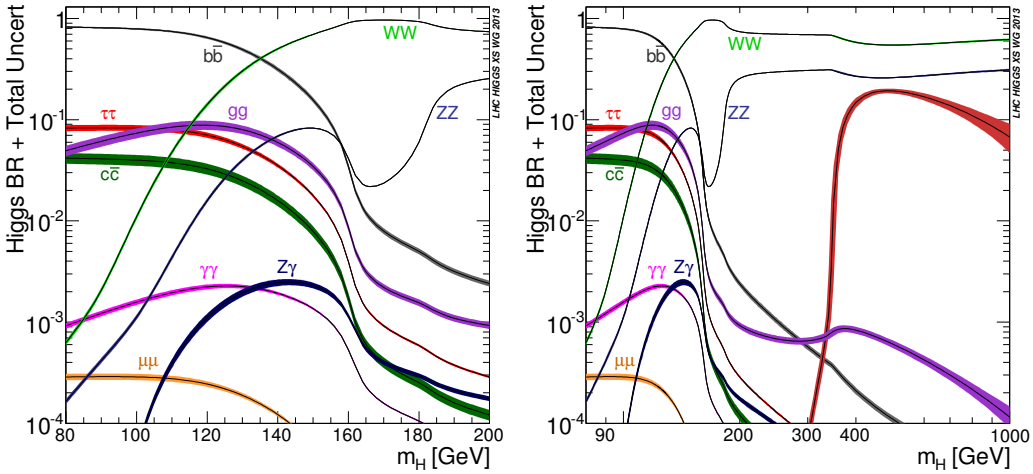

Figure 1.11 – Standard Model Higgs boson decay branching ratios are shown in the left plot for Higgs boson mass in the range [80,200] GeV and in the right plot for Higgs boson mass in the range [80, 1000] GeV.

events). Irreducible backgrounds dominate in both channels. In the $H \to Z\gamma$ analysis, the leading-order diagrams for the irreducible processes ($q\bar{q} \to \ell\ell\gamma$) are shown in Fig. 1.12. In the $H \to \gamma\gamma$ analysis, the irreducible background is given by QCD $\gamma\gamma$ production, whose lowest order diagrams are shown in Fig. 1.13.

In the $H \to \gamma\gamma$ channel, interference between the signal from $gg \to H \to \gamma\gamma$ and the background from $gg \to \gamma\gamma$ can affect the signal decay rate [17] [18], and shift the central value of the di-photon mass peak [19]. By assuming the signal invariant mass resolution to be a Gaussian function, Fig. 1.14 shows the expected di-photon invariant mass distribution (after reconstruction) with and without the inclusion of the interference effects. The central value of the Higgs boson mass shifts to lower values by about 240 MeV.

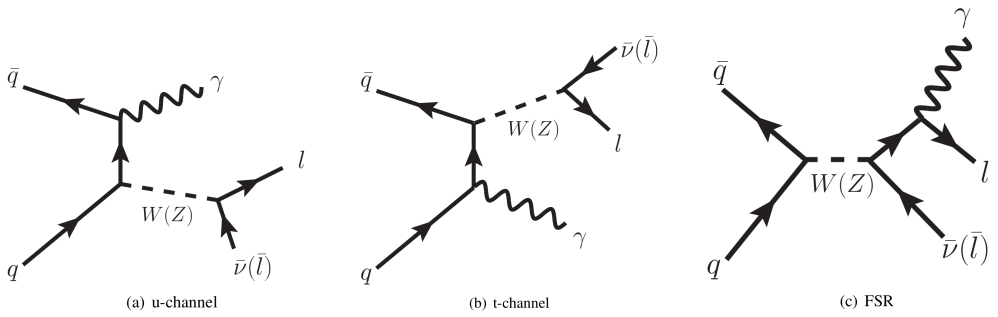

Figure 1.12 – Feynman diagrams of Z+photon production, at leading order(LO).

The $H \to Z\gamma$ kinematics can be described by three angular degrees (Θ, θ and ϕ) as illustrated in Figure 1.15, while only one angle Θ describes the $H \to \gamma\gamma$ kinematics. The angles are defined in the following way:

— Θ: polar angle of the $\gamma\gamma$ or $Z\gamma$ axis in the Higgs rest frame with respect to the LHC beam direction.

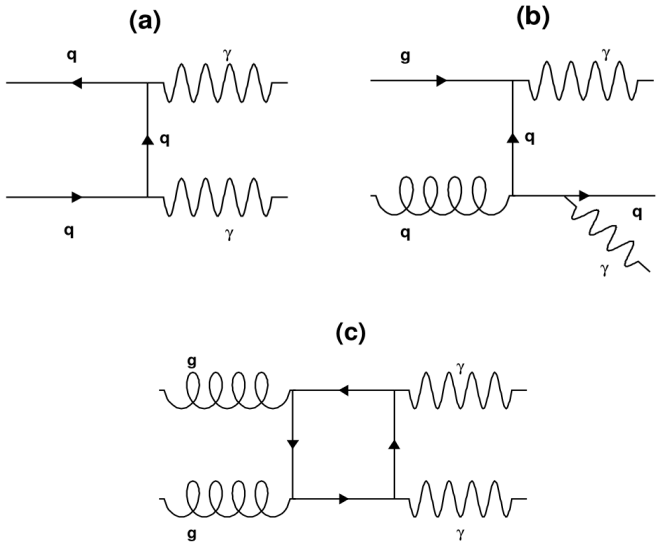

Figure 1.13 – Feynman diagrams of photon pair production, at leading order (LO).

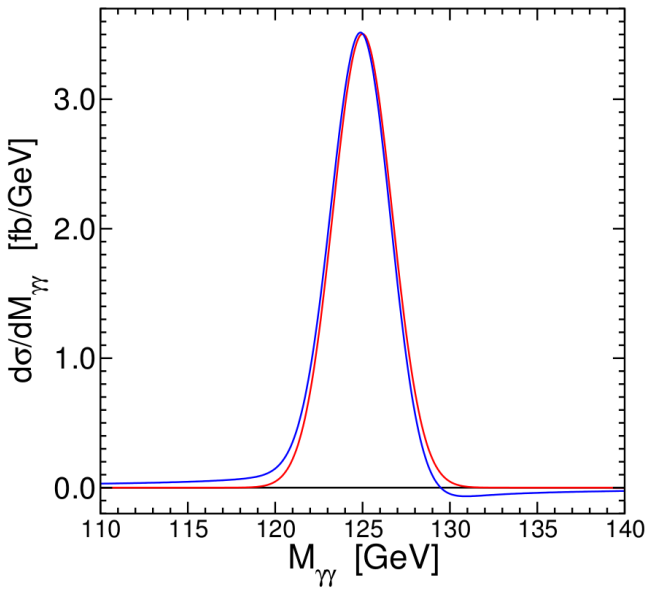

Figure 1.14 – Di-photon invariant mass distributions with a Gaussian mass resolution of width $\sigma_{MR} = 1.7$ GeV. The red curve includes only the Higgs contribution without interference, while the blue curve includes the interference contribution [19].

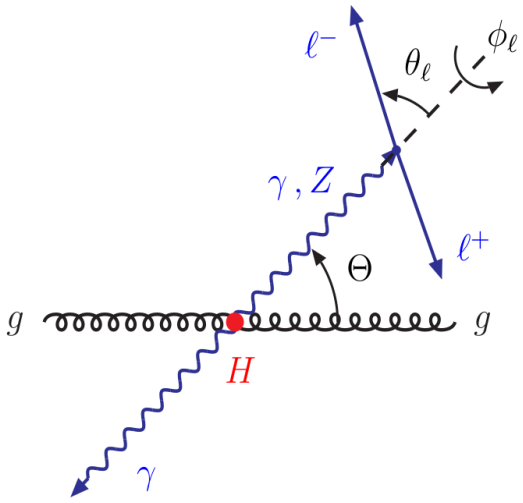

Figure 1.15 – Definition of kinematics of angular in $H \to \gamma\gamma(Z\gamma)$ gluon-gluon fusion production. Θ is defined in the Higgs boson rest frame while θ and η are defined in the Z boson rest frame.

— θ: polar angle of the leptons in the Z decay frame.
— ϕ: azimuthal angle of the leptons in the Z decay frame.

These three angular variables provide good discriminants between alternative Higgs boson spin assignments [20], as well as additional separation between signal and background. The spin-0 characteristic of the Standard Model Higgs boson reflects itself in isotropic decay distribution:

$$\begin{aligned} \frac{1}{\Gamma_{\gamma\gamma}}\frac{d\Gamma_{\gamma\gamma}}{d\cos\Theta} &= 1 \\ \frac{1}{\Gamma_{Z\gamma}}\frac{d\Gamma_{Z\gamma}}{d\cos\Theta} &= 1/2 \end{aligned} \tag{1.70}$$

For any other spin assignment, its distribution would be given by the Wigner function [21]: $|d_{m,\lambda_\gamma-\lambda'_\gamma}(\Theta)|^2$ and $|d_{m,\lambda_Z-\lambda'_\gamma}(\Theta)|^2$, where m denotes the spin component being either 0 or ± 2, while $\lambda_\gamma - \lambda'_\gamma = 0, \pm 2$ and $\lambda_Z - \lambda'_\gamma = 0, \pm 1, \pm 2$. The separations of the Standard Model Higgs boson(spin-0) from various spin-2 hypothesises and background process are significant in $\cos\Theta$ distributions, as shown in Fig. 1.16. The $\cos\theta$ and ϕ distributions of spin-0 and various spin-2 hypotheses are shown in Fig. 1.17 [22].

In the Standard Model $H \to \gamma\gamma$ and $Z\gamma$ decays are rare decays induced by loop diagrams, and are thus sensitive to physics beyond the Standard Model, for instance to the presence of scalar singlets [23], Gauge-Higgs unification models [24], and Two Higgs Doublet Models(2HDM) [25], which can enhance or suppress their branching ratios compared to the SM prediction. If the Higgs boson is a composite Nambu-Goldstone boson [26], its decays to $Z\gamma$ can be modified by the exchange of new particles with mass much larger than the electroweak scale. These effects can provide the possibility to probe the dynamics underlying electroweak symmetry breaking. As an example, in the Inert Doublet Model(IDM) [27], decay rates of $H \to \gamma\gamma$ (denoted as $R_{\gamma\gamma}$) and $H \to Z\gamma$ (denoted as $R_{Z\gamma}$) normalised by their respective SM expectations correlate positively as shown in figure 1.18. The continuous line represents the behaviour of $H \to \gamma\gamma$ and $Z\gamma$ rates enhanced or suppressed by the same parameters associated with charged scalar. While the straight

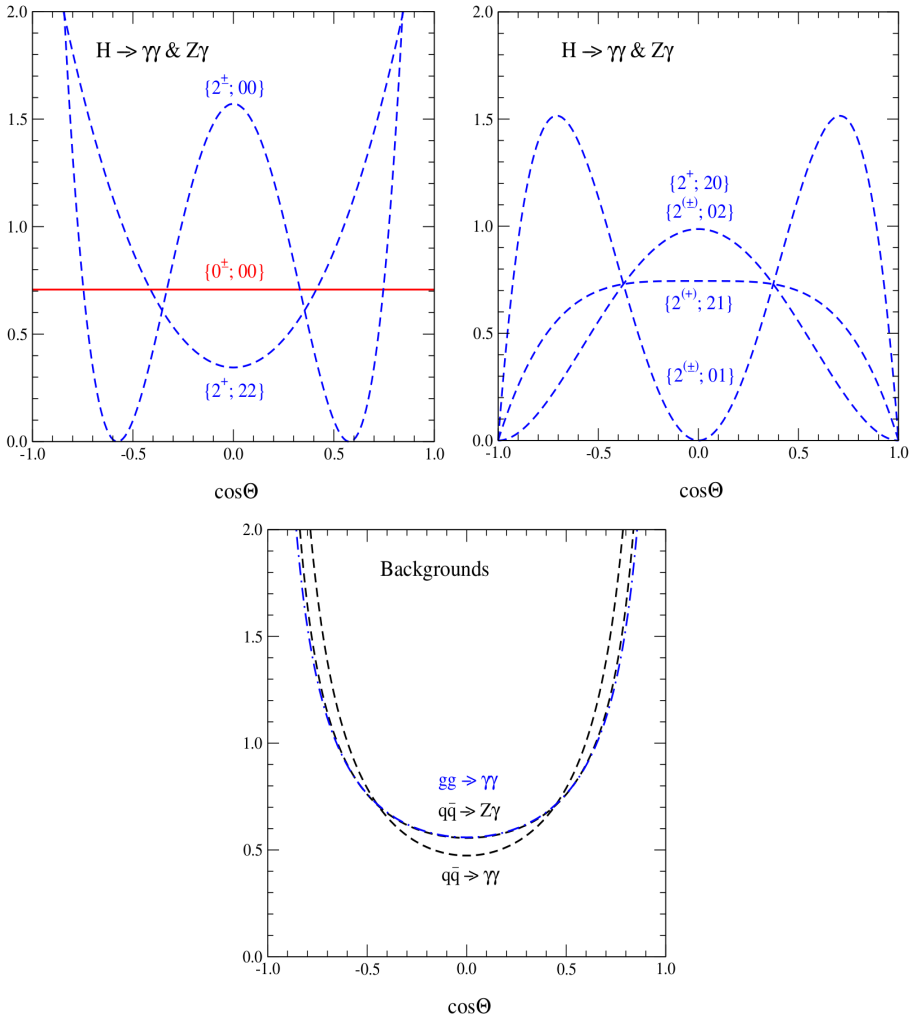

Figure 1.16 – Angular distributions of signal ($H \to \gamma\gamma$ or $Z\gamma$) and background ($\gamma\gamma$ or $Z\gamma$ in QCD processes). Top-left: spin-0 and spin-2 (even or odd parity) signal distributions; Top-right: all the spin-2 distributions. Bottom: background distributions [20].

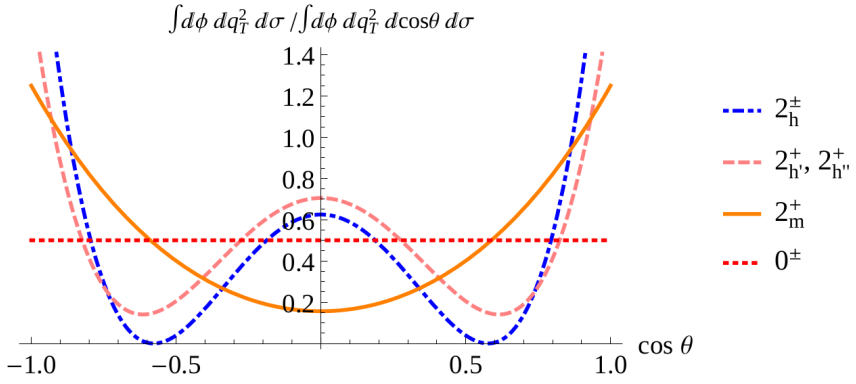

Figure 1.17 – Distributions of $\cos\theta$ in the $H \to \gamma\gamma$ channel, for a spin-0 Higgs boson and for various spin-2 scenarios [22].

line below (1,1) is for the case that $R_{\gamma\gamma}$ and $R_{Z\gamma}$ are damped by a big common constant from invisible decay channels where the Higgs boson decays to inert scalars (also called dark scalars or D-scalars), which dominates over the charged scalar contributions. This correlation gives a probe to examine IDM.

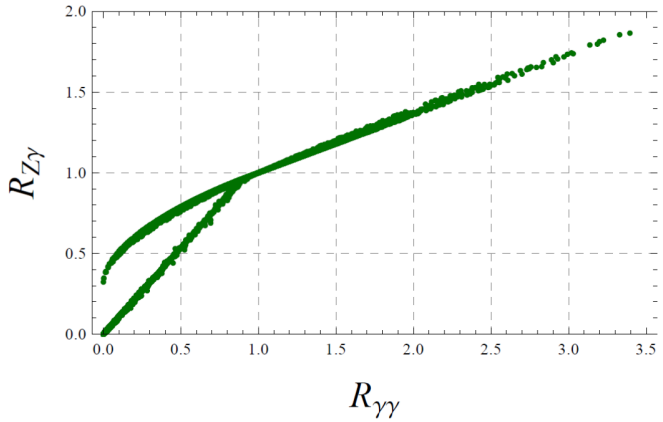

Figure 1.18 – Correlation between $R_{\gamma\gamma}$ and $R_{Z\gamma}$ is predicted in Inert Doublet Model [27]. The continuous line and the straight line below (1,1) represent the effects of two models, which is explained in text.

Chapter 2

The Large Hadron Collider and the ATLAS detector

2.1 The Large Hadron Collider

The Large Hadron Collider (LHC) is the world's largest and most powerful particle accelerator. It is installed in the 27 km-long LEP [28, 29] tunnel, located 100 meters underground, beneath the Franco-Swiss border near Geneva. It was built by the European Organization for Nuclear Research (CERN) from 1998 to 2008. Its main goals are precise tests of the Standard Model and searches for the Higgs boson and physics beyond the Standard Model. It accommodates four main experiments: ATLAS, ALICE, CMS and LHCb. ATLAS (A Toroidal LHC ApparatuS) [30] and CMS (Compact Muon Solenoid) [31] are two general-purpose detectors, which investigate a wide range of physics, from searches for new phenomena such as the Higgs boson, extra dimensions and dark matter particles to measurements of known processes with higher precision and at previously unexplored high energies. ALICE (A Large Ion Collider Experiment) is a detector designed for the study of the physics of strongly interacting matter at extreme energy densities, where a state of matter called quark-gluon plasma forms [32]. The LHCb (Large Hadron Collider beauty) experiment investigates the slight differences between matter and antimatter by studying the properties of hadrons containing a b quark [33].

The LHC injector complex is shown in Fig. 2.1. The protons are originally stripped off hydrogen gas by an electric field and injected into the first accelerator, Linac2. There they are accelerated to an energy of 50 MeV before being injected into the Proton Synchrotron Booster (PSB). The PSB accelerates the protons to 1.4 GeV and is followed by the Proton Synchrotron (PS), which increases the proton energy to 25 GeV. The protons are then sent to the Super Proton Synchrotron (SPS), where they are accelerated to 450 GeV. They are finally transferred to the two beam pipes of the LHC, in which proton bunches circulate in opposite directions. The proton beams are linearly accelerated by the electric field in radio frequency (RF) cavities and are bent in the magnetic field generated by superconducting dipoles. The magnets, providing a magnetic field maximum of 8.3 T, are built from coils of NbTi Rutherford cable kept at cryogenic temperatures ($-271.3°$C). For this reason, much of the accelerator is connected to a distribution system of liquid helium which cools the magnets, as well as to other supply services.

The LHC is designed to provide proton-proton collisions at centre-of-mass energy of 14 TeV (7 TeV per beam), with a peak luminosity of 10^{34} cm^{-2}s^{-1}. Fig. 2.2 shows the cross sections of several processes of interest based on the center-of-mass energy of proton-(anti)proton collisions.

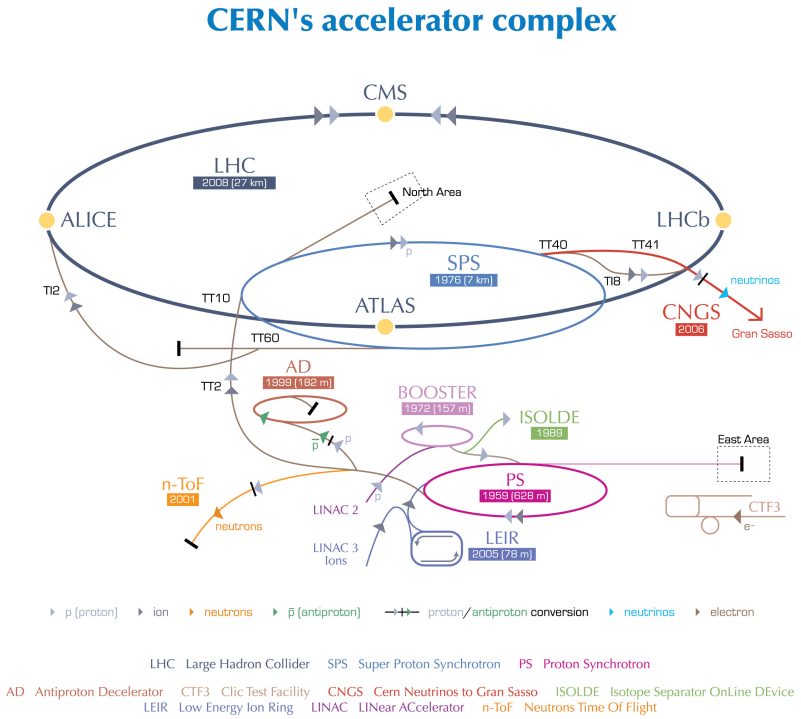

Figure 2.1 – The LHC accelerator injection complex.

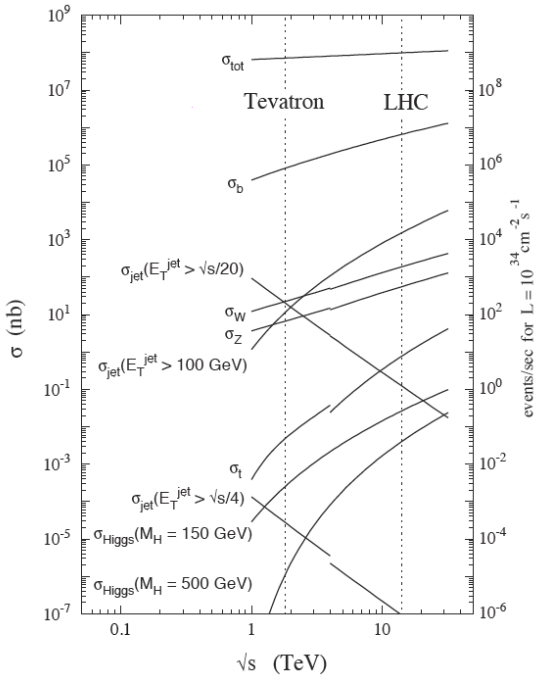

Figure 2.2 – Cross sections (σ) versus centre-of-mass energy ($\sqrt{s}$) for specific physics processes. The two dotted lines show the centre-of-mass energies of two hadron colliders: the Tevatron at 1.96 TeV, and the LHC at the design value of 14 TeV.

The first proton-proton collisions of the LHC were produced on November 23, 2009 at the injection energy of 450 GeV per beam. On March 30, 2010, the first collision took place between 3.5 TeV beams, setting a world record for the highest-energy man-made particle collisions. During 2010 and 2011, both ATLAS and CMS detectors collected about 5.1 fb^{-1} of pp collisions at $\sqrt{s} = 7$ TeV, with a peak instantaneous luminosity increasing from 10^{27} $\text{cm}^{-2}\text{s}^{-1}$ to 3.65 $\times$ 10^{33} $\text{cm}^{-2}\text{s}^{-1}$. In 2012, the beam energy was increased to 4 TeV and the peak luminosity rised to 7.7 $\times 10^{33} cm^{-2} s^{-1}$. In almost one year of running, about 21.3 fb^{-1} of pp collisions at $\sqrt{s} = 8$ TeV were delivered to both ATLAS and CMS. The LHC was then shut down for consolidation and upgrade. It will be restarted in 2015 with a center-of-mass energy close to the design value of $\sqrt{s} = 14$ TeV and a peak luminosity of 10^{34} $\text{cm}^{-2}\text{s}^{-1}$. Fig. 2.3 shows the integrated luminosity delivered to ATLAS at $\sqrt{s} = 7$ and 8 TeV as a function of time. A summary of the running parameters at $\sqrt{s} = 7$ and 8 TeV as well as the design values are given in Table 2.1.

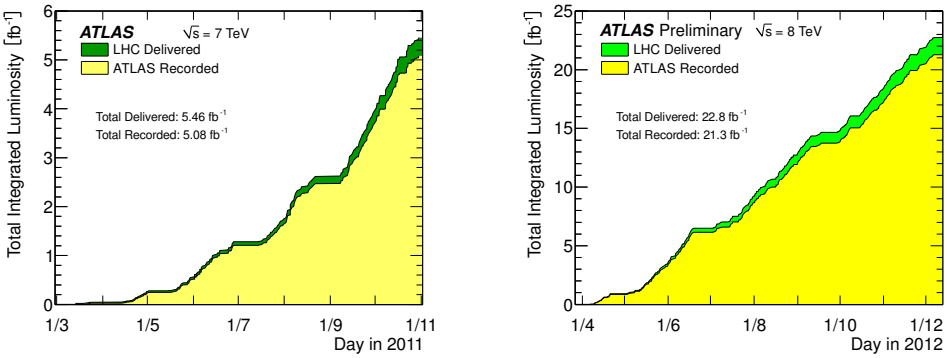

Figure 2.3 – Integrated luminosity delivered by LHC and collected by ATLAS are shown: 2011 at $\sqrt{s} = 7$ TeV (left), 2012 at $\sqrt{s} = 8$ TeV (right).

Table 2.1 – Summary of the running parameters at $\sqrt{s} = 7$ and 8 TeV and at the design value of $\sqrt{s} = 14$ TeV.

Parameter	2010	2011	2012	nominal
circumference [km]		27		
beam energy [TeV]	3.5	3.5	4.0	7.0
peak instantaneous luminosity (L) [$\text{cm}^{-2}\text{s}^{-1}$]	2.1×10^{32}	3.7×10^{33}	7.7×10^{33}	1.0×10^{34}
integrated luminosity ($\int Ldt$) per year [fb^{-1}]	0.045	5.1	21.3	80
number of colliding bunches (n_b) per beam	368	1380	1380	2808
time between collisions [ns]	150	50	50	25
protons per bunch	1.2×10^{11}	1.5×10^{11}	1.6×10^{11}	1.15×10^{11}

2.2 The ATLAS Detector

ATLAS is the largest particle detector ever constructed. It is 46 m long, 25 m high, 25 m wide, weighs 7000 tons, and covers almost the whole 4π solid angle. The detector layout is shown in Fig. 2.4. ATLAS is composed of 3 subdetectors: the Inner Detector (ID), the calorimeter and the Muon Spectrometer (MS). The ID is composed of three subdetectors,

the Pixel detector, the Silicon Micro strip (SCT) detector and the Transition Radiation Tracker (TRT) detector. The calorimeter, based on LAr and scintillating tile sections, has an electromagnetic component and a hadronic component. A solenoidal magnet surrounds the ID and provides a magnetic field of 2T inside its volume, while 3 toroid magnets generate the magnetic field needed for tracking inside the MS. To reduce the enormous amount of data produced by the pp collisions, ATLAS records events conditionally using an advanced "trigger" system that keeps only events that are potentially interesting for the ATLAS physics programme. The design performance goals of the ATLAS detector are summarized in Table 2.2. More details on the sub-detectors and their performance are given in the following sections.

ATLAS uses the following right-handed Cartesian coordinate system. The origin of the coordinate system corresponds to the nominal beam interaction point, located at the center of the detector. The z-axis is given by the beam direction and the $x-y$ plane is orthogonal to the beam direction. The x-axis points from the interaction point towards the center of the LHC ring. The y-axis points upwards. The azimuthal angle in the x-y plane is referred to as ϕ, while θ is the polar angle with respect to the z-axis. The pseudorapidity is defined as $\eta = -\ln[\tan(\theta/2)]$.

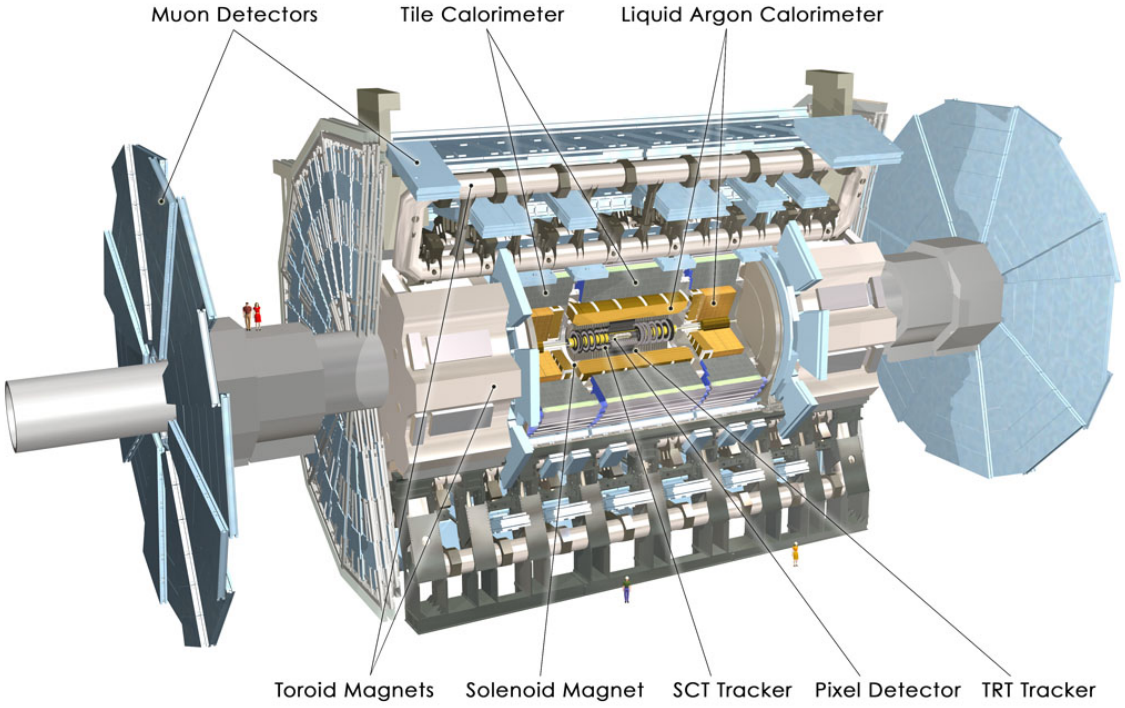

Figure 2.4 – Cut-away view of the ATLAS detector.

2.2.1 The Magnet System

ATLAS features a unique hybrid system of four large superconducting magnets. This magnetic system is 22 m in diameter and 26 m in length, with a stored energy of 1.6 GJ. It consists of a central solenoid, a barrel toroid and two end-cap toroids. The central solenoid is aligned on the beam axis and provides a 2 T axial magnetic field for the inner detector. To achieve the desired calorimeter preformance, its material thickness was optimised to

Table 2.2 – ATLAS general design performance goals.

Detector component	Required resolution (E: [GeV])	η coverage (Measurement)	η coverage (Trigger)
Tracking	$\sigma_{p_T}/p_T = 0.05\%/p_T \oplus 1\%$	± 2.5	
EM calorimetry	$\sigma_E/E = 10\%/\sqrt{E} \oplus 0.7\%$	± 3.2	$\pm$ 2.5
Hadron calorimetry(jets)			
barrel and end-cap	$\sigma_E/E = 50\%/\sqrt{E} \oplus 3\%$	± 3.2	± 3.2
forward	$\sigma_E/E = 100\%/\sqrt{E} \oplus 10\%$	$3.1 < \|\eta\| < 4.9$	$3.1 < \|\eta\| < 4.9$
Muon spectrometer	$\sigma_{p_T}/p_T = 10\%$ at $p_T = 1$TeV	± 2.7	± 2.4

be as low as possible, resulting in the solenoid assembly contributing a total of ~ 0.66 radiation lengths (X_0) at normal incidence.

The barrel and two end-cap toroids produce toroidal magnetic field of ~ 0.5 T and ~ 1 T for the muon detectors in the central and end-cap regions. The barrel toroid consists of eight coils encased in individual racetrack-shaped, stainless-steel vacuum vessels. Each end-cap toroid consists of a single cold mass built up from eight flat, square coil units and eight keystone wedges, bolted and glued together into a rigid structure to withstand the Lorentz forces. The two end-cap toroids generate the magnetic field in the end-cap regions in order to optimising the bending power of the muon spectrometer system.

2.2.2 The Inner Detector

At design luminosity and centre-of-mass energy, about 1000 particles emerge from the collision point every 25 ns within the $|\eta| < 2.5$ region. Within the same brunching crossing, about 40 inelastic pp collisions, called "in-time pile-up", take place at high instantaneous luminosity. This presents a challenge for the ATLAS Inner detector to disentangle a track from the others. Reconstructing the collision points (primary vertices), secondary vertices from decays of long-lived particles or interactions with the detector material and measuring precisely the charge particles' momenta are achieved by the precision tracking detectors (Pixel and SCT detector) in conjunction with the TRT detector. A schematic view of the Inner detector is shown in Fig. 2.5. The Pixel and SCT detectors provide precision tracking in the $|\eta| < 2.5$ region. In the Pixel detector, three layers of concentric cylinders are arranged around the beam axis in the barrel region, with silicon pixel sensors whose intrinsic hit accuracies are 10μm $\times 115\mu$m in $R - \phi \times z$. In the end-cap region there are six disks of sensors (three disks in each end-cap region) perpendicular to the beam axis, with silicon pixels providing intrinsic accuracies of 10μm $\times 115\mu$m in $R - \phi \times R$. The innermost pixel layer (also called the B-layer) is located at a radius of 50 mm from the beampipe, and provides precision information for vertexing. The SCT consists of 8 layers of silicon micro strips in the barrel which provide 4 space points for a crossing track with stereo pairs of SCT layers, and nine disks in each end-cap. Its intrinsic accuracy is 17μm $\times 580\mu$m in $R - \phi \times z$ in the barrel region, and 17μm $\times 580\mu$m in $R - \phi \times R$ in the end-cap region. The TRT only provides $R - \phi$ information for the hit by means of straw tubes in $|\eta| < 2.0$. Typically, 36 hits per track are detected. The intrinsic accuracy is 130 μm in $R - \phi$. In the barrel region, the straws are parallel to the beam axis while in the end-cap region they are arranged radially in wheels.

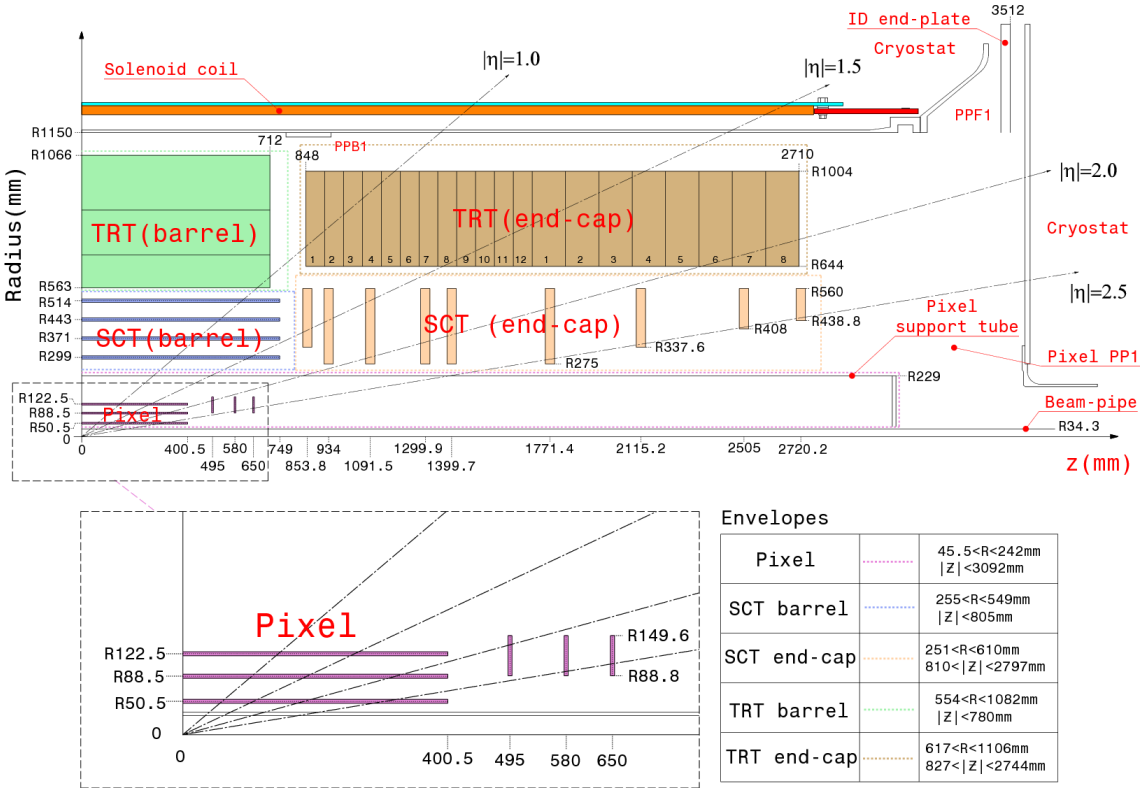

Figure 2.5 – Side view of the Inner Detector with its main elements, active dimensions and envelope.

2.2.3 The Calorimeters

A cut-away view of the calorimeter system is shown in Fig. 2.6. The calorimeter covers the $|\eta| < 4.9$ region and is composed by an Electromagnetic Calorimeter (ECAL) and a Hadronic Calorimeter (HCAL). Fine granularity in the central region ($|\eta| < 2.5$) is provided by the ECAL for precision measurements of photons and electrons. Coarser granularity in the forward region extends the acceptance for jet reconstruction and improves the missing E_{T} (E_{T}^{miss}) resolution.

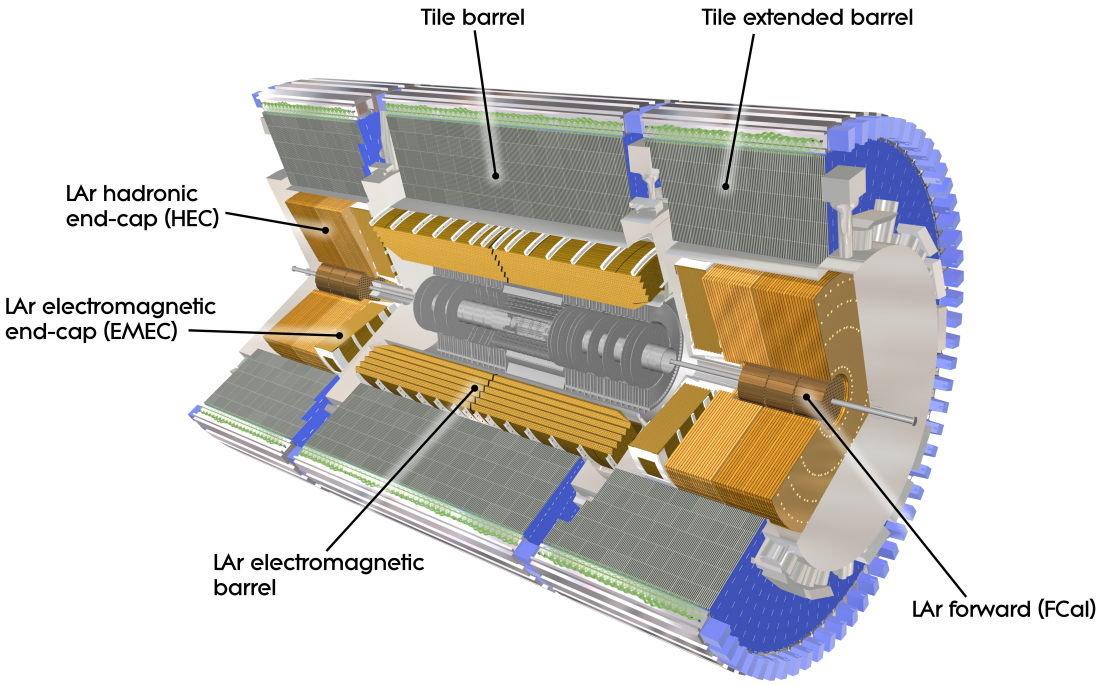

Figure 2.6 – Cut-away view of the ATLAS calorimeter system.

The thickness of the ECAL is more than 22 radiation lengths (X_0) in the barrel and more than 24 X_0 in the end-cap, in order to fully contain the showers of photons and electrons. The ECAL is a lead-liquid argon sampling detector with accordion-shaped kapton electrodes and lead absorber plates. It consists of a barrel section, which covers the pseudorapidity region $|\eta| < 1.475$ and has three longitudinal layers, and two end-cap sections covering $|\eta|$ in [1.375, 3.20]. The end-cap is longitudinally segmented into three layers for $|\eta|$ in [1.375, 2.5] and into two layers in the more forward region (covering $|\eta|$ in [2.5, 3.2]). A sketch of an electromagnetic calorimeter barrel module is shown in Fig. 2.7. The first layer (also called "strip layer") has a typical granularity of 0.0031 $\times$ 0.098 in $\Delta\eta \times \Delta\phi$, providing a powerful discrimination between showers initialted by single isolated photons and those due to multiple photons from decays of neutral mesons within jets. The strip layer also offers a precise measurement of the pseudorapidity of the impact point and thus of the photon direction when combined with information from either the second layer, the event primary vertex or, in case of photon conversions, the position of the conversion vertex. The second layer of the ECAL, which collects most of the energy of photon and electron showers, has a granularity of $\Delta\eta \times \Delta\phi = 0.025 \times 0.025$. The

third layer collects only the tail of the EM shower and has thus a coarser segmentation in η. It is used to estimate the energy leaking in the HCAL and as a presampler for the reconstruction of hadronic jets. The transverse size of the cells in this layer is $\Delta\eta \times \Delta\phi = 0.05 \times 0.025$. In the region $|\eta| < 1.8$, a LAr pre-sampler detector is used to estimate the energy lost by photons and electrons upstream of the calorimeter.

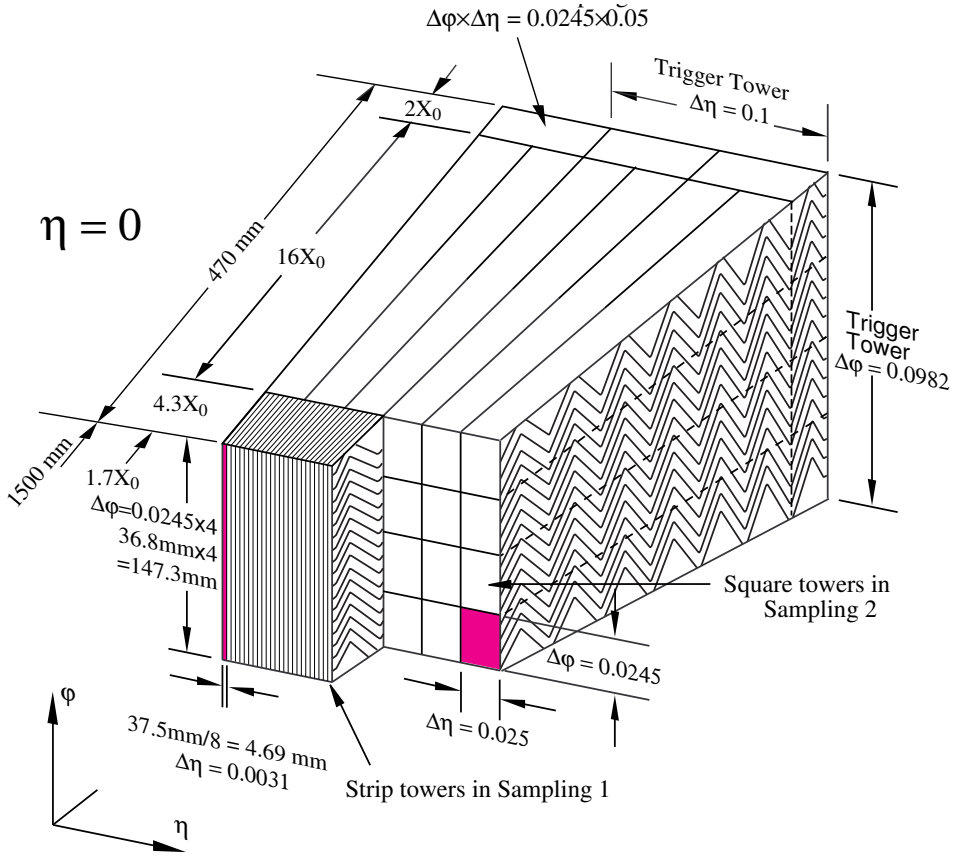

Figure 2.7 – Sketch of a barrel module of the Electromagnetic Calorimeter with the different layers in depth.

The Hadronic Calorimeter is divided into three parts: a tile calorimeter in the barrel, a liquid argon hadronic end-cap calorimeter (HEC) and a liquid-argon forward calorimeter (FCal). The tile calorimeter is a sampling detector using steel as the absorber and scintillator as the active medium. It covers the region $|\eta| < 1.7$, and is subdivided into a central barrel ($|\eta| < 1.0$) and two extended barrels ($0.8 < |\eta| < 1.7$). The HEC is a copper/liquid-argon sampling calorimeter, with a flat-plate design, located in the end-cap region $1.5 < |\eta| < 3.2$. The FCal is a copper-tungsten/liquid-argon sampling calorimeter located in the same cryostat as the end-cap calorimeter, and covers the forward region of $3.1 < |\eta| < 4.9$. The overlaps of the HEC with the tile calorimeter ($1.5 < |\eta| < 1.7$), and with the FCal ($3.1 < |\eta| < 3.2$) are used to improve the energy measurement in the transition regions.

2.2.4 The Muon Spectrometer

The MS, shown in Fig. 2.8, surrounds the hadronic calorimeter. It provides, for charged particles passing beyond the HCAL, precision momentum measurement for $|\eta| < 2.7$ and trigger capability for $|\eta| < 2.4$. Muon momenta down to ∼3 GeV can be measured by the MS alone. The muon spectrometer can also provide adequate momentum resolution (about 10%) and excellent charge identification at very high p_T, up to 3 TeV. In the barrel region, precision-tracking chambers are located between and on the eight coils of the superconducting barrel toroid magnet. The chambers are arranged in three concentric cylindrical shells around the beam axis at radii of approximately 5 m, 7.5 m and 10 m. In the end-cap region, the muon chambers are installed in front and behind the end-cap toroid magnets. They are located at distances of $|z| \approx 7.4$ m, 10.8 m, 14 m and 21.5 m from the interaction point.

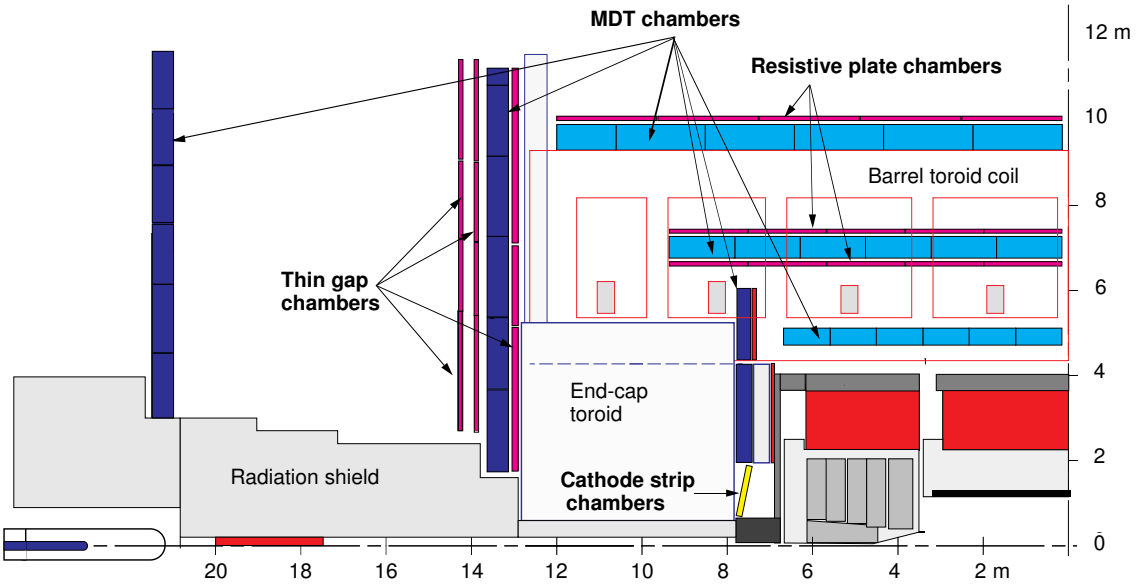

Figure 2.8 – Cross-section of the muon system in R-z plane.

The muon spectrometer uses four different detection technologies: Monitored Drift Tubes (MDTs), Cathode Strip Chambers (CSCs), Resistive Plate Chambers (RPCs) and Thin Gap Chambers (TGCs). Magnetic bending is provided by a large barrel toroid in $|\eta| < 1.6$ and by two end-cap toroids in $1.4 < |\eta| < 2.7$. The MDTs measure the track momenta precisely over most of the η range, and are supplemented by CSCs at larger pseudorapidities ($2.0 < |\eta| < 2.7$). The trigger system uses RPCs in the barrel and TGCs in the end-cap. In the $|\eta| < 0.1$ region there is a gap for services to the inner components of the ATLAS detector. The main parameters of the muon spectrometer are listed in table 2.3.

2.2.5 The ATLAS Trigger

The ATLAS trigger system is divided into three levels: Level-1 (L1), Level-2 (L2) and Event Filter (EF). Each trigger level operates on events that pass the selection at the previous level. The L1 trigger is based on custom-made electronics. It selects events with signatures of muons, electrons, photons, jets and τ leptons with transverse momenta above certain thresholds. It also selects events with large missing transverse energy (E_{T}^{miss}) or

Table 2.3 – Main parameters of the muon spectrometer.

Component	MDTs	CSCs	RPCs	TGCs
Coverage ($\|\eta\|$)	< 2.7 (inner most layer < 2.0)	[2.0, 2.7]	< 1.05	[1.05, 2.7] (2.4 for triggering)
Number of chambers	1088 (1150)	32	544 (606)	3588
Number of channels	339000 (354000)	31000	359000 (373000)	318000

large total transverse energy. The L1 trigger makes a decision within 2.5 μs after each bunch crossing based on event data of reduced granularity of a subset of detectors and accepts events at a rate of about 75 kHz, using a limited amount of the total detector information. In each selected event, the L1 trigger defines one or more Regions-of-Interest (RoIs), where potentially interesting signatures are identified. These regions correspond to about 2% of the total detector. The L2 and EF triggers together are called the High-Level-Trigger (HLT). The L2 trigger selects events based on the partial event information in the ROIs. Its execution time is about 40 ms. The designed acceptance rate is below 3.5 kHz. The EF level trigger uses full event information and the same object reconstruction algorithms as offline. The designed acceptance rate is 200 Hz. Its execution time is about 4 second per event.

2.3 Photon Reconstruction

Photons in ATLAS are reconstructed through their interactions with the ECAL or by detecting their conversions to e^+e^- in the material upstream of the calorimeter. The reconstruction of photon conversions increases the reconstruction efficiency of particles decaying to photon final states, e.g. Higgs boson or graviton decaying to photon pairs. Mapping the photon conversion vertices also provides a precise localisation of the Inner Detector materials.

Both photons and electrons deposit their energy in the EMC, forming a cluster of calorimeter cells with significant energy deposits. Electrons and photon conversions are characterized by at least one track mateched to an EM cluster. In the case of photon conversions, the track (tracks) is (are) originating from a conversion vertex candidate. The unconverted photons are reconstructed as a cluster with no track matched to it.

Photons which convert within a radial distance of 300 mm from the beam axis may be reconstructed with high efficiency from standard Si-seeds tracks (inside-out tracking), while photons which convert further from beam axis may be reconstructed from tracks formed with TRT seeds with few Si hits (outside-in tracking) or no Si hits at all (TRT-standalone).

The inside-out track reconstruction is sensitive to conversions inside Pixel detector. A segment is first formed using the hits in the silicon detectors. A Kalman fitter is then used to add successive hits to the track. Finally, a possible TRT extension is used to do a global fit. According to the fit quality with or without additional TRT extension, the reconstructed inside-out tracks are classified into three categories:

- Tracks with extensions which are used in the global fit.
- Tracks with extensions which are not used in the global fit.
- Tracks without TRT extension ($|\eta| > 2$).

A good track is required to have at least seven hits in the SCT.

The outside-in track reconstruction is used to reconstruct mainly conversions that take place beyond the silicon detectors. It starts by forming TRT segment seeds, extrapolates them to the Si detectors, and tries to match them with hits not already used to reconstruct inside-out tracks. It is only effective in the $|\eta| < 2.1$ region because of the limited acceptance of the TRT. The initial TRT segments are formed using a histogram technique [34], and extended back to the SCT, where at least two hits in the last three layers are required. A minimum of two space points together with the third one provided by the first hit in the initial TRT segment is fitted to form a track candidate. Finally, a global fit is performed on the track candidate and its extensions in the TRT detector.

After the previous two steps of reconstructions, the remaining TRT segments not extended to the Si detectors are used to find stand-alone TRT tracks. There is no fit in this step, but all segments are scored and arranged to reject the tracks which share too many straw hits.

Conversion vertices associated to two tracks are reconstructed by performing a constraint fit on the parameters of the two electron tracks with the constraints originating from the photon being massless. In some cases, only one conversion track may be reconstructed, typically for very asymmetric decays in which one of the two electrons is very soft (less than 0.5 GeV), or the conversion happened at high radii where the TRT resolution is insufficient to separate the two tracks. In those cases, the conversion vertex is defined as the first measurement of the participating track.

The conversion track candidates (single- and double-track conversions) are matched to electromagnetic clusters to form the (single- and double-track) converted photons. The matching is done as follows. The measured track in the ID is extrapolated to the second layer of the electromagnetic calorimeter. If there is any clusters inside a cone of radius 0.05 in (η, ϕ) around the impact point of the track at the calorimeter, the cluster is considered to be matched to the track. The cone size is extended to 0.1 in ϕ on the side where the bremsstrahlung losses are expected during the track extrapolation. There are three algorithms to do the track-cluster matching extension:

- single-track extension: the track is extrapolated to the second sample of the electromagnetic calorimeter.
- double-track extension where one of the track momenta is 4 times smaller than the other: the original converted photon direction is reconstructed from the two electron tracks and a straight line (originating from conversion vertex and going along in the reconstrcuted photon direction) is extended to the second layer of the electromagnetic calorimeter.
- double-track extension where the two track momentums are not very much different (less than a factor of 4) from each other: the two tracks are extended individually to the electromagnetic and matched to two clusters. If both two tracks are matched to electromagnetic clusters, the conversion vertex is considered as matched to the EM cluster.

In order to clean backgrounds from the electromagnetic clusters, the fraction of energy in each longitudinal compartment of the ECAL with respect to the total must be less than 90% in the PS and the strip-layer, 98% in the second layer and 80% in the third one.

Almost all the converted photons and around 10% of the unconverted photons (typically at low p_T) are reconstructed as electrons. Recovery of photons from the electron collection is done in the following way. Electrons are considered as converted photons if their best matched track (the one with the impact point closest to the energy barycenter)

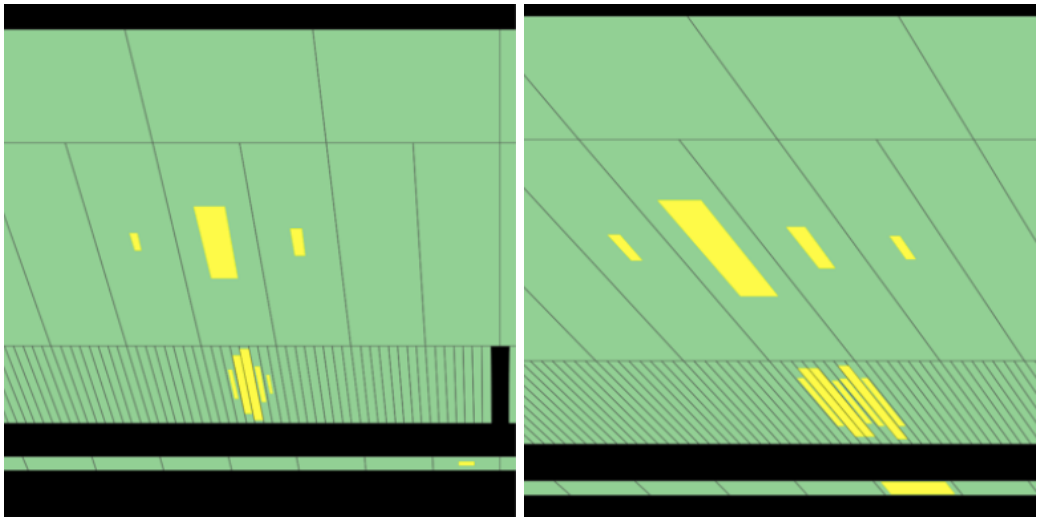

Figure 2.9 – Event display of a prompt photon candidate (left) and of a fake photon candidate (right).

coincides with any of the tracks originating from a conversion vertex and matched to the same cluster. The only exception is the case of double-track conversions where only one track has a B-layer hit. Electrons with only TRT hits and with $p_T > 2$ GeV and $E/p < 10$ are also considered as converted photons. Electrons whoses tracks have one TRT hit and $p_T < 2$ GeV are considered as unconverted photons. Finally, electrons which failed to be considered as converted photons and have track $p_T < 2$ GeV or $E/p > 10$, are treated as unconverted photons.

2.4 Photon Identification

In collision events, after the reconstruction the collection of photon candidates contains a significant number of background candidates ("fake" photons) from jets with a large electromagnetic component. Most of the fake photons are due to neutral particles (π^0, η) decaying to photon pairs. Two event displays of a photon candidate and of a fake photon candidate are shown in Figure 2.9. Prompt photons deposit narrow showers in the EM calorimeter and have less leakage in the hadron calorimeter compared to fake photons. A group of discriminating variables (DVs) based on the lateral and longitudinal profiles of the energy deposited in the calorimeter is used to distinguish photons from fakes. These variables are defined in the following way:

- **Leakage in the hadronic calorimeter**
  The photons are expected to have less leakage in the HCAL, located beyond the ECAL, compared to the fakes from hadronic jets. The total transverse energy $E_{\mathrm{T}}^{\mathrm{had}}$ deposited in the hadronic calorimeter, normalized to the total transverse energy E_{T} of the photon candidate is:

$$R_{\mathrm{had}} = \frac{E_{\mathrm{T}}^{\mathrm{had}}}{E_{\mathrm{T}}} \tag{2.1}$$

  The energy deposited in the first layer of the HCAL is used to compute $E_{\mathrm{T}}^{\mathrm{had}}$ except in $0.8 < |\eta| < 1.37$ region, where a more effective quantity, the energy in

the full hadronic calorimeter, is used.

- **Variables using the second ("middle") layer of the electromagnetic calorimeter**
  The discriminating variables based on the energy deposited in the second layer of the electromagnetic calorimeter are:

  — *Middle η energy ratio*

  $$R_\eta = \frac{E^{S2}_{3\times7}}{E^{S2}_{7\times7}} \tag{2.2}$$

  is the ratio between the sum $E^{S2}_{3\times7}$ of the energies in the second layer cells of the electromagnetic calorimeter contained in a 3×7 rectangle in $\eta \times \phi$ (measured in unit of granularity of the calorimeter cells), and the sum $E^{S2}_{7\times7}$ of the energies in a 7×7 rectangle, both centered around the cluster seed.

  — *Middle ϕ energy ratio*

  $$R_\phi = \frac{E^{S2}_{3\times3}}{E^{S2}_{3\times7}} \tag{2.3}$$

  is defined similarly to R_η. R_ϕ behaves very differently for unconverted and converted photons, since the electrons and positrons generated by the latter bend in different directions in ϕ because of the solenoid magnetic field, producing wider showers in the ϕ direction than the unconverted photons.

  — *Middle lateral width*

  $$w_{\eta 2} = \sqrt{\frac{\sum E_i \eta_i^2}{\sum E_i} - \left(\frac{\sum E_i \eta_i}{\sum E_i}\right)^2} \tag{2.4}$$

  measures the shower lateral width along η in the second layer of the electromagnetic calorimeter, using all cells in a window of $\eta \times \phi = 3 \times 5$ measured in unit of number of cells.

- **Variables using the first ("strip") layer of the electromagnetic calorimeter**
  The discriminating variables based on the energy deposited in the first layer of the electromagnetic calorimeter are:

  — *Front side energy ratio*

  $$F_{\text{side}} = \frac{E(\pm3) - E(\pm1)}{E(\pm1)} \tag{2.5}$$

  measures the lateral containment of the shower, along the η direction. $E(\pm n)$ is the energy in the $\pm n$ strip cells around the one with the largest energy.

  — *Front lateral width (3 strips)*

  $$w_{s3} = \sqrt{\frac{\sum E_i (i - i_{\max})^2}{\sum E_i}} \tag{2.6}$$

  measures the shower width along η in the first layer of the electromagnetic calorimeter, using two strip cells around the maximal energy deposit. The index i is the strip identification number, $i_{\max}$ identifies the strip cell with the greatest energy, E_i is the energy deposit in each strip cell.

— *Front lateral width (total)*
$w_{\mathrm{s,tot}}$ measures the shower width along η in the first layer of the electromagnetic calorimeter using all cells in a window $\Delta\eta \times \Delta\phi = 0.0625 \times 0.2$, corresponding approximately to 20×2 strip cells in $\eta \times \phi$. The width definition is the same as for w_{s3}.

— *Front second maximum difference.*

$$\Delta E = \left[E^{S1}_{2^{\mathrm{nd}}\mathrm{max}} - E^{S1}_{\mathrm{min}}\right] \tag{2.7}$$

is the difference between the energy of the strip cell with the second greatest energy $E^{S1}_{2^{\mathrm{nd}}\mathrm{max}}$, and the energy in the strip cell with the least energy found between the greatest and the second greatest energy E^{S1}_{min} ($\Delta E = 0$ when there is no second maximum).

— *Front maxima relative ratio*

$$E_{\mathrm{ratio}} = \frac{E^{S1}_{1^{\mathrm{st}}\,\mathrm{max}} - E^{S1}_{2^{\mathrm{nd}}\,\mathrm{max}}}{E^{S1}_{1^{\mathrm{st}}\,\mathrm{max}} + E^{S1}_{2^{\mathrm{nd}}\,\mathrm{max}}} \tag{2.8}$$

measures the relative difference between the energy of the strip cell with the greatest energy $E^{S1}_{1^{\mathrm{st}}\,\mathrm{max}}$ and the energy in the strip cell with second greatest energy $E^{S1}_{2^{\mathrm{nd}}\,\mathrm{max}}$ ($E_{\mathrm{ratop}} = 1$ when there is no second maximum).

The variables E_{ratio} and ΔE provide rejection against fake photons from $\pi^0 \to \gamma\gamma$ decays when the two showers give separated energy maxima in the first layer, while F_{side}, w_{s3} and the others provide additional rejection even when the two showers are overlapped to form a wider bump.

Two algorithms with different working points, based on "rectangular cuts" on these variables, are implemented in ATLAS: a "loose" identification algorithm and a "tight" one. The DVs used by each of the two selections are summarised in Table 2.4. The "loose" selection is the same for converted and unconverted photons and matches the corresponding electron one, and is used for triggering purposes. The "tight" criteria are separately optimized for unconverted and converted photons, depending on the photon $|\eta|$ direction. The expected photon efficiency and jet rejection for the loose and tight criteria defined before the 7 TeV data taking [35] are given in Table 2.5. More details on the distributions of the DVs for prompt and fake photons are given in section 3.3.

2.5 Photon Energy Calibration

The photon energy is reconstructed by summing the energy of all the cells of the four layer of the ECAL belonging to a a cluster of fixed size, and is corrected by applying a dedicated energy calibration afterwards. The number of cells used in the energy reconstruction depends on the photon conversion status. In the barrel region, a cluster with transverse size of $\Delta\eta \times \Delta\phi = 3 \times 5$ in units of second layer cells around the photon shower barycenter is used for unconverted photons while a cluster with size $\Delta\eta \times \Delta\phi = 3 \times 7$ in the same units is used for converted photons. The wider size in the ϕ direction is used to compensate for the opening between the conversion products due to the solenoidal magnetic field. In the end-cap, where the opening of the conversion electrons is smaller due to the smaller inner radius of the calorimeter, the same cluster size $\Delta\eta \times \Delta\phi = 5 \times 5$ is used for converted and unconverted photons.

The calibration can be divided into three steps:

Table 2.4 – Variables used for the "loose" and "tight" photon identification algorithms.

Category	Description	Name	Loose	Tight
Acceptance	$\|\eta\| < 2.37$, $1.37 < \|\eta\| < 1.52$ excluded	–	✓	✓
Hadronic leakage	Ratio of E_{T} in the first sampling of the hadronic calorimeter to E_{T} of the EM cluster (used over the range $\|\eta\| < 0.8$ and $\|\eta\| > 1.37$)	R_{had1}	✓	✓
	Ratio of E_T in all the hadronic calorimeter to E_T of the EM cluster (used over the range $0.8 < \|\eta\| < 1.37$)	R_{had}	✓	✓
EM Middle layer	Ratio in η of cell energies in 3×7 versus 7×7 cells	R_η	✓	✓
	Lateral width of the shower	$w_{\eta 2}$	✓	✓
	Ratio in ϕ of cell energies in 3×3 and 3×7 cells	R_ϕ		✓
EM Strip layer	Shower width for three strips around strip with maximum energy deposit	w_{s3}		✓
	Total lateral shower width	$w_{\mathrm{s,tot}}$		✓
	Energy outside core of three central strips but within seven strips divided by energy within the three central strips	F_{side}		✓
	Difference between the energy associated with the second maximum in the strip layer, and the energy reconstructed in the strip with the minimal value found between the first and second maxima	ΔE		✓
	Ratio of the energy difference associated with the largest and second largest energy deposits over the sum of these energies	E_{ratio}		✓

Table 2.5 – Expected overall photon efficiencies and jet background rejections for the two sets of identification cuts and an E_T-threshold of 20 GeV.

		Efficiency(%)	Jet rejection
Loose	All	95.45±0.01	908±4
	Unconverted	97.80±0.01	
	Converted	91.73±0.01	
Tight	All	82.88±0.02	4770±40
	Unconverted	85.04±0.03	
	Converted	79.44±0.04	

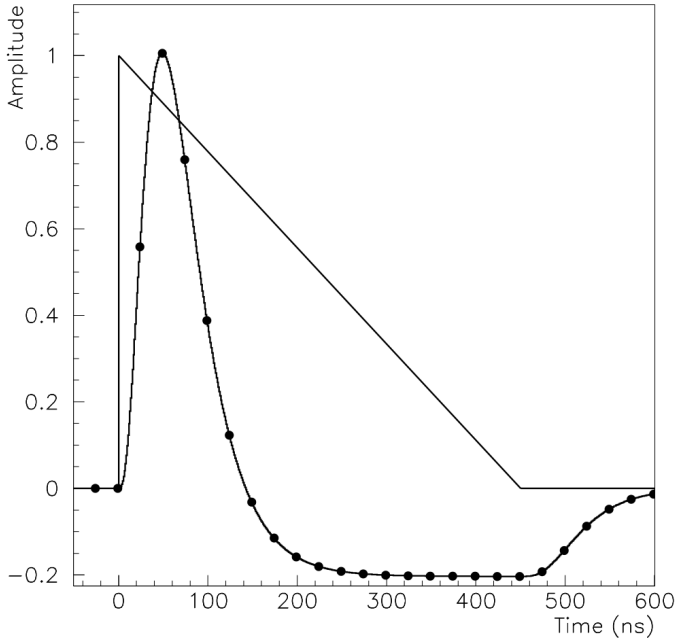

Figure 2.10 – The triangular current pulse in the LAr barrel cell and the sampled impulse after bi-polar shaping.

- the raw electronic signal from each calorimeter cell is converted into a deposited energy using the electronic calibration constants;
- the energy loss due to inactive material and lateral or longitudinal leakage outside of the cluster is corrected based on a detailed Monte Carlo (MC) simulation of the detector response;
- an overall ("in-situ") calibration is applied to correct for data-MC discrepancies using scale factors extracted from $Z \to ee, Z \to \ell\ell\gamma$ and $J/\psi \to ee$ events.

The LAr signal is generated from the ionisation electrons drifting in the electric field provided by the high voltage between the electrodes and absorbers, and collected by the electrodes. The ionisation current follows a triangular shape:

$$I(t) = \frac{N_e q_e}{t_d}(1 - \frac{t}{t_d}) \tag{2.9}$$

where t_d is the average drift time of electrons in the LAr (about 450 ns), N_e is the number of electrons generated in the LAr gap at $t = 0$ and q_e is the electric charge. The triangular signal is amplified to suppress noise and is shaped with a bi-polar filter $CR - (RC)^2$. The shaped signals are sampled at the nominal LHC bunch crossing period (25 ns). The triangular current pulse and the shaped pulse are shown in Fig. 2.10 for the case of a barrel ECAL cell.

In the second step, the energy of the photon is estimated from the sum of the energies deposited in the cells of the pre-sampler and of the three layers of the ECAL. Corrections are applied to take into account the energy loss upstream of the pre-sampler, the longitudinal leakage, the lateral leakage and the fraction of energy that is deposited in the inactive part of the electromagnetic calorimeter. The reconstructed energy can be written

as:

$$E = [\underbrace{a(E_{\text{tot}}^{\text{Acc}}, |\eta|) + b(E_{\text{tot}}^{\text{Acc}}, |\eta|) \times E_{\text{ps}} + c(E_{\text{tot}}^{\text{Acc}}, |\eta|) \times E_{\text{ps}}^2}_{\text{Energy upstream of the accordion calorimeter } (E_{\text{front}})} + \underbrace{\frac{s_{\text{cl}}^{\text{Acc}}(X, |\eta|)}{f_{\text{out}}(X, |\eta|)} \times \left(\sum_{i=1,3} E_i \right)}_{\text{Energy in the accordion calorimeter } (E_{\text{tot}}^{\text{Acc}})} \times \underbrace{(1 + f_{\text{leak}}(X, |\eta|))}_{\text{Longitudinal leakage}}] \times \underbrace{F(|\eta|, \phi)}_{\text{Energy modulation}} \quad (2.10)$$

where:

- $a(E_{\text{tot}}^{\text{Acc}}, |\eta|)$, $b(E_{\text{tot}}^{\text{Acc}}, |\eta|)$ and $c(E_{\text{tot}}^{\text{Acc}}, |\eta|)$ are parameters determined as a function of the energy deposited in the three layers of the accordion ($E_{\text{tot}}^{\text{Acc}}$) and of the photon pseudorapidity, $|\eta|$. The coefficient is set to zero for all $|\eta|$ except for $1.55<|\eta|<1.8$.
- E_{ps} is the energy measured in the pre-sampler corrected for the fraction deposited in the passive materials.
- X is the longitudinal barycenter of the shower (shower depth), defined as:

$$X = \frac{\sum_{i=0}^{3} E_i X_i}{\sum_{i=0}^{3} E_i} \quad (2.11)$$

  where X_i (i=0 for the pre-sampler, i=1,2,3 for the three layers of accordion calorimeter) is the depth, expressed in radiation lengths, of the longitudinal center of each compartment computed from the center of ATLAS.
- $s_{\text{cl}}^{\text{Acc}}(X, |\eta|)$ is the correction factor to account for the accordion sampling fraction.
- $f_{\text{out}}(X, |\eta|)$ is the lateral leakage correction.
- $f_{\text{leak}}(X, |\eta|)$ is the longitudinal leakage correction.
- $F(|\eta|, \phi)$ is an energy correction that refines the previous corrections (which are based on the $|\eta|$ position of the geometric center of the cell) by taking into account the impact point of a photon inside a cell, which affects the amount of absorber that is traversed (as a function of ϕ) and the lateral leakage.

The coefficients (a, b, c, s_{cl}, f_{out}, f_{leak} and F) are determined from single photon simulation samples covering the p_T range in [5, 1000] GeV, $|\eta| < 2.5$ and $|\phi| < \pi$. As shown in Fig. 2.11, the deviation from 1 of the linearity of calorimeter response is expected to be less than 0.5% for unconverted photons and 1.0% for converted photons everywhere except the $1.7 < |\eta| < 2.2$ region, where it reaches 1.5% for low energy converted photons.

The above technique is the "standard" calibration used in ATLAS until spring 2014 for both electrons and photons. Recently a new approach based on multivariate analysis (MVA) techniques has been implemented. The correction factor of the true energy to the measured energy in the accordion (E_{true}/E_{acc}) is estimated from the simultaneous study of the following quantities:

- total energy in the accordion, E_{acc};
- ratio of the energy in the presampler to the energy in the accordion, E_0/E_{acc}, used only for clusters with $|\eta| < 1.8$;
- shower depth X;
- pseudorapidity $\eta_{cluster}$ in the ATLAS frame;

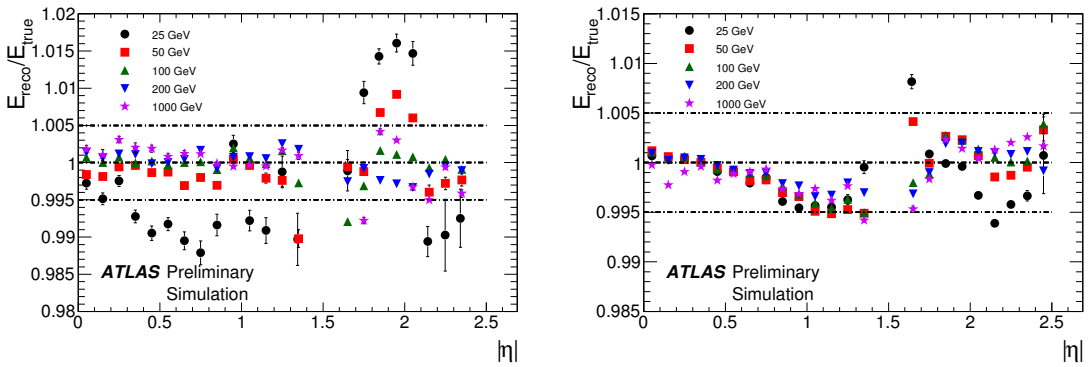

Figure 2.11 – Expected linearity of response of the EM calorimeter for unconverted photons (left) and converted photons (right) as a function of pseudorapidity [35].

- cell index: an integer number between 0 and 99 defined as the integer part of the division $\eta_{calo}/\Delta\eta$ where η_{calo} is the pseudorapidity of the cluster in the calorimeter frame and $\Delta\eta$= 0.025 is the size of one cell in the middle layer. This variable is more sensitive to non-uniformities of the calorimeter than the previous one.
- η with respect to the cell edge;
- ϕ with respect to the lead absorbers.

Additional quantities are used for converted photons:

- radius of the conversion.
- ratio of the conversion p_{T} to the E_{T} in the accordion.
- fraction of the conversion p_{T} carried by the highest-p_{T} conversion track.

More detail can be found in reference [36]. The linearity performance of the MVA calibration is illustrated in Figure 2.12. The non-linearity of the MVA calibration is below few per mil for E_{T} above 10 GeV and typically better than 1% at lower transverse energies, reaching up to 2% in a few cases for converted photons. In general there is an improvement of more than a factor two over the standard calibration, in particular in the high $|\eta|$ region. For the resolution, improvements of about 3% to 10% in the barrel and 10% to 15% in the endcap are observed for unconverted photons with transverse energies up to few hundreds of GeV. For converted photons in the same energy range the resolution is improved by typically 20% compared to the standard calibration.

In the third step, an "in-situ" calibration of the type $E(\eta) \rightarrow \frac{E(\eta)}{1+\alpha(\eta)}$ is applied to photons in data. The calibration coefficients α are extracted by comparing the reconstructed Z ($\rightarrow ee$) mass peak in data and MC. The reconstructed mass of $Z \rightarrow ee$ candidate is computed as:

$$M_{reco} = \sqrt{2E^1_{reco}E^2_{reco}(1 - cos\theta)} \tag{2.12}$$

where the $E^{1,2}_{reco}$ are the energies of the two electrons measured in the calorimeter and θ is the angle between the two electrons measured by the Inner Detector. For a given region "i (or j)", the reconstructed electron energy can be related to its truth energy by the calibration constant $\alpha^i (or\ \alpha^j)$ as:

$$E^{i(or\ j)}_{reco} = E^{i(or\ j)}_{true}(1 + \alpha^{i(or\ j)}) \tag{2.13}$$

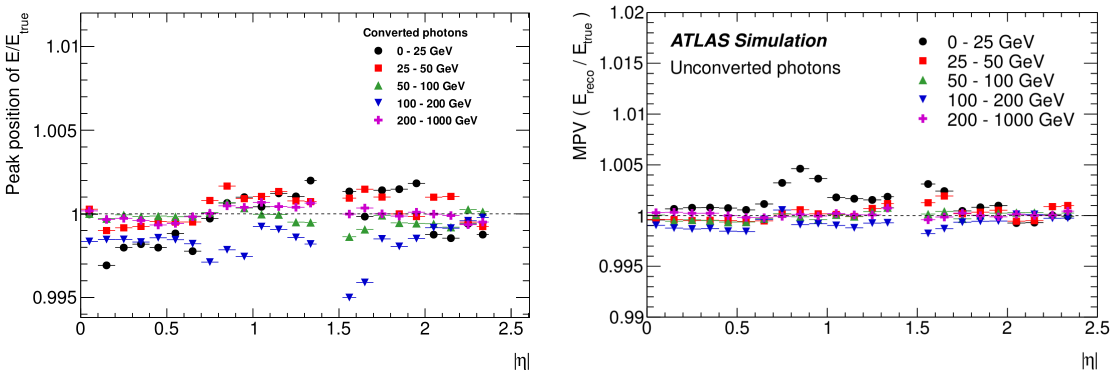

Figure 2.12 – Expected linearity of the energy response of the MVA calibration for unconverted photons (left) and converted photons (right) as a function of pseudorapidity [36].

Ignoring the second-order terms and assuming that the angle θ is perfectly known, the reconstructed di-electron mass is:

$$M^{ij}_{reco} = M^{ij}_{true}(1 + \frac{\alpha^i + \alpha^j}{2}) \tag{2.14}$$

where the indices $i(j)$ denote the pseudorapidity bin of $e_i(e_j)$. The parameters (α^i, α^j) are extracted by minimising the following log-likelihood:

$$-lnL_{tot} = \sum_{i,j}\sum_{n=1}^{N_{ij}} -lnL_{ij}(\frac{M_n}{1 + \frac{\alpha^i+\alpha^j}{2}}) \tag{2.15}$$

where N_{ij} sums over all the $Z \to ee$ candidates. $L_{ij}(M)$ is the unbinned likelihood function constructed from the probability density function of the Z line-shape. Fig. 2.13 shows the measured energy scale correction factors α as a function of the pseudorapidity by using 40 pb^{-1} of data collected in 2010 [37]. Measurement of the ratio E/p between the energy (from the calorimeter) and the momentum (from the ID) of electrons from $W \to e\nu$ provides an independent cross check of the electron energy scale. The results have been updated with 13 fb^{-1} 2012 data [38], as shown in Fig. 2.14, and are now being finalised with the full 2012 data set. Both the $Z \to ee$ invariant mass distribution and the $W \to e\nu$ E/p one exhibit peaks that are stable within 0.1% as a function of the average number of interactions per bunch crossing.

The energy resolution of the electromagnetic calorimeter is parametrized as:

$$\frac{\sigma_E}{E} = \frac{a}{\sqrt{E}} \oplus \frac{b}{E} \oplus c, \tag{2.16}$$

where:

- a is the sampling term (also called the stochastic term). It reflects event-by-event variations in the energy deposited in the LAr medium, induced by the fluctuations in the shower development. The design value is around 10% in the barrel and 15% in the end-cap of the electromagnetic calorimeter.
- b is the noise term. It describes the fluctuations mainly from pile-up and electronic noises. It is around 300 MeV and therefore is important only for low-energy particles ($E \leq 10$ GeV).

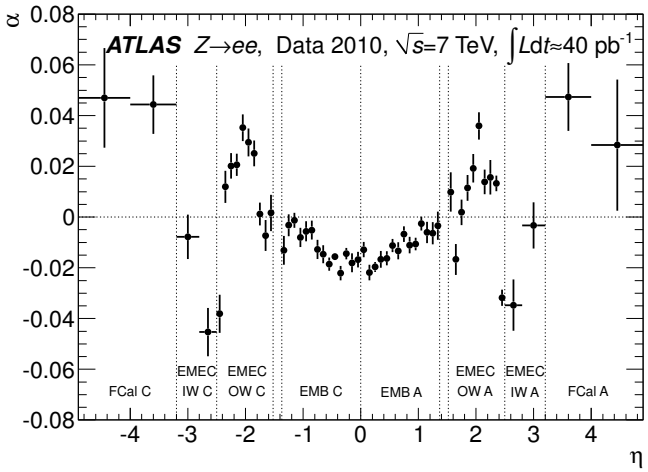

Figure 2.13 – The energy-scale correction factor α as a function of the pseudorapidity of the electron cluster derived from fits to $Z \to ee$ data. The uncertainties are statistical only [37].

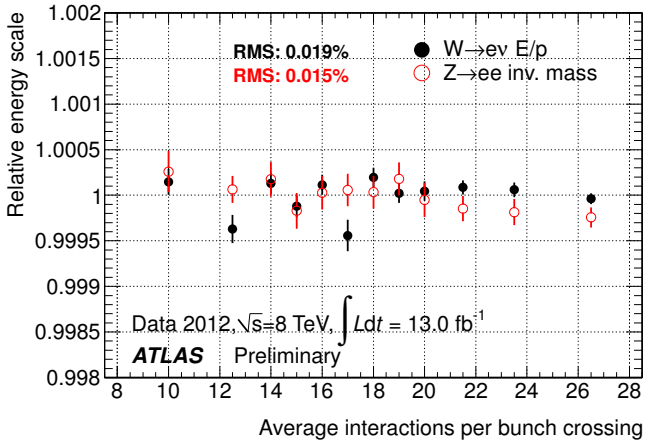

Figure 2.14 – Electron energy response stability vs mu in 2012 data [38].

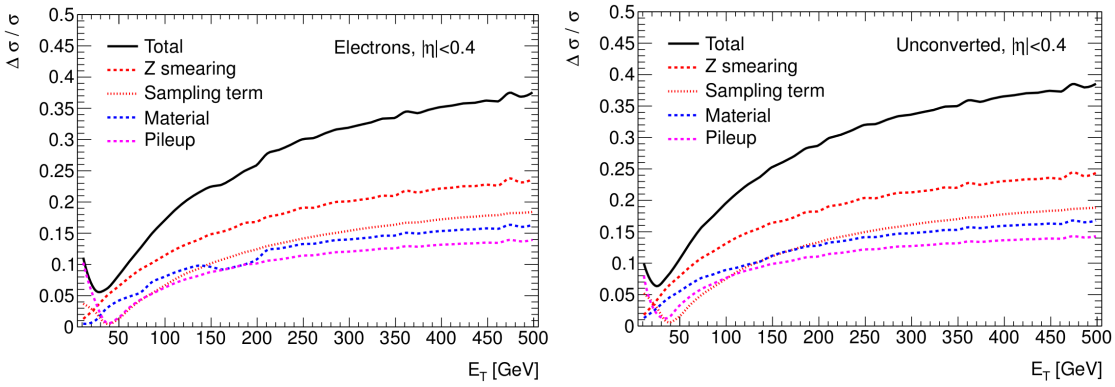

Figure 2.15 – Contributions of the different uncertainties to the relative resolution uncertainty as a function of E_{T} for electrons (left) and unconverted photons (right) with $|\eta| < 0.4$ [36].

- c is the constant term. It is due to the non-uniformities in the response of the calorimeter: material non-uniformity, temperature gradient, imperfections in mechanical structures, radiation damages, energy reconstruction scheme and stability in time, etc. The nominal value is around 0.7%.

The resolution in data is studied using electrons from $Z \to ee$ and $J/\psi \to ee$ decays, by inspecting the width of the reconstructed ee invariant mass distribution. These studies show a data-MC agreement for the sampling term to better than 10%, while the constant term in data is larger than that in the simulation. More details can be found in reference [36]. Figure 2.15 shows the contributions of the different uncertainties to the relative resolution uncertainty for unconverted photons and electrons with $|\eta| < 0.4$.

2.6 Lepton Reconstruction and Identification

2.6.1 Electrons

Electrons are reconstructed by the same algorithms described for photons in section 2.3. In 2012, the track-fitting algorithm has been improved, using a Gaussian Sum Filter (GSF) technique to account for bremsstrahlung energy losses and to improve the performance of track-cluster matching [39]. The electron reconstruction efficiency, measured using an electron sample of high purity from $Z \to ee$ selected by using a "Tag and Probe" method [40, 41], is larger than 90% in 2011 and 95% in 2012 for $p_T > 15$ GeV as shown in Fig. 2.16.

Electron identification uses the information of the shower shape measured in the calorimeter and the track measured in the ID. Table 2.6 lists all discriminating variables. Based on these discriminating variables, there are two types of identification menus. The first set of identification algorithms is based on rectangular cuts and, according on the number of variables used and on the tightness of the selection criteria, provides four different working points, called "loose", "multilepton", "medium" and "tight". The second set is based on a likelihood built from the various discriminating variables, and depending on the cut on the likelihood value four different working points are provided: "VeryLooseLLH", "LooseLLH", "TightLLH" and "VeryTightLLH". The 2012 menus are optimized to be more robust against pile up. Their efficiencies are measured using an electron sample of high

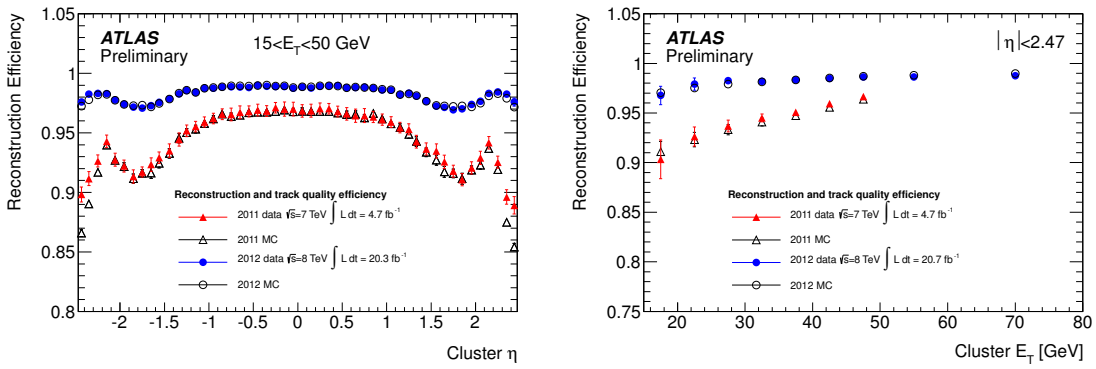

Figure 2.16 – Electron reconstruction efficiency versus η (left) and E_{T} (right), in both 2011 and 2012 data [41].

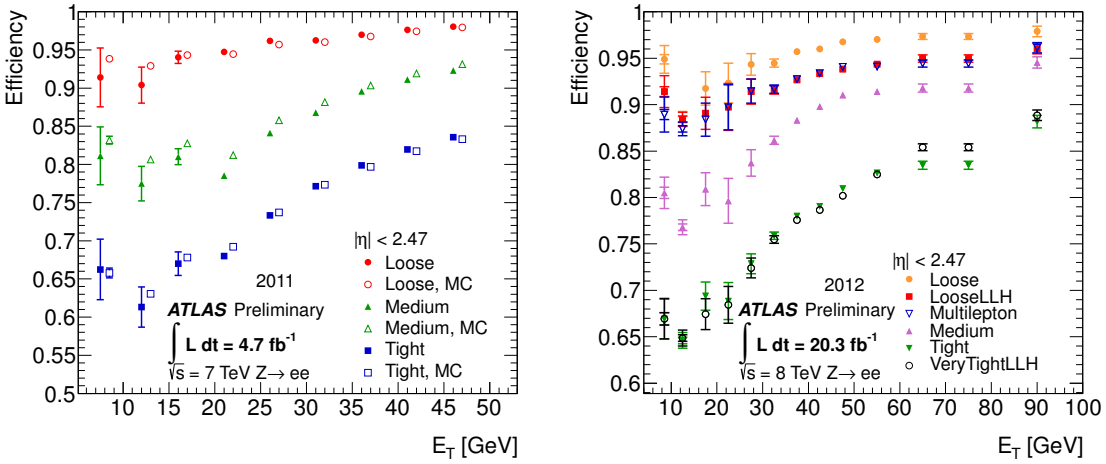

Figure 2.17 – Electron identification efficiency versus electron E_{T} measured in data in 2011 (left) and in 2012 (right). In the left plot the efficiencies expected from the simulation are also shown for comparison [41].

purity from $Z \to ee$ selected by using a "Tag and Probe" method, and shown in Fig. 2.17. The efficiency of different algorithms, corresponding to different working points, shows a very weak dependence on the number of primary vertices in the event, as illustrated in Fig. 2.18.

2.6.2 Muons

Muon reconstruction and identification use the information from the two tracking systems, the Inner Detector (covering $|\eta| < 2.5$) and the Muon Spectrometer (covering $|\eta| < 2.7$), which provide independent measurements of the muon momentum. The combination of the ID and MS information increases the muon purity and provides good muon momentum resolution over a large p_{T} range. Muons are reconstructed and classified into four types according to the information from the Inner Detector, the Muon Spectrometer and the calorimeter:

- Stand-alone (SA) muons: the muon trajectory is reconstructed only in the Muon

Table 2.6 – Definition of the electron discriminating variables used to distinguish between prompt and fake electrons [42].

Type	Description	Name
Hadronic leakage	Ratio of E_{T} in the first layer of the hadronic calorimeter to E_{T} of the EM cluster (used over the range $\lvert\eta\rvert < 0.8$ and $\lvert\eta\rvert > 1.37$)	R_{had1}
	Ratio of E_{T} in the hadronic calorimeter to E_{T} of the EM cluster (used over the range $0.8 < \lvert\eta\rvert < 1.37$)	R_{had}
Third layer of EM calorimeter	Ratio of the energy in the third layer to the total energy	f_3
Middle layer of EM calorimeter	Lateral shower width, $\sqrt{(\Sigma E_i \eta_i^2)/(\Sigma E_i) - ((\Sigma E_i \eta_i)/(\Sigma E_i))^2}$, where E_i is the energy and η_i is the pseudorapidity of cell i and the sum is calculated within a window of 3×5 cells	$w_{\eta 2}$
	Ratio of the energy in 3×3 cells over the energy in 3×7 cells centered at the electron cluster position	R_ϕ
	Ratio of the energy in 3×7 cells over the energy in 7×7 cells centered at the electron cluster position	R_η
Strip layer of EM calorimeter	Shower width, $\sqrt{(\Sigma E_i (i - i_{\mathrm{max}})^2)(\Sigma E_i)}$, where i runs over all strips in a window of $\Delta\eta \times \Delta\phi \approx 0.0625 \times 0.2$, corresponding typically to 20 strips in η, and i_{max} is the index of the highest-energy strip	$w_{\mathrm{s,tot}}$
	Ratio of the energy difference between the largest and second largest energy deposits in the cluster over the sum of these energies	ΔE_{max}
	Ratio of the energy in the strip layer to the total energy	f_1
Track quality	Number of hits in the B-layer (discriminates against photon conversions)	n_{Blayer}
	Number of hits in the pixel detector	n_{Pixel}
	Number of total hits in the pixel and SCT detectors	n_{Si}
	Transverse impact parameter	$d0$
	Significance of transverse impact parameter defined as the ratio of $d0$ and its uncertainty	σ_{d0}
	Momentum lost by the track between the perigee and the last measurement point divided by original momentum	$\Delta p/p$
TRT	Total number of hits in the TRT	n_{TRT}
	Ratio of the number of high-threshold hits to the total number of hits in the TRT	n_{TRT}
Track–cluster matching	$\Delta\eta$ between the cluster position in the strip layer and the extrapolated track	$\Delta\eta_1$
	$\Delta\phi$ between the cluster position in the middle layer and the extrapolated track	$\Delta\phi_2$
	Defined as $\Delta\phi_2$, but the track momentum is rescaled to the cluster energy before extrapolating the track to the middle layer of the calorimeter	$\Delta\phi_{Res}$
	Ratio of the cluster energy to the track momentum	E/p
Conversions	Veto electron candidates matched to reconstructed photon conversions	!isConv

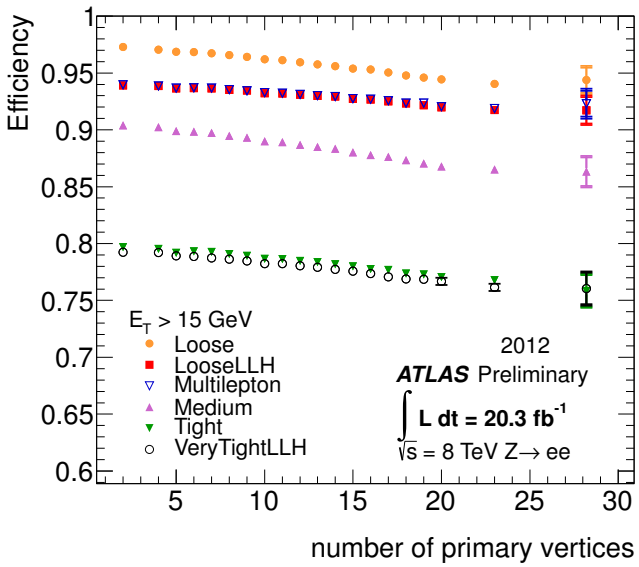

Figure 2.18 – Electron identification efficiency versus number of primary vertices measured in data collected in 2012 [41].

Spectrometer. The impact parameters are determined by extrapolating the MS track back to the point of closest approach to the beam line. The energy loss in the calorimeter is taken into account in the extrapolation. Stand-alone muons are typically muons in the region $2.5 < |\eta| < 2.7$, outside of the ID acceptance.

- Combined (CB) muons: the muon tracks in the Inner detector and in the Muon Spectrometer are reconstructed independently, and then are combined successfully in a single muon track. This algorithm is applicable for muons in the region $0.1 < |\eta| < 2.5$ covered by both the ID and the MS.
- Segment-tagged (ST) muons: a track in the Inner detector is identified as a ST muon if it is matched to any track segment in the MDT or CSC.
- Calorimeter-tagged (CaloTag) muons: a track in the Inner detector is identified as a CaloTag muon if it is matched to an energy deposition in the calorimeter which is consistent with that expected from a minimum ionizing particle. The identification criteria are optimized to recover muons in the region $|\eta| < 0.1$, corresponding to the gap in the MS needed for the routing of the services to the inner subdetectors.

The CB muons have the highest purity, but their reconstruction algorithm is affected by the acceptance limitation in the MS, i.e the gap of the MS in $|\eta| < 0.1$ and the incomplete installation of the chambers in the region of $1.1 < |\eta| < 1.3$. The efficiency in these regions is recovered by using the other algorithms. The first three types of muons can be reconstructed using two independent and complementary strategies (named "chains"): the first chain (called "Staco") performs a statistical combination of the parameters of the ID and SA muon tracks, while the second chain ("Muid") performs a global fit on the hits from both ID and MS detectors.

The muon reconstruction efficiency, including the efficiency of ID and MS track reconstruction and of their matching, is measured using a pure muon control sample selected from $Z \to \mu\mu$ decays by using a "Tag and probe" method [43]. The muon reconstruction

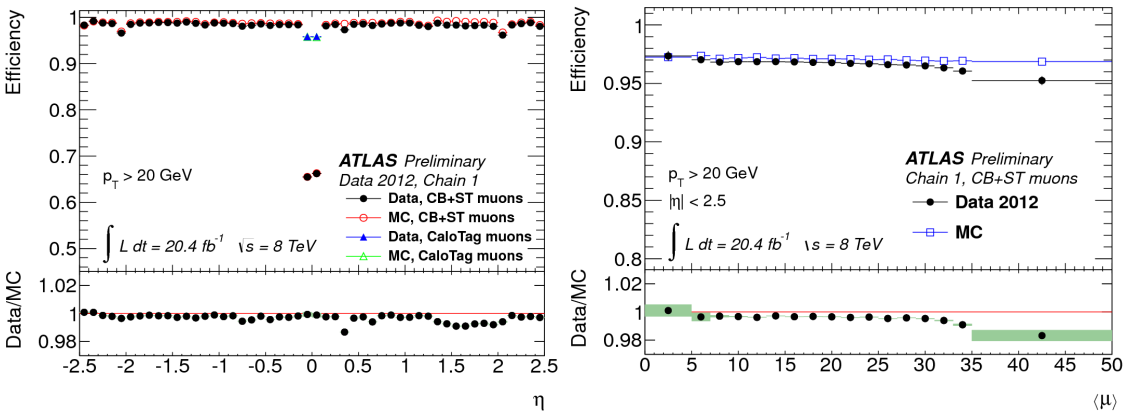

Figure 2.19 – Muon reconstruction efficiency as a function of $|\eta|$ (left) and $<\mu>$ for muons with $p_{\mathrm{T}} > 20$ GeV and different muon reconstruction types. CB and SA muon types are reconstructed using the staco reconstruction algorithm. CaloTag muons are used only in the region $|\eta|<0.1$. The panel at the bottom shows the ratio between the measured and predicted efficiencies. [43]

efficiency measured in 2012 is shown in Fig. 2.19. It has very small pile-up dependence.

2.7 Jet and Missing E_{T} Reconstruction

2.7.1 Jets

Jets of particles are reconstructed using the anti-k_t algorithm [44] with distance parameters $R = 0.4$ or $R = 0.6$ with the $FASTJET$ software [45]. Two types of jets are reconstructed: calorimeter jets and track jets.

The calorimeter jets are reconstructed from three-dimensional topological clusters of calorimeter cells (topo-cluster) or from calorimeter towers. The topological clusters are seeded from a cell with energy greater than 500 MeV and signal-to-noise ratio (S/N) larger than 4. Neighbouring cells with S/N >2 are then added to the topo-cluster. The topo-cluster four-momentum is computed from the sum of the four-momenta of each cell, assumed to have zero mass. The calorimeter towers are built directly from the calorimeter cells in $\Delta\eta\times\Delta\phi = 0.1\times0.1$. Two types of calorimeter towers are formed: with and without noise suppression. Noise-suppressed towers make use of the topo-cluster algorithm, i.e. only calorimeter cells that are included in topo-clusters are used. Therefore, for a fixed geometrical area, the noise-suppressed calorimeter towers have the same energy content as the topo-clusters. The energy of a calorimeter tower is given by the sum of the energies of all the calorimeter cells within the tower.

The track jets are built from tracks originating from the primary hard scattering vertex, defined as the vertex with the sum of the squared transverse momenta of the tracks associated to it. The following criteria are applied to the tracks to suppress pile-up and fake jet backgrounds:

- $p_{\mathrm{T}} > 0.5$ GeV, $|\eta| < 2.5$.
- at least one (six) hits in the Pixel (SCT) detector.
- transverse (d_0) and longitudial (z_0) impact parameters with respect to the primary vertex: $|d_0| < 1.5$ mm, $|z_0 sin\theta| < 1.5$ mm.

The jet must have at least two associated tracks and $p_{\mathrm{T}} > 3$ GeV.

The energy and direction of jets with p_{T} >20 GeV and $|\eta|$ <4.5 are calibrated using corrections determined from the simulation. The jet energy scale (JES) systematic uncertainty is estimated using the single isolated hadron response measured *in situ* and in test-beams. The JES is validated for jet transverse momenta up to 1 TeV to the level of a few percent using several *in situ* techniques [46]. The JES systematic uncertainty determined from a combination of *in situ* techniques are consistent with the one derived from single hadron response measurements. For central jets ($|\eta|$<1.2) with 20< p_{T} < 800 GeV, a photon or a Z bosons are used as reference objects. A system of low-p_{T} jets is ued to extend the JES validation up to the TeV regime. The smallest JES uncertainty, of less than 1%, is found for jets with 55 < p_{T} < 500 GeV. For jets with $p_{\mathrm{T}} = 20$ GeV the uncertainty is about 3%. For $p_{\mathrm{T}} > 1$ TeV the JES uncertainty is estimated from single hadron response measurements *in situ* and in beam tests and is about 3%. The JES uncertainty for forward jets is derived from di-jet p_{T} balance measurements. The resulting uncertainty is largest for low-p_{T} jets at $|\eta| = 4.5$ and amounts to 6%.

2.7.2 Missing E_{T} (E_{T}^{miss})

The E_{T}^{miss} is reconstructed by the energy deposits in the calorimeter ($E_{x(y)}^{miss,calo}$) and by muons ($E_{x(y)}^{miss,\mu}$) reconstructed in the muon spectrometer:

$$E_{x(y)}^{miss} = E_{x(y)}^{miss,calo} + E_{x(y)}^{miss,\mu} \tag{2.17}$$

The calorimeter term ($E_{x(y)}^{miss,calo}$) is reconstructed using calorimeter cells associated to identified particles or objects (electrons, photons, hadronically decaying τ-leptons, jets, muons) and topo-clusters which are not included in any reconstructed objects:

$$E_{x(y)}^{miss,calo} = E_{x(y)}^{miss,e}+E_{x(y)}^{miss,\gamma}+E_{x(y)}^{miss,\tau}+E_{x(y)}^{miss,jets}+E_{x(y)}^{miss,soft-jets}+E_{x(y)}^{miss,calo-\mu}+E_{x(y)}^{miss,CellOut} \tag{2.18}$$

where each term is calculated from a negative sum of all cell energies associated to that object:

$$\begin{aligned} E_x^{miss,term} &= -\sum_{i=1}^{N_{cell}^{term}} E_i sin\theta_i cos\phi_i \\ E_y^{miss,term} &= -\sum_{i=1}^{N_{cell}^{term}} E_i sin\theta_i sin\phi_i \end{aligned} \tag{2.19}$$

- $E_{x(y)}^{miss,e}, E_{x(y)}^{miss,\gamma}, E_{x(y)}^{miss,\tau}$ are reconstructed from the cells in the clusters associated to the electrons, photons and hadronically decaying τ-leptons
- $E_{x(y)}^{miss,jets}$ is reconstructed from the cells in the clusters associated to jets with calibrated $p_{\mathrm{T}} > 20$ GeV jets.
- $E_{x(y)}^{miss,soft-jets}$ is reconstructed from the cells in the clusters associated to jets with p_{T} between 7 and 20 GeV.
- $E_{x(y)}^{miss,calo-\mu}$ is reconstructed from the muon energy loss in the calorimeter.
- $E_{x(y)}^{miss,CellOut}$ is reconstructed from the energies of topo-clusters not used in any reconstructed objects.

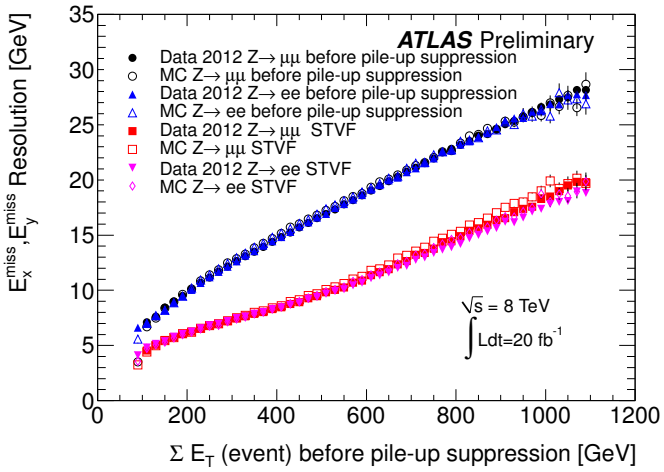

Figure 2.20 – $E^{miss}_{x(y)}$ resolution as a function of the total transverse energy in the event calculated by summing the p_{T} of muons and the total transverse energy in the calorimeter in data. Resolution in data and MC simulation are compared in $Z \to \mu\mu$ and $Z \to ee$ events [47].

The muon term ($E^{miss,\mu}_{x(y)}$) is reconstructed from the muon track transverse momenta in $|\eta| < 2.7$:

$$E^{miss,\mu}_{x(y)} = -\sum_{muons} p^{\mu}_{x(y)} \tag{2.20}$$

The CB muons are used in the region of $|\eta| < 2.5$ and the SA muons are used in the region of $2.5 < |\eta| < 2.7$. The ST muons are used for supplementing the CB muons in $|\eta| < 0.1$ and $1.1 < |\eta| < 1.3$.

The value of E^{miss}_{T} is reconstructed from the components of $E^{miss}_{x(y)}$:

$$E^{miss}_{\mathrm{T}} = \sqrt{E^{miss}_{x} * E^{miss}_{x} + E^{miss}_{y} * E^{miss}_{y}} \tag{2.21}$$

and its azimuthal coordinate (ϕ^{miss}) is calculated as:

$$\tan\phi^{miss} = \frac{E^{miss}_{y}}{E^{miss}_{x}} \tag{2.22}$$

The E^{miss}_{T} calibration strongly depends on the calibration of the constituent objects. The cells are calibrated differently according to the particle hypothesis. Figure 2.20 shows the E^{miss}_{T} resolution for $Z \to \ell\ell$ events from data as a function of $\sum E_{\mathrm{T}}$, before and after pile-up suppression [47]. The resolution in MC is illustrated for comparison. The resolution in data and in MC are in excellent agreement both before and after pile-up suppression. The resolutions are very similar for the electron and muon channels. More details can be found in Ref. [47].

Chapter 3

Photon performance

In this chapter, the photon trigger and identification efficiency measurements in ATLAS are introduced.

3.1 Photon Trigger Optimization for the 2012 data taking

An overview of the ATLAS trigger system has been given in section 2.2.5. The hardware-based L1 trigger and the software-based high-level (L2 and EF) trigger reduce the rate to an acceptable level for the ATLAS data recording system.

During the 2011 data taking period, the trigger rate was reduced to about 60 kHz at L1 level to below 5 kHz at L2 level, and then below 400 Hz at EF level. Part of this bandwidth was allocated to "loose" photon triggers, used to collect events with high-p_{T} photons, for Standard Model cross-section measurements and searches of high-mass di-photon resonances (Higgs boson, graviton, ...). The loose trigger criteria apply cuts on the $R_{\mathrm{had}}(R_{\mathrm{had1}})$, R_{η} and $w_{\eta 2}$ shower information.

For the 2012 data taking period, the EF-level trigger selections were re-optimized to limit the trigger rate to below 530 Hz while maintaining a good signal selection efficiency even for large pile-up. A simple strategy to reduce the trigger rate is to prescale it: only 1 out of N_{prescale} events passing the trigger are recorded, while for the others the trigger response is reset to `false`. This strategy, however, implies a reduction by a factor N_{prescale} of the signal efficiency. In order to maintain full efficiency for a possible di-photon signal from a Higgs boson and for the SM di-photon cross section measurement, a different strategy was adopted for the (di)photon triggers. The goal is to increase the jet rejection of the photon trigger by a factor around 1.5, in order for the di-photon triggers to use have a few Hz of unique rate, while keeping the efficiency with respect to photons passing the offline identification criteria close to 100%. This is achieved by a reoptimization of the requirements on the shower shape variables used in the loose trigger and by additional requirements on discrimination variables used for the offline photon selection but not exploited in the photon triggers used in 2011. A second goal of these studies is also to reduce the dependence of the trigger efficiency on pile-up, in order to maintain similar efficiency over the large range of number of pile-up collisions per bunch crossing expected to take place during the 2012 run.

These two targets have been achieved by loosening the cuts on the most pile-up dependent quantities used in the loose photon triggers, R_{had} and R_{η}, which are sensitive to the energy deposited in the hadronic calorimeter and around the core of the photon cluster in the second layer of the ECAL, while tightening the requirement on $w_{\eta 2}$, and adding to the trigger selection a requirement on E_{ratio}, a DV computed from the energy

deposited in the first layer which shows weak correlation with the other variables already exploited at trigger level and which is peaked near 1 for signal but has a broad, flat tail extending down towards 0 for fake photons. Different sets of cuts on E_{ratio} ("loose++", "medium", "medium++", "tight") have been investigated, and the corresponding signal and background efficiencies have been studied. Care has been taken to ensure that the requirements applied to E_{ratio} at trigger level are always looser than the ones applied to photon candidates at offline level. The left plot of Fig. 3.1 shows the efficiencies of the different selections as a function of the number of primary vertices, while the right one shows their corresponding background rejection, for single-photon triggers with a nominal p_{T} threshold of 20 GeV, estimated on samples of simulated di-jet events. For comparison the curves corresponding to the 2011 trigger ("`EF_g20_loose`") are also shown. The re-optimized trigger menus are significantly less pile-up dependent than the trigger used during 2011, and the jet rejection compared to the 2011 trigger is increased, for different requirements on E_{ratio}, between 30% and 85%. The efficiency of the various trigger menus for true photons in photon-jet events passing the offline photon identification requirements is shown in Fig. 3.2. For any of the alternative trigger selections the efficiency is higher than 99% for any value of the transverse momentum above the nominal threshold.

Following these studies the medium di-photon trigger, based on the "medium++" selection on E_{ratio}, have been used in 2012 to collect events used for SM $\gamma\gamma$ cross section measurements (trigger `EF_2g20_medium`, with nominal p_{T} thresholds of 20 GeV for both photons) and for the $H \to \gamma\gamma$ search (trigger `EF_g30_medium_g20_medium`, with asymmetric thresholds of 20 and 30 GeV), as a backup of the default `EF_g35_loose_g25_loose` trigger. Data collected in 2012 with the default and the backup triggers allowed to fully validate the medium di-photon trigger, which will be used in Run2 as the default one to collect data for $H \to \gamma\gamma$ studies, given its larger (2x) background rejection.

In conclusion, Table 3.1 lists the lowest-threshold unprescaled photon triggers used in 2012, together with their L1 seeds and rates at each level. In addition to the di-photon triggers previously discussed, The `g120_loose` trigger is a single-photon trigger with a minimum p_{T} threshold of 120 GeV and loose requirements on the three DVs R_{had}, R_{η} and $w_{\eta 2}$.

Trigger Signature	L1 Seed	L1 Rate (Hz)	L2 Rate (Hz)	EF Rate (Hz)
`g120_loose`	EM30	7000	45	11
`g35_loose_g25_loose`	2EM12_EM16V	8500	70	16
`g30_medium_g20_medium`	2EM12_EM16V	8500	130	11
`2g20_vh_medium`	2EM10VH	5567	152	15

Table 3.1 – Lowest threshold, unprescaled photon triggers, with their L1 seeds and their L1, L2 and EF rates at the beginning of a typical LHC fill in 2012.

3.2 Photon Trigger Efficiency Measurement

In measurements with photons in the final state performed on data collected with photon triggers, like $H \to \gamma\gamma$ or SM prompt photon cross section measurements, the trigger efficiency with respect to the off-line tight selection is a quantity that has to be known in order to extract the signal cross section. Two methods have been developed by

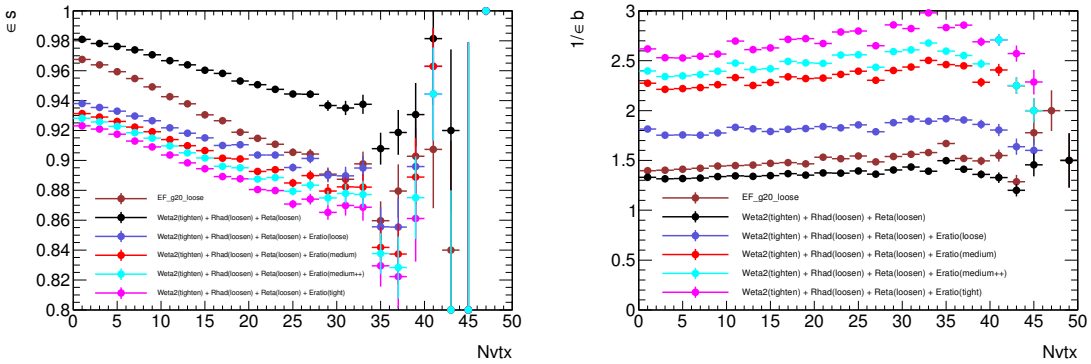

Figure 3.1 – The left plot shows the efficiencies of various cut menus as a function of the number of primary vertices, while the right plot shows the corresponding background rejection, using simulated events at $\sqrt{s} = 8$ TeV.

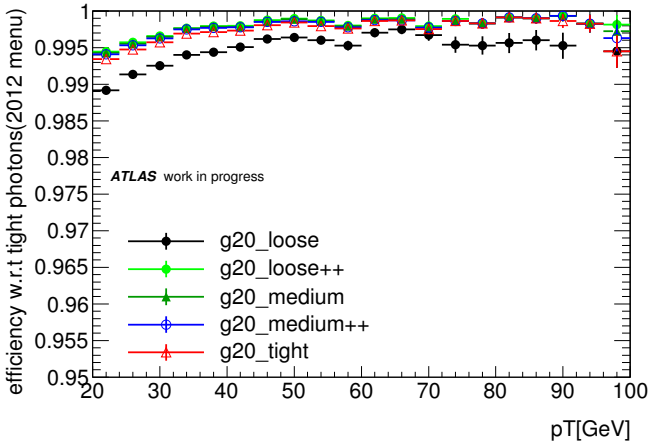

Figure 3.2 – The trigger efficiency versus the reconstructed photon p_{T} for various cuts, using simulated events at $\sqrt{s} = 8$ TeV.

ATLAS in order to measure this efficiency from the data, the *bootstrap* and the radiative Z decay methods. The *bootstrap* method uses collision events passing looser triggers, typically a pre-scaled lower-threshold L1 trigger being part of a chain where the HLT trigger is in pass-through mode. The efficiency of the HLT trigger is then measured with respect to the off-line photons matched to L1 trigger objects, and multiplied by the L1 trigger efficiency with respect to the off-line selection (≈100%), measured with minimum-bias events. More detail can be found in the Ref. [48]. Here, I focus on my work on the measurement of the trigger efficiency using the other method, based on a clean sample of prompt, isolated photons of relatively low transverse momentum from $Z \to \ell\ell\gamma$ ($\ell = e, \mu$) decays, in which a photon is produced from the final state radiation (FSR) of one of the two leptons from the Z boson decay. These events are selected by kinematic requirements on the di-lepton pair and on the three-body invariant mass and quality requirements on the two leptons, thus not biasing the reconstruction and selection of the photon probe. The measurement is based on the full ATLAS data set collected in 2012.

Events are required to pass the lowest-threshold unprescaled single- and di-lepton triggers:

- `EF_2e12Tvh_loose1` or `EF_e24vhi_medium1` for $Z \to ee\gamma$ channel
- `EF_mu24i_tight`, `EF_mu20it_tight`, `EF_mu40_MSonly_barrel_tight` or `EF_2mu13` for $Z \to \mu\mu\gamma$ channel

The following requirements are applied to both electrons:

- $p_{\mathrm{T}} > 15$ GeV, $|\eta| < 1.37$ or $1.52 < |\eta| < 2.47$.
- shower-shape, transition radiation and E/p consistent with the electron hypothesis ("`medium++`" identification).
- impact parameter with respect to the primary vertex (along z), $|z_0|$, less than 10 mm and transverse impact parameter significance $|d_0|/\sigma_{d_0}$ less than 10.
- calorimeter transverse isolation energy corrected for out-of-cluster leakage and pile-up less than 5 GeV in a cone of radius 0.4 (in $\eta - \phi$) around the electron.

In the muon channel, each muon candidate is required to pass the following criteria:

- to be a "combined " muon.
- $p_{\mathrm{T}} > 15$ GeV, $|\eta| < 2.4$.
- at least 1 hit in the B-layer and one more hit in the pixel detector, 5 hits in the SCT (a dead sensor is considered as a hit), at most 2 missing hits in total.
- an η-dependent requirement is applied on the number of reconstructed hits in the TRT and the fraction of outliers [1].
- impact parameter with respect to the primary vertex along z, $|z_0|$, less than 10 mm, and transverse impact parameter significance, $|d_0|/\sigma_{d_0}$, less than 10.
- track isolation (scalar sum of tracks' transverse momenta) in a cone of radius 0.2 around the muon less than 10% of the muon p_{T}.

The photon candidate is required to pass the following quality and kinematic requirements:

1. N = (mu_staco_nTRTOutliers+mu_staco_nTRTHits), f = mu_staco_nTRTOutliers/N if abs(mu_staco_eta)<1.9 && abs(mu_staco_eta) >0.1, N>5 && f<0.9 is required, otherwise N≤5 or f<0.9 is required.

- $p_{\mathrm{T}} > 10$ GeV and $|\eta| < 1.37$ or $1.52 < |\eta| < 2.37$
- cluster not containing bad cells of the ECAL. In particular, we define a photon as bad if its cluster is affected by either
  1. A dead FEB in the first or second sampling.
  2. A dead HV region affecting one of the three samplings.
  3. A masked cell in the core of the cluster (3x3 cells in the second sampling).
  4. At least one of the 8 central strips of the cluster in the first sampling is masked.

The $Z \to \ell\ell\gamma$ candidates are selected by applying the following preselection:

- two opposite-sign charged leptons of same flavour.
- minimum separation of $\Delta R_{\mathrm{min}} > 0.2$ (0.4) between the photon and each of the muons (electrons) in order to reduce effects of energy deposition of the lepton in the calorimeter on the photon shower shape variables

The two-dimensional distribution of the $\ell\ell\gamma$ and $\ell\ell$ invariant masses in data events passing the previous criteria is shown in Figure 3.3. Final state radiation (FSR) events (where the photon is radiated from the Z: $m_{\ell\ell\gamma} \approx m_Z, m_{\ell\ell} < m_Z$) and initial state radiation (ISR) events (where the photon is radiated before the Z decays to $\ell\ell$: $m_{\ell\ell\gamma} > m_Z, m_{\ell\ell} \approx m_Z$) are clearly visible. Since photon candidates from ISR are largely affected by the Z+jets

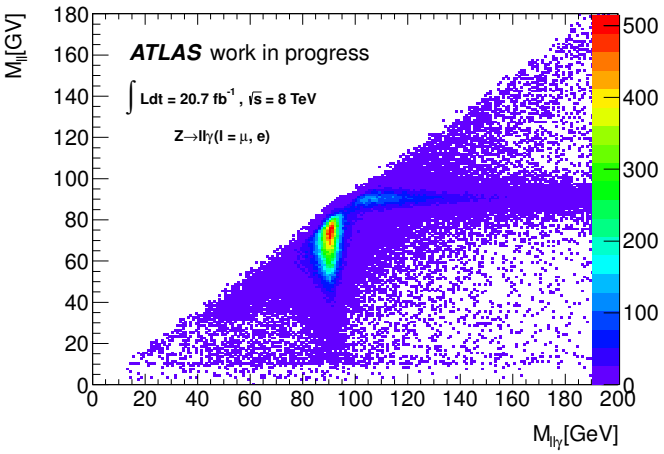

Figure 3.3 – 2-D distributions of $m_{\ell\ell\gamma}$ and $m_{\ell\ell}$ from the photon candidates in data after all $Z \to \ell\ell\gamma$ selection criteria, except those on $m_{\ell\ell\gamma}$ and $m_{\ell\ell}$. Events from FSR and ISR processes are clearly visible.

background, where a jet fakes a photon (the cross section for Z+jets is about three orders of magnitudes higher than for $Z + \gamma$, and a non-negligible fraction of jets contains high-momentum π^0's decaying to collimated photon pairs), only FSR events are used in this analysis. Therefore we require $70 < m_{\ell\ell\gamma} < 100$ GeV and $40 < m_{\ell\ell} < 83$ GeV.

With the previous selection we are able to obtain a clean photon control sample. An off-line selection can then be applied to these photon candidates and the efficiency for these probes to pass a particular photon trigger can be measured. In this thesis, photons from radiative Z decays are required to pass the typical requirements used in many ATLAS measurements of processes with photons in the final state, *i.e.* to pass the *tight* cut-based identification criteria and the calorimeter isolation requirement $E_{\mathrm{T}}^{\mathrm{iso}} < 4$ GeV, based on

the transverse energy in calorimeter cells belonging to topological 3D clusters within a cone of radius 0.4 around the photon direction.

After all requirements, 79452 tight photon candidates with $E_{\mathrm{T}} > 10$ GeV are selected in the two channels in the full 2012 data sets. Their 2-D (η, E_{T}) distribution is shown in Figure 3.4, while their 1D transverse momentum and pseudorapidity distributions in data and simulation are shown in Figure 3.5. The agreement between data and simulation is very good.

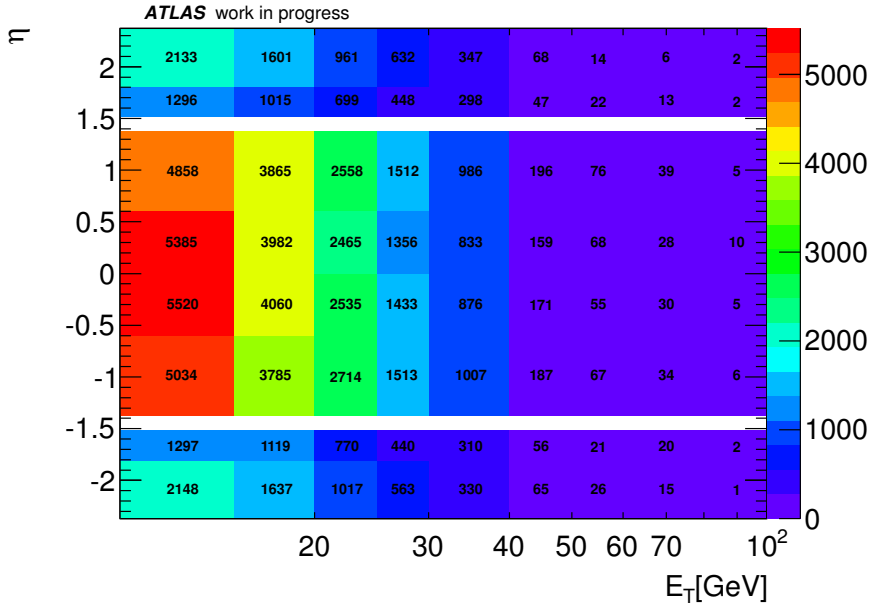

Figure 3.4 – 2-D distribution of E_{T} and η for photon candidates selected in data collected in 2012 after the full $Z \to \ell\ell\gamma$ selection is applied.

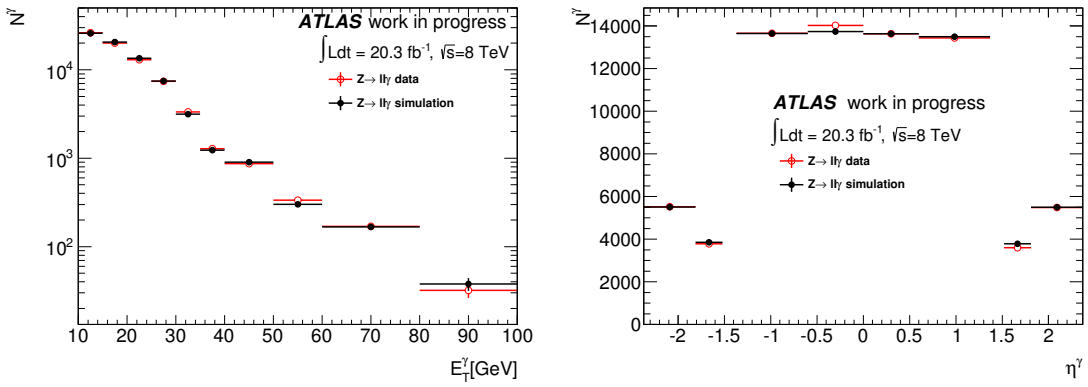

Figure 3.5 – Distributions of E_{T} (left) and η (right) for photon candidates selected in data (red) collected in 2012 and simulation (black), scaled to the same luminosity as the data, after the full $Z \to \ell\ell\gamma$ selection is applied.

The photon purity of the selected sample is checked through a signal+background fit to the three-body invariant mass, $m_{\ell\ell\gamma}$, where the signal (radiative $Z \to \ell\ell\gamma$ events) and background (Z+jets) distributions are taken from the simulation. All simulation samples used here are given in Table 3.2. For photon transverse momenta between 10 and 15 GeV

the purity is around 96%, while it increases to 99% and above for $E_{\mathrm{T}} > 15$ GeV. As an example, the results of the fits for $p_{\mathrm{T}}^{\gamma} > 15$ GeV are shown in Figure 3.6.

Data Set	Process	σ [pb]	Filter type	Filter threshold [GeV]	Generator
147770	$Z \to ee$	1.2079E+6	no filter	-	SHERPA
147771	$Z \to \mu\mu$	1.2078E+6	no filter	-	SHERPA
145161	$Z \to ee\gamma$	3.2261E+1	p_{T}^{γ}	10 GeV	SHERPA
145162	$Z \to \mu\mu\gamma$	3.2317E+1	p_{T}^{γ}	10 GeV	SHERPA

Table 3.2 – Monte Carlo samples used in the measurements.

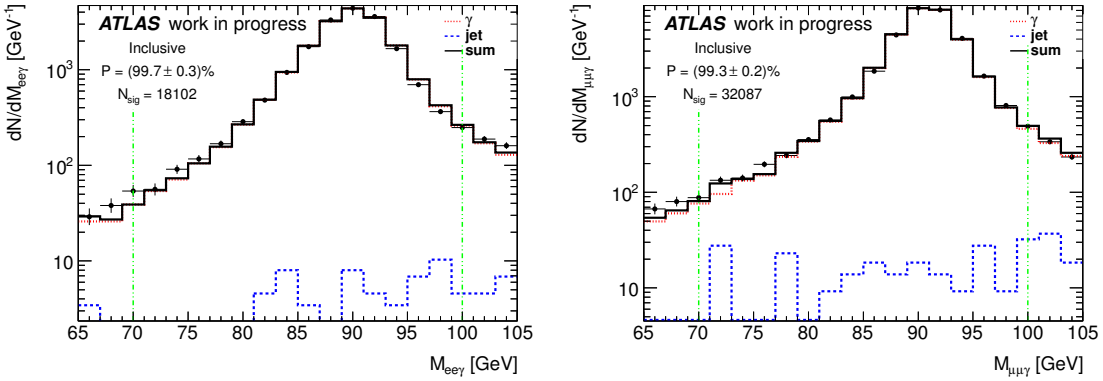

Figure 3.6 – Three-body invariant mass distribution ($m_{\ell\ell\gamma}$) of selected $Z \to \ell\ell\gamma$ events in data collected in 2012 and result of the fit used to estimate the signal purity. Left: $Z \to ee\gamma$. Right: $Z \to \mu\mu\gamma$. The red dashed lines are the photon templates. The blue dashed lines are the background (fake photon) templates. The black solid lines are the sum of signal (red) and background (blue) templates after a fit to the data (black dots). The photons have transverse momenta greater than 15 GeV.

The single photon trigger efficiency is measured and then used to calculate the di-photon trigger efficiency, by assuming that the probabilities of the two photons passing the trigger requirements are independent. Figure 3.7 shows the efficiency of the `EF_g20_loose` and `EF_g20_medium` triggers as a function of the off-line photon transverse momentum. Error bars indicate statistical uncertainties only.

The systematic uncertainties originate from the small background contamination of the selected control sample, if the trigger efficiency is different between photons and fake candidates. However, since the photon purity is more than 99% above 15 GeV and the fake candidates passing the tight identification criteria are rather similar to prompt photons in the calorimeter, the bias is expected to be very small. A systematic uncertainty due to the presence of a small fake photon contamination is estimated by repeating the measurement after selecting $Z \to \ell\ell\gamma$ candidates with different requirements on the three-body mass $m_{\ell\ell\gamma}$. Both the lower and upper bounds are varied independently by ±10 GeV, and the photon purity of the selected candidates varies by at most 1.3%, thus covering the estimated difference between the purity of the default control sample and a 100% pure photon sample. The presence of a QCD background in addition to the Z+jets background that was considered so far in the $m_{\ell\ell\gamma}$ fit to estimate the photon purity is assessed by using $\ell\ell\gamma$ events in which the leptons have the same charge to determine the shape of the $m_{\ell\ell\gamma}$

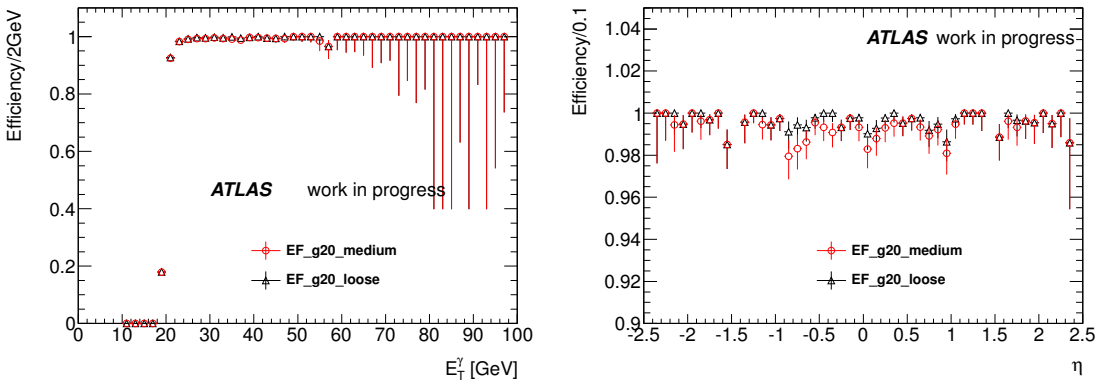

Figure 3.7 – Trigger efficiency as a function of the photon transverse momentum (left) and $|\eta|$ (right) for the `EF_g20_loose` and the `EF_g20_medium` triggers used in 2012 data taking.

distribution of this background, and using the sideband regions $40 < m_{\ell\ell\gamma} < 65$ GeV and $105 < m_{\ell\ell\gamma} < 120$ GeV in events in which the leptons have opposite charge to estimate the overall normalization. The QCD background yield in the selected control sample was found to be small (around 20 events), with an impact on the efficiency estimated to be less than 0.01%. A possible systematic uncertainty associated to the matching criterion between the off-line photon candidate and the photon trigger objects is also estimated by varying the ΔR matching distance between 0.1 and 0.2. No change in the efficiency is observed.

For the `g35_loose_g25_loose` trigger used in the $H \to \gamma\gamma$ analysis, the efficiency measured in the $H \to \gamma\gamma$ simulation ($\epsilon_{\gamma\gamma}^{35-25}$) and the efficiency measured in the $Z \to \ell\ell\gamma$ simulation ($\epsilon_\gamma^{35} * \epsilon_\gamma^{25}$) are compared to account for a possible difference of the kinematics between these two processes. The efficiency $\epsilon_{\gamma\gamma}^{35-25}$ is evaluated by counting the fraction of events passing the `g35_loose_g25_loose` trigger criteria. The efficiency $\epsilon_\gamma^{35} * \epsilon_\gamma^{25}$ is the product of the efficiencies of two single-photon trigger objects with $p_T > 35(25)$ GeV passing the loose cuts. Table 3.3 gives the single photon trigger efficiencies measured using the radiative Z decays method. The di-photon trigger efficiencies are estimated by multiplying two single photon trigger efficiencies and given in Table 3.4. For comparison, the `EF_g35_loose_g25_loose` trigger efficiency measured with the *bootstrap* method is $99.4 \pm 0.2\%$ [48], in very good agreement with this measurement.

In conclusion, with the radiative Z decay method the efficiency of photon triggers with relatively low E_T thresholds, for which the statistics of the photon control sample is large, uncertainties at the level of 0.2% for single-photon triggers and 0.4% for di-photon triggers have been achieved. These uncertainties are much smaller than other uncertainties affecting measurements with photons in the final state.

Trigger	Efficiency (%)
g20_loose	$99.62^{+0.05}_{-0.06}(stat)^{+0.05}_{-0.05}(syst)$
g25_loose	$99.74^{+0.06}_{-0.08}(stat)^{+0.05}_{-0.05}(syst)$
g35_loose	$99.74^{+0.13}_{-0.21}(stat)^{+0.05}_{-0.05}(syst)$
g20_medium	$99.33^{+0.07}_{-0.08}(stat)^{+0.05}_{-0.05}(syst)$

Table 3.3 – Efficiency of single photon triggers with photons from radiative Z decays.

Trigger	Efficiency (%)
2g20vh_medium	$98.66^{+0.14}_{-0.16}(stat)^{+0.10}_{-0.10}(syst)$
g35_loose_g25_loose	$99.48^{+0.19}_{-0.29}(stat)^{+0.10}_{-0.10}(syst)$
g30_medium_g20_medium	$98.71^{+0.22}_{-0.26}(stat)^{+0.10}_{-0.10}(syst)$

Table 3.4 – Efficiency of di-photon triggers with photons from radiative Z decays.

3.3 Photon Identification Efficiency Measurements

Photon identification plays a crucial role in measurements of Standard Model cross sections and searches for the Higgs boson and new physics with photons in the final state. An excellent photon identification (ID) capability, with high signal efficiency and large background rejection, is required for photons with transverse momentum from a dozen of GeV up to the TeV scale. The precise measurement of the ID efficiency is necessary to reduce the uncertainty on these physics studies. Photons are distinguished from fakes (i.e. π^0 decays to photon pairs) based on the shower shape discriminating variables (DVs), which have been introduced in section 2.4. The DVs distributions of photons (both from simulation and from a pure photon data sample from radiative Z decays) and fakes are shown in Fig. 3.8 for unconverted photons and in Fig. 3.9 for converted photons.

Two identification algorithms are used in ATLAS: a cut-based one and one based on an artificial neural-network. The two methods use the same DVs as input. The cut-based identification is used for most analyses, while the neural network identification is used only for the $H \to \gamma\gamma$ analysis of 2011 data. Comparing to the cut-based one in 2011, the neural network identification achieves gains in efficiency of 8-10% for the same background rejection [49]. The efficiencies of both selections are measured using three data-driven methods: the radiative Z decays [50], electron extrapolation [51] and matrix method [52].

- radiative Z decays: the same method adopted for the photon trigger efficiency measurement is used. The photons have typically low E_{T}, in the [10, 60] GeV region, and high purity.
- electron extrapolation: exploiting the similarity between the electron and photon EM showers. A large and pure sample of electrons is selected from $Z \to ee$ decays, and is used to deduce the photon DV distributions using an electron-to-photon mapping extracted from the simulation, assuming the differences between electron and photon showers are well modeled by the simulations. Given the typical E_{T} distribution of electrons from Z boson decays, this method provides precise results for E_{T} in [20, 80] GeV.
- matrix method: a technique to determine the prompt photon purity in samples of candidates passing or failing the photon ID criteria by using an independent quantity to discriminant photons from fakes. It can be used for photon E_{T} from 20 GeV up to 1 TeV.

The efficiency is measured for photons having calorimeter transverse topocluster-based isolation (corrected for out-of-cluster leakage and underlying event), denoted as $E_{\mathrm{T}}^{\mathrm{Topo40}}$, less than 4 GeV. This is a typical requirement for all analyses with photons in the final states to reduce the large background from jets misreconstructed as photons. This requirement also reduces the fraction of QCD γ+jet events due to parton-to-photon fragmentation, which are typically characterized by a smaller photon identification efficiency

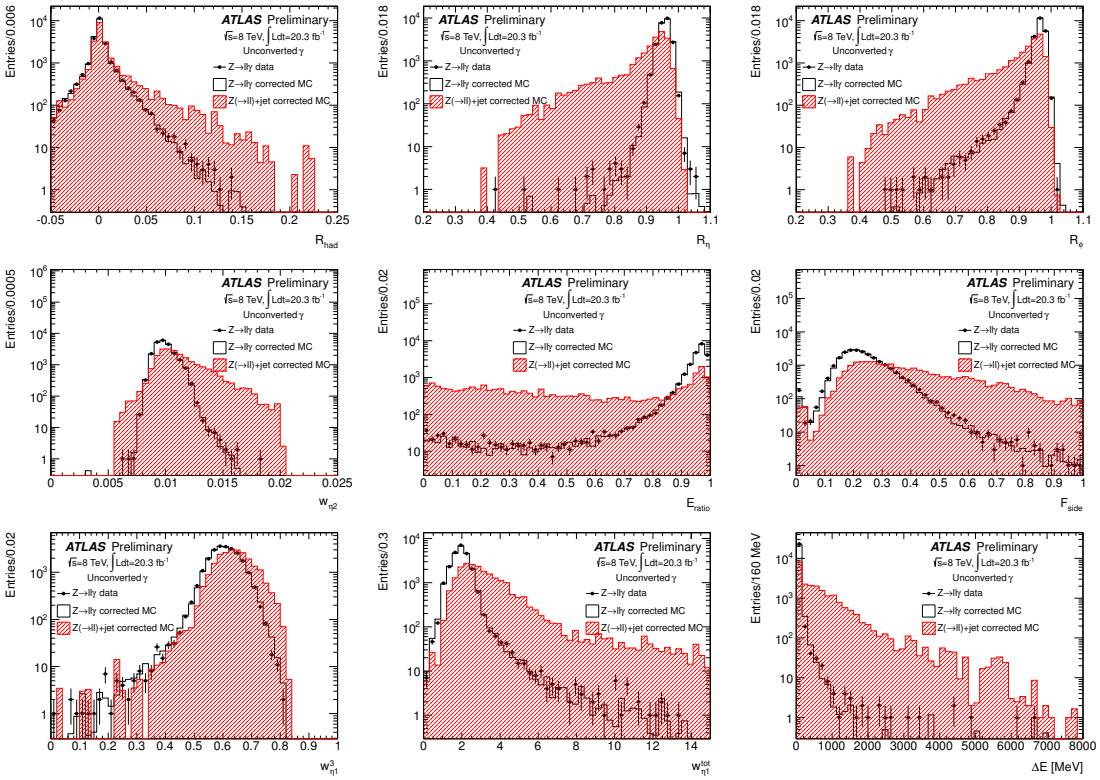

Figure 3.8 – Distribution of the calorimetric discriminating variables (DVs) for unconverted photon candidates with $E_{\mathrm{T}} > 20$ GeV and $|\eta|$ <2.37 (excluding 1.37<$|\eta|$<1.52) selected from $Z \to \ell\ell\gamma$ events obtained from the 2012 data sample (dots). The distributions for true photons from simulated $Z \to \ell\ell\gamma$ events (black hollow histogram) and for fake photons from hadronic jets in Z($\to \ell\ell$)+jets (red hatched histogram) are also shown, after reweighting their 2D E_{T} and $|\eta|$ distributions to match that of the data candidates, and correcting their values by the average shift between data and simulation distributions determined from the inclusive sample of isolated photon candidates passing the tight selection per bin of (η, E_{T}) and conversion status. Photon isolation is required on the photon candidate but no criteria on the shower shape are applied. The photon purity of the data sample is about 99%.

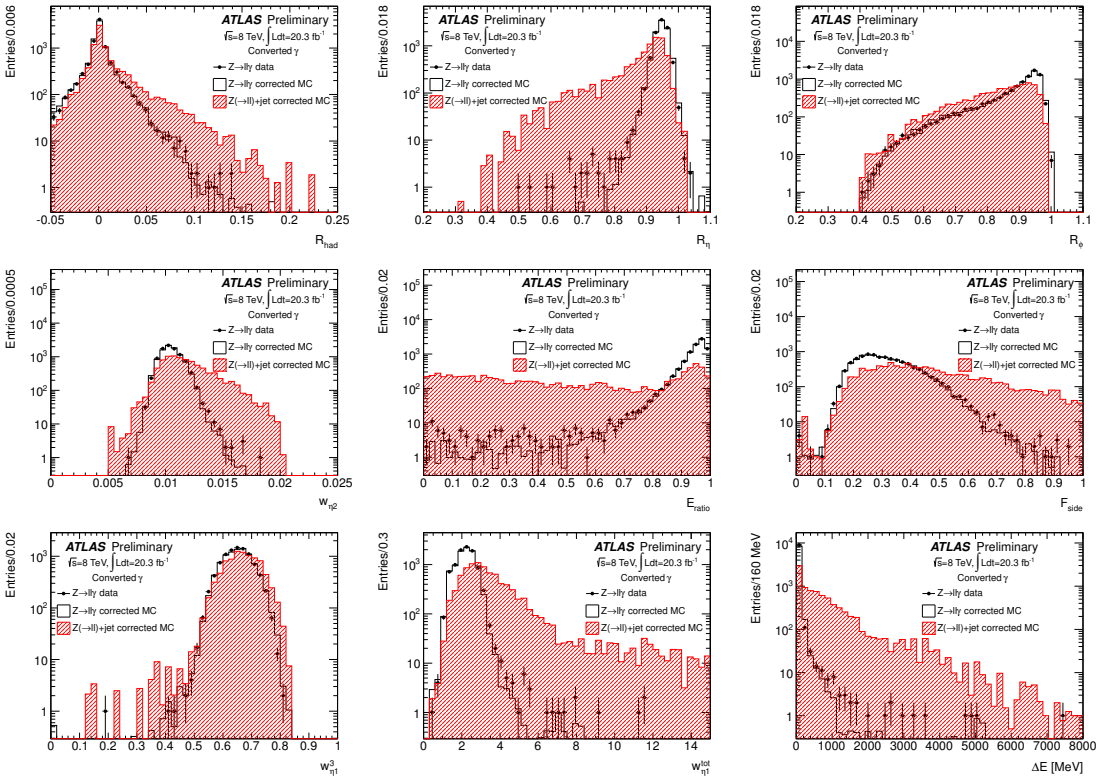

Figure 3.9 – Distribution of the calorimetric discriminating variables (DVs) for converted photon candidates with $E_{\mathrm{T}} > 20$ GeV and $|\eta|$ <2.37 (excluding 1.37<$|\eta|$<1.52) selected from $Z \to \ell\ell\gamma$ events obtained from the 2012 data sample (dots). The distributions for true photons from simulated $Z \to \ell\ell\gamma$ events (black hollow histogram) and for fake photons from hadronic jets in $Z(\to \ell\ell)$+jets (red hatched histogram) are also shown, after reweighting their 2D E_{T} and $|\eta|$ distributions to match that of the data candidates, and correcting their values by the average shift between data and simulation distributions determined from the inclusive sample of isolated photon candidates passing the tight selection per bin of (η, E_{T}) and conversion status. Photon isolation is required on the photon candidate but no criteria on the shower shape are applied. The photon purity of the data sample is about 99%.

because of the other fragmentation products. However, as shown in Fig. 3.10 and Fig. 3.11, the photon identification efficiency versus transverse momentum for photons for different simulated physics processes (γ+jet, with or without fragmentation, radiative Z decays, $H \to \gamma\gamma$ decays) after the isolation requirement is very similar.

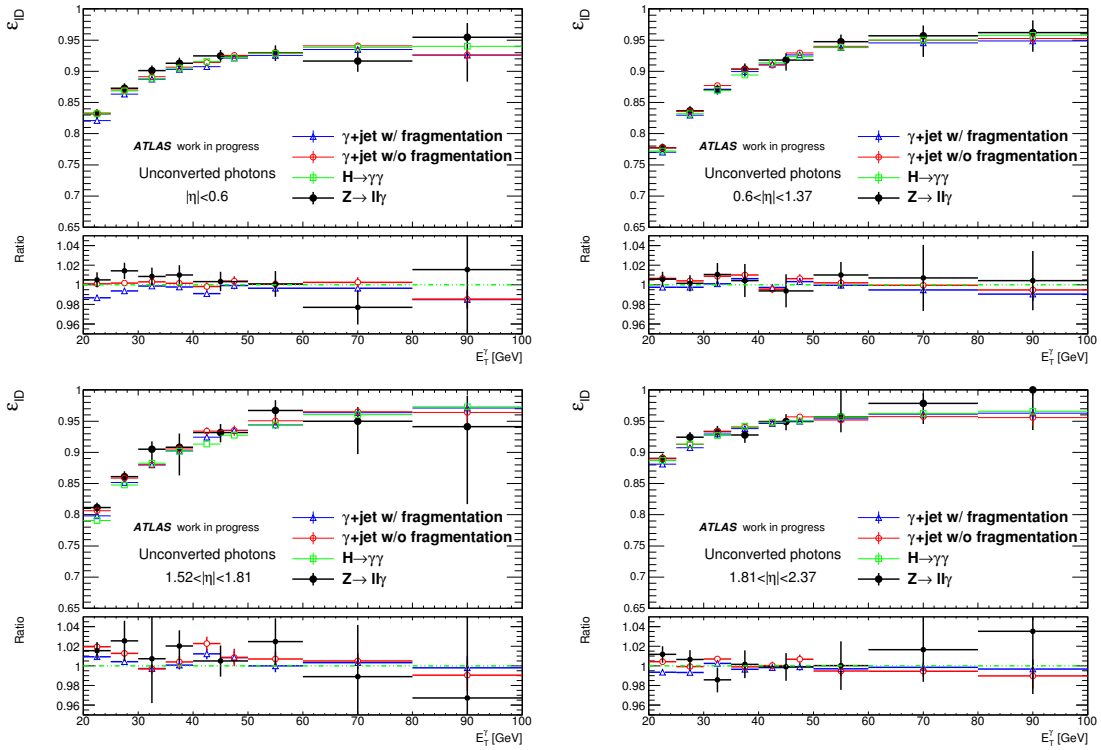

Figure 3.10 – Tight identification efficiency for unconverted photons as a function of photon E_{T}, for four different pseudorapidity intervals, after an isolation requirement, in various simulated samples at $\sqrt{s} = 8$ TeV: γ+jet with fragmentation (blue), γ+jet without fragmentation (red), $H \to \gamma\gamma$ (green), $Z \to \ell\ell\gamma$ (black).

In the following I will describe the three methods and their results, as well as their combination; my work focused in particular on the first and the third methods.

3.3.1 The Radiative Z Decays Method

Photons radiated from leptons in Z-boson decays ($Z \to \mu\mu\gamma$ and $Z \to ee\gamma$) are used as probes. In order to obtain a pure control sample of photons from $Z \to \ell\ell\gamma$ ($\ell = e, \mu$) without biasing the distributions of their shower shape variables, we use selections based on the properties of the two leptons (isolation, identification, impact parameters) and on the di-lepton and the $\ell\ell\gamma$ invariant masses, as described in section 3.2. There is no requirement on the photon shower shape information.

For simplicity only the measurement based on the 2012 data is described in the following. We select 53879 (19944) unconverted (converted) photon candidates in the $Z \to \mu\mu\gamma$ channel, and 32272 (11754) unconverted (converted) photon candidates in $Z \to ee\gamma$ channel. Their transverse momentum distributions are given in Fig. 3.12.

The efficiency of the tight identification is measured as the fraction of selected photons

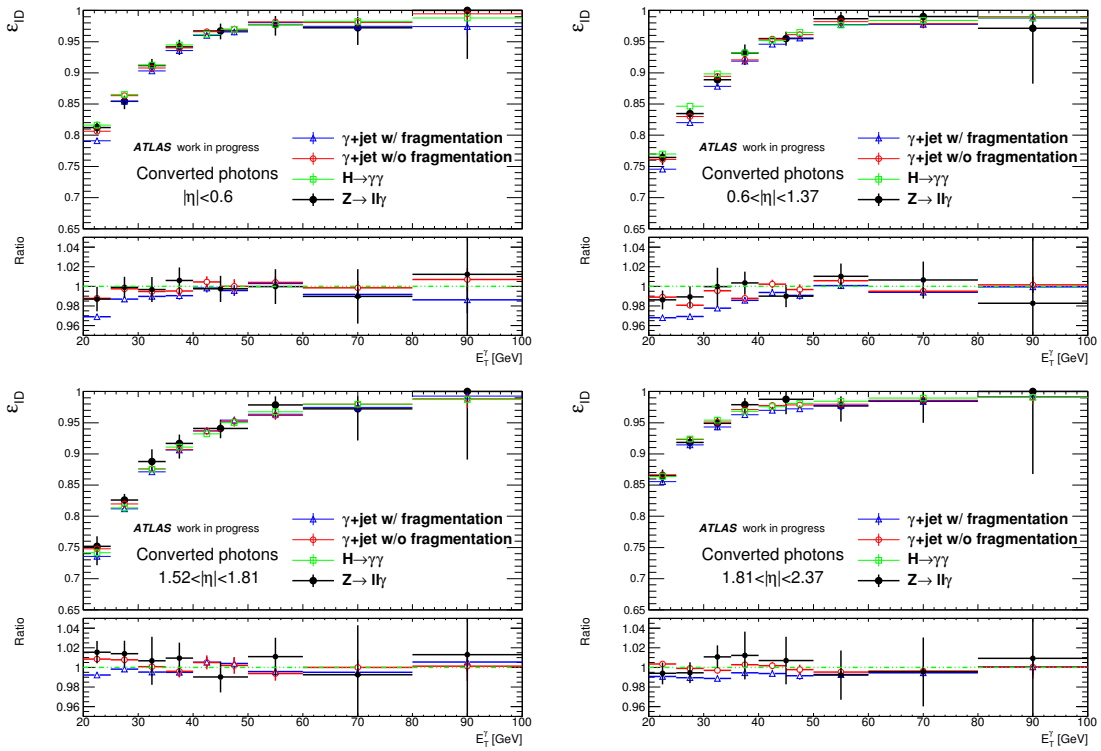

Figure 3.11 – Tight identification efficiency for converted photons as a function of photon E_{T}, for four different pseudorapidity intervals, after an isolation requirement, in various simulated samples at $\sqrt{s} = 8$ TeV: γ+jet with fragmentation (blue), γ+jet without fragmentation (red), $H \to \gamma\gamma$ (green), $Z \to \ell\ell\gamma$ (black).

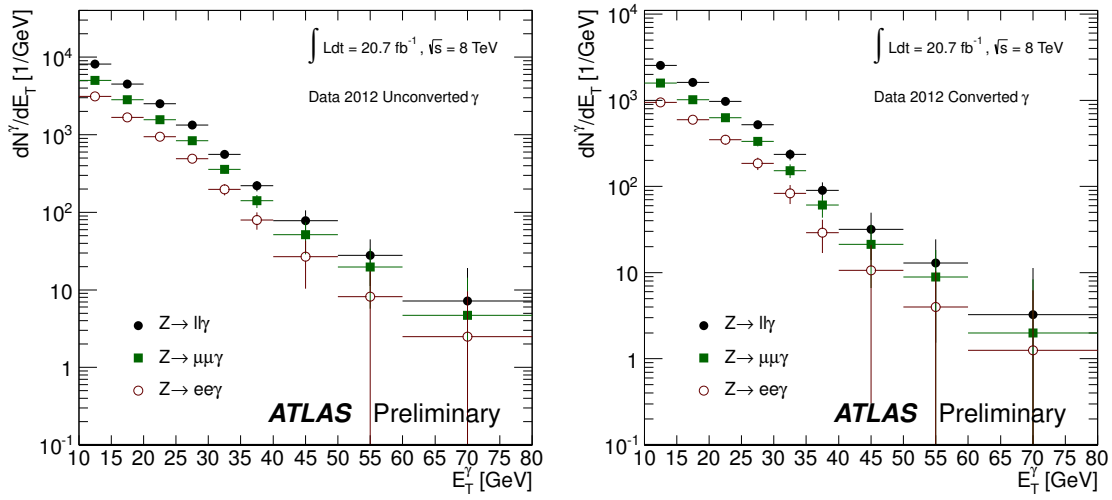

Figure 3.12 – E_{T} spectra of photon candidates selected in data collected at $\sqrt{s} = 8$ TeV from $Z \to \mu\mu\gamma$ and $Z \to ee\gamma$ candidates and from the combination of the two samples. Left: unconverted photons. Right: converted photons.

(probes) that pass the tight identification criteria:

$$\varepsilon_{\rm ID} = \frac{N_{\rm probes,tight}}{N_{\rm probes}}. \tag{3.1}$$

This approximation is valid if the selected probe sample is free of any background contamination. However, in the selected photon sample there is a residual contamination due to jets, misidentified as photons, from Z+jets events. The fraction of this background in the selected sample depends on the reconstructed photon transverse energy, varying between $\approx 10\%$ for $10 < E_{\rm T} < 15$ GeV and $\leq 2\%$ for higher-$E_{\rm T}$ regions. This background is estimated in data and subtracted for $10 < E_{\rm T} < 15$ GeV, while for higher $E_{\rm T}$ the background is neglected and a systematic uncertainty is assigned. The background subtraction in the region $10 < E_{\rm T} < 15$ GeV and the estimation of the background fraction in the higher $E_{\rm T}$ interval is performed through a template fit to the $m_{\ell\ell\gamma}$ distribution, as described in the previous section.

The fits for photon candidates with $10 < E_{\rm T} < 15$ GeV are shown in Fig 3.13, using templates extracted from the Z+γ and Z+jet simulated samples generated with Sherpa. In the signal region used for the efficiency measurement ($80 < m_{\ell\ell\gamma} < 96$ GeV) the purity is 93.7% (89.7%) for the $\mu\mu\gamma$ ($ee\gamma$) channel and the corresponding signal yield N_S is 31107 (18044). The results are cross-checked by re-doing the fit using a signal template extracted from the Pythia Z+γ samples or using a background template extracted from the Alpgen Z+jet samples. The results are consistent within 0.5% with the nominal one. Using the same template-fit procedure, after applying the tight photon ID criteria, the purity is estimated to be 98.9% (97.9%) as shown in Fig. 3.14, the number of tight photons ($N_{S,tight}$) is 16500 (9705) and the number of fakes ($N_{B,tight}$) is 319 (262) for $\mu\mu\gamma(ee\gamma)$ channel. The PID efficiency in the $10 < E_{\rm T} < 15$ GeV region is:

$$\varepsilon_{\rm ID} = \frac{N_{S,\rm tight}}{N_S} = \frac{N_{\rm probes,tight} - N_{B,\rm tight}}{N_{\rm probes} - N_B}. \tag{3.2}$$

For $E_{\rm T} > 15$ GeV, the efficiency is computed as in equation (3.1). The systematic uncertainty from residual background is estimated by performing two fits to $m_{\ell\ell\gamma}$, one for all the events after the nominal selection, and and one for the events in which the photon candidates also pass the tight ID requirements. From these fits we determine the signal purity in the signal region 80 GeV$< m_{\ell\ell\gamma} <$ 96 GeV: before the tight ID requirements, the purity P_{before} is 98.4% (97.8%) for unconverted (converted) photons for $\mu\mu\gamma$, and 98.8% (98.0%) for $ee\gamma$. After applying the tight identification criteria, the photon purity $P_{\rm after}$ is larger than 99%. The relative difference ($\sigma = (P_{\rm after} - P_{\rm before})/P_{\rm before}$), 1.3% (1.6%) for unconverted (converted) photons in the $Z \to \mu\mu\gamma$ sample and 1.1% (1.7%) for unconverted (converted) photons in the $Z \to ee\gamma$ channel, is assigned as the systematic uncertainty on the efficiency due to the residual background in the selected sample.

3.3.2 The Electron Extrapolation Method

This method exploits the similarity between the electromagnetic showers induced by electrons and photons, and benefits of the large statistics of a pure electron sample with $E_{\rm T}$ between 20 and 80 GeV obtained from $Z \to ee$ decays using a "tag-and-probe" method. The DV distribution showing the largest difference between electrons and converted photons is that of R_ϕ, due to the opening of the e^+e^- pair in the magnetic field. However, the converted photon cut on R_ϕ is relatively loose, reducing the impact of this difference on the efficiency difference between electrons and converted photons. It is found in the

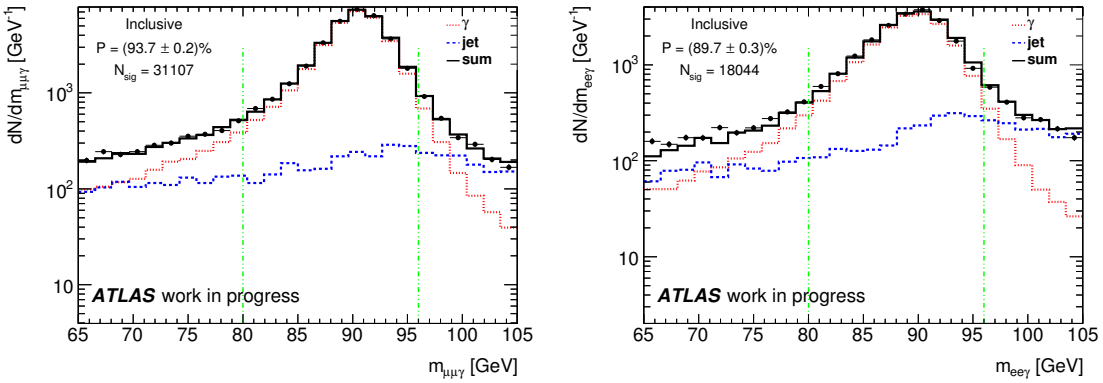

Figure 3.13 – Invariant mass ($m_{\ell\ell\gamma}$) distribution of events in which the photon has $10 < E_{\mathrm{T}} < 15$ GeV, selected in data at $\sqrt{s} = 8$ TeV after applying all the $Z \to \ell\ell\gamma$ selection criteria except that on $m_{\ell\ell\gamma}$ (black dots). The solid black line represents the result of the fit of the data distribution with the sum of the signal (red dashed line) and background (blue dotted line) invariant mass distributions obtained from Sherpa MC. Left: $l = \mu$. Right: $l = e$.

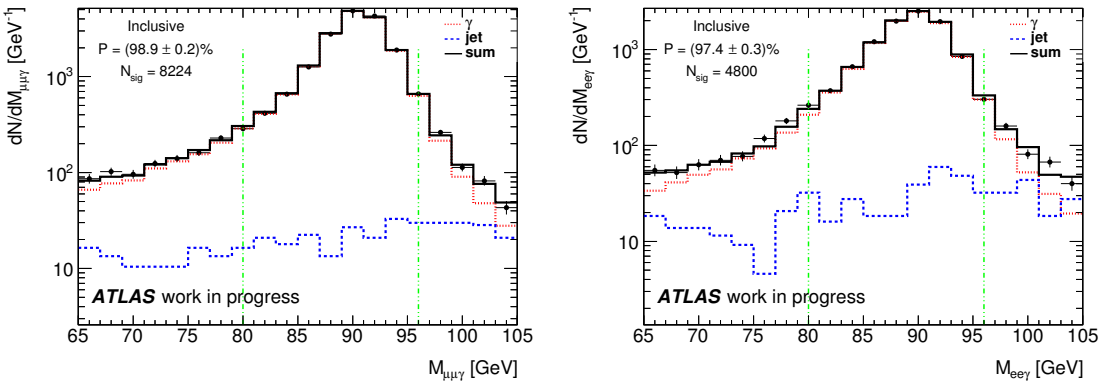

Figure 3.14 – Invariant mass ($m_{\ell\ell\gamma}$) distribution of events in which the photon has $10 < E_{\mathrm{T}} < 15$ GeV, selected in data at $\sqrt{s} = 8$ TeV after applying all the $Z \to \ell\ell\gamma$ selection criteria except that on $m_{\ell\ell\gamma}$ (black dots). The photons are required to pass the tight identification criteria. The solid black line represents the result of the fit of the data distribution with the sum of the signal (red dashed line) and background (blue dotted line) invariant mass distributions obtained from Sherpa MC. Left: $l = \mu$. Right: $l = e$.

simulation that applying the converted photon identification criteria directly to the DVs of a pure sample of electrons yields the converted photon efficiency to within $\mathcal{O}(3\%)$. On the other hand, the unconverted photon EM shower on average initiates later than that of electrons, and thus tends to produce narrower shower shape distributions in the strip layer of the EMC. Additionally, the lack of radiation in the ϕ plane makes the R_ϕ distribution particularly distinct from that of electrons. Since for unconverted photons the identification criteria on R_ϕ as well as on the strip layer variables are relatively tight, significant, $\mathcal{O}(15-20\%)$ differences between the efficiency obtained using simulated electrons and simulated unconverted photons are observed to reduce this difference. A Smirnov transform [53], obtained from simulated samples of electrons and photons, is used to correct on an event-by-event basis the values of the DVs of the electron probes in order to obtain the expected distributions for converted or unconverted photons. Figure 3.15 illustrates the process for one shower shape. Initially, the cumulative distribution functions (CDFs) of both electrons and photons are calculated in the simulation for the given shower shape variable. A mapping is derived, giving for each source value the shift which is necessary to apply to the shower shape value with the same CDF value in the target distribution. By deriving and applying this shift for each shower shape, the electron sample in data can be transformed into a sample of objects with photon-like shower shapes. Smirnov transformations are invariant under systematic shifts which are correlated between the source and target distributions, which reduces the impact of uncertainties in the MC samples used in this study. Due to differences in the $|\eta|$ and p_{T} distribution of the source and target samples, and dependency of shower shapes and photon identification cuts on $|\eta|$, p_{T} and conversion status, this process is applied separately for converted and unconverted photons, and in regions of p_{T} and $|\eta|$. As the process is applied to each shower shape independently, correlations between shower shapes in the initial sample are preserved. The different systematics break down as follows:

- the efficiencies measured in transformed electron sample are compared to the photon one in simulation to asses the impact of differences in how the shower shape distributions are correlated, as well as differences in the η and p_{T} distributions within a given bins. These are found to be of at most $\mathcal{O}(2\%)$ for unconverted photons, and less for converted ones.
- the Smirnov transformation is calculated alternatively using simulation with additional material in the ATLAS detector, to test the sensitivity of efficiency to wrong simulation of the Smirnov map. These are found to be at most of $\mathcal{O}(5\%)$ for converted photons and $\mathcal{O}(15\%)$ for unconverted photons.
- the isolation criteria on the "tag" and "probe" electron sample is varied to test the sensitivity to presence of residual impurity in the data electron sample. The effect on the efficiency is found to be smaller than 1%.
- a background-subtraction procedure is applied and the impact on the efficiency of the small amount of background present in the sample is estimated to be within 1% for all E_{T} and η regions considered.

3.3.3 The Matrix Method

The photon identification efficiency is estimated from data using a track isolation requirement to statistically discriminate between prompt and fake photons in the samples of reconstructed photon candidates passing or failing the identification criteria. Suppose that, after some preselection, N^T_{pass} photon candidates – consisting of N^S_{pass} prompt photons

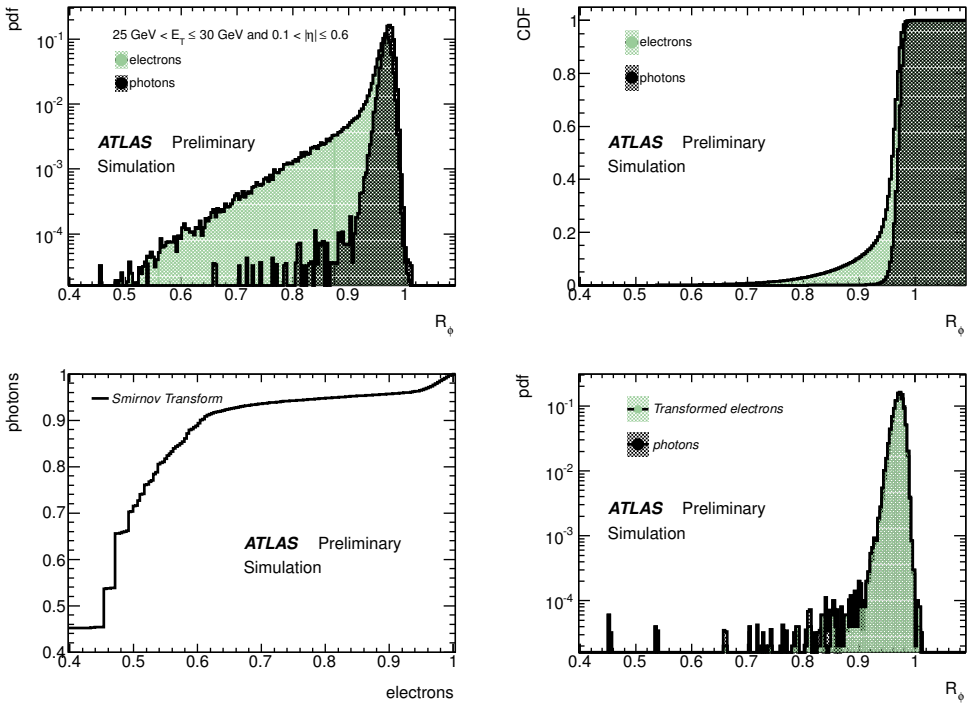

Figure 3.15 – Diagram illustrating the process of Smirnov transformation. R_ϕ is chosen as an example shower shape which is particularly divergent between electrons and photons. The R_ϕ distribution in each sample (top left) is used to calculate the respective CDF (top right). From the two CDFs, a Smirnov transformation can be derived (bottom left). Applying the transformation leads to an R_ϕ distribution of the transformed electrons which closely resembles the photon distribution.

and $N^B_{\rm pass}$ fake photons – pass the tight identification criteria, while $N^T_{\rm fail}$ candidates – consisting of $N^S_{\rm fail}$ prompt photons and $N^B_{\rm fail}$ fake photons – fail the tight identification criteria. The tight ID efficiency is

$$\varepsilon^{tight-ID} = \frac{N^S_{\rm pass}}{N^S_{\rm pass} + N^S_{\rm fail}}. \tag{3.3}$$

Introducing the signal purity in data, for photon candidates passing the tight cut (P):

$$P \equiv \frac{N^S_{\rm pass}}{N^T_{\rm pass}}, \tag{3.4}$$

and for photon candidates failing the tight cut (F):

$$F \equiv \frac{N^S_{\rm fail}}{N^T_{\rm fail}}, \tag{3.5}$$

one can see with some algebra that the tight ID efficiency can be also rewritten as:

$$\varepsilon^{tight-ID} = \frac{1}{1 + \frac{F}{P}\frac{N^T_{\rm fail}}{N^T_{\rm pass}}}. \tag{3.6}$$

We use the track isolation of the selected photons to estimate $N^S_{\rm fail}$ and $N^S_{\rm pass}$ (together with $N^B_{\rm fail}$ and $N^B_{\rm pass}$), or equivalently the purities P and F. The track isolation is defined as the number of tracks or the sum of p_T of the tracks, with transverse momentum above 0.5 GeV, in a cone of $\Delta R = \sqrt{(\Delta\eta)^2 + (\Delta\phi)^2} < 0.2, 0.3, 0.4$ around the direction of photon candidate, subtracting energy deposited within an inner cone of $\Delta R = 0.1$. By definition, we have

$$N^T_{\rm pass} = N^S_{\rm pass} + N^B_{\rm pass} \tag{3.7}$$
$$N^T_{\rm fail} = N^S_{\rm fail} + N^B_{\rm fail} \tag{3.8}$$

Let us denote the number of isolated candidates with $N^{Iso}_{\rm pass}$ ($N^{Iso}_{\rm fail}$) if they pass (fail) the tight identification criteria. Let ε^s_p (ε^s_f) be the track isolation efficiency for prompt photons passing (failing) the tight identification criteria, and ε^b_p (ε^b_f) be the track isolation efficiency for fake photons passing (failing) the tight identification criteria, respectively. We have therefore:

$$N^{Iso}_{\rm pass} = \varepsilon^s_p \times N^S_{\rm pass} + \varepsilon^b_p \times N^B_{\rm pass} \tag{3.9}$$
$$N^{Iso}_{\rm fail} = \varepsilon^s_f \times N^S_{\rm fail} + \varepsilon^b_f \times N^B_{\rm fail} \tag{3.10}$$

If we know the four track isolation efficiencies ε^s_p, ε^s_f, ε^b_p and ε^b_f, from equations 3.7–3.10, we can get both $N^S_{\rm pass}$ and $N^S_{\rm fail}$ from the observed number of events $N^T_{\rm fail}$, $N^{Iso}_{\rm fail}$, $N^T_{\rm pass}$ and $N^{Iso}_{\rm pass}$ in data:

$$N^S_{\rm pass} = \frac{N^{Iso}_{\rm pass} - \varepsilon^b_p \times N^T_{\rm pass}}{\varepsilon^s_p - \varepsilon^b_p} \tag{3.11}$$
$$N^S_{\rm fail} = \frac{N^{Iso}_{\rm fail} - \varepsilon^b_f \times N^T_{\rm fail}}{\varepsilon^s_f - \varepsilon^b_f}, \tag{3.12}$$

as well as the purities P and F:

$$P = \frac{\varepsilon_p - \varepsilon_p^b}{\varepsilon_p^s - \varepsilon_p^b} \ , \tag{3.13}$$

$$F = \frac{\varepsilon_f - \varepsilon_f^b}{\varepsilon_f^s - \varepsilon_f^b} \ , \tag{3.14}$$

where $\varepsilon_p \equiv \frac{N^{Iso}_{\rm pass}}{N^{T}_{\rm pass}}$ is the fraction of tight photon candidates that pass the track isolation criteria and $\varepsilon_f \equiv \frac{N^{Iso}_{\rm fail}}{N^{T}_{\rm fail}}$ is the fraction of non-tight photon candidates that pass the track isolation criteria.

The prompt photon track isolation efficiencies are estimated from simulated prompt photon events. The accuracy of the simulation is varified by comparing the track isolation efficiency of electrons selected by using a "tag-and-probe"method in data and simulation. The difference is taken as a systematic uncertainty: it is of the order of 1%. The fake photon track isolation efficiencies (ε_p^b and ε_f^b) are estimated from a data sample enriched in fake photons, selected by reversing the tight identification criteria on the shower shape variables based on the lateral energy deposition pattern in a few strips near the hottest one in the first compartment of the LAr electromagnetic calorimeter: $F_{\rm side}$, w_3, ΔE, $E_{\rm ratio}$. These variables are only weakly correlated (linear correlations of few %) with the photon track isolation. We refer to this group of variables as "narrow-strip" variables. Since no candidate passes the tight identification criteria but fails at the same time the subset of cuts on the narrow-strip variables, for the fake photon track isolation efficiency measurement we relax the tight criteria, based on the nine quantities $R_{\rm had}$, R_η, R_ϕ, $w_{\eta 2}$, $F_{\rm side}$, w_3, $w_{\rm tot}$, ΔE and $E_{\rm ratio}$, by dropping the requirements on the narrow-strip variables. We call this selection criteria "relaxed-tight". Because of the very small correlation between the track isolation and the narrow-strip variables, we expect the fake photon track isolation efficiency to be similar for photon passing tight or relaxed-tight criteria. This hypothesis is tested with simulated di-jet samples; the differences are included in the systematic uncertainties. An illustration of the photon candidate classification according to their identification criteria is shown in Fig. 3.16:

- region 1+3 contains the photon candidates passing relaxed-tight criteria
- region 2+4 contains the photon candidates failing relaxed-tight criteria
- region 1+2 contains the candidates that pass the cuts on the narrow-strip variables
- region 3+4 contains the candidates that fail the cuts on the narrow-strip variables

Candidates in region 3 pass the relaxed-tight cuts but fail the criteria on the narrow-strip variables. The candidates in this region are used to estimate the fake photon track isolation efficiency for fake candidates that pass tight identification criteria (region 1). Candidates in region 4, which fail both relaxed-tight and narrow-strip cuts, are used to estimate the track isolation efficiency of fake photons failing the tight identification criteria (region 2+3+4). The signal contribution to the control regions 3 and 4 is significantly suppressed, but a residual contamination exists. It is estimated using prompt photon MC samples to determine the fraction of signal in regions 3 and 4 with respect to the signal in region 1, and subtracted from the data yields as described below. We introduce a few definitions according to Fig. 3.16:

- N_A: total number of photon candidates in region 3.
- N_B: total number of photon candidates in region 4.

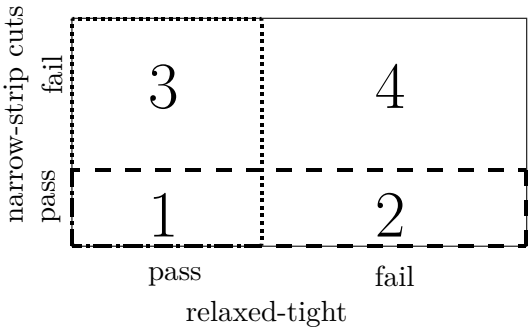

pass relaxed-tight cuts

pass all cuts on narrow-strip variables

1: pass tight cuts
2: pass narrow-strip variable cuts but fail relaxed-tight cuts
3: pass relaxed-tight but fail narrow-strip cuts
4: fail relaxed-tight and fail narrow-strip cuts variables

Figure 3.16 – A graphical illustration of photon candidate classification in the data sample. Candidates in region 3 and region 4 on the graph are used to estimated the track isolation efficiencies for background ε_p^b and ε_f^b after having subtracted residual signal photons.

- ε_p: fraction of photon candidates that are isolated in the tracker after passing tight criteria (region 1).
- ε_f: fraction of photon candidates that are isolated in the tracker after failing tight criteria (region 2+3+4).
- $\varepsilon_p^{b^+}$: fraction of photon candidates in region 3 that are isolated in the tracker.
- $\varepsilon_f^{b^+}$: fraction of photon candidates in region 4 that are isolated in the tracker.

We also remind the previous definitions of:

- N_{pass}^T: total number of photon candidates that pass tight criteria (region 1).
- N_{fail}^T: total number of photon candidates that fail tight criteria (region 2+3+4).

The above quantities ($N_A, N_B, \varepsilon_p, \varepsilon_f, \varepsilon_p^{b^+}, \varepsilon_f^{b^+}, N_{\text{pass}}^T, N_{\text{fail}}^T$) are determined in data.

From the prompt photon MC sample we extract the following quantities for prompt photons:

- f_p: fraction of prompt photons that leak in region 3.
- f_f: fraction of prompt photons that leak in region 4.
- ε_p^s: track isolation efficiency for prompt photons in region 1.
- ε_f^s: track isolation efficiency for prompt photons in region 2+3+4.
- $\varepsilon_p^{s^+}$: track isolation efficiency for prompt photons in region 3.
- $\varepsilon_f^{s^+}$: track isolation efficiency for prompt photons in region 4.

The track isolation efficiency for fake photons passing or failing relaxed-tight cuts are ε_p^b and ε_f^b, respectively. They relate to the quantities defined previously through the following equations. The total number of signal photons in regions 1-2-3-4, N_{total}^S, can be evaluated as:

$$N_{\text{total}}^S = N_{\text{pass}}^S + N_{\text{fail}}^S = N_{\text{pass}}^T \times P + N_{\text{fail}}^T \times F = N_{\text{pass}}^T \times \frac{\varepsilon_p - \varepsilon_p^b}{\varepsilon_p^s - \varepsilon_p^b} + N_{\text{fail}}^T \times \frac{\varepsilon_f - \varepsilon_f^b}{\varepsilon_f^s - \varepsilon_f^b} \quad (3.15)$$

The first term on the right-hand side of the equation is the number of photons passing tight criteria, while the second term is the number of prompt photons failing the tight criteria. With the total number of signal events in the data sample, we can get the

number of prompt photons in regions 3 and 4 using the fractions of prompt photons in these two regions from the signal simulation. We subtract the signal leakage from both the numerators and denominators to obtain ε_p^b and ε_f^b.

$$\varepsilon_p^b = \frac{N_A \times \varepsilon_p^{b^+} - N_{\text{total}}^S \times f_p \times \varepsilon_p^{s^+}}{N_A - N_{\text{total}}^S \times f_p} \tag{3.16}$$

$$\varepsilon_f^b = \frac{N_B \times \varepsilon_f^{b^+} - N_{\text{total}}^S \times f_f \times \varepsilon_f^{s^+}}{N_B - N_{\text{total}}^S \times f_f} \tag{3.17}$$

We can solve the three equations 3.15-3.17 to obtain the three unknowns (N_{total}^S, ε_p^b, ε_f^b). The equations are nonlinear and an iterative procedure is used to find the numerical solutions. This iterative procedure begins using as input for equation 3.15 (N_{pass}^T,N_{fail}^T, ε_p, ε_f) from data and (ε_p^s,ε_f^s,ε_p^b,ε_f^b) from the simulation. Then N_{total}^S is used in Eq. 3.16 and 3.17, from which ε_p^b and ε_f^b are calculated using (N_A, N_B) from data and ($\varepsilon_p^{s^+}$, $\varepsilon_f^{s^+}$, $\varepsilon_p^{b^+}$, $\varepsilon_f^{b^+}$) from the simulation. Then the previous procedure is repeated with these new estimates of ε_p^b and ε_f^b. The procedure is terminated when

$$\sqrt{(\varepsilon_p^b - \varepsilon_p^{b^*})^2 + (\varepsilon_f^b - \varepsilon_f^{b^*})^2} < 0.001 \tag{3.18}$$

where $\varepsilon_p^{b^*}$ and $\varepsilon_f^{b^*}$ means the values in the previous iteration. The procedure always converges after a number of iterations between 3 and 6.

Figures 3.17 and 3.18 show the true and fake photon track isolation efficiencies as a function of E_{T} in the four $|\eta|$ regions for unconverted and converted photon candidates respectively. The photon purity and identification efficiency can be deduced from these curves as explained previously.

One of the major sources of systematic uncertainty comes from the signal leakage into the background-enriched sample. It is estimated by carrying out the same procedure in a simulated sample and comparing the obtained background track isolation efficiencies with the true ones in the simulation. Unfortunately, a large component of the uncertainty arises from lack of events in the simulated sample used to cross-check the signal leakage subtraction procedure described above. Since the statistical uncertainty is not disentangled from actual systematic uncertainties arising from correlations between track isolation and the DVs using the first EMC layer, the entire difference in MC is conservatively taken as a systematic uncertainty. For converted photons, this results in a systematic uncertainty of up to $\pm$ 20% for the efficiency of background events passing the tight photon selections, while it is about 5% for unconverted photons.

3.3.4 Efficiency Comparison and Combination

The results from different methods are in good agreements within errors. To achieve a better accuracy the results from the different methods are combined together. The combination in 2011 measurement follows the prescription in PDG [54], whilest in 2012 measurement it follows the Best Linear Unbiased Estimate (BLUE) method [55, 56, 57].

The identification efficiencies measured in 2011 with the three data-driven methods are compared in the top panels of the plots of Figure 3.19 for unconverted photons and of Figure 3.20 for converted photons.

Their uncertainties are treated as completely uncorrelated, and the weighted mean ($\bar{\varepsilon}_{\text{ID}}$) and its uncertainty ($\sigma_{\bar{\varepsilon}_{\text{ID}}}$) are computed as:

$$\bar{\varepsilon}_{\text{ID}} \pm \sigma_{\bar{\varepsilon}_{\text{ID}}} = \frac{\sum_i w_i \varepsilon_{IDi}}{\sum_i w_i} \pm (\sum_i w_i)^{-\frac{1}{2}} \qquad w_i = \frac{1}{(\sigma_{\varepsilon_{IDi}})^2} \tag{3.19}$$

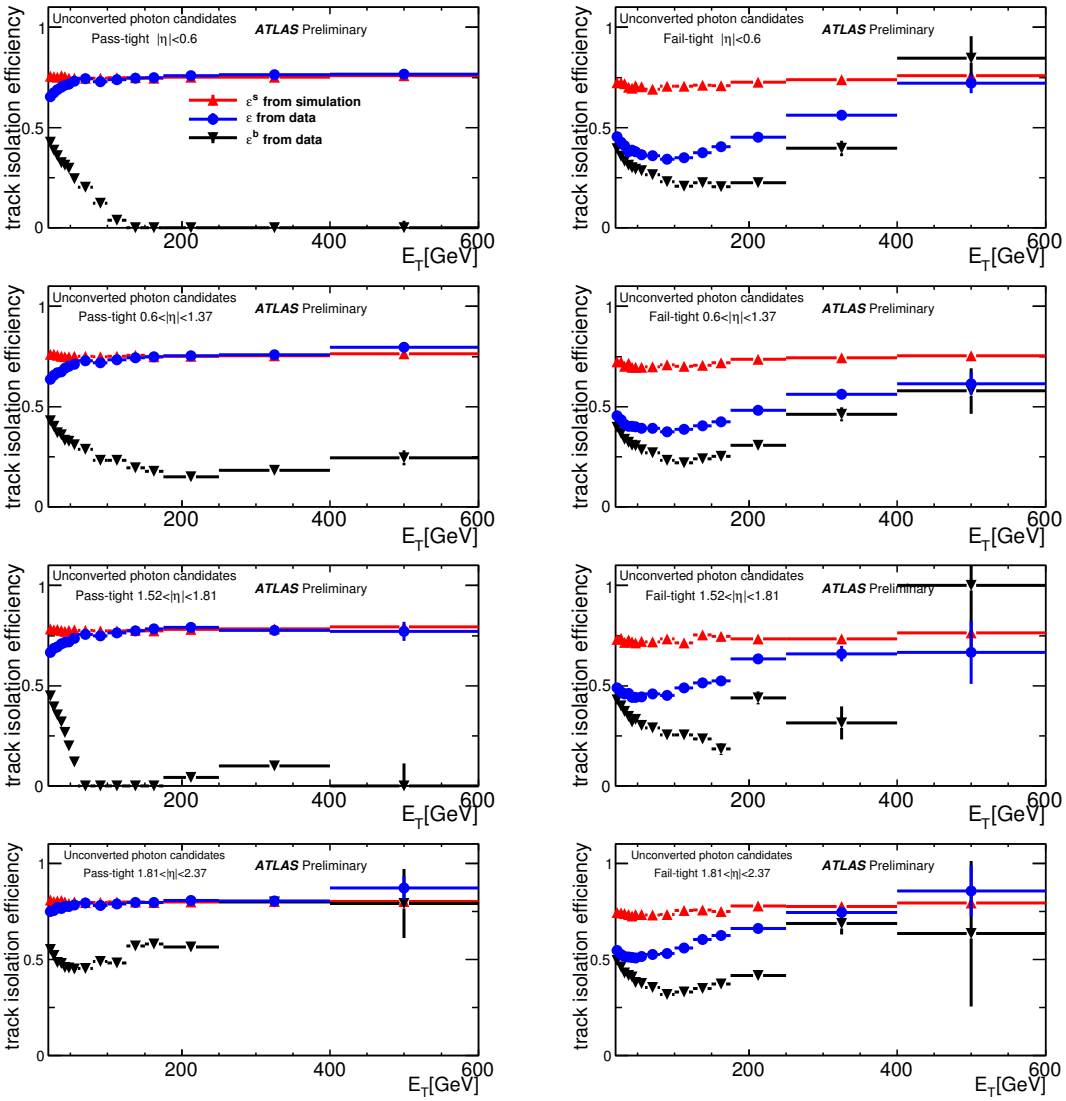

Figure 3.17 – Track isolation efficiencies for unconverted prompt and fake photon candidates at $\sqrt{s} = 7$ TeV passing (ε_p: left column) or failing (ε_f: right column) the relaxed-tight criteria, as measured in data and from simulations. The red triangular markers show the signal track isolation efficiencies as obtained from simulation, whereas the black triangular markers show that of background, as determined from data. The blue circular markers show the overall track isolation efficiency found in data (prompt and fake photon together)

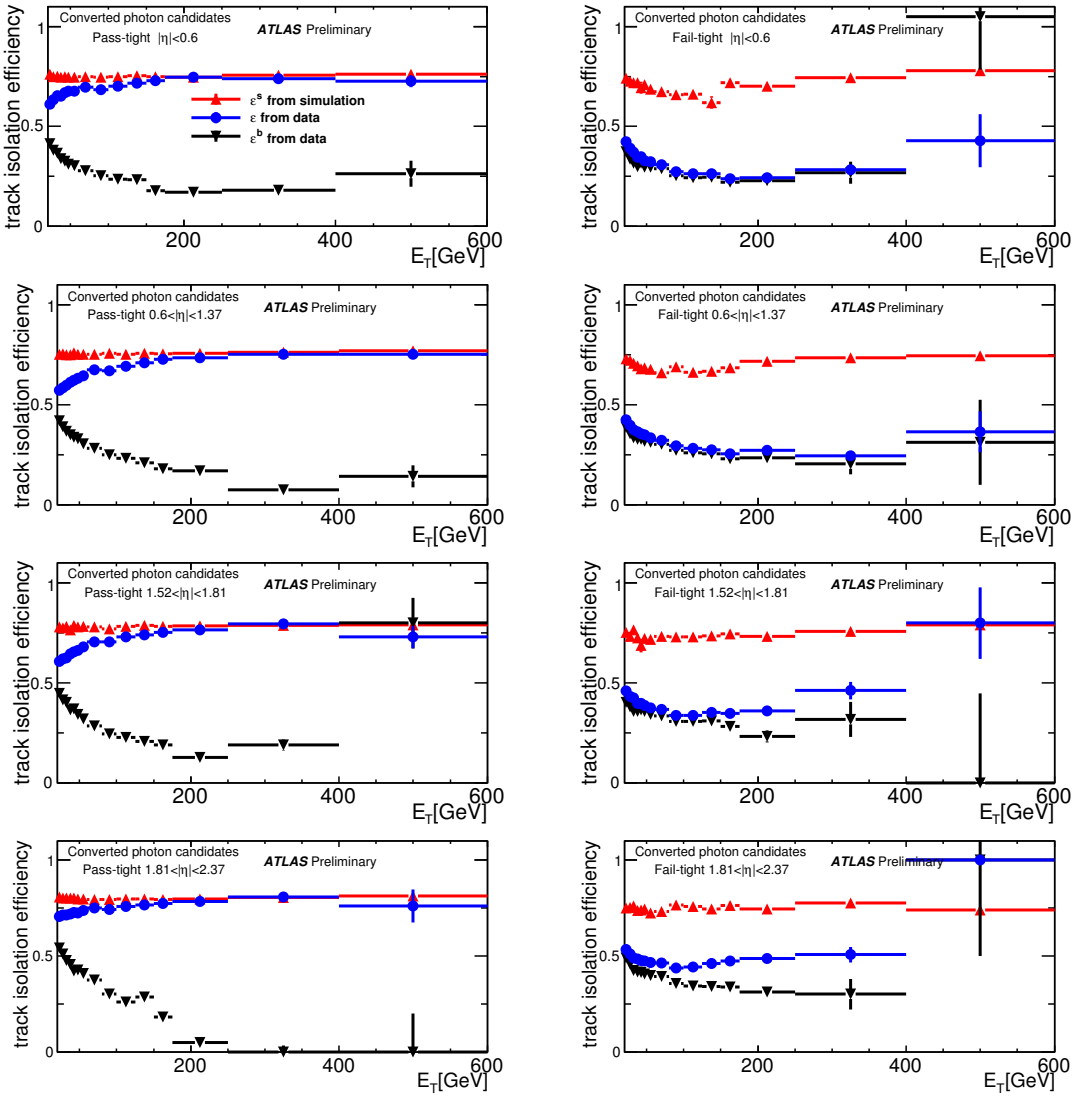

Figure 3.18 – Track isolation efficiencies for converted prompt and fake photon candidates at $\sqrt{s} = 7$ TeV passing (ε_p: left column) or failing (ε_f: right column) the relaxed-tight criteria, as measured in data and from simulations. The red triangular markers show the signal track isolation efficiencies as obtained from simulation, whereas the black triangular markers show that of background, as determined from data. The blue circular markers show the overall track isolation efficiency found in data (prompt and fake photon together)

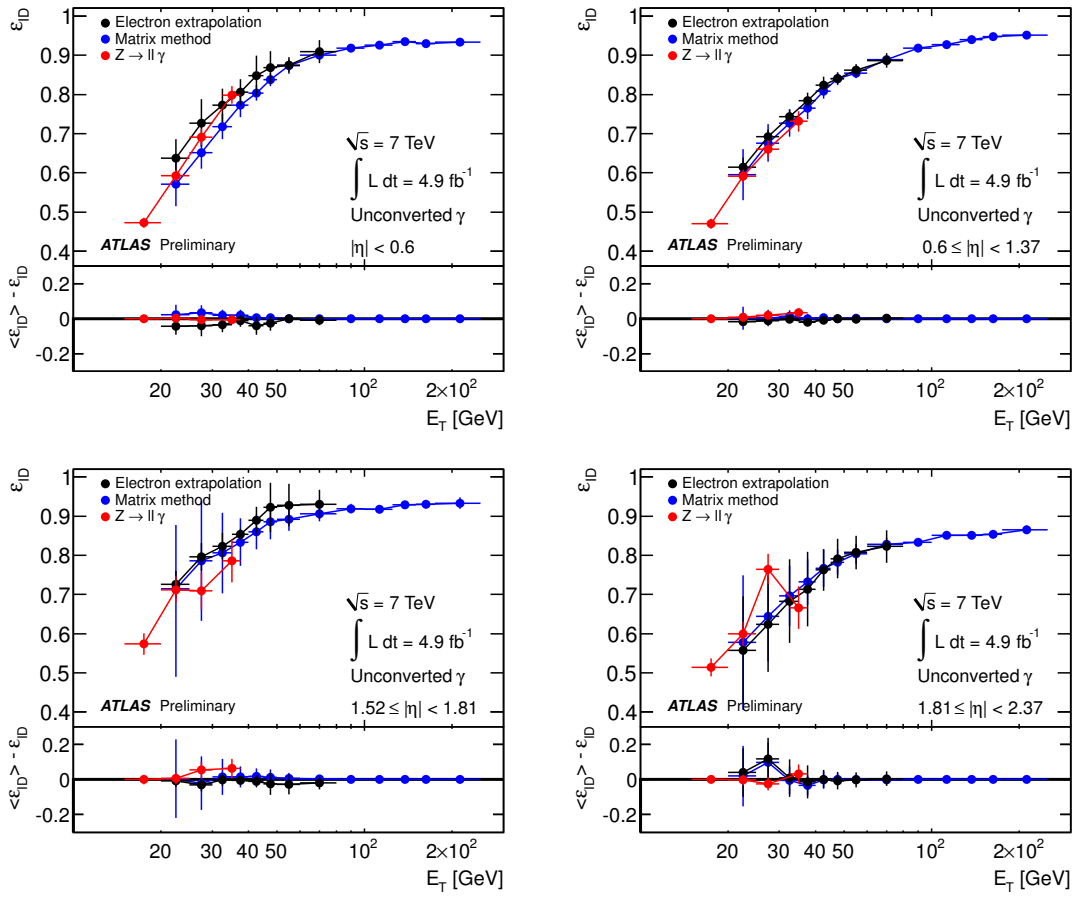

Figure 3.19 – Comparison of the data-driven measurements of the identification efficiency for unconverted photons in the region 15 GeV $< E_{\mathrm{T}} <$ 300 GeV, in 2011 data. The efficiency curves are shown in four different η regions. The results from the $Z \to \mu\mu\gamma$ and $Z \to ee\gamma$ analyses are shown as a single curve. The error bars represent the quadratic sum of the statistical and systematic uncertainties estimated in each method. The difference of each of the curves to the weighted mean value is shown in the bottom panel of each figure.

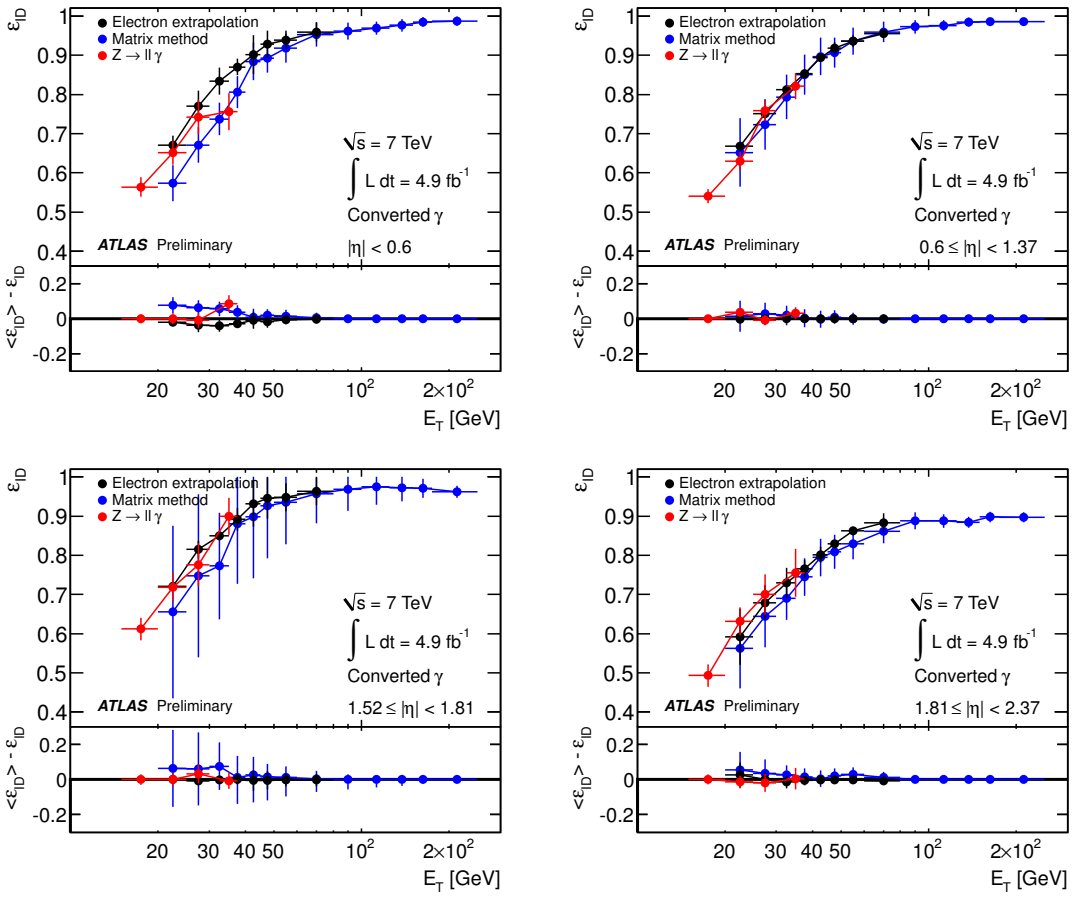

Figure 3.20 – Comparison of the data-driven measurements of the identification efficiency for converted photons in the region 15 GeV $< E_{\mathrm{T}} <$ 300 GeV, in 2011 data. The efficiency curves are shown in four different η regions. The results from the $Z \to \mu\mu\gamma$ and $Z \to ee\gamma$ analyses are shown as a single curve. The uncertainty lines represent the quadratic sum of the statistical and systematic uncertainties estimated in each method. The difference of each of the curves to the weighted mean value is shown in the bottom panel of each figure.

where the sums run over the three data-driven results in a given (E_{T}, η) bin and the uncertainty on each measurements $\sigma_{\varepsilon_{IDi}}$ is the sum in quadrature of the associated statistical and systematic uncertainties. The χ^2 of the combination is compared to $(N-1)$ for each (E_{T}, η) bin, where N is the number of measurements used in the combination. Only 3 bins have $1 < \chi^2/(N-1) < 2$, and no bin has $\chi^2/(N-1) > 2$. In such bins, the errors are increased by a factor $\sqrt{\chi^2/(N-1)}$, following the prescription in Ref. [54]. The bottom panels in the plots of Figure 3.19 and Figure 3.20 show how the efficiency in each measurement compares to the mean value. The combined efficiency curves are given in Figure 3.21 and Figure 3.22, with the predicted efficiencies in simulation with and without a shower-shape based corrections, called "fudge-factor". The fudge-factors are simple shifts applied to the simulated DVs. They determined from the difference between the averages of the DV distributions in data and Monte Carlo, in samples of inclusive photon candidates passing tight identification requirements:

$$\Delta_{DV} = \langle DV_{data} \rangle - \langle DV_{MC} \rangle \tag{3.20}$$

In the simulation, a mixture of photon-jet and di-jet events normalised to the photon purity measured in data is used. The fudge factors are computed in bins of (E_{T}, η) [58].

The efficiencies of three measurements using 2012 data are shown in Fig. 3.23 for unconverted photons and in Fig. 3.24 for converted photons. From the ratio $\varepsilon_{\mathrm{ID}}^{data}/\varepsilon_{\mathrm{ID}}^{MC}$ between the data and MC efficiency, scale factors (SF) are extracted, as shown in Figure 3.25 and Figure 3.26. The results from each methods are in good agreements within errors. The scale factor uncertainties are calculated as:

$$\begin{aligned} \sigma_{\mathrm{stat}} &= \frac{\varepsilon_{\mathrm{ID}}^{data}}{\varepsilon_{\mathrm{ID}}^{MC}} \sqrt{\left(\frac{\sigma_{\mathrm{ID,stat}}^{data}}{\varepsilon^{data}}\right)^2 + \left(\frac{\sigma_{\mathrm{ID,stat}}^{MC}}{\varepsilon^{MC}}\right)^2} \\ \sigma_{\mathrm{syst}} &= \frac{\sigma_{\mathrm{ID,syst}}^{data}}{\varepsilon_{\mathrm{ID}}^{MC}} \end{aligned} \tag{3.21}$$

The scale factors from the three measurements are combined with the following method. For n measurements x_i of the same value, the covariance matrix V_x is defined by:

$$(V_x)_{ij} = \rho_{ij}\sigma_i\sigma_j \tag{3.22}$$

where ρ_{ij} is the correlation coefficient and σ_i is the uncertainty on x_i. The diagonal members of V_x are the variances, for example $(V_x)_{ii} = \sigma_i^2$. The best linear estimator is defined by:

$$\overline{x} = \sum_i w_i.x_i \tag{3.23}$$

with

$$w_i = \frac{\sum_k (V_x)_{ik}^{-1}}{\sum_{jk} (V_x)_{jk}^{-1}} \tag{3.24}$$

The uncertainty on x_i is then defined by:

$$\sigma_{\overline{x}}^2 = \sum_{ij} w_i.w_j.(V_x)_{ij} \tag{3.25}$$

Four sources of uncertainties are considered in this measurement:

- a statistical uncertainty for all methods;

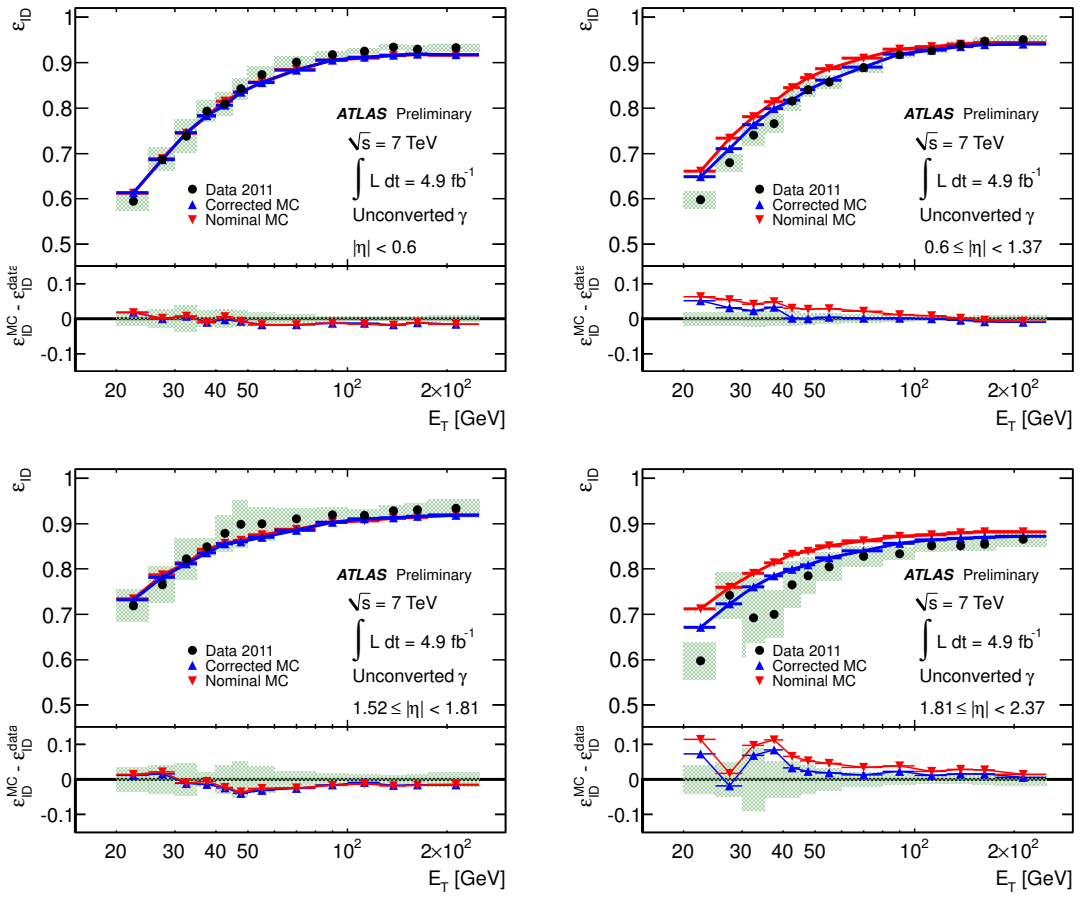

Figure 3.21 – Comparison of weighted mean of the data-driven measurements of unconverted $\varepsilon_{\mathrm{ID}}$ to the nominal and corrected MC predictions in the region 15 GeV $< E_{\mathrm{T}} <$ 300 GeV, in 2011 data. The $\varepsilon_{\mathrm{ID}}$ curves are shown in four different η regions. The green uncertainty band corresponds to the addition in quadrature of the statistical and systematic uncertainties estimated for the combination of the data-driven methods. Only the statistical uncertainties are shown for the MC predictions. The bottom figures show the difference between the data-driven curve and nominal and corrected MC predictions.

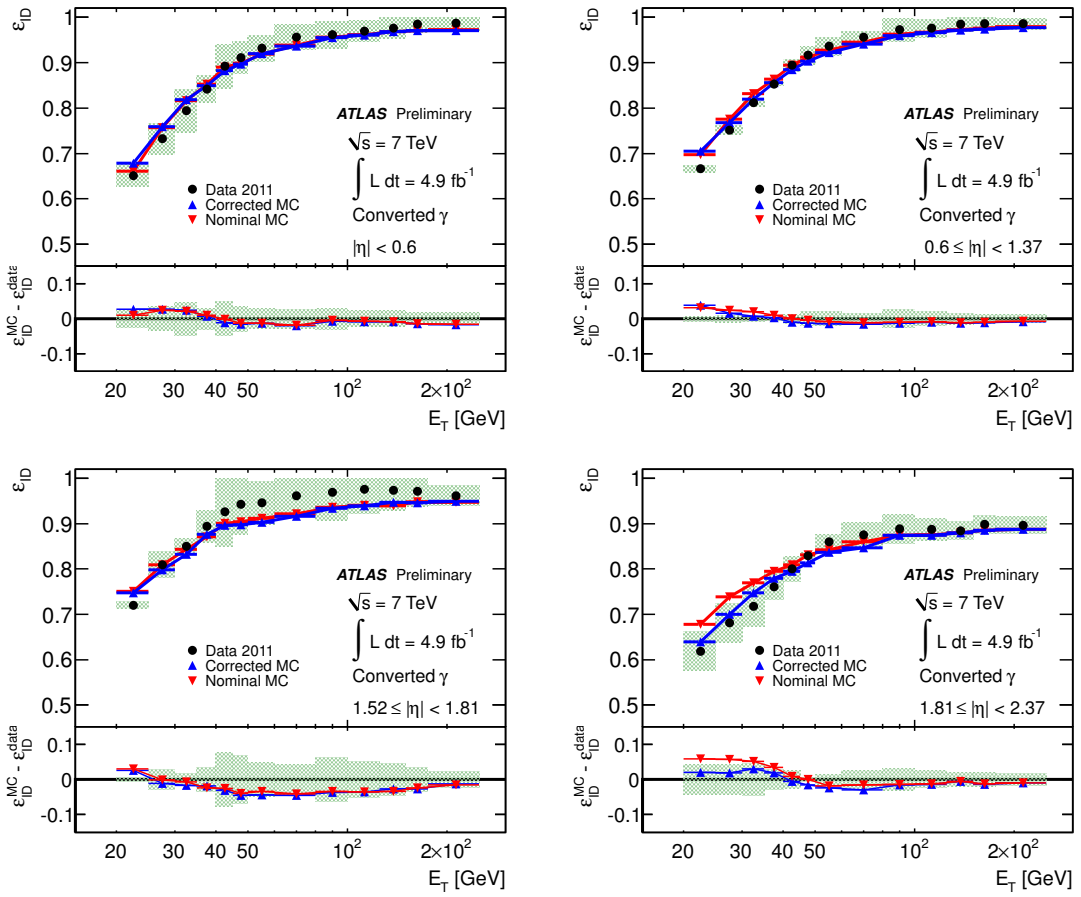

Figure 3.22 – Comparison of weighted mean of the data-driven measurements of converted $\varepsilon_{\mathrm{ID}}$ to the nominal and corrected MC predictions in the region 15 GeV $< E_{\mathrm{T}} <$ 300 GeV, in 2011 data. The $\varepsilon_{\mathrm{ID}}$ curves are shown in four different η regions. The green uncertainty band corresponds to the addition in quadrature of the statistical and systematic uncertainties estimated for the combination of the data-driven methods. Only the statistical uncertainties are shown for the MC predictions. The bottom figures show the difference between the data-driven curve and nominal and corrected MC predictions.

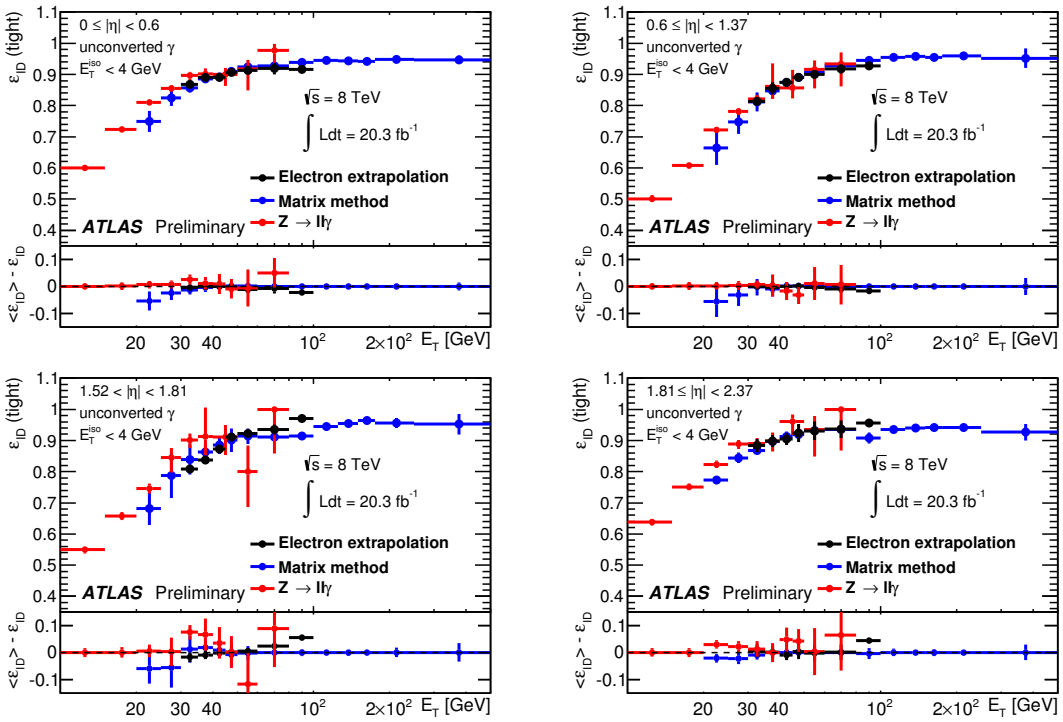

Figure 3.23 – Comparison of the data-driven measurements of the identification efficiency for unconverted photons in the region 10 GeV$< E_{\mathrm{T}} <$ 500 GeV, in 2012 data. The curves are shown in four different η regions. The error bars represent the quadratic sum of the statistical and systematic uncertainties estimated in each method.

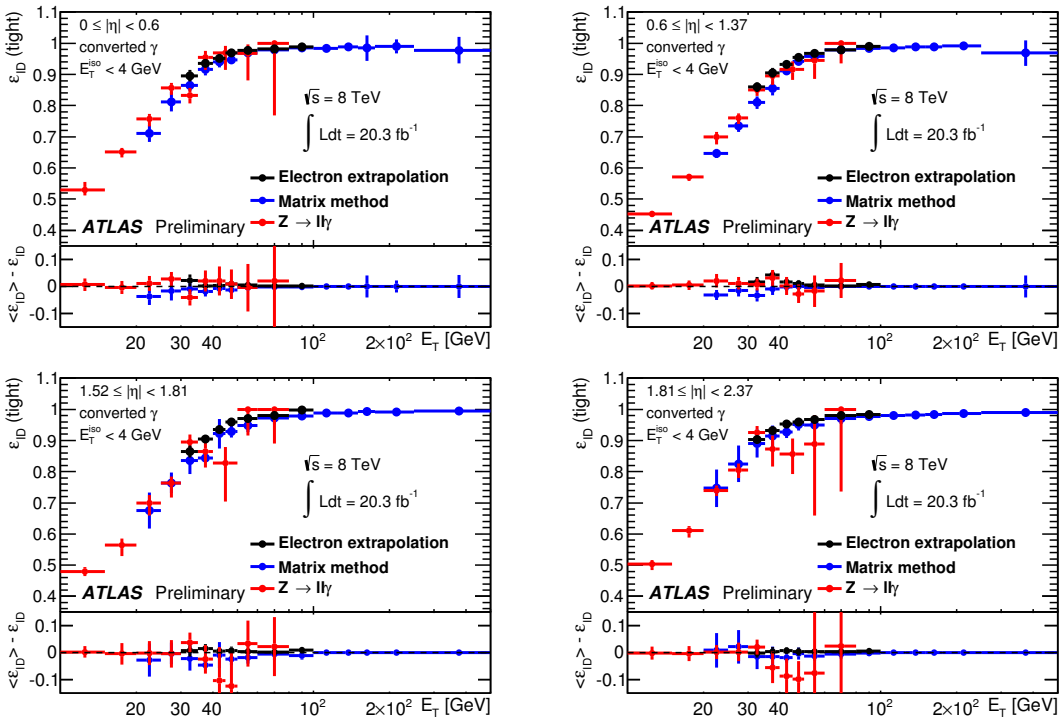

Figure 3.24 – Comparison of the data-driven measurements of the identification efficiency for converted photons in the region 10 GeV$< E_{\mathrm{T}} <$ 500 GeV, in 2012 data. The curves are shown in four different η regions. The error bars represent the quadratic sum of the statistical and systematic uncertainties estimated in each method.

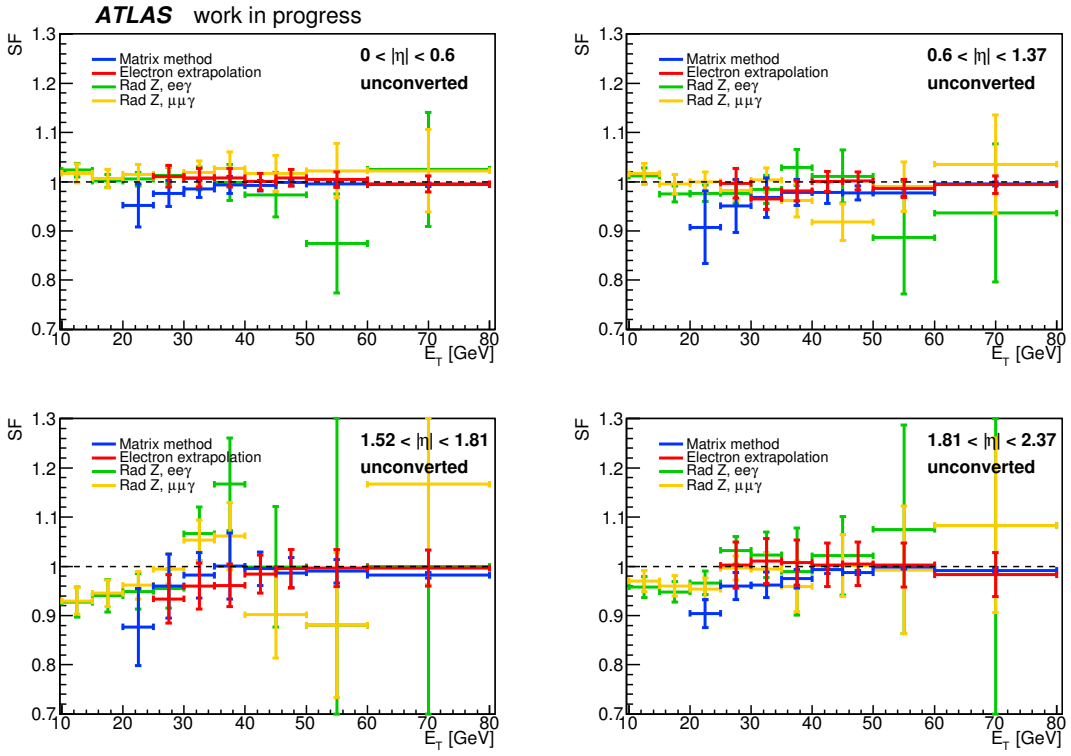

Figure 3.25 – Comparison of the efficiency scale factors for unconverted photons in the region 10 GeV$< E_{\mathrm{T}} <$ 80 GeV, for $\sqrt{s} = 8$ TeV. The curves are shown in four different η regions. The error bars represent the quadratic sum of the statistical and systematic uncertainties estimated in each method.

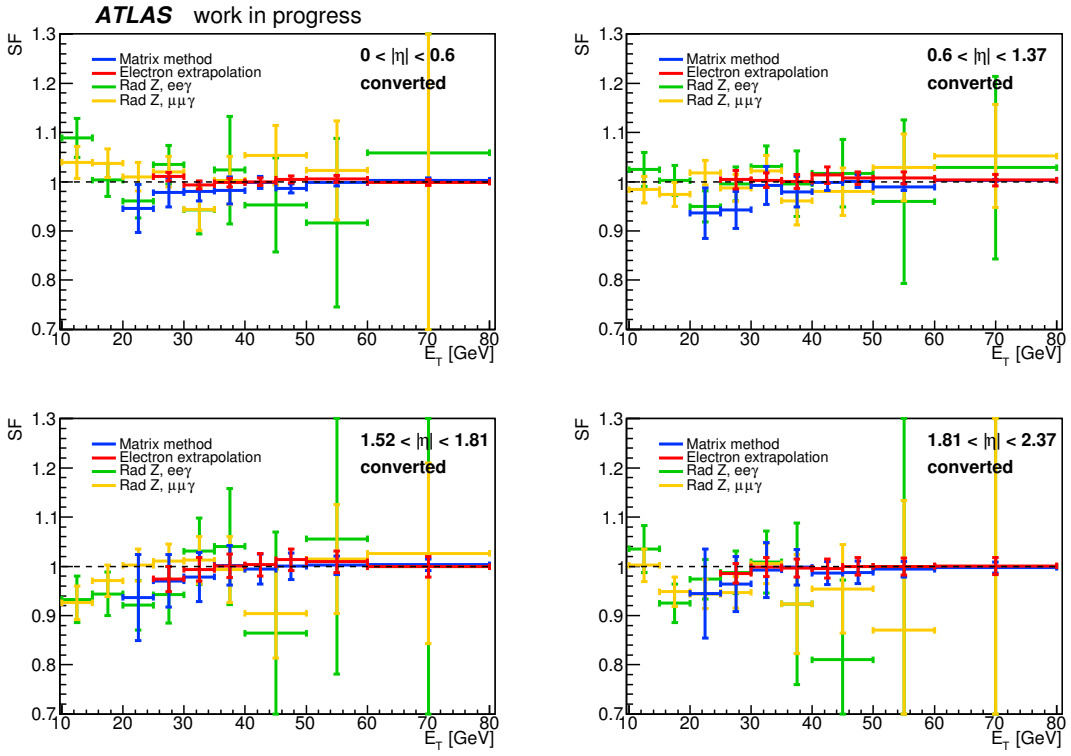

Figure 3.26 – Comparison of the scale factors for converted photons in the region 10 GeV$< E_{\mathrm{T}} <$ 80 GeV, for $\sqrt{s} = 8$ TeV. The curves are shown in four different η regions. The error bars represent the quadratic sum of the statistical and systematic uncertainties estimated in each method.

- a background uncertainty for radiative Z decays and matrix method;
- a material uncertainty for electron extrapolation and matrix method;
- a closure uncertainty for electron extrapolation.

For each (E_{T}, η) bin the $\chi^2 = \sum w_i(\overline{SF} - SF_i)^2$ is computed and compared to $N-1$, where N is the number of measurements combined for that point. For the points with $\chi^2/(N-1) > 1$, the error on the combined value is increased by a factor $\sqrt{\chi^2/(N-1)}$, following the prescription in the reference of [54]. The combined efficiencies are given in Figure 3.27 and Figure 3.28. The combined scale factors are given in Figure 3.29 and Figure 3.30.

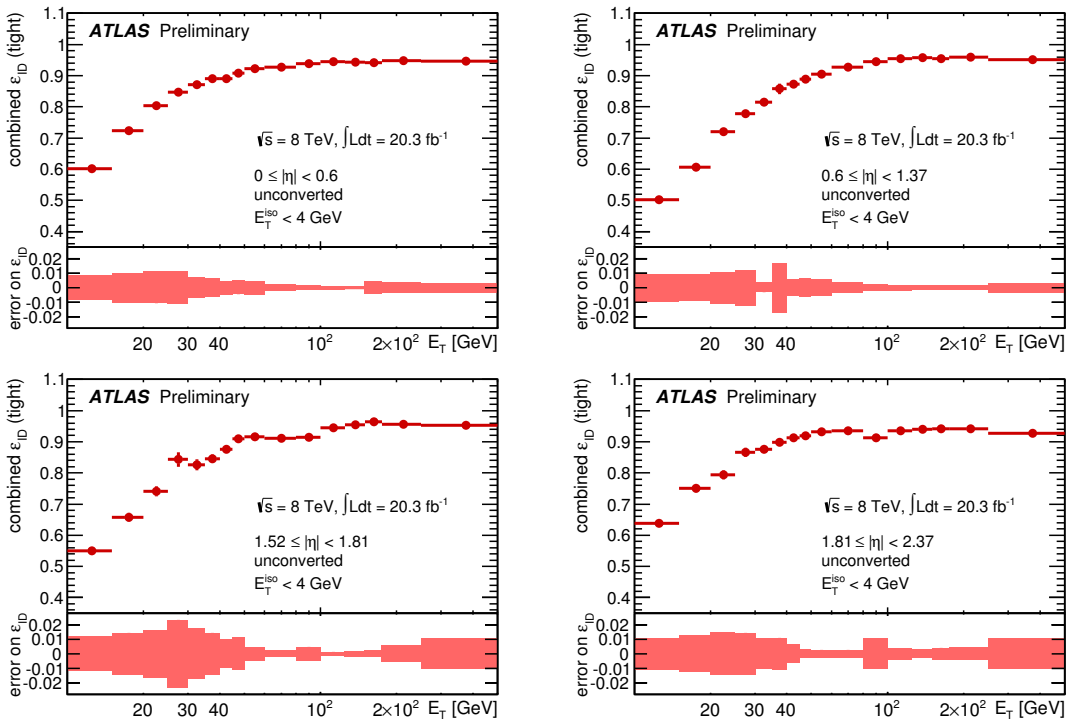

Figure 3.27 – Combined identification efficiency for unconverted photons in the region 10 GeV $< E_{\mathrm{T}} <$ 500 GeV, in 2012 data. The curves are shown in four different η regions.

3.4 Pile-up Dependence of the Photon Identification Efficiency

Pile-up can affect the photon identification efficiency, since the DV distributions of photons become broader because of the additional energy deposited in the calorimeter by the products of the pile-up collisions. The efficiency thus decreases with the number of reconstructed primary vertices (N_{PV}), which is proportional to the number of pp collisions in the same bunch. In physics analyses performed in ATLAS the simulated samples used to study the signal efficiency are reweighted in order to match the pile-up distribution of the data. Therefore, if the dependence of the efficiency on N_{PV} is well modeled by the simulation, no systematic error on the efficiency for photon signals arises from this effect. On the other hand, if the simulation predicts a different slope for the ε_{ID} vs N_{PV} curve than the data, this will affect the signal efficiency, in particular for the analyses of 2012

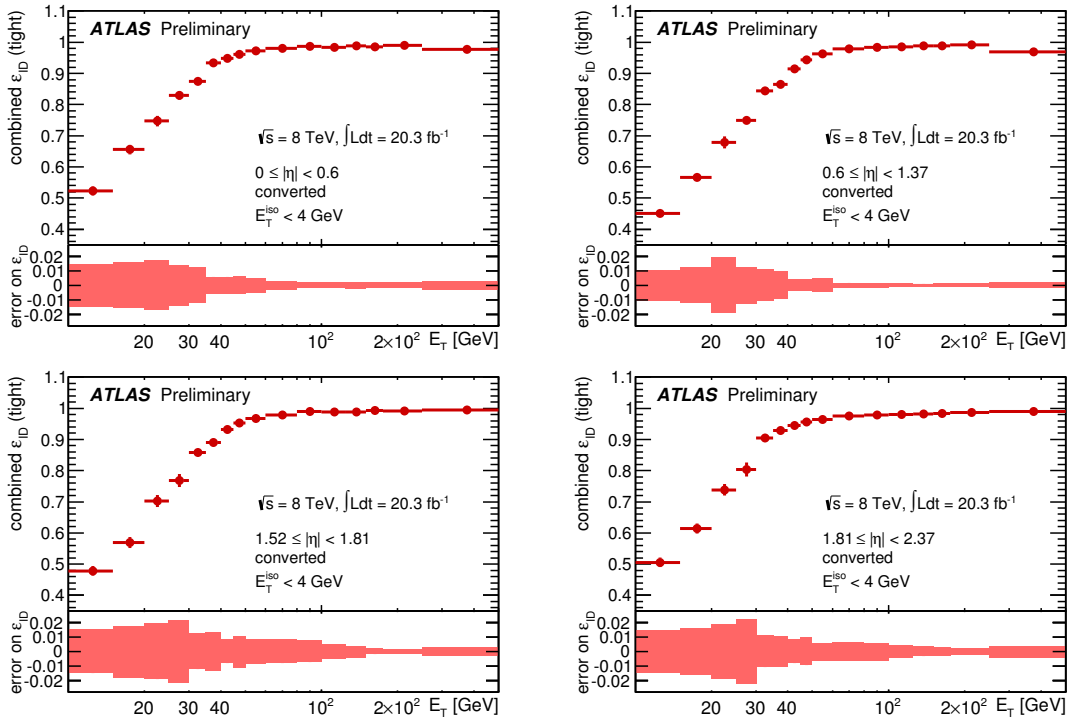

Figure 3.28 – Combined identification efficiency for converted photons in the region 10 GeV $< E_{\mathrm{T}} <$ 500 GeV, in 2012 data. The curves are shown in four different η regions.

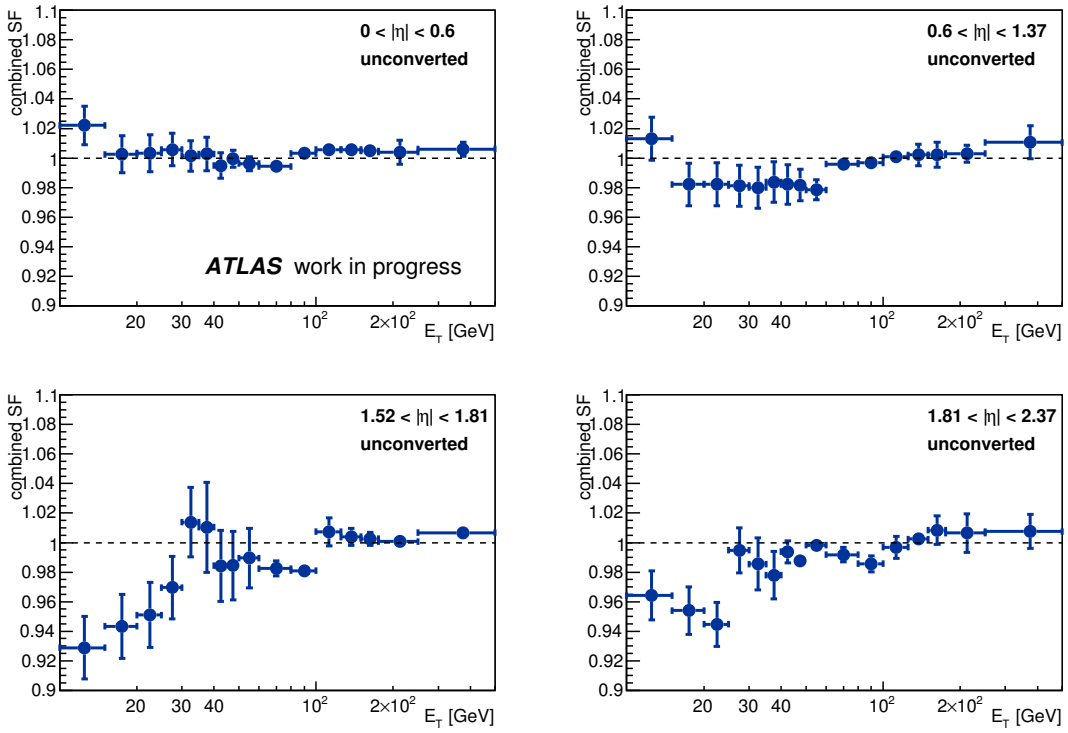

Figure 3.29 – Combined scale factors for unconverted photons in the region 10 GeV $< E_{\mathrm{T}} <$ 300 GeV, for $\sqrt{s} = 8$ TeV. The curves are shown in four different η regions.

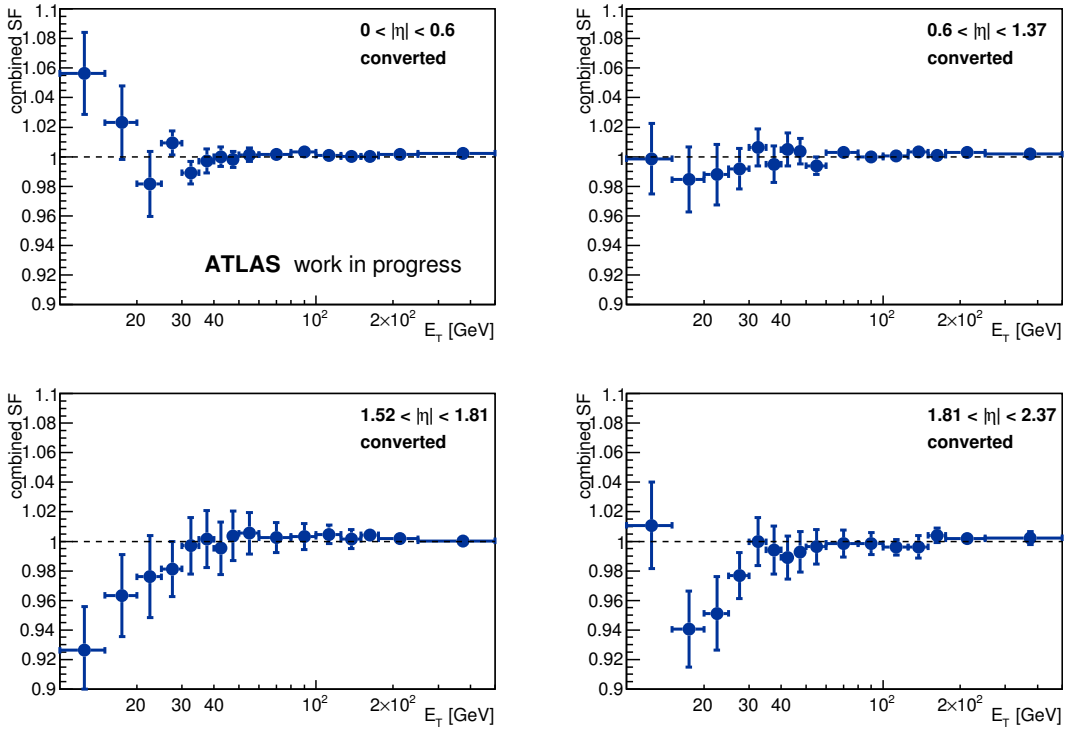

Figure 3.30 – Combined scale factors for converted photons in the region 10 GeV $< E_{\mathrm{T}} <$ 300 GeV, for $\sqrt{s} = 8$ TeV. The curves are shown in four different η regions.

data, in which the range of N_{PV} is much larger than in 2011. The scale factors versus N_{PV} are shown in Fig. 3.31 and Fig. 3.32 for the 2011 measurement of the photon ID efficiency using the electron extrapolation method. Compatible results from the matrix method are observed. In 2012, the measured efficiencies versus N_{PV} in data and MC from radiative Z decays, together with their ratios, are shown in Fig. 3.33. The SFs are expected to be independent of N_{PV} if the pile-up dependence of the photon ID efficiency is modeled well in the simulation. Their average values can be different from 1, since the integrated efficiency value may be different in data and simulation. The spread of the SFs with respect to their weighted average is computed as:

$$\sigma_{pileup} = \sqrt{\frac{\sum_{i=0}^{k_{N_{PV}}} w_i \times (x - \hat{x})^2}{\sum_{i=0}^{k_{N_{PV}}} w_i}} \tag{3.26}$$

where $k_{N_{PV}}$ is the number of bins in the N_{PV} range, x_i is the scale factor (ratio) in a given bin, and $\hat{x}$ is the mean value. The weight w_i is $\frac{1}{\sigma_i}$, where σ_i represents the total uncertainty in the given bin associated to the x_i value. The σ_{pileup} values are evaluated separately in four η bins in the 2011 measurement, as given in Table 3.5. In the 2012 measurement, the σ_{pileup} values are estimated in (E_{T}, η) bins, as given in Table 3.6. In the low E_{T} (in [10, 30]GeV) bin, the numbers are estimated using the radiative Z decays method, while in the other two higher E_{T} bins, the numbers are estimated using the electron extrapolation method. In 2011 measurement, the variation of the scale factors with respect to pile-up is taken as a systematic uncertainty. In the 2012 measurement, this variation is found to be smaller than the statistical uncertainties and is thus neglected.

$\|\eta\|$	unconverted photon(%)	converted photon (%)
0-0.6	1.2	1.2
0.6-1.37	1.6	0.8
1.52-1.81	2.2	2.7
1.81-2.37	3.5	2.6

Table 3.5 – Estimated uncertainty σ_{pileup} in the 2011 measurement, associated with the discrepancies of the pileup description in the simulation with respect to the data.

η	$10 < E_T < 30$ GeV		$30 < E_T < 45$ GeV		$E_T > 45$ GeV	
	unconv (%)	conv (%)	unconv (%)	conv (%)	unconv (%)	conv (%)
0-0.6	1.02	0.88	1.22	1.83	1.22	1.35
0.6-1.37			0.97	1.46	0.98	1.07
1.52-1.81			1.62	1.84	1.21	1.25
1.81-2.37			1.92	1.05	1.03	0.95

Table 3.6 – Estimated uncertainty σ_{pileup} in the 2012 measurement, associated with the discrepancies of the pileup description in the MC simulation with respect to the data.

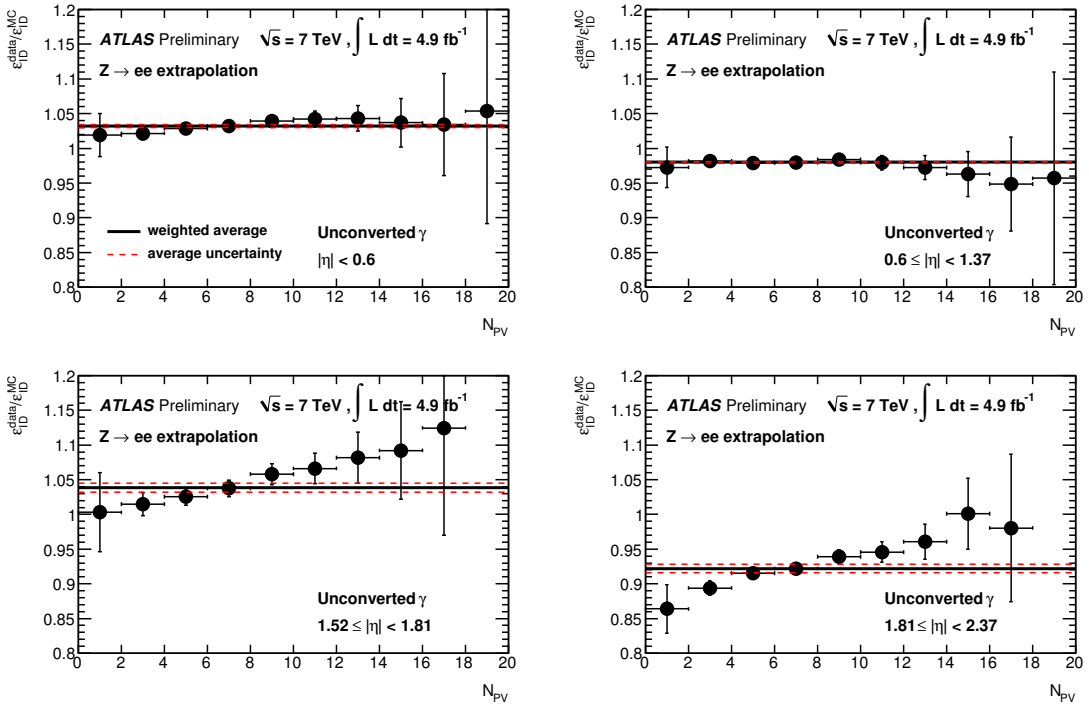

Figure 3.31 – Ratio between the measured $\varepsilon_{\mathrm{ID}}$ in data and the corresponding value predicted by the corrected MC simulation in each bin of N_{PV}, as obtained using the electron extrapolation method, for unconverted photons, in 2011 measurement. The point at $N_{PV} = 19$ is missing in some of the plots due to a lack of sufficient number of events in data.

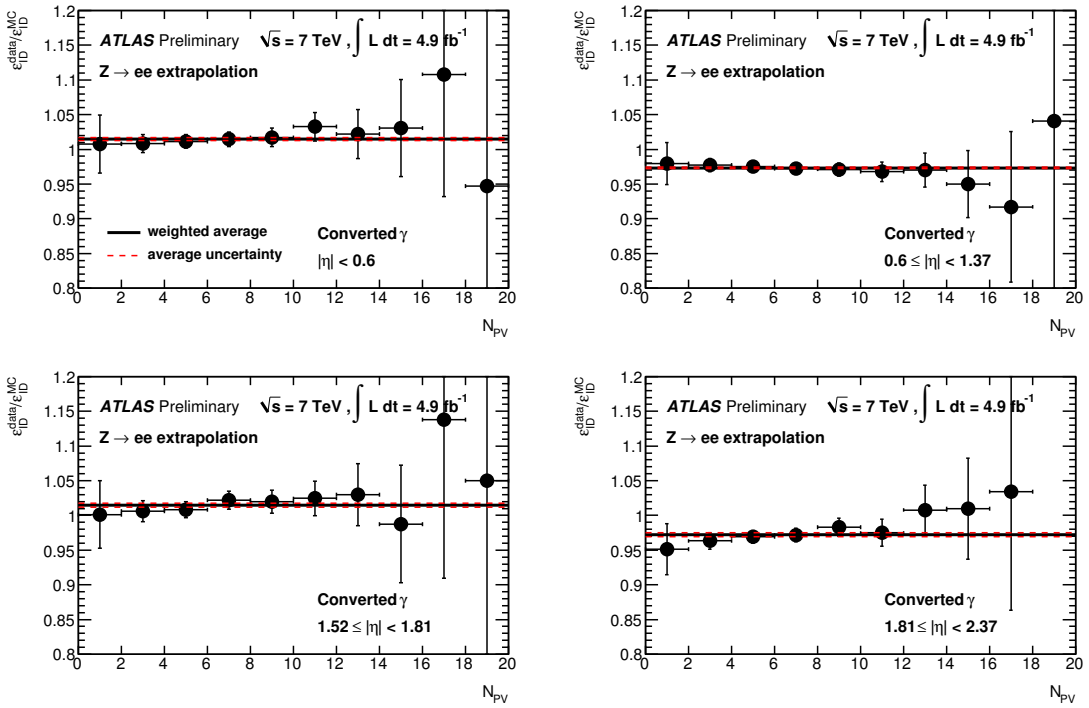

Figure 3.32 – Ratio between the measured $\varepsilon_{\mathrm{ID}}$ in data and the corresponding value predicted by the corrected MC simulation in each bin of N_{PV}, as obtained using the electron extrapolation method, for converted photons, in 2011 measurement. The point at $N_{PV} = 19$ is missing in some of the plots due to a lack of sufficient number of events in data.

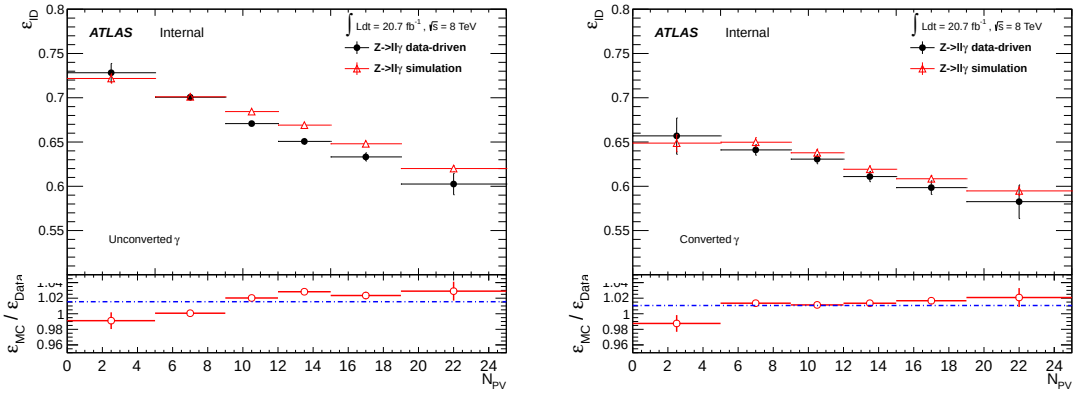

Figure 3.33 – Tight identification efficiencies versus number of primary vertices for reconstructed unconverted photons (left plot) and converted photons (right plot) after the calorimeter isolation requirement, in 2012 measurement.

3.5 Summary

For the conditions of high pile-up and increased luminosity conditions in 2012 data collision, I proposed the photon medium trigger. It reduces the trigger rate and keeps high signal efficiency. A medium di-photon trigger has been used to collect data in 2012 as nominal trigger for the SM di-photon cross section measurement and as a support trigger for the $H \to \gamma\gamma$ search; it will be the default ATLAS trigger for $H \to \gamma\gamma$ candidates in the next LHC run. I measured the photon trigger efficiencies using photons from radiative Z decays. In particular, the efficiency of di-photon triggers used for the $H \to \gamma\gamma$ search has been measured with an uncertainty around 0.4% and is much smaller than the other experimental uncertainties. A publication on the trigger efficiency measurements is in preparation [48].

For the photon identification efficiency measurements, I developed two techniques: the matrix method and the radiative Z decays. In the analysis of early ATLAS data, the photon identification efficiency was estimated from the simulation, after correcting the shower shapes with some fudge factors, and was affected by large systematic uncertainties (around 11% for $H \to \gamma\gamma$). The methods I developed on the other hands are based on data and allow a significant reduction of the uncertainties. The radiative Z decays allow to measure the photon identification efficiency down to low p_{T} (10 GeV) photons. The matrix method provides a way to measure the efficiency above 100 GeV, where both photons from radiative Z events and electrons from $Z \to ee$ become scarce. The combination of these two methods and a third one based on electrons from $Z \to ee$ has allowed a significant reduction of the systematic uncertainty due to photon identification on the $H \to \gamma\gamma$ efficiency, down to $\approx 1\%$ for the 2012 criteria. Efficiency measurements for the 2011 identification criteria are documented in Refs. [50, 52] and in a public conference note [59]. Together with the measurements of the efficiencies of the 2012 identification criteria [60, 61], they will be published during 2014 in a photon performance paper.

Chapter 4

Search for a Higgs boson in $H \to Z\gamma \to \ell\ell\gamma$

4.1 Introduction

The decay of the Higgs boson to a Z boson and a photon, $H \to Z\gamma$, is a rare process in the Standard Model, with a production cross section times branching ratio of $\sigma \times BR$ = 26.72 (34.08) fb at $\sqrt{s}$ = 7 TeV (8 TeV) for m_H = 125 GeV. It is sensitive to new physics beyond the SM, as discussed in section 1.7. In particular, it could be enhanced in models of singlet scalars, in Gauge-Higgs unification model, in Two Higgs Doublet Models (2HDM) and in models of composite Higgs. In this chapter, the search for the decay $H \to Z\gamma, Z \to \ell\ell$ where $\ell = e$ or μ, is presented, using the data collected in year 2011 and 2012. The Higgs boson is assumed to have SM-like spin and production properties, but in order to retain sensitivity to additional, non-SM Higgs bosons, its mass is allowed to take any value between 120 and 150 GeV. This work started in fall 2012; preliminary results were shown at the Moriond EW conference in February 2013 [62], and the final results have been recently published [63].

Based on the simulation of the SM Higgs boson signal events at $\sqrt{s}$ =8 TeV, a few kinematic distributions of the $\ell\ell\gamma$ final states are shown in Figure 4.1. The distributions are for $Z \to \mu\mu$ channel. The distributions for $Z \to ee$ channel are similar. The true photon transverse momentum distribution peak around 25 GeV with a sharp drop above 30 GeV and a long tail below 20 GeV, while the lepton transverse momentum spectra are harder, peaking around 50 GeV for the leading one and peaking around 40 GeV for the sub-leading one. The photon and the leptons tend to be central in pseudorapidity and uniformly distributed in azimuth. Figure 4.2 shows the transverse momenta distributions of photons and leptons in the final states in five Higgs production processes. The spectra are harder in the case of vector-boson fusion (VBF) and associated production, as expected since the Higgs boson is more boosted compared to gluon-fusion production. These distributions are rather similar at $\sqrt{s}$ = 7 TeV and 8 TeV.

The main backgrounds are expected to originate from $Z+\gamma$ events, either from diboson production in the t, u channel (also referred to as initial state radiation), from final-state-radiation (FSR) in radiative Z boson decays ($Z \to \ell\ell\gamma$) or from parton fragmentation to photon being a kind of Z+jets (with the jet energy dominated by the photon), and production of a Z boson in associated with jets, followed by a $Z \to \ell\ell$ decay, and misidentification of a jet as a photon. Smaller contributions arise from other backgrounds ($t\bar{t}$ and WZ processes). After our full selection, as will be described later, the relative contributions from the different backgrounds to the selected data are about 82%, 17% and 1% for

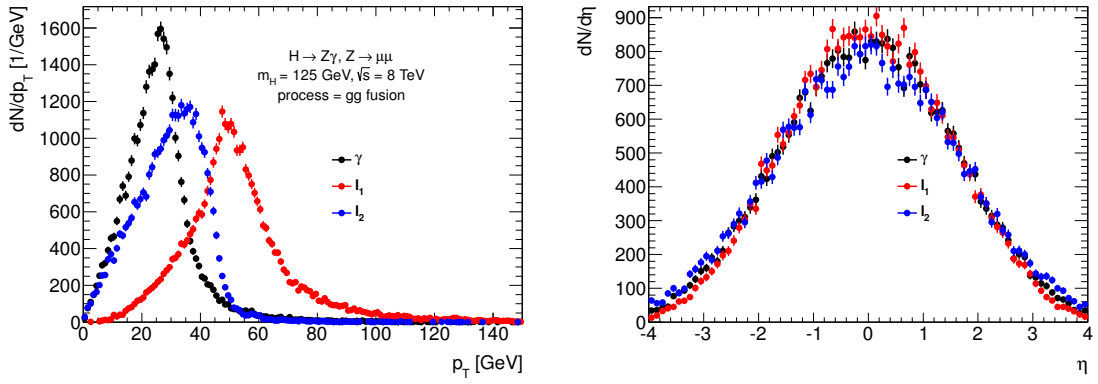

Figure 4.1 – Kinematic distributions at generator level of the three final state objects produced in $H \to Z\gamma$, $Z \to \mu\mu$ for a Higgs of 125 GeV produced in gluon-fusion at $\sqrt{s} = 8$ TeV. Left: transverse momenta. Right: pseudorapidities.

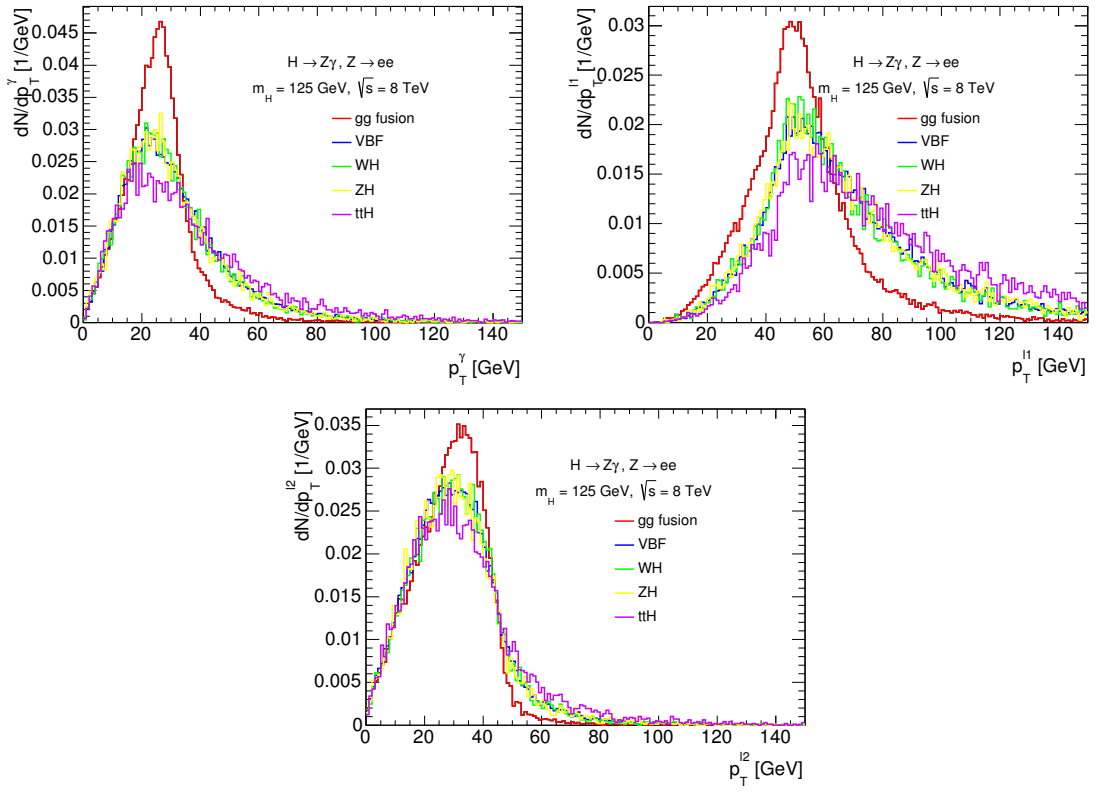

Figure 4.2 – Transverse momenta at generator level of the photon (top-left), the leading lepton (top-right) and the subleading lepton (bottom) produced in $H \to Z\gamma$, $Z \to ee$ for $m_H = 125$ GeV at $\sqrt{s} = 8$ TeV, for different Higgs boson production processes.

$Z+\gamma$, $Z+$jets and $t\bar{t}+WZ$, respectively.

This chapter is organized as follows. Data and simulation samples used by this study are given in section 4.2. The event selection is discussed in section 4.3. The calculation of the $\ell\ell\gamma$ invariant mass ($m_{\ell\ell\gamma}$), used to discriminate the signal from the background, is described in section 4.4. In order to enhance the analysis sensitivity, events after selection are classified in categories. The event classification is introduced in section 4.5. The study of the background composition is shown in section 4.6. The modeling of the signal and background $m_{\ell\ell\gamma}$ distribution are studied in section 4.7 and section 4.8. The systematic uncertainties are summarized in section 4.9. The statistical method used to extract the limits is explained in section 4.10. Finally, section 4.11 shows the limit on the production cross section times branching ratio and the compatibility between data and the background-only hypothesis, quantified by the p-value of the null hypothesis, p_0.

4.2 Data and Simulation Samples

The analysed data have been collected using the lowest-threshold unprescaled single- and di-lepton triggers in pp collisions at $\sqrt{s} = 7$ TeV and 8 TeV during the year 2011 and 2012. Events in which the ATLAS detector is not fully operational, or show data quality problems, are excluded. The fraction of events removed by these requirement are around 13% and 5% in 2011 and 2012 data. The integrated luminosity after data quality requirements corresponds to 4.5 (20.3) fb^{-1}, with a relative uncertainty of 1.8% (2.8%) at $\sqrt{s} = 7$ (8) TeV [64, 65].

Events are recorded using the lowest-threshold unprescaled lepton triggers. In the electron channel, the electron p_{T} threshold is 20 or 22 GeV for single electron triggers and 12 GeV for both objects for di-electron triggers for the 2011 collision data. While the electron p_{T} threshold is 24 or 60 GeV for single electron triggers and 12 GeV for both objects for di-electron triggers for the 2012 collision data. In the muon channel, the muon p_{T} threshold is 18 GeV for single muon triggers, and is 10/10 GeV for leading/sub-leading objects for di-muon triggers for the 2011 collision data. While the muon p_T threshold is 24 or 36 GeV for single muon triggers, and is 13/13 or 18/8 GeV for leading/sub-leading objects for di-muon triggers for the 2012 collision data. The trigger efficiency with respect to the full analysis selection is estimated to be around 99% for events in which the Z boson decays to ee pairs and 92% for events in which the Z boson decays to $\mu\mu$ pairs in both 7 TeV and 8 TeV. The ineffiency in the muon channel is due to the reduced acceptance of the muon trigger system (not covering $|\eta| < 0.1$ and $|\eta| > 2.4$).

To study the characteristics of signal and background events, MC samples are produced using various event generators. The simulated samples contain bunch-train pile-up, to give a realistic description of the experimental conditions under which data are taken. The particle interaction with the detector materials is modelled with Geant4 [66] and the detector response is simulated. The events are then reconstructed with the same software releases and the same algorithms used for collision data. More details on the event generation and simulation infrastructure are provided in [67].

Signal samples, for a Standard Model Higgs boson produced in gluon fusion and VBF events and decaying to $Z\gamma$, are generated with `POWHEG` [68, 69], interfaced to `PYTHIA` 8.170 [70] for showering and hadronization. The CT10 [71] parton distribution functions (PDFs) is used. Signal samples for a SM Higgs boson produced in association with W, Z or $t\bar{t}$ and decaying to $Z\gamma$ are generated with `PYTHIA` 8.170 using the CTEQ6L PDFs [72]. Signal events are generated for 7 different Higgs mass points, between 120 and 150 GeV, in intervals of 5 GeV.

The Higgs boson cross sections, branching ratios [73, 74, 75] and their uncertainties are compiled in [76, 77]. The Higgs boson production cross sections are computed up to next-to-next-to-leading order (NNLO) [78, 79, 80, 81, 82, 83] in α_s for the gluon-fusion process. The next-to-leading order (NLO) EW corrections are applied [84, 85]. These results are compiled in [86, 87, 88] assuming factorization between QCD and EW corrections. The cross sections for the VBF process are calculated with full NLO QCD and EW corrections [89, 90, 91], and approximate NNLO QCD corrections are applied [92]. The WH and ZH processes are calculated at NLO [93] and at NNLO [94] in QCD respectively, and NLO EW radiative corrections [95] are applied. The full NLO QCD corrections for $t\bar{t}H$ are calculated [96, 97, 98, 99]. The Higgs boson branching ratios are computed using the HDECAY and Prophecy4f programs [73, 74, 75].

SM Z+γ MC samples are generated with `SHERPA` 1.4.0 (1.4.1) [100, 101, 102] using the CT10 PDFs at $\sqrt{s} = 7$ (8) TeV. Separate samples are produced for Z bosons decaying either to $ee\gamma$ or $\mu\mu\gamma$. Up to three partons are produced in the hard scattering processes, with matrix elements implemented at LO. The generated photon transverse momentum is greater than 10 GeV and the minimum generated dilepton mass is 40 GeV. A minimum distance $\Delta R > 0.1$ between the photon and the leptons and partons is required.

Z+jets events are generated with `SHERPA` 1.4.0 and with `ALPGEN` 2.13 [103] interfaced to `HERWIG` 6.510 [104] for parton showering and fragmentation into particles and to `JIMMY` 4.31 [105] to model underlying-event contributions, using the AUET2-CTEQ6L1 tune [106]. Separate samples are produced for Z bosons decaying either to electron or muon pairs. The `ALPGEN` samples are generated using the CTEQ6L1 [72] PDFs, while the `SHERPA` samples use the CT10 ones. `PHOTOS` [107] is used to simulate final state QED radiation in the `ALPGEN` samples. In both samples the LO matrix elements for the production of up to 5 partons are used for the event generation. In all samples at 7 TeV, the generator-level dilepton invariant mass is required to be greater than 40 GeV, while at 8 TeV it is required to be greater than 60 (40) GeV in the `ALPGEN` (`SHERPA`) Z+jets samples.

Background events from the $t\bar{t}$ process are generated with `MC@NLO`, interfaced to `HERWIG` 6.510 for parton showering and fragmentation and to `JIMMY` 4.31 to model underlying-event contributions. A filter requiring two leptons with invariant mass above 60 GeV is applied between event generation and full simulation. The CT10 PDFs are used.

WZ events are generated with `SHERPA` 1.3 using the CTEQ6L1 PDFs. Both the W and the Z decay leptonically. Up to three partons are produced in the hard scattering. The generated dilepton invariant mass is required to be above 60 GeV.

All Monte Carlo samples are processed through a complete simulation of the ATLAS detector response based on Geant4. Additional pp interactions in the same and nearby bunch crossings (pile-up) are included in the simulation. The MC samples are reweighted to reproduce the distribution of the mean number of interactions per brunch crossing (9 and 21 on average in the data taken at $\sqrt{s} = 7$ and 8 TeV, respectively) and the length of the luminous region observed in data. Simulated events are also weighted by scale factors accounting for the differences of the lepton trigger efficiency, of lepton reconstruction and identification efficiency and of the photon identification efficiency between data and simulation.

For the ggH signal Monte Carlo, more precise calculations from `HRes` [108], are now available to compute the differential cross section at NNLO, including the resummation of soft gluons up to NNLL. The version `2.0` of this program [109] even includes the effects of the finite top- and bottom-quark masses. To take into account these last developments from theory, it was chosen to reweight the `POWHEG` sample to the p_T spectrum of `HRes2.0`, leading to a slightly softer p_T spectrum (black curves on Fig. 4.3). A difference is observed

between the 7 and the 8 TeV weights, due to the fact that for the 8 TeV sample, a tuning of the POWHEG generator (see Section 4.2 of [110]) was done in order to make the POWHEG spectrum closer to HRes.

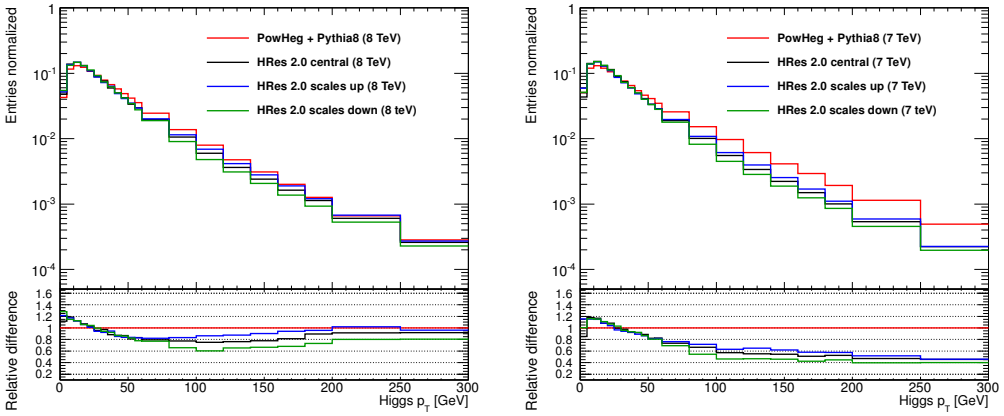

Figure 4.3 – p_T weight and the uncertainty bands (see text)

4.3 Event Selection

Events that pass the selection described below have always at least one reconstructed primary vertex. The vertex with the largest sum of the squared transverse momenta of the tracks associated with it is considered as the primary vertex of the hard interaction. It has been verified in signal events that – due to the presence of the two leptons from the Z decay – this choice yields the primary vertex closest to the vertex of the hard process in more than 99.9% of the cases.

4.3.1 Lepton and Photon Selection

The lepton selection, with the exception of the p_{T} threshold, follows closely the one used for the selection of electrons and muons in the $H \to 4\ell$ search, while the photon selection is similar to the one adopted for $H \to \gamma\gamma$. The use of common selections for the final-state particles of different Higgs searches makes it easier to correctly account for correlated systematic uncertainties when combining all the results together.

Muon selection

Combined (CB) muons, Stand-alone (SA) muons or Segment-tagged (ST) muons (collectively termed "STACO" muons) and CT muons are used. The ID and TRT hit requirements for both CB and ST muons are summarised in Table 4.1, while those for CT muons are summarised in Table 4.2.

STACO muons are required to have transverse momentum $p_{\mathrm{T}} > 10$ GeV, while calorimeter tagged muons, which have worse purity, must have $p_{\mathrm{T}} > 15$ GeV. CB and ST muons are required to have $|\eta| < 2.7$, SA muons are required to have $2.5 < |\eta| < 2.7$, and CT muons must have $|\eta| < 0.1$. ST candidates are required to have at least 3 TGC ϕ hits or at least 2 tagging segments. The ID track associated to CB, ST and CT muons is required to have transverse (longitudinal) impact parameter $|d_0|$ ($|z_0|$), with respect to the primary vertex, smaller than 1 mm (10 mm).

Table 4.1 – List of Inner Detector hit requirements for the muon tracks reconstructed in the ID using the STACO algorithm.

	2012
ID Si hit requirement	No. of pixel hits + No. of crossed dead pixel sensors > 0
	No. of SCT hits + No. of crossed dead SCT sensors > 4
	No. of pixel holes + No. of SCT holes < 3
TRT hit requirement	if $(0.1 < \lvert\eta\rvert \leq 1.9)$ require (Hits + Outliers > 5)
	AND $\left(\frac{\text{Outliers}}{\text{Hits+Outliers}} < 0.9\right)$
	2011
ID Si hit requirement	expectBLayerHit=false or numberOfBLayerHits ≥ 1
	No. of pixel hits + No. of crossed dead pixel sensors > 1
	No. of SCT hits + No. of crossed dead SCT sensors > 5
	No. of pixel holes + No. of SCT holes < 3
TRT hit requirement	if $(\lvert\eta\rvert < 1.9)$: require (Hits + Outliers > 5)
	AND $\left(\frac{\text{Outliers}}{\text{Hits+Outliers}} < 0.9\right)$
TRT hit requirement	if $((\lvert\eta\rvert \geq 1.9)$ AND (Hits + Outliers $> 5))$
	require $\left(\frac{\text{Outliers}}{\text{Hits+Outliers}} < 0.9\right)$

Table 4.2 – List of Inner Detector hit requirements for the CT muon tracks reconstructed in the ID.

	2012
ID Si hit requirement	No. of pixel hits + No. of crossed dead pixel sensors > 0
	No. of SCT hits + No. of crossed dead SCT sensors > 4
	No. of pixel holes + No. of SCT holes < 3
	2011
ID Si hit requirement	expectBLayerHit=false or numberOfBLayerHits ≥ 1
	No. of pixel hits + No. of crossed dead pixel sensors > 1
	No. of SCT hits + No. of crossed dead SCT sensors > 5
	No. of pixel holes + No. of SCT holes < 3
TRT hit requirement	(Hits + Outliers < 6) OR $\left(\frac{\text{Outliers}}{\text{Hits+Outliers}} < 0.9\right)$

In order to remove overlaps between muon candidates reconstructed by different algorithms from the same particle, SA muon candidates within $\Delta R < 0.2$ of a selected ST muon candidate, as well as CT muon candidates within $\Delta R < 0.1$ of a selected STACO muon candidate are rejected.

Electron selection

Electrons reconstructed near regions of the calorimeter affected by read-out or high-voltage failures are not considered. Electron candidates are required to have a transverse energy $E_{\mathrm{T}} > 10$ GeV and pseudorapidity $|\eta| < 2.47$ in order to exploit the central section of the electromagnetic calorimeter for electron/jet discrimination. They must have well reconstructed ID track pointing to an electromagnetic calorimeter cluster, and the cluster should satisfy a set of identification criteria that require the longitudinal and transverse shower profiles to be consistent with those expected for electrons and photons showers [40].

The four-momentum of the electron is formed using the energy measured by the calorimeter and the track azimuth and pseudorapidity measured in the inner detector.

The electron track is required to have a hit in the b-layer when the track is expected to traverse an active b-layer module. This selection reduces fake electron candidates from photon conversions. The track is also required to have a longitudinal impact parameter, with respect to the primary vertex, smaller than 10 mm.

If two electron candidates have identical track parameters, only the candidate with highest E_{T} is retained. In the analysis of 2012 data, because of the larger pileup, the two electron clusters are required not to be too close to each other. If the two electron clusters are closer than $|\Delta\eta| < 0.075$ and $|\Delta\phi| < 0.125$, the electron cluster with highest E_{T} is kept. In addition, if the track associated to an electron candidate is within a distance $\Delta R < 0.02$ from the track associated to a muon candidate passing all the muon selection criteria, the electron candidate is rejected.

Photon selection

In order to exploit the fine segmentation of the first layer of the electromagnetic calorimeter to discriminate between genuine prompt photons and fake photons within jets, the photon candidate pseudorapidity must satisfy $|\eta| < 1.37$ or $1.52 < |\eta| < 2.37$. Photons reconstructed near regions of the calorimeter affected by read-out or high-voltage failures are not considered. Photons are required to have a transverse energy $E_{\mathrm{T}} > 15$ GeV. The identification of photons is performed through a cut-based selection based on shower shapes measured in the electromagnetic calorimeter. Photons are required to pass tight identification criteria based on the values of their shower shape discriminating variables. To further suppress hadronic background, an isolation requirement is applied: $E_{\mathrm{T}}^{Topo-iso} < 4$ GeV.

Photon candidates that are within $\Delta R < 0.3$ of a selected electron or muon candidate are rejected, thus suppressing background from final-state-radiation (FSR) $Z+\gamma$ events and signal from radiation of photons in $H \to \ell\ell$.

4.3.2 $Z \to \ell\ell$ Reconstruction and Selection

Z boson candidates are reconstructed from pairs of same flavor, opposite sign leptons passing the previous selection. The invariant mass of the Z boson candidate is computed from the sum of the 4-momenta of the two leptons. In case of multiple Z candidates being found, the one with invariant mass closest to the Z pole is chosen. It is required that one (both) of the leptons used in the reconstruction of the selected Z boson candidate match the trigger object(s) of the single (double) lepton trigger used in this analysis.

In $Z \to \mu\mu$ events with a Final State Radiation (FSR) photon collinear to either muon and reconstructed in the electromagnitic calorimeter, the reconstructed Z boson 4-momentum is corrected by adding the collinear photon 4-momentum. Details of the study on collinear FSR photon reconstruction in Z boson decays to muons can be found in [111]. In this analysis, candidate FSR photon clusters should satisfy the following requirements:

- the distance between the cluster and the muon is $\Delta R_{\mathrm{cluster},\mu} = \sqrt{\Delta\eta^2 + \Delta\phi^2} < 0.15$,
- the transverse energy of the cluster is $E_{\mathrm{T}} > 1.5$ GeV,
- the fraction of energy in the strips is $f_1 > 0.1$.

If more than one cluster is found in the cone of $\Delta R = 0.15$, then the one with highest E_{T} is selected. The full inclusive $Z \to \mu\mu$ invariant mass resolution, $(Z_{\mathrm{rec}} - Z_{\mathrm{true}})/Z_{\mathrm{rec}}$, before and after the FSR photons correction in simulated events, is shown in Figure 4.4. The additional FSR correction significantly improves the mass resolution.

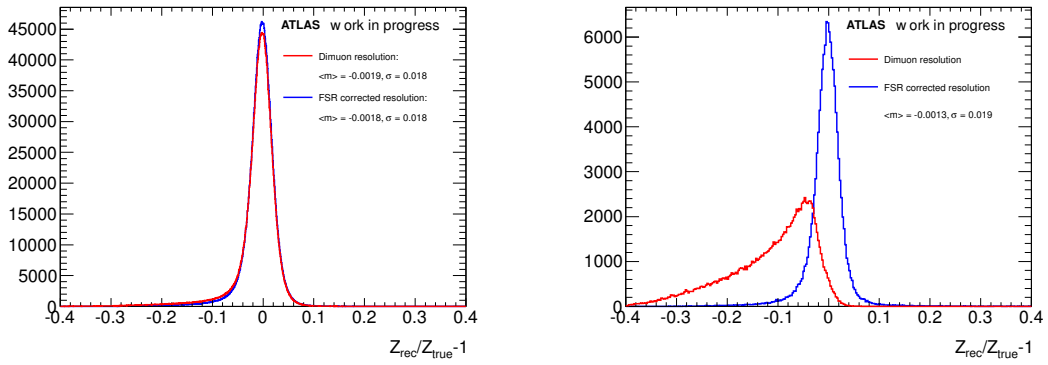

Figure 4.4 – Invariant mass resolution of $Z \to \mu^+\mu^-$ simulated events, $(Z_{\mathrm{rec}}/Z_{\mathrm{true}}) - 1$, before (red) and after (blue) FSR correction. The mean value $\langle m \rangle$ and the σ of each distribution are obtained from a gaussian fit. Inclusive events in $Z \to \mu\mu$ are used in the left plot, while only FSR corrected events are used in the right plot.

4.3.3 $H \to Z\gamma$ Reconstruction and Selection

Higgs boson candidates are reconstructed from the combination of the Z candidate with invariant mass closest to the Z pole and a photon with largest transverse energy. After selecting the Higgs boson candidate, track isolation and calorimeter isolation requirements are applied to the leptons used in the Higgs candidate reconstruction.

The normalised track isolation is defined as the sum $\sum p_{\mathrm{T}}$ of the transverse momenta of the tracks, inside a $\Delta R = 0.2$ cone around the lepton, excluding the lepton track, divided by the lepton p_{T}. The tracks considered in the sum are of good quality: they have at least four hits in the pixel and silicon strip detectors (silicon hits) and $p_{\mathrm{T}} > 1$ GeV for muons, and at least nine silicon hits, one hit in the b-layer and $p_{\mathrm{T}} > 0.4$ GeV for electrons. Each lepton is required to have a normalised track isolation smaller than 0.15. The normalised calorimetric isolation for electrons, computed as the sum of the positive energy topological clusters with a reconstructed barycenter falling in a cone of $\Delta R < 0.2$ around the candidate electron cluster divided by the electron E_{T}, must be lower than 0.30 (0.20) in 2011 (2012) data. The cells within 0.125×0.175 in $\eta \times \phi$ around the electron barycenter are excluded. In the case of muons, the normalised calorimetric isolation discriminant is defined as the sum of the calorimeter cells, $\sum E_{\mathrm{T}}$, inside a $\Delta R = 0.2$ around the muon direction, divided by the muon p_{T}. Muons are required to have a normalised calorimetric isolation less than 0.30 (0.15 in case of muons without an ID track). For both the track- and calorimeter-based isolation, any contributions arising from the other lepton from the candidate Z decay are subtracted.

Additional track impact significance selections are also applied to the leptons from the Z candidate decay. The transverse impact parameter significance $|d_0|/\sigma_{d_0}$ of the ID track associated with a lepton within the acceptance of the inner detector is required to be less than 3.5 and 6.5 for muons (except for the SA ones) and electrons, respectively. The electron impact parameter is affected by bremsstrahlung and it thus has a broader distribution.

Finally, to suppress events from FSR $Z + \gamma$, the dilepton invariant mass is required to be larger than 81.18 GeV. This also removes non-resonant $H \to \gamma\gamma^* \to \gamma\ell\ell$ events.

4.4 Discriminating Variable

The $\ell\ell\gamma$ invariant mass ($m_{\ell\ell\gamma}$) is used to discriminate signal from background. To improve the three-body invariant mass resolution for signal events and thus improve discrimination against non-resonant background events, we apply three corrections to the three-body mass $m_{\ell\ell\gamma}$ of selected $H \to Z\gamma$ decay candidates.

- The photon pseudorapidity η^γ and its transverse energy $E_{\mathrm{T}}^\gamma = E^\gamma / \cosh \eta^\gamma$ are recalculated from the identified primary vertex (instead of the nominal interaction point used in the standard ATLAS photon reconstruction) and the photon impact point in the calorimeter.
- The muons are corrected for collinear FSR photons as described in Section 4.3.2.
- The lepton four-momenta are recomputed by means of a kinematic fit which minimizes the χ^2 between the measured momenta and the best-fit values under the constraint that the dilepton invariant mass be equal to its most probable value, determined in the hypothesis of a true $Z \to \ell\ell$ decay with a power $m_{\ell\ell}$ probability density function described by a Breit-Wigner function and assuming an unbiased Gaussian resolution function for the detector reconstruction of the mass.

A comparison between the $m_{\ell\ell\gamma}$ distributions without and with the corrections for simulated signal events (from $gg \to H$ at $m_H = 125$ GeV) is shown in Figure 4.5. The Z mass constraint in particular helps to recover part of the momentum lost by the lepton because of bremsstrahlung and brings the signal peak closer to the true Higgs generated mass, reducing at the same time the tail at low values of the reconstructed mass.

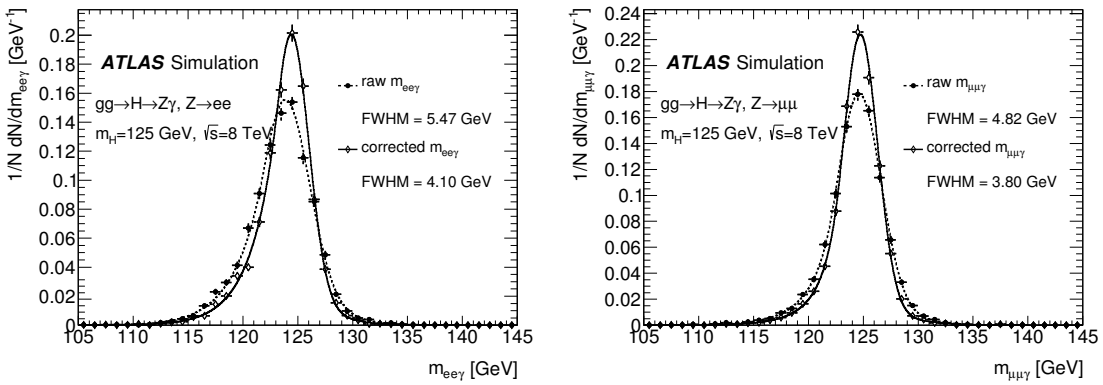

Figure 4.5 – Three-body invariant mass distribution (normalised to unity) for $gg \to H \to Z\gamma$ selected events in the 8 TeV, $m_H = 125$ GeV signal simulation, after standard reconstruction (full circles) and after choosing the event primary vertex as the photon origin, applying the FSR correction and also applying the Z-mass-constraint to the dilepton mass (open diamonds). The dashed and solid lines show the results of the fits to the invariant mass distributions with the sum of a Crystal Ball line shape and a Gaussian function. Left: $Z \to ee$ channel, right: $Z \to \mu\mu$ channel.

4.5 Event Classification

To enhance the analysis sensitivity, the selected events are divided into categories with different signal-to-background ratios and different invariant mass resolutions, based on:

- The absolute value of pseudorapidity difference between the photon and the Z boson, $|\Delta\eta_{Z\gamma}|$.
- The component of the Higgs candidate p_{T} that is orthogonal to the axis defined by the direction of $p_T^{\gamma} - p_T^{Z}$, p_{Tt} (see Figure 4.6).

Since the photon and Z from the Higgs boson decays are boosted, a small $|\Delta\eta|$ between the photon and Z is expected when compared to its main background of $Z+\gamma$ ISR events. The Higgs p_{Tt} is largly correlated with the Higgs p_{T} but has better resolution [112] and has been used in the $H \to \gamma\gamma$ analysis. Its value on average is expected to be larger for signal events than for background events.

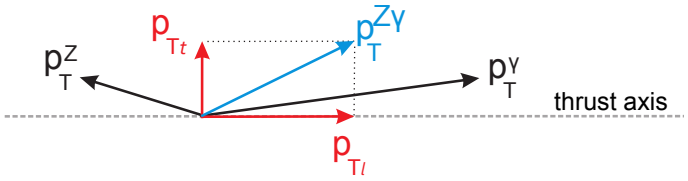

Figure 4.6 – Vector diagram of the Higgs p_{Tt} variable, defined as the component of the Higgs candidate p_{T} that is orthogonal to the axis defined by the difference between the photon and the Z boson momenta

The distributions of p_{Tt} and $|\Delta\eta_{Z\gamma}|$ in data and signal simulations are shown in Figs. 4.7 and 4.8. Since the data sample is dominated by background events, its p_{Tt} and $|\Delta\eta_{Z\gamma}|$ distributions are as similar to the one from the main background of $Z+\gamma$ events. In general, events from the signal processes have on average larger p_{Tt} values than background events. Events from the gg fusion process have on average smaller p_{Tt} values comparing to events from the other signal processes. Since events from the Higgs boson decays are boosted, the average values of $|\Delta\eta_{Z\gamma}|$ for events from the signal processes are smaller than the one from background events. The VBF, VH and ttH signal events are more boosted comparing to events from the gg fusion production.

Figure 4.9 shows the expected significance versus the thresholds on p_{Tt} and $|\Delta\eta_{Z\gamma}|$ used to classify events, using the 2012 muon data. Three categories are considered: *high-* (*low-*)p_{Tt} candidates if p_{Tt} is greater (lower) than a certain threshold; low-p_{Tt} candidates are further split in two classes, *high-* and *low-*$|\Delta\eta_{Z\gamma}|$, in 2012 data. The significance is computed as the sum in quadrature of $S/\sqrt{B}$ in each category, where S is the expected signal (from the theoretical cross sections and the signal MC efficiency) and B is the expected background (extrapolated from the $m_{\ell\ell\gamma}$ sidebands in data). The maximum significance is found for a p_{Tt} thresholds around 55 GeV and $|\Delta\eta_{Z\gamma}|$ threshold at 2.0. However, in order not to introduce a background peak in the $m_{\ell\ell\gamma}$ fit region near the signal for events in the high p_{Tt} category, a lower threshold (30 GeV) is chosen instead, with only a slight decrease of the expected significance. Higgs boson candidates are thus classified as *high-* (*low-*)p_{Tt} candidates if p_{Tt} is greater (lower) than 30 GeV. In the analysis of $\sqrt{s} = 8$ TeV data, low-p_{Tt} candidates are further split in two classes, *high-* and *low-*$|\Delta\eta_{Z\gamma}|$, whether $|\Delta\eta_{Z\gamma}|$ is greater or lower than 2.0. For 2011 data, since the statistics is limited, no $|\Delta\eta_{Z\gamma}|$ categories are used.

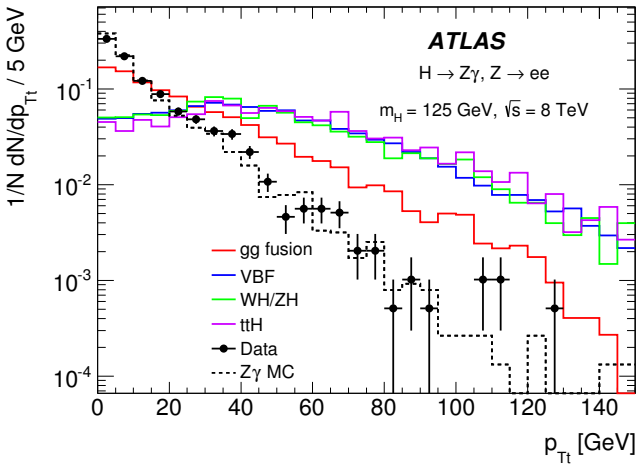

Figure 4.7 – p_{Tt} distributions of simulated Higgs signal events (at 125 GeV) in the different production processes, compared to the distribution of background events selected either in a simulated sample of $Z\gamma$ events or in data. The full selection (including the $m_{\ell\ell} > 81.12$ GeV requirement and the $115 < m_{\ell\ell\gamma} < 170$ GeV requirement described later) is applied.

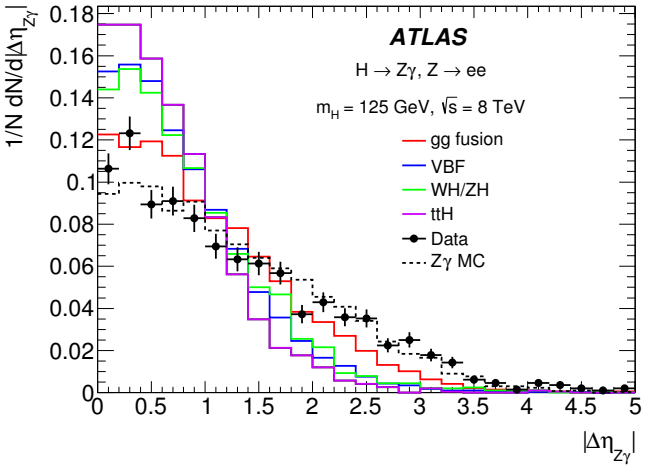

Figure 4.8 – $|\Delta\eta_{Z\gamma}|$ distributions of simulated Higgs signal events (at 125 GeV) in the different production processes, compared to the distribution of background events selected either in a simulated sample of $Z\gamma$ events or in data. The full selection (including the $m_{\ell\ell} > 81.12$ GeV requirement and the $115 < m_{\ell\ell\gamma} < 170$ GeV requirement described later) is applied.

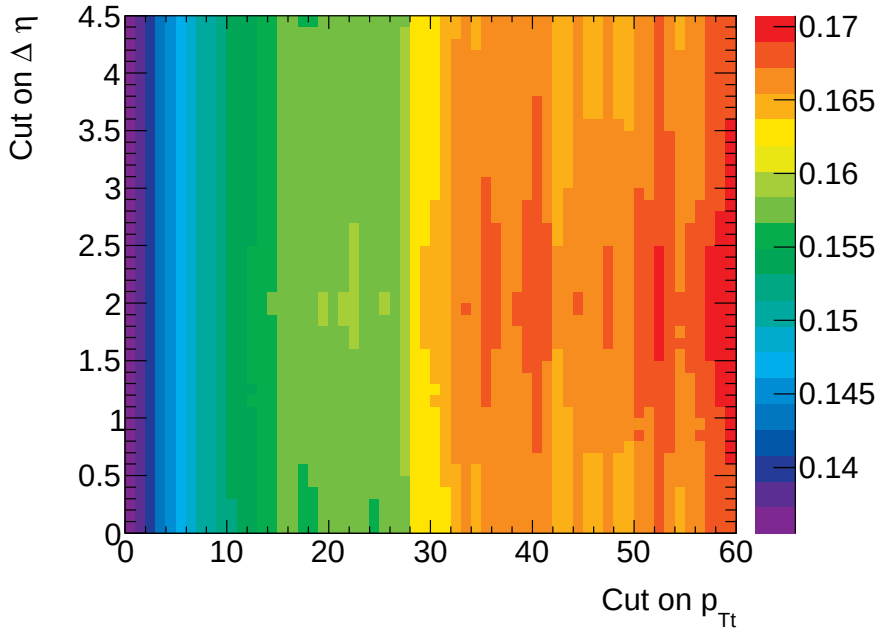

Figure 4.9 – Significance of the $H \to Z\gamma$ signal as a function of the thresholds used to classify the events into p_{Tt} and $|\Delta\eta_{Z\gamma}|$ categories, based on 8 TeV $\mu\mu\gamma$ data and signal MC.

4.6 Data-driven Background Estimation

Even though it is not used for final limit extraction, a background decomposition of the selected data is performed, in order to understand where the selected final states come from and to estimate the accuracy of the simulation of background events, which are used for the optimization of the selection criteria and to perform the studies of the bias introduced by the particular background model chosen in the final fit used to measure the $H \to Z\gamma$ yield. The main backgrounds are expected to originate from Z+γ and Z+jets events, with minor contributions from $t\bar{t}$ and WZ events. In Z+γ, the invariant mass requirement $m_{\ell\ell} \approx m_Z$ suppresses the contribution from FSR, and the photon isolation requirement reduces the importance of the fragmentation component.

A "side band" method is used, based on photon identification and isolation variables to discriminate on a statistical basis $Z + \gamma$ and Z+jet events in data. To this purpose, photon candidates are classified as:

- Isolated, if $E_{\mathrm{T}}^{Topo-iso} < 4$ GeV;
- Non-isolated, if $E_{\mathrm{T}}^{Topo-iso} > 5$ GeV;
- Tight, if it passes the tight photon identification criteria;
- Non-tight, if it fails at least one of the tight requirements on four shower shape variables (w_{s3}, F_{side}, ΔE, E_{ratio}) computed from the energy deposits in a few cells of the first layer of the electromagnetic calorimeter, but passes all the other tight identification criteria.

In the two-dimensional plane [113] formed by the photon transverse isolation energy and the photon tight identification variable, we define four regions:

- A : the *signal* region, containing tight, isolated photon candidates (mostly Z+γ events).
- B : the *non-isolated* Z+jet background control region, containing tight, non-isolated photon candidates.
- C : the *non-identified* Z+jet background control region, containing isolated, non-tight photon candidates.
- D : the Z+jet background control region containing non-isolated, non-tight photon candidates.

The Z+γ yield $N_A^{Z\gamma}$ in the signal region is estimated from the number of events in data in the four regions (after subtracting the $t\bar{t}$ and WZ yields estimated from the simulation using the NLO cross-section from MC@NLO), N_K^{ZX} ($K \in \{A, B, C, D\}$), through the relation

$$N_A^{Z\gamma} = N_A^{ZX} - (N_B^{ZX} - c_B N_A^{Z\gamma}) \frac{(N_C^{ZX} - c_C N_A^{Z\gamma})}{(N_D^{ZX} - c_D N_A^{Z\gamma})} R^{Zj} \ , \tag{4.1}$$

where $c_K \equiv N_K^{Z\gamma}/N_A^{Z\gamma}$ are *signal leakage fractions* that can be extracted from simulated Z+γ samples ($c_B \simeq 0.1, c_C \simeq 0.09, c_D \simeq 0.01$), and

$$R^{Zj} \equiv \frac{N_A^{Zj} N_D^{Zj}}{N_B^{Zj} N_C^{Zj}} \tag{4.2}$$

quantifies the correlation between the isolation and identification variables for the jets faking photons in Z+jets events ($R^{Zj} = 1$ in case of vanishing correlations). R^{Zj} ($\simeq 1$–1.2) is obtained from high statistics Z+jet simulated events, after removing – using the truth information – the contributions from Z+γ processes. Equation 4.1 leads to a second-order polynomial equation in $N_A^{Z\gamma}$ that has only one physical ($N_A^{Z\gamma} > 0$) solution.

The following sources of systematic uncertainties are considered:

- Definition of the non–isolated control regions. In the nominal result, we use the region $E_{\mathrm{T}}^{Topo-iso} > 5$ GeV as control region for non-isolated photons. A systematic uncertainty is estimated by recomputing the various background yields by changing the definition of the non-isolated regions by ± 1 GeV.
- Definition of the non–tight control region. In the nominal result, non–tight photon candidates are required to pass the tight identification criteria on five variables (R_{had}, $w_{\eta 2}$, R_η, R_ϕ, $w_{s,\mathrm{tot}}$) and to fail at least one of the criteria on the other four variables used for photon identification. A systematic uncertainty is estimated by recomputing the various background yields using two alternative definitions of the non-tight control region, either requiring the photon candidates to fail at least one of the criteria on the two variables w_{s3}, F_{side}, and to pass the tight criteria on the other seven ones, or by requiring the photon candidates to fail at least one of the criteria on the five variables w_{s3}, F_{side}, ΔE, E_{ratio}, $w_{s,\mathrm{tot}}$ and to pass the tight criteria on the remaining four.
- Background correlations in control regions. In the nominal results the value for R^{Zj} from the Alpgen Z+jets samples is used. As alternatives, the signal purity is computed neglecting these correlations (setting $R^{Zj} = 1$) or using the (larger) value of the correlation obtained from the Sherpa Z+jet sample.
- Photon leakage in the jet control regions. We recompute the signal leakage in the background control regions varying the photon isolation by ± 100 MeV (typical difference observed between data and simulation for electrons and photons)

and by removing the shower shape corrections that account for data-MC photon identification efficiency differences.

- $t\bar{t}$ and WZ backgrounds. We vary the nominal cross sections by $\pm 50\%$, to take into account both the uncertainties on their production cross sections and the jet and lepton to photon fake rates.

At $\sqrt{s} = 7$ (8) TeV, the average $Z+\gamma$ purity in the two channels is around 84% (81%), the fraction of Z+jets events is around 15% (18%) and the other backgrounds are less than 1% of the total sample. Including the systematic uncertainties listed before, the $Z+\gamma$ purity is estimated to be $81 \pm 3(stat) \pm 2(syst)\%$ ($80 \pm 2 \pm 3\%$) in the $ee\gamma$ channel and $87 \pm 2(stat)^{+1}_{-4}(syst)\%$ ($81 \pm 2 \pm 3\%$) in the $\mu\mu\gamma$ channel.

A comparison between the invariant mass distributions in data and MC after scaling each MC background contribution to the number of events estimated in data is shown in Figure 4.10. A good agreement between data and simulation is observed. A similar agreement is observed in the distribution of other quantities used in the selection of the final sample.

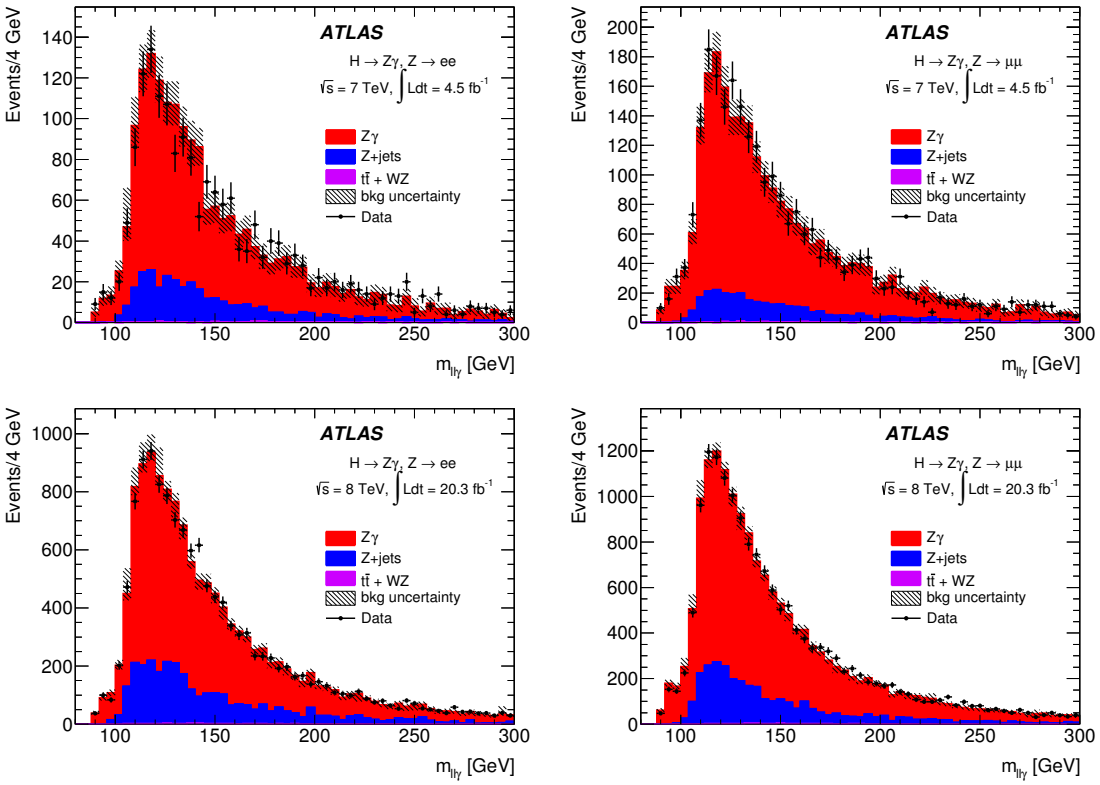

Figure 4.10 – Three-body invariant mass ($m_{\ell\ell\gamma}$) distribution of selected events in data (dots) and from the various background sources (histograms) for $Z \to ee$ (left) and $Z \to \mu\mu$ (right) channels, at $\sqrt{s} = 7$ TeV (top) and 8 TeV (bottom).

4.7 Signal Parameterization

The signal efficiency and its $m_{\ell\ell\gamma}$ distribution are studied using simulated SM Higgs signal events. We test Higgs boson mass hypotheses between 120 and 150 GeV, for which

the SM branching ratio is larger than 0.001, in steps of 0.5 GeV. In each of the production decay modes i and in the jth category, for a Z boson decaying to a lepton pair $\ell\ell$, the expected signal yield is:

$$N^{\mathrm{SM}}_{i,j,\ell}(m_H) = \int \mathcal{L}dt \times \sigma_i(m_H) \times \mathcal{B}_{H\to Z\gamma}(m_H) \times \mathcal{B}_{Z\to\ell\ell} \times \varepsilon_{i,j,\ell}(m_H) \tag{4.3}$$

where

1. $\int \mathcal{L}dt$ is the integrated luminosity of the data sample, (20.3 ± 0.5) fb^{-1} at 8 TeV and (4.5 ± 0.3) fb^{-1} at 7 TeV and
2. $\sigma_i(m_H)$ is the SM Higgs boson production cross section for a Higgs boson of mass m_H, in the production process i (gg, VBF, ..),
3. $\mathcal{B}_{H\to Z\gamma}(m_H)$ is the branching fraction for the decay to $Z\gamma$ of a SM Higgs boson of mass m_H,
4. $\mathcal{B}_{Z\to\ell\ell} = (3.3658 \pm 0.0023)\%$ is the $Z \to \ell\ell$ branching fraction,
5. $\varepsilon_{i,j,\ell}(m_H)$ is the selection efficiency of the ith production mode in the jth event category for $H \to Z\gamma$, $Z \to \ell\ell$ events.

The second and third inputs are given in Refs. [76, 77], the fourth input is taken from the PDG world average [54], while the fifth input is estimated from the ATLAS full simulation of signal events. The expected total yield in each event category, for each lepton flavor, is:

$$N^{\mathrm{SM}}_{j,\ell}(m_H) = \sum_i N^{\mathrm{SM}}_{i,j,\ell}(m_H) \tag{4.4}$$

The signal efficiency at each mass point for which a signal MC sample is available is computed as

$$\varepsilon_{i,j,\ell} = \frac{\sum_m w^{\mathrm{reco}}_{m,i,j,\ell}}{\sum_k w^{\mathrm{true}}_{k,\ell}} \tag{4.5}$$

for production mode i and event category j, where:

- $\sum_k w^{\mathrm{true}}_{k,\ell}$ is the sum, over the events k in which the generated Z boson decays to a $\ell\ell$ pair (identified by inspecting the MC truth record, around 1/3 of the total sample), of the product of the "initial" weights, *i.e.* those for pile-up and z-vertex reweighting ($w^{\mathrm{true}}_k = w^{\mathrm{pile-up}}_k \times w^{\mathrm{z-vtx}}_k$)
- $\sum_m w^{\mathrm{reco}}_{m,i,j,\ell}$ is the sum, over the events m in which the generated Z boson decays to a $\ell\ell$ pair and passes the full $H \to Z(\ell\ell)\gamma$ selection, of the product of the "final" weights, *i.e.* the initial weights and the efficiency scale factors for the trigger, the leptons and the photon ($w^{\mathrm{reco}}_m = w^{\mathrm{true}}_m \times w^{\ell_1}_m \times w^{\ell_2}_m \times w^{\gamma}_m \times w^{\mathrm{trigger}}_m$)

For the signal efficiency, it is observed on fully simulated signal samples that a 2nd order polynomial ($\varepsilon(m_H) = p_0 + p_1 \times m_H + p_2 \times m_H^2$) is able to model its dependence on the Higgs boson mass, as shown in Fig. 4.11 for $H \to Z\gamma, Z \to \mu\mu$ events $\sqrt{s} = 8$ TeV. With the fitted mass dependencies of the signal efficiency, and the production cross section and branching fractions tabulated in Refs. [76, 77], we can estimate the number of signal events expected after the full selection for the various Higgs boson mass hypotheses. The expected yields for an integrated luminosity of 20.3 fb^{-1} at 8 TeV in $H \to Z\gamma, Z \to \mu\mu$ channel are listed in Tables 4.3. An estimation of composition of signal production processes in the categories based on simulations are shown in Fig. 4.12, for a Higgs mass of 125 GeV.

It is observed on MC that the $m_{\ell\ell\gamma}$ distribution for signal events is well described empirically by the sum of a Crystal Ball line shape (CB) (a Gaussian with a power-law

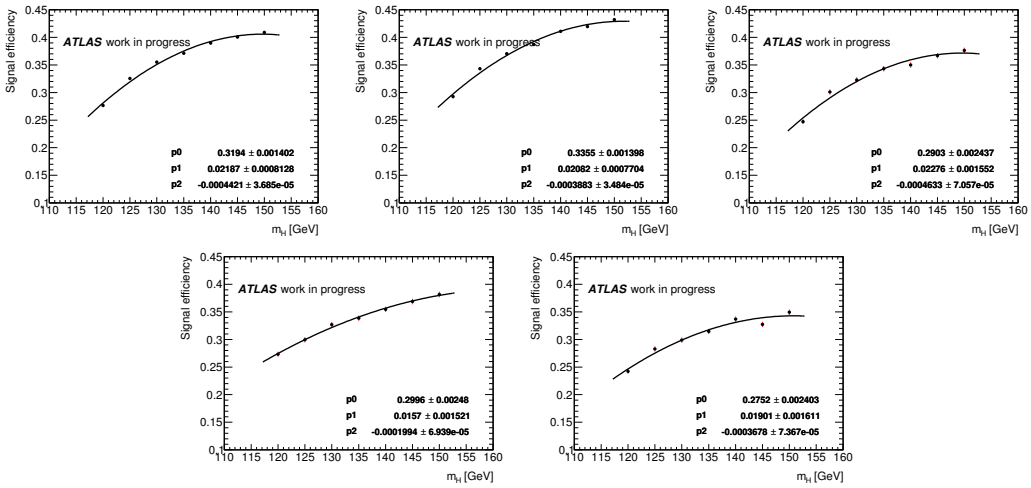

Figure 4.11 – Signal selection efficiency versus nominal Higgs mass for events produced in pp collisions at $\sqrt{s} = 8$ TeV, $H \to Z\gamma$, $Z \to \mu\mu$. They are produced from Higgs production modes of, from left to right, on the top: gluon-fusion, VBF, WH and on the bottom: ZH and $t\bar{t}H$ processes.

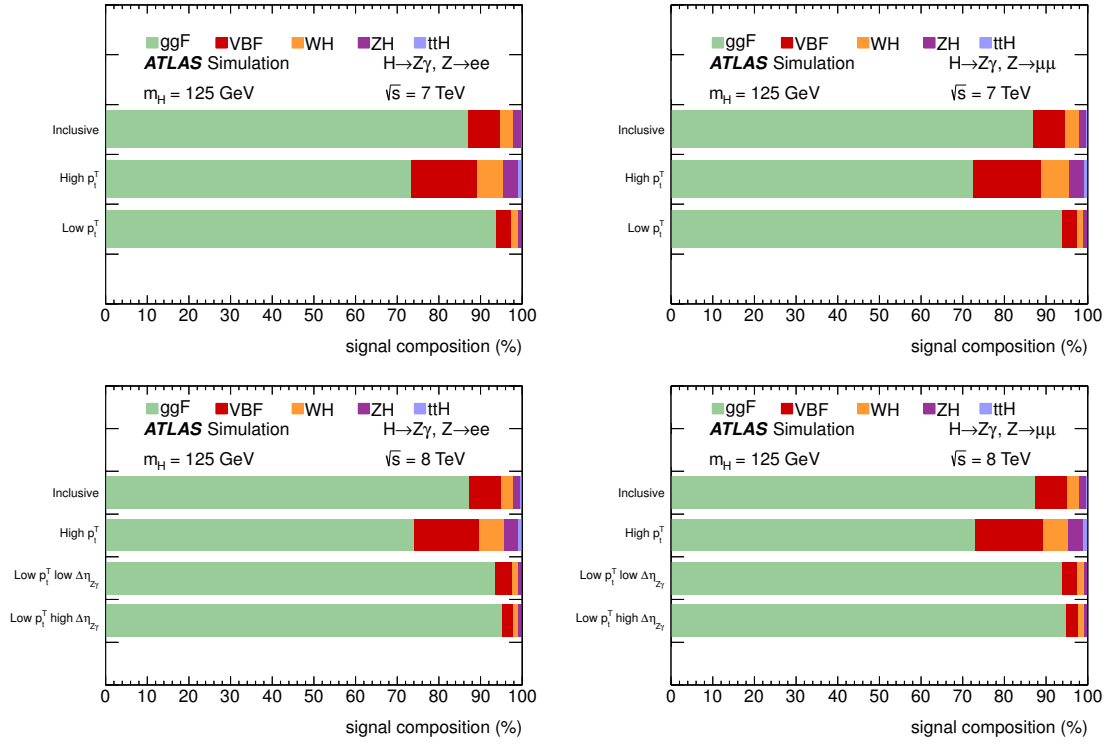

Figure 4.12 – Signal composition of each physics category and of the inclusive sample (for a given center-of-mass energy and lepton flavor) in terms of the various production processes, for $m_H = 125$ GeV.

Table 4.3 – Number of expected signal events for each production process and Higgs boson masses in 5 GeV steps between 120 and 150 GeV, for 20.3 fb^{-1} at $\sqrt{s} = 8$ TeV and $Z \to \mu\mu$.

mass	$gg \to H$		VBF		WH		ZH		$t\bar{t}H$		Total	
[GeV]	ε[%]	N_{evt}	ε[%]	N_{evt}	ε[%]	N_{evt}	ε[%]	N_{evt}	ε[%]	N_{evt}	ε[%]	N_{evt}
120	0.286	4.945	0.303	0.413	0.260	0.173	0.284	0.111	0.254	0.031	0.286	5.672
125	0.325	7.185	0.344	0.622	0.303	0.245	0.299	0.143	0.288	0.043	0.325	8.238
130	0.353	9.153	0.369	0.811	0.323	0.290	0.328	0.175	0.303	0.051	0.352	10.479
135	0.368	10.330	0.386	0.946	0.343	0.315	0.338	0.186	0.320	0.055	0.368	11.833
140	0.387	10.905	0.409	1.039	0.352	0.306	0.355	0.188	0.340	0.057	0.387	12.495
145	0.398	10.630	0.418	1.030	0.369	0.288	0.370	0.177	0.333	0.050	0.398	12.175
150	0.406	9.469	0.431	0.950	0.380	0.244	0.382	0.152	0.358	0.045	0.407	10.860

tail), representing the "core" of well-reconstructed events, and a small wider Gaussian component (GA) describing the tails of the distribution ("outliers"):

$$R\left(m_{\ell\ell\gamma}, \mu_{CB}, \alpha_{CB}, \sigma_{CB}, n_{CB}, f_{CB}, \sigma_{GA}\right) = f_{CB} CB\left[m_{\ell\ell\gamma}, \mu_{CB}, \alpha_{CB}, f_{CB}, \sigma_{CB}, n_{CB}\right] + \left(1 - f_{CB}\right) GA\left[m_{\ell\ell\gamma}, \mu_{CB}, \sigma_{GA}\right] \tag{4.6}$$

where the Crystal Ball functional form is:

$$N \cdot \begin{cases} e^{-t^2/2} & \text{if } t > -\alpha_{CB} \\ \left(\frac{n_{CB}}{|\alpha|}\right)^n \cdot e^{-|\alpha_{CB}|^2/2} \cdot \left(\frac{n_{CB}}{|\alpha_{CB}|} - |\alpha_{CB}| - t\right)^{-n_{CB}} & \text{otherwise} \end{cases} \tag{4.7}$$

Here, $t = (m_{\ell\ell\gamma} - \mu_{CB})/\sigma_{CB}$ and N is a normalization parameter (such that the integral of the CB is equal to unity). The parameters that appear in the previous formulae are the following. σ_{CB}, μ_{CB} and σ_{GA} represents the $\ell\ell\gamma$ invariant mass resolution and mean value of the core and the outliers respectively. n_{CB} and α_{CB} parameterize the non-Gaussian tail (α_{CB} is a measure of how far from the peak the distribution becomes non-Gaussian while n_{CB} is related to the slope of the tail), and f_{CB} represents the fraction of the integral of the full composite model due to events in the Crystal Ball core.

From the available signal MC samples at different mass points we identify the parameters that depend on the nominal Higgs boson mass m_H (μ_{CB},α_{CB},σ_{CB},σ_{GA}) and the parameters with a mild dependence on it. We observe that μ_{CB}, α_{CB}, σ_{CB} scale linearly with m_H while the ratio σ_{GA}/σ_{CB} and the parameters n_{CB} and f_{CB} are rather independent of m_H. For this reason, to obtain the parameters of the signal invariant mass distribution for any value of m_H between 120 and 150 GeV, we perform a simultaneous fit of all the available signal samples (for a certain lepton flavor production process and $\Delta\eta - p_{Tt}$ category) with a CB+GA model, where μ_{CB}, α_{CB}, σ_{CB} are a linear function of m_H, and σ_{GA}/σ_{CB}, f_{CB} and n_{CB} are independent of m_H. In total, 9 parameters per category (3 shape parameters with linear dependence of the Higgs boson mass and 3 global parameters) are extracted from a single fit to all available Monte Carlo samples, and then used to estimate the signal invariant mass distribution parameters at each mass value.

Figures 4.13 and 4.14 show the distribution of $m_{\ell\ell\gamma}$ for signal events passing the full selection in varies categories, for $m_H = 125$ GeV, with the projection of the global resolution fit.

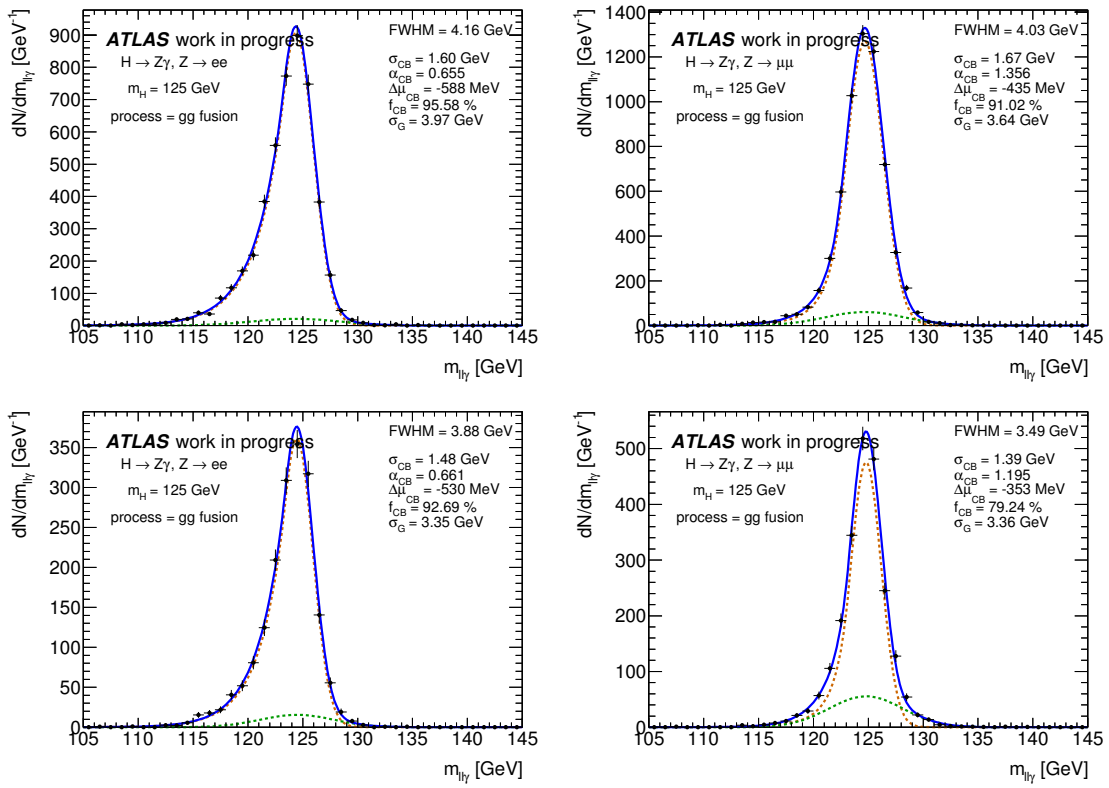

Figure 4.13 – Distribution (normalized to 1 fb^{-1}) of the final state three-body invariant mass $m_{\ell\ell\gamma}$ for $\sqrt{s} = 7$ TeV signal events passing the full selection (dots), in different categories. The line overlaid represents the fit of the distribution with a model composed of the sum of a Crystal Ball (red dashed line) and a Gaussian function (green dashed line). Left: electron channel. Right: muon channel. Top: low p_{Tt}. Bottom: high p_{Tt}.

.

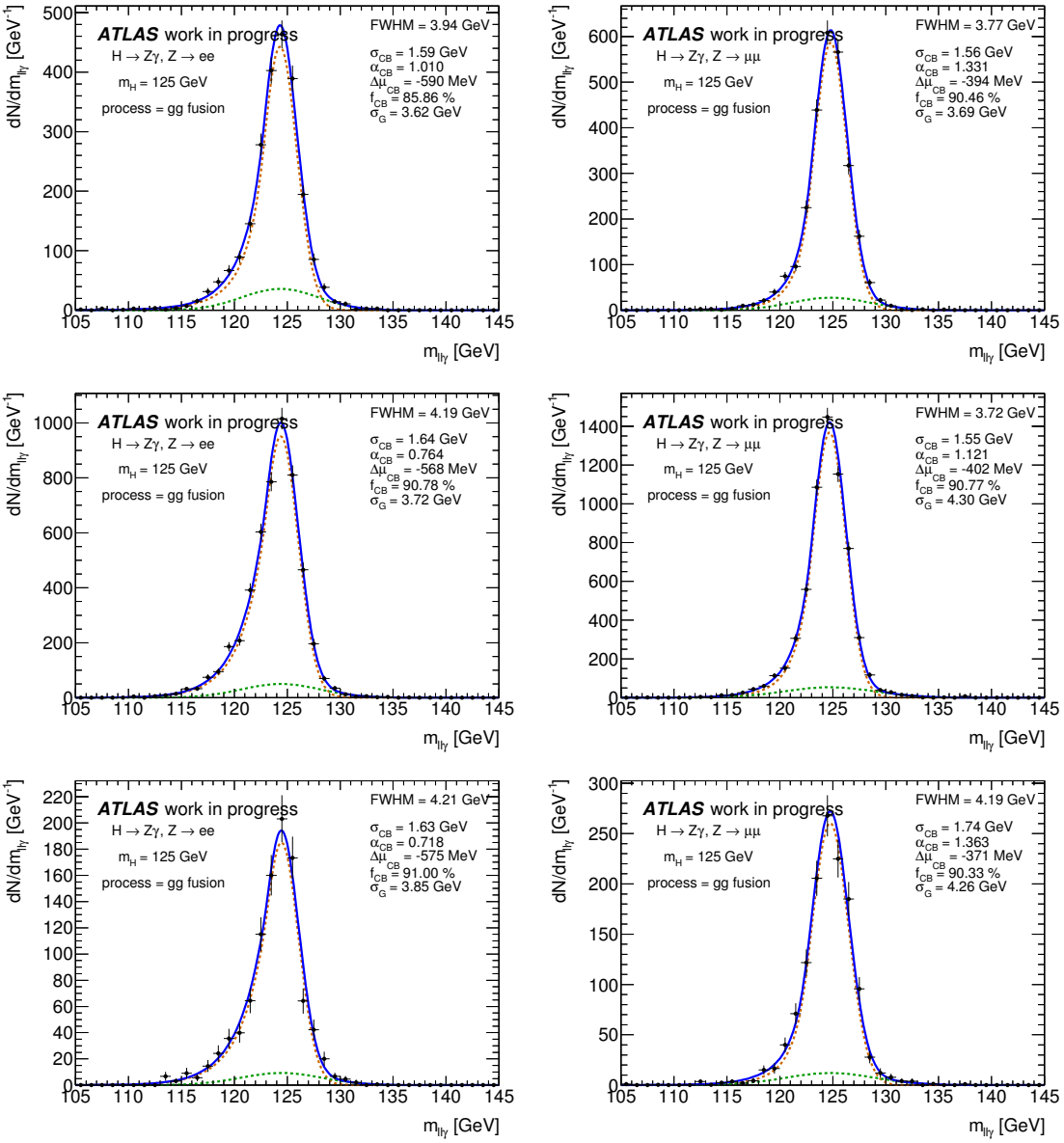

Figure 4.14 – Distribution (normalized to 1 fb^{-1}) of the final state three-body invariant mass $m_{\ell\ell\gamma}$ for $\sqrt{s} = 8$ TeV signal events passing the full selection (dots), in different categories. The line overlaid represents the fit of the distribution with a model composed of the sum of a Crystal Ball (red dashed line) and a Gaussian function (green dashed line). Left: electron channel. Right: muon channel. Top: high p_{Tt}. Middle: low p_{Tt}, low $\Delta\eta$. Bottom: low p_{Tt}, high $\Delta\eta$.

.

4.8 Background Properties

The signal and background yields are extracted directly from a fit to the $m_{\ell\ell\gamma}$ data distribution. In the fit, we use a smooth function with free parameters to model the background shape. The fit function and fit range are chosen in order not to produce a large potential bias on the fitted signal while retaining good statistical power. The function should therefore be as simple as possible (with a reduced number of free parameters) in order to reduce the uncertainty on the extrapolated background below the signal, but also sufficiently flexible to follow the data distribution without introducing artificial peaks when a signal+background fit is performed on a background-only sample.

An optimization study is performed on high statistics simulation samples, testing a number of analytical forms which include polynomials of varying order, and non-polynomial functions such as exponential, Crystal Ball, Crystal Ball+Gaussian, and Crystal Ball+Landau distributions. The high statistic sample contains 40 million truth-level $Z + \gamma$ events generated with Sherpa for both the $ee\gamma$ and $\mu\mu\gamma$ channels. $Z + \gamma$ is by far the dominant background contribution to the selected sample, and we observed on fully simulated MC samples that the same analytical form can describe both the $Z+\gamma$ and $Z+X$ ($X = \gamma$, jet) invariant mass shapes in the fit range. In each event category, an unbinned likelihood fit of signal+background is performed in a range of the observable $m_{\ell\ell\gamma}$. The signal + background model is fit to the background-only $m_{\ell\ell\gamma}$ distribution, whose shape is extracted in high statistics $Z + \gamma$ Sherpa sample and normalized to the data luminosity. The fitted signal yield is called "spurious signal". We require the spurious signal to be less than $\pm 20\%$ of its fitted error, so that the possible bias, neglected in the nominal result and treated as a systematic uncertainty, gives an almost neglibigle contribution to the total error when summed in quadrature with the other uncertainties. Among the fit ranges and functional forms satisfying this requirement, we choose the one with the best sensitivity to the signal. Figures 4.15-4.16 show the level of spurious signal divided by its uncertainty caused by background fluctuation as a function of the Higgs boson mass for various background models in each category in the 8 TeV data and for the fit range 115-170 GeV, which is found to be the optimal one.

Table 4.4 shows the background model chosen for each category, together with the expected signal and background yield for the Higgs boson mass of 125 GeV.

Figures 4.17 and 4.18 show the unbinned maximum likelihood fit to the data in each category using a background-only hypothesis, together with the SM signal multiplied by a factor of 50. The fits describe well the observed distributions. The inclusive background shape (summing all fitted background shapes in all individual categories) and the inclusive signal shape (summing all signal shapes together) are shown with inclusive data in Figure 4.19.

4.9 Systematic Uncertainties

The main sources of systematic uncertainties are described in this section. Most of the uncertainties are estimated from the simulation and then "profiled" in the final maximum likelihood fit to the data.

4.9.1 Theoretical uncertainties

Theory uncertainty on the production cross section includes two components, the uncertainty related to the energy scales used for the fixed-order calculation ("scale uncer-

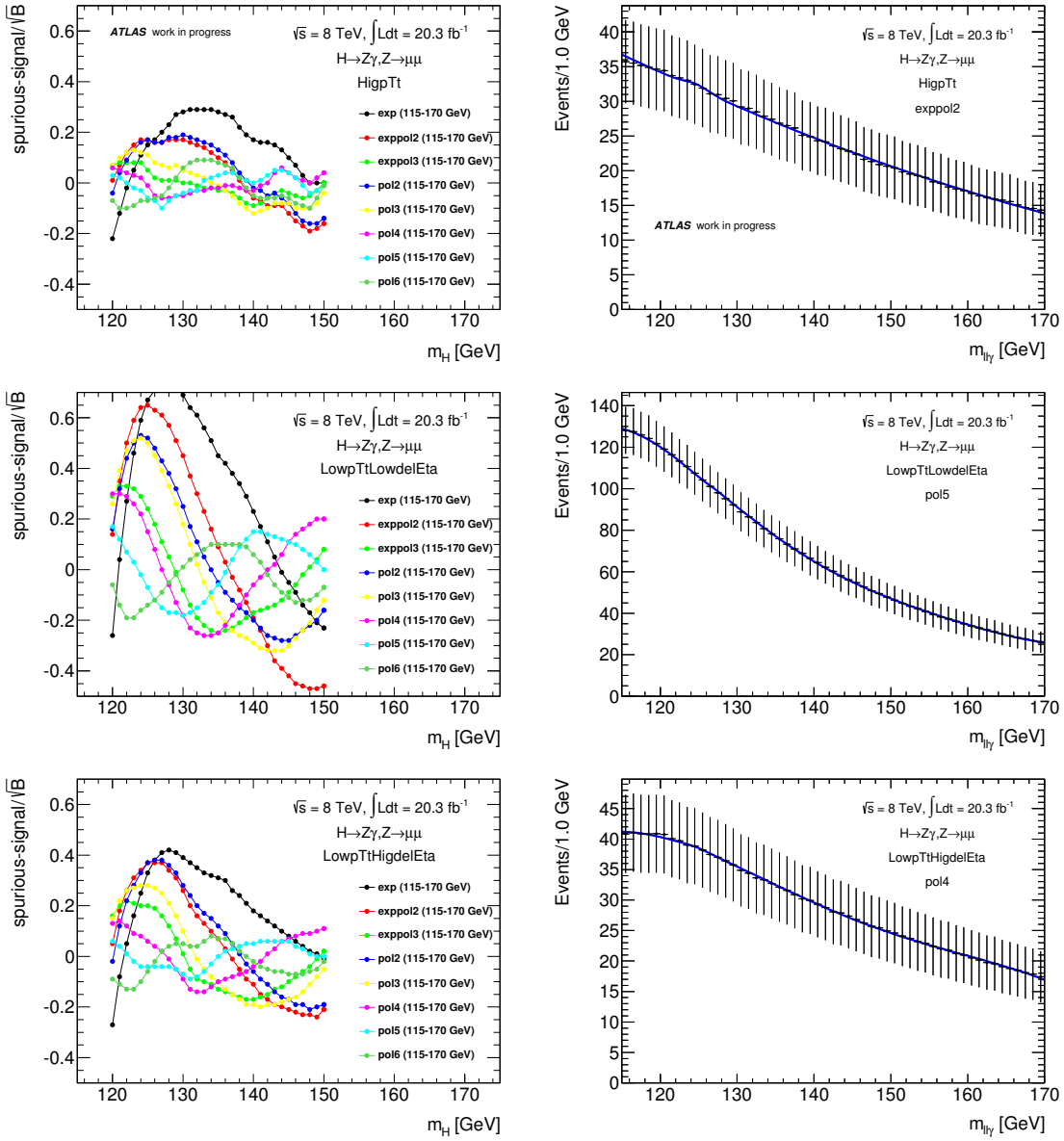

Figure 4.15 – Spurious signal as a function of Higgs mass in the 2012 $\mu\mu\gamma$ categories (left) and the background-only $m_{\ell\ell\gamma}$ distribution fitted with S+B using the nominal model (right), for the High p_{Tt} category (top), the Low p_{Tt} & Low $\Delta\eta$ category (middle), and the Low p_{Tt} & High $\Delta\eta$ category (bottom).

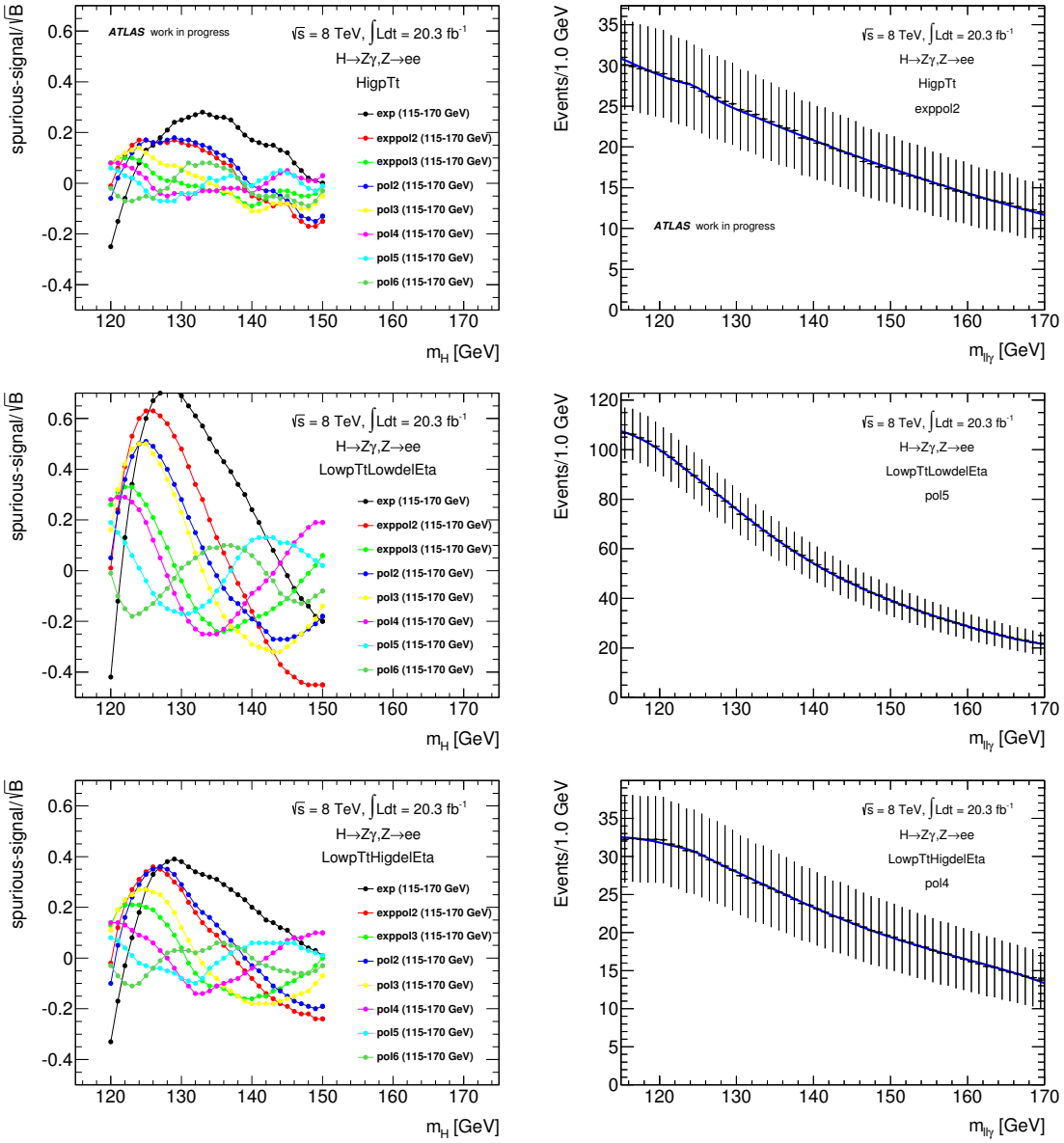

Figure 4.16 – Spurious signal as a function of Higgs mass in the 2012 $ee\gamma$ categories (left) and the background-only $m_{\ell\ell\gamma}$ distribution fitted with S+B using the nominal model (right), for the High p_{Tt} category (top), the Low p_{Tt} & Low $\Delta\eta$ category (middle), and the Low p_{Tt} & High $\Delta\eta$ category (bottom).

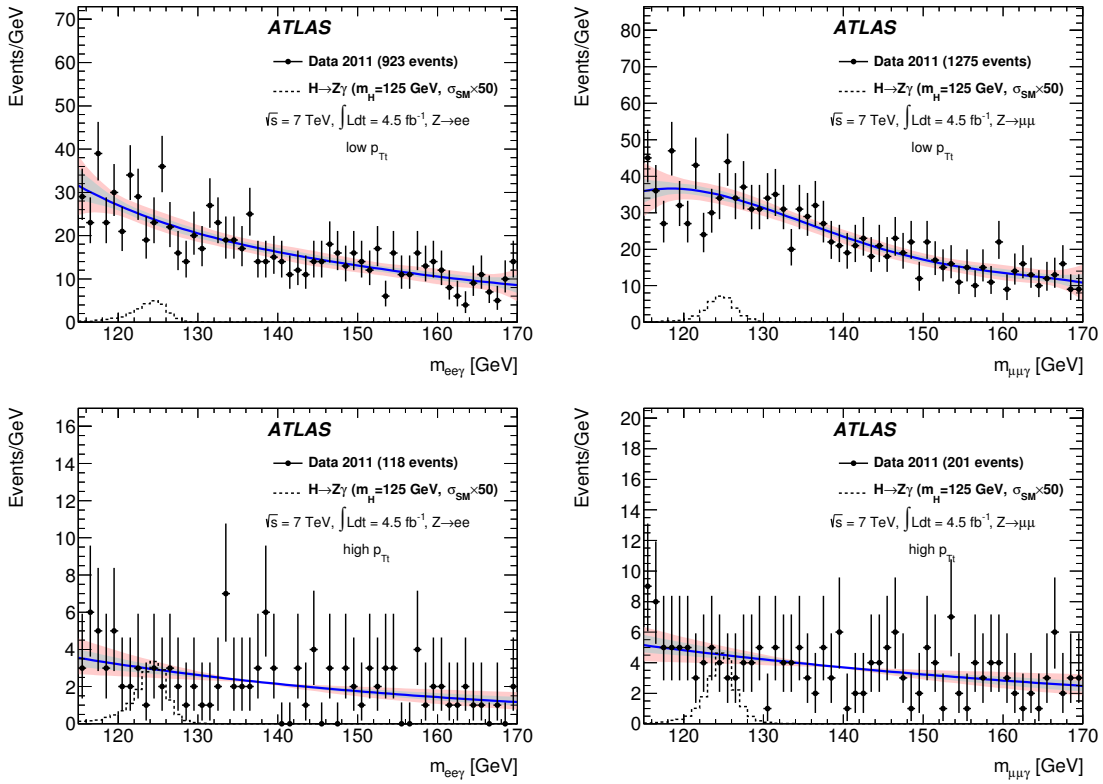

Figure 4.17 – Background-only fit to the three-body invariant mass distribution of selected events in data, for $Z \to ee$ (left) and $Z \to \mu\mu$ (right), low p_{Tt} (top) and high p_{Tt} (bottom), at $\sqrt{s} = 7$ TeV. Dots represent data. The light blue line is the fit result, while the dark blue and red bands are the 1σ and 2σ bands from the statistical uncertainties on the fitted values of the parameters of the polynomials. The dashed line is the SM signal multiplied by a factor of 50.

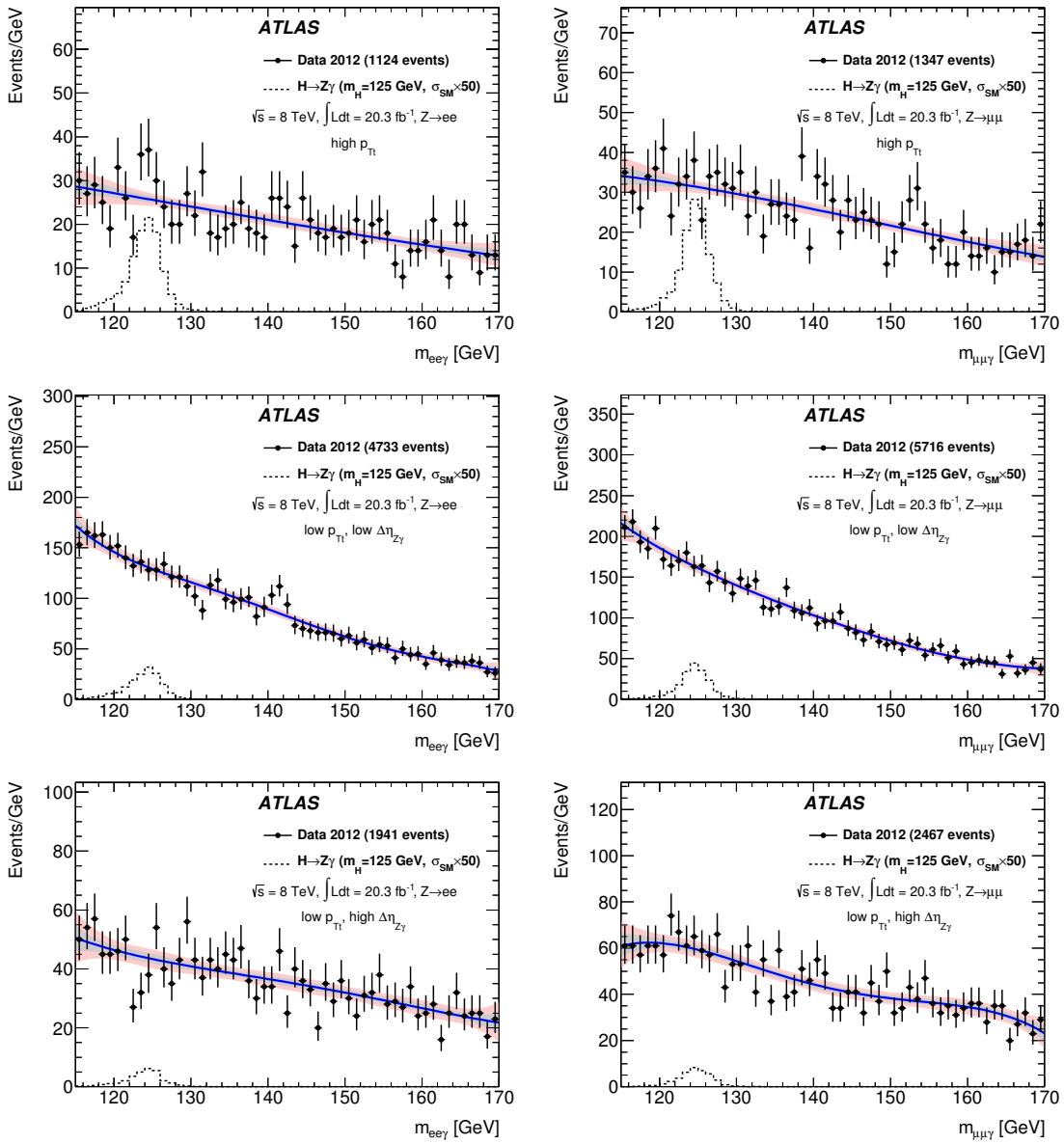

Figure 4.18 – Background-only fit to the three-body invariant mass distribution of selected events in data, for $Z \to ee$ (left) and $Z \to \mu\mu$ (right), high p_{Tt} (top) and low p_{Tt} low $\Delta\eta$ (middle) and low p_{Tt} high $\Delta\eta$ (bottom), at $\sqrt{s} = 8$ TeV. Dots represent data. The light blue line is the fit result, while the dark blue and red bands are the 1σ and 2σ bands from the statistical uncertainties on the fitted values of the parameters of the polynomials. The dashed line is the SM signal multiplied by a factor of 50.

Table 4.4 – Expected signal (N_S) and background (N_B) yields in a ±5 GeV mass window around $m_H = 125$ GeV for each of the event categories under study. In addition, the observed number of events in data (N_D) and the FWHM of the signal invariant-mass distribution, modelled as described in Section 4.7, are given. The signal is assumed to have SM-like properties, including the production cross section times branching ratio. The background yield is extrapolated from the selected data event yield in the invariant-mass region outside the ±5 GeV window around $m_H = 125$ GeV, using an analytic background model. The uncertainty on the FWHM from the limited size of the simulated signal samples is negligible in comparison to the systematic uncertainties described in Section 4.9.

$\sqrt{s}$ [TeV]	ℓ	Category	Model	N_S	N_B	N_D	$\frac{N_S}{\sqrt{N_B}}$	FWHM [GeV]
8	μ	high p_{Tt}	Exp. of 2nd order pol.	2. 3	310	324	0.13	3.8
8	μ	low p_{Tt}, low $\|\Delta\eta\|$	5^{th} order Chebyshev pol.	3.7	1600	1587	0.09	3.8
8	μ	low p_{Tt}, high $\|\Delta\eta\|$	4^{th} order Chebyshev pol.	0.8	600	602	0.03	4.1
8	e	high p_{Tt}	Exp. of 2nd order pol.	1.9	260	270	0.12	3.9
8	e	low p_{Tt}, low $\|\Delta\eta\|$	5^{th} order Chebyshev pol.	2.9	1300	1304	0.08	4.2
8	e	low p_{Tt}, high $\|\Delta\eta\|$	4^{th} order Chebyshev pol.	0.6	430	421	0.03	4.5
7	μ	high p_{Tt}	Exponential	0.4	40	40	0.06	3.9
7	μ	low p_{Tt}	4^{th} order Chebyshev pol.	0.6	340	335	0.03	3.9
7	e	high p_{Tt}	Exponential	0.3	25	21	0.06	3.9
7	e	low p_{Tt}	4^{th} order Chebyshev pol.	0.5	240	234	0.03	4.0

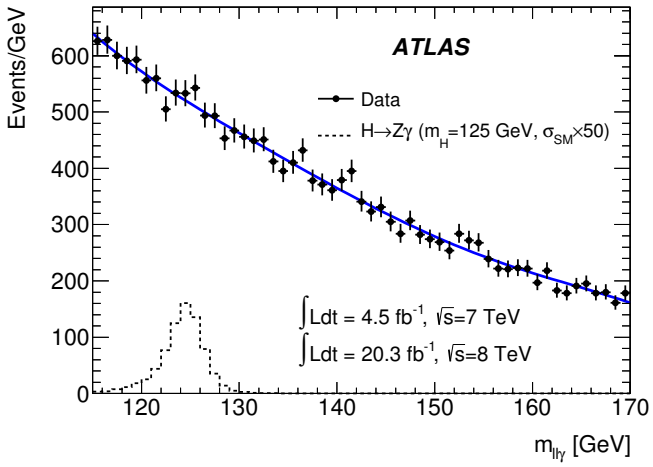

Figure 4.19 – Background-only fit to the three-body invariant mass distribution of selected events in data. Dots represent inclusive data. The blue line is the sum of the fitted background results in all categories. The dashed black line is the sum of the SM signal histograms in all categories, which is multiplied by a factor of 50.

tainty"), and the uncertainty from the parton distribution functions (PDFs) and the value of α_s used in the perturbative calculation. In Table 4.5 we summarize the uncertainties at the boundaries (120 and 150 GeV) of the explored Higgs boson mass range.

In addition, the contributions on theoretical calculation from $H \to \ell\ell^* \to \ell\ell\gamma$ decays and interference between $H \to \ell\ell^* \to \ell\ell\gamma$ and $H \to Z\gamma$ are studied [114]. These effects are

neglected in the calculation of Refs. [76, 77]. As a cross check, using `MadGraph5` generator, the invariant mass distributions for the inclusive $H \to \mu\mu\gamma$ decay and $H \to Z\gamma \to \mu\mu\gamma$ are compared and shown in Figure 4.20. The $H \to \mu\mu^* \to \mu\mu\gamma$ decay and interference increase the cross section by 1%-5% in muon channel. Similar value is seen in electron channel. An extra 5% uncertainty is added in quadrature to the branching ratio.

Table 4.5 – Theoretical systematic uncertainties for the SM Higgs boson production cross section and branching fraction of the $H \to Z\gamma$ decay at the boundaries of the tested Higgs boson mass range (120 and 150 GeV). In each column, the first number is the uncertainty for $m_H = 120$ GeV, the second is the uncertainty for $m_H = 150$ GeV.

Uncertainty source	Relative uncertainty (%)			
	7 TeV		8 TeV	
$\sigma(gg \to H)$ (scale)	$^{+7.2}_{-7.9}$	$^{+6.6}_{-7.4}$	$^{+7.3}_{-7.9}$	$^{+6.7}_{-7.4}$
$\sigma(gg \to H)$ (PDF)	$^{+7.6}_{-7.0}$	$^{+7.6}_{-7.5}$	$^{+7.5}_{-6.9}$	$^{+7.4}_{-7.0}$
σ(VBF) (scale)	$^{+0.3}_{-0.4}$	$^{+0.2}_{-0.1}$	$^{+0.2}_{-0.2}$	$^{+0.3}_{-0.2}$
σ(VBF) (PDF)	$^{+2.4}_{-2.1}$	$^{+2.7}_{-2.1}$	$^{+2.6}_{-2.8}$	$^{+2.5}_{-2.7}$
$\sigma(WH)$ (scale)	$^{+0.9}_{-0.9}$	$^{+0.9}_{-0.9}$	$^{+1.0}_{-1.0}$	$^{+1.0}_{-1.0}$
$\sigma(WH)$ (PDF)	$^{+2.6}_{-2.6}$	$^{+3.6}_{-3.6}$	$^{+2.5}_{-2.5}$	$^{+2.5}_{-2.6}$
$\sigma(ZH)$ (scale)	$^{+2.8}_{-2.8}$	$^{+3.0}_{-3.0}$	$^{+3.0}_{-3.0}$	$^{+3.9}_{-3.9}$
$\sigma(ZH)$ (PDF)	$^{+2.8}_{-2.8}$	$^{+3.7}_{-3.7}$	$^{+2.5}_{-2.5}$	$^{+2.7}_{-2.7}$
$\sigma(t\bar{t}H)$ (scale)	$^{+3.4}_{-9.3}$	$^{+2.8}_{-9.1}$	$^{+3.9}_{-9.3}$	$^{+3.4}_{-9.1}$
$\sigma(t\bar{t}H)$ (PDF)	$^{+8.4}_{-8.4}$	$^{+8.5}_{-8.5}$	$^{+8.1}_{-8.1}$	$^{+8.2}_{-8.2}$
$\mathcal{B}(H \to Z\gamma)$	$^{+9.4}_{-9.3}$	$^{+6.4}_{-6.5}$	$^{+9.4}_{-9.3}$	$^{+6.4}_{-6.5}$

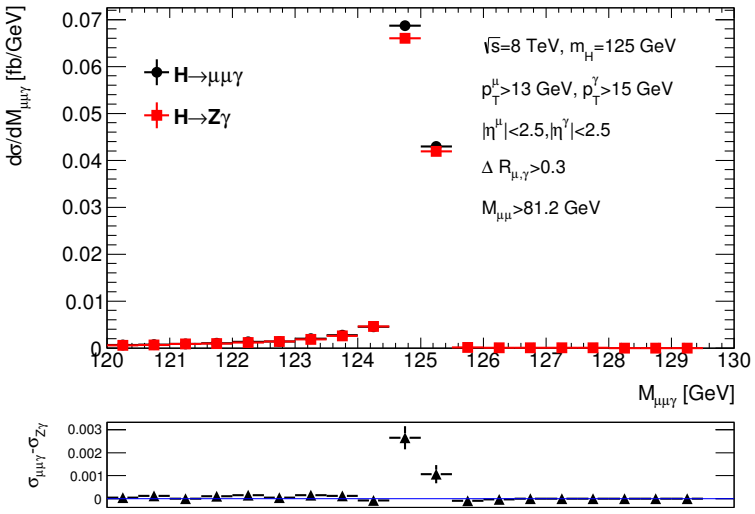

Figure 4.20 – $m_{\ell\ell\gamma}$ mass distribution for $H \to Z\gamma \to \mu\mu\gamma$ (red) and $H \to \mu\mu\gamma$ with the full interference between channels (black)

Theoretical uncertainties on the background cross section do not enter the $H \to Z\gamma$ search, because the background normalization and shape are obtained through a fit on the data.

4.9.2 Experimental uncertainties

Luminosity

The overall normalization uncertainty of the integrated luminosity is 1.8% and 2.8% for 7 TeV data and 8 TeV data, respectively.

Photon reconstruction and identification

The photon reconstruction uncertainty arises primarily from the knowledge of the detector material, since a small inefficiency affects converted photons, and a non-perfect modelling of the conversion fraction in the simulation could lead to a bias in the estimated reconstruction efficiency of the whole signal. The uncertainty has been evaluated by comparing the reconstruction efficiency in simulation samples produced either with the nominal detector geometry or with more material added to it, consistently with the current bounds on the additional material obtained with data-driven techniques. The alternative detector model contains an additional $\sim$10% of X_0 in the cryostat, $\sim$5% of X_0 in the presampler and the strips, and $\sim$15% of X_0 in the end-cap region. The largest effect on the reconstruction efficiency is about 0.5%, which is negligible compared to the photon identification efficiency uncertainty.

Data-driven measurements are used to estimate the photon identification efficiency in data as discussed in section 3.3 and compared to Monte Carlo in order to assign systematic uncertainties on the photon identification efficiency as a function of the photon transverse energy, pseudorapidity and conversion category. These are propagated to the measurement by recomputing the signal yield by shifting the photon efficiency by its uncertainty.

Photon and electron isolation requirements

Differences of the order of 100 MeV (500 MeV) between data and simulation have been observed for the topological-cluster (standard cell) based isolation of photons and electrons, selected either in di-photon enriched events or in a control sample of electrons from $Z \to ee$. We repeat the selection on signal MC by shifting the photon and electron isolation, event-by-event, by $\pm$100 MeV (or $\pm$500 MeV for electrons in the 7 TeV analysis), and use the relative signal yield variation with respect to the nominal result as the corresponding systematic uncertainty.

Photon and electron energy scale

The difference between the electromagnetic (photon and electron) energy scales in data and simulation introduces an uncertainty both on the signal efficiency and thus the expected yield (because of the uncertainty on the efficiency of the $E_T^\gamma > 15$ GeV and $E_T^e > 10$ GeV requirements) and on the position of the signal peak in the fit discriminating variable. This uncertainty is assessed by varying the electron and photon energy scales within their uncertainties and recomputing the efficiency and the expected signal yield. The signal $m_{\ell\ell\gamma}$ distribution is also recomputed, and the relative shift of the peak position is quoted as a systematic uncertainty on the signal PDF. The effects of the uncertainty from the $Z \to ee$ method used to extract the scale factors, of the limited knowledge of the material, of the uncertainty on the presampler energy scale and of the low-p_T scale factor uncertainties are evaluated separately as is done in ATLAS for the study of $H \to \gamma\gamma$ and $H \to \ell\ell ee$. For photons, additional uncertainties have been considered from lateral shower

shapes difference between electrons and photons (0.1%), and from E_1/E_2 bias between photons and electrons (0.2%).

Photon and electron energy resolution

The difference between the constant term of the electromagnetic calorimeter resolution observed in MC compared to the data introduces an additional uncertainty, on both the signal yield (though small) and on the width of the $m_{\ell\ell\gamma}$ distribution. The nominal yields are estimated, as described previously, by correcting the simulation adding an extra smearing of the energy resolution in order to match the data one. The uncertainty on the resolution is propagated to this measurement by varying the smearing correction within its uncertainties. The signal yield and the $m_{\ell\ell\gamma}$ distribution are recomputed, and the relative variation of the yield and of the width of the signal PDF are taken as systematic uncertainties.

Electron trigger, reconstruction and identification efficiency

The trigger, reconstruction and identification electron efficiency uncertainties are estimated by varying the efficiency scale factors, estimated from electrons from $Z \to ee$ with a tag-and-probe method and used to correct the simulation to match the data efficiency, within their uncertainties [40].

Muon momentum

The uncertainty on the $p_T > 10$ GeV cut (15 GeV for CT muons) is estimated by varying the muon momentum corrections in MC by their uncertainties. The muon momentum is varied by its scale and resolution uncertainties [43]. The deviations in expected signal yields and signal peak position and resolution are taken as systematic uncertainties.

Muon trigger, reconstruction and identification efficiency

The trigger, reconstruction and identification muon efficiency uncertainties are estimated by varying the efficiency scale factors – estimated from muons from $Z \to \mu\mu$ with a tag-and-probe method and used to correct the simulation to match the data efficiency – within their uncertainties [43].

Background modeling

The method to estimate the average expected bias on the signal from the choice of the background model has been discussed in Section 4.8: using high statistics MC samples, the events after passing all selections are grouped in categories and normalized to the data luminosity. The three body invariant mass distribution of the background is fitted with the full $S + B$ model, for different hypotheses of the Higgs boson mass.

The maximum possible bias across the full range of tested Higgs boson mass hypotheses is considered as a systematic uncertainty on the fitted signal yield. It varies between 0.5 events in poorly populated categories and 8.3 events in highly populated ones.

Higgs p_T reweighting uncertainty

For the ggH signal samples, the uncertainties related to the Higgs p_{T} description are estimated according to the prescription of the `HRes2.0` authors. Four scales are used

in `HRes2.0`: the renormalization scale $\mu_R = m_H$, the factorization scale $\mu_F = m_H$, the traditional resummation scale $Q_1 = m_H/2$ and a new scale introduced when considering separately the bottom quark effect $Q_2 = m_b$. These four scales are varied in the following way:

- μ_R, μ_F: varied between $m_H/2$ and $2m_H$, for $1/2 \leq \mu_R/\mu_F \leq 2$;
- Q_1: varied between $m_H/4$ and m_H because its recommended central value is $m_H/2$;
- Q_2: varied between $m_b/3$ and $3m_b$ to be conservative.

The envelope of the different predictions is used to derive two extremal weights, and the uncertainty is estimated by repeating the analysis with these extremal weights instead of the nominal one.

Summary

The list of the main sources of systematic uncertainties and their contributions to the $H \to Z\gamma$ expected signal yields and the parameters of the $m_{\ell\ell\gamma}$ PDFs are listed in Tables 4.6 and 4.7 for $m_H = 125$ GeV and $\sqrt{s} = 7$ or 8 TeV, respectively. All systematic uncertainties are taken as correlated between 7 TeV and 8 TeV categories, except the one of luminosity. The correlations between electron and muon categories are listed in the last column of the table.

4.10 Statistical Method

4.10.1 Statistical methods for evalution of limits and p-values

We use likelihood-based statistical tests to interpret our selected data samples in terms of a background plus the contribution of a Higgs boson decaying to $Z\gamma$. The tests are similar to those used in the search for the Higgs boson in other decay channels. The results are expresssd in terms of a "signal-strength" parameter μ, which is defined as the ratio

$$\mu = \frac{N_{\text{signal}}}{N^{SM}_{\text{signal}}} \tag{4.8}$$

of the measured number of signal events to the value expected in the Standard Model. For a Standard Model Higgs boson decaying to $Z\gamma$, the value of μ observed in each of the orthogonal categories in which the dataset is subdivided should be consistent with a single value equal to unity within statistical uncertainties.

The Modified Frequentist method (CL_s method) [115] is adopted to interpret the data. First, in order to quantify the significance of a possible observation, a hypothesis test is performed to evaluate the compatibility between the data and the null hypothesis, which assumes that the selected data contains only background events. If the hypothesis test shows no presence of any significant excess in data, a limit on the ratio of the $H \to Z\gamma$ cross section over the Standard Model expectation is set.

p-value calculation

The compatibility of the data with the background-only (B-only) hypothesis ($\mu = 0$) is quantified by the p-value of the null hypothesis, p_0, which represents the probability, under the background-only hypothesis, that the data can fluctuate to give a signal yield at least as large as the observed one. Only upwards deviations from the B-only hypothesis,

Table 4.6 – Summary of the systematic uncertainties on the signal yield and invariant mass distribution for $m_H = 125$ GeV, at $\sqrt{s} = 7$ TeV. The numbers are listed in two categories: high p_{Tt} (top), low p_{Tt} (bottom).

Systematic Uncertainty	$H \to Z(\mu\mu)\gamma(\%)$	$H \to Z(ee)\gamma(\%)$	Uncertainty Treatment
Signal Yield			
Luminosity	1.8	1.8	correlated
Trigger	0.74	0.17	uncorrelated
	0.70	0.14	
γ ID efficiency	2.59	2.57	correlated
	3.01	2.98	
electron reco+ID efficiency	–	2.57$\oplus$1.18	uncorrelated
	–	1.75$\oplus$1.06	
μ reco+ID efficiency	0.69	–	uncorrelated
	0.65	–	
e/γ Energy Scale	0.3	0.4	correlated
	0.2	0.4	
ZeeAllUp	0.05	0.15	
	0.04	0.21	
Material	0.28	0.38	
	0.02	0.15	
Presampler	0.13	0.12	
	0.11	0.17	
Low pt	0.05	0.13	
	0.16	0.31	
e vs γ differences	0.09	0.09	
e/γ isolation	0.38	0.19	correlated
	0.17	0.31	
e/γ energy resolution	0.13	0.20	correlated
	0.12	0.39	
μ momentum scale	0.28	–	correlated
	0.06	–	
μ momentum resolution	0.3	–	correlated
	0.2	–	
Signal $m_{\ell\ell\gamma}$ resolution			
e/γ Energy Resolution	3.25	9.95	correlated
μ momentum Resolution	1.5	–	
Signal $m_{\ell\ell\gamma}$ peak position			
e/γ Energy Scale	0.2 GeV	0.2 GeV	correlated
muon momentum scale	negligible	–	negligible
Signal migration			
Higgs p_T mis-modeling	3.69	3.69	correlated
	2.20	2.32	

Table 4.7 – Summary of the systematic uncertainties on the signal yield and invariant mass distribution for $m_H = 125$ GeV, at $\sqrt{s} = 8$ TeV. The numbers are listed in three categories: high p_{Tt} (top), low p_{Tt} & low $\Delta\eta$ (medium), low p_{Tt} & high $\Delta\eta$ (bottom).

Systematic Uncertainty	$H \to Z(\mu\mu)\gamma(\%)$	$H \to Z(ee)\gamma(\%)$	Uncertainty Treatment
Signal Yield			
Luminosity	2.8	2.8	correlated
Trigger	0.87	0.44	uncorrelated
	0.83	0.41	
	0.67	0.36	
γ ID efficiency	2.51	2.53	correlated
	3.10	3.09	
	3.13	3.07	
electron reco+ID efficiency	–	1.46$\oplus$2.41	uncorrelated
	–	1.42$\oplus$2.46	
	–	1.36$\oplus$2.08	
μ reco+ID efficiency	0.65	–	uncorrelated
	0.64	–	
	0.65	–	
e/γ Energy Scale	0.6	1.6	correlated
	0.2	1.7	
	0.7	2.6	
ZeeAllUp	0.47	1.56	
	0.09	1.63	
	0.33	2.60	
Material	0.35	0.35	
	0.05	0.20	
	0.28	0.32	
Presampler	0.12	0.18	
	0.09	0.17	
	0.13	0.18	
Low pt	0.10	0.12	
	0.21	0.36	
	0.55	0.42	
e vs γ differences	0.09	0.09	
e/γ isolation	0.34	0.40	correlated
	0.38	0.35	
	0.59	0.32	
e/γ energy resolution	0.19	0.26	correlated
	0.09	0.05	
	0.31	1.25	
μ momentum scale	0.35	–	correlated
	0.03	–	
	0.03	–	
μ momentum resolution	0.30	–	correlated
	0.20	–	
	0.30	–	
Signal $m_{\ell\ell\gamma}$ resolution			
e/γ energy resolution	2.69	10.62	correlated
μ momentum resolution	0.5	–	negligible
Signal $m_{\ell\ell\gamma}$ peak position			
e/γ energy scale	0.2 GeV	0.2 GeV	correlated
muon momentum scale	negligible	–	negligible
Signal migration			
Higgs p_T mis-modeling	3.57	3.42	correlated
	1.82	1.80	
	1.82	1.80	

which would correspond to a positive signal strength, are considered. Large p_0 therefore correspond to datasets that agree well with the B-only hypothesis, while small p_0 can be interpreted as a suggestion of a significant positive signal. The p_0 is computed from the q_0 test statistic, defined as

$$q_0 = \begin{cases} -2\ln\frac{L(0,\hat{\hat{\boldsymbol{\theta}}}(0))}{L(\hat{\mu},\hat{\boldsymbol{\theta}})} & \hat{\mu} \geq 0 \\ +2\ln\frac{L(0,\hat{\hat{\boldsymbol{\theta}}}(0))}{L(\hat{\mu},\hat{\boldsymbol{\theta}})} & \hat{\mu} < 0 \end{cases} \tag{4.9}$$

where L is the likelihood function described in Section 4.10.2; $\hat{\mu}$ and $\hat{\boldsymbol{\theta}}$ are the best-fit values for μ and $\boldsymbol{\theta}$ with all parameters floating; and $\hat{\hat{\boldsymbol{\theta}}}(0)$ are the best-fit values of $\boldsymbol{\theta}$ in the B-only ($\mu = 0$) hypothesis. The p-value of the null hypothesis is

$$p_0 = \int_{q_{0,\mathrm{obs}}}^{\inf} f(q_0|0, m_H, \hat{\hat{\boldsymbol{\theta}}}(0))dq_0 \tag{4.10}$$

where f is the distribution of the test statistics. In this scheme, small p_0 occurs only for $q_0 > 0$, which happens only for $\hat{\mu} \geq 0$. This corresponds to the one-sided prescription mentioned above, where only positive ("physical") values of the signal are considered. Negative fluctuations of the signal are assigned p_0 values in the interval $[0.5, 1]$, with values close to 0.5 corresponding to small negative fluctuations, and values close to 1 for large negative fluctuations.

In the expression for $\hat{\mu} > 0$, the numerator corresponds to the the maximum likelihood under the B-only hypothesis, while the denominator corresponds to the best value in the "S+B" hypothesis including both signal and background. For datasets which are compatible with the B-only hypothesis, both should be of similar magnitude and q_0 small. Conversely, in the presence of a signal the denominator (S+B hypothesis) should be much larger than the numerator (B-only hypothesis), yielding a large value for q_0. In the asymptotic regime, which is usually a good approximation for the models studied here, p_0 values can be directly computed from the q_0 values using closed-form "asymptotic formulae" [116]. Alternatively, the p_0 can be computed by sampling the distribution of q_0 in the B-only hypothesis using pseudo-experiments. Unless otherwise stated, asymptotic formulae will be used in the results presented in this thesis.

In the following we present both *observed* p_0 results, computed using real data, and *expected* p_0, which are computed from an Asimov dataset [116] in the $\mu = 1$ hypothesis.

Limit setting

Upper limits on the signal strength are set using a modified frequentist (CL_s) [115] method, using a CL_{s+b} based on the $\tilde{q}_\mu$ statistic:

$$\tilde{q}_\mu = \begin{cases} -2\ln\frac{L(\mu,\hat{\hat{\boldsymbol{\theta}}}(\mu))}{L(\hat{\mu},\hat{\boldsymbol{\theta}})} & 0 \leq \hat{\mu} \leq \mu \\ 0 & \hat{\mu} > \mu \\ -2\ln\frac{L(0,\hat{\hat{\boldsymbol{\theta}}}(0))}{L(\hat{\mu},\boldsymbol{\theta}(\hat{\mu}))} & \hat{\mu} < 0 \end{cases} \tag{4.11}$$

where L is the likelihood function described in Section 4.10.2; $\hat{\mu}$ and $\hat{\boldsymbol{\theta}}$ are the best-fit values for μ and $\boldsymbol{\theta}$ with all parameters floating; and $\hat{\hat{\boldsymbol{\theta}}}(\mu)$ are the best-fit values for $\boldsymbol{\theta}$ for a fixed value of μ. The statistic estimates the compatibility of the data with the μ hypothesis using the ratio of likelihood for the case of a floating μ (denominator), and the

case where it is fixed at the hypothesis value (nominator). As for the case of q_0, a one-sided prescription is used, assigning $\tilde{q}_\mu = 0$ if the fitted value $\hat{\mu}$ is above the hypothesis. Finally, if $\hat{\mu} < 0$, the case $\mu = 0$ is used instead to avoid technical issues with negative PDFs.

The CL_{s+b} p-value is defined as:

$$p_\mu = \int_{\tilde{q}_{\mu,\text{obs}}}^{\text{inf}} f(\tilde{q}_\mu|\mu, m_H, \hat{\hat{\boldsymbol{\theta}}}(\mu))d\tilde{q}_\mu \tag{4.12}$$

and the CL_s p-value is

$$p'_\mu = \frac{p_\mu}{1 - p_b} \tag{4.13}$$

where

$$p_b = 1 - \int_{\tilde{q}_{\mu,\text{obs}}}^{\text{inf}} f(\tilde{q}_\mu|0, m_H, \hat{\hat{\boldsymbol{\theta}}}(0))d\tilde{q}_\mu \tag{4.14}$$

The value of p'_μ and of the corresponding CL_s exclusion are obtained using either asymptotic formulae [116] or pseudo-data generation. Limits at 95% confidence level on the value of the signal strength μ are then computed by scanning values of the μ hypothesis, computing the CL_s exclusions and identifying the μ_{up} for which this value equals 0.05.

I will present both observed limits, computed using real data, and expected limits computed using an Asimov dataset [116] generated in the $\mu = 0$ hypothesis. Having observed a Higgs boson with $m_H = 125.5$ GeV and μ compatible with 1, I will also show, for $m_H = 125.5$ GeV, the expected limit for $\mu = 1$.

4.10.2 Likelihood

The results are obtained using an unbinned maximum likelihood (ML) depending on a single observable x, $\ell\ell\gamma$ the invariant mass. We consider a single parameter of interest, the ratio μ given by Equation 4.8. In addition, the likelihood may depend on additional *nuisance* parameters θ, like the number of background events or the parameters of the probability distribution functions of the variable x for signal and background events. For some of these nuisance parameters, additional prior information may be available, for instance from theoretical calculations or from measurements performed in control samples; in that case, the corresponding probability density function for those parameters is incorporated into the full likelihood function.

The dataset is split into $n_{cat} = 10$ orthogonal categories c. The subscript c represents the quantity in each category. A simultaneous unbinned maximum likelihood fit to the distribution of x in all the categories is performed to extract the results. The full likelihood is:

$$L\left(\mu, \boldsymbol{\theta} = \bigcup_{c=1}^{n_{cat}} \boldsymbol{\theta}_c | \boldsymbol{x} = \bigcup \boldsymbol{x}_c\right) = \prod_{c=1}^{n_{cat}} L_c(\mu, \boldsymbol{\theta}_c|\boldsymbol{x}_c) \tag{4.15}$$

L_c is the likelihood for category c:

$$L_c(\mu, \boldsymbol{\theta}_c|\boldsymbol{x}_c) = e^{-N'_c} {N'_c}^{N_c} \prod_{k=1}^{N_c} \mathcal{L}_c(x_k|\mu, \boldsymbol{\theta}_c) \tag{4.16}$$

where N_c is the number of selected events, x_k is the value of x measured in event k, $N_{\text{signal},c}$ and $N_{\text{bkg},c}$ are the numbers of signal and background events, and $N'_c = (N_{\text{signal},c} + N_{\text{bkg},c})$ (each quantity refers to category c). $e^{-N'_c} {N'_c}^{N_c}$ is a Poisson probability factor for $N'_c =$

$N_{\text{signal},c} + N_{\text{bkg},c}$. $\mathcal{L}_c(x_k|\mu, \boldsymbol{\theta}_c)$ is the per-event likelihood:

$$\mathcal{L}_c(x|\mu, \boldsymbol{\theta}_c) = \frac{N_{\text{signal},c}(\mu, \boldsymbol{\theta}_c^{norm})}{N_{\text{signal},c} + N_{\text{bkg},c}} f_{\text{signal},c}(x|\boldsymbol{\theta}_c^{shape}) + \frac{N_{\text{bkg},c}}{N_{\text{signal},c} + N_{\text{bkg},c}} f_{\text{bkg},c}(x|\boldsymbol{\theta}_c^{bkg}) \tag{4.17}$$

$f_{\text{signal},c}$ and $f_{\text{bkg},c}$ are the signal and background probability density functions for category c, and $\boldsymbol{\theta}_c^{norm}$, $\boldsymbol{\theta}_c^{shape}$ and $\boldsymbol{\theta}_c^{bkg}$ are the nuisance parameters used in the description of respectively the expected signal yield, the signal PDF and the background PDF. The full set of nuisance parameters for each category c can thus be identified as $\boldsymbol{\theta}_c = \boldsymbol{\theta}_c^{norm} \cup \boldsymbol{\theta}_c^{shape} \cup \boldsymbol{\theta}_c^{bkg} \cup \{N_{\text{bkg},c}\}$.

The number of signal events in category c is written as

$$\begin{aligned} N_{\text{signal},c}(\mu, \boldsymbol{\theta}_c^{norm}) = \mu \times [&N_{\text{gg},c}^{SM}(\boldsymbol{\theta}^{gg}) + N_{\text{VBF},c}^{SM}(\boldsymbol{\theta}^{VBF}) + N_{\text{WH},c}^{SM}(\boldsymbol{\theta}^{WH}) \\ &+ N_{\text{ZH},c}^{SM}(\boldsymbol{\theta}^{ZH}) + N_{\text{ttH},c}^{SM}(\boldsymbol{\theta}^{ttH})] \times f(\boldsymbol{\theta}_{\varepsilon,BF}) \end{aligned} \tag{4.18}$$

where $N_{i,c}^{SM}(\boldsymbol{\theta}^i)$ $(i = gg, VBF, WH, ZH, ttH)$ is the number of expected SM $H \to Z\gamma$ decays in the category c of the selected sample, in which the Higgs boson is produced by the process i (see Equation 4.3), $\boldsymbol{\theta}^i$ is the set of (nuisance) parameters on which the theoretical production cross section σ_i depends, and $f(\boldsymbol{\theta}_{\varepsilon,BF})$ is a function of additional nuisance parameters which account for the uncertainties on the $H \to Z\gamma$ branching fraction and on the selection efficiencies.

4.10.3 Systematic uncertainties and nuisance parameters

Systematic uncertainties are evaluated by introducing in the full likelihood a nuisance parameter θ for each source of uncertainty, so that the signal and background expectations (yields or parameters of the model) become functions of θ. The likelihood is then multiplied by a "constraint" term, which exploits the best estimate that we have of each systematic uncertainty. The nuisance parameters are then fitted ("profiled") to the data, together with the parameters of interest (μ), when minimizing $-\log L$. Typically the constraint is either a Gaussian or a Log-normal function of the nuisance parameter. For systematic uncertainties affecting the expected yields, the log-normal form is preferred in order to avoid the negative tails of the Gaussian distribution, while for uncertainties on shape parameters of migrations between categories, a Gaussian constraint is used. For a systematic uncertainty for which a Gaussian constraint is assumed, the quantity in the likelihood affected by this uncertainty is multiplied by a term of the form

$$(1 + \sigma\theta) \tag{4.19}$$

and the likelihood is multiplied by $G(\theta)$, where θ is the nuisance parameter, G is a normal distribution with width equal to unity and centered at zero, and σ is the "best estimate" of the relative uncertainty as obtained for instance from the simulation. For a systematic uncertainty for which a log-normal constraint is used instead, the quantity in the likelihood affected by the uncertainty is multiplied by a term of the form:

$$e^{\sqrt{\log(1+\sigma^2)}\theta} \tag{4.20}$$

and the likelihood itself is multiplied by $G(\theta)$. This means that the logarithm of the quantity $e^{\sqrt{\log(1+\sigma^2)}\theta}$ has a Gaussian PDF with mean 0 and width equal to one. In a few cases where the uncertainty is asymmetric, an asymmetric Gaussian is used as constraint.

The theoretical uncertainties affecting the calculations of the Higgs production cross sections are accounted for by using log-normal constraints for the scale uncertainties and Gaussian constraints for the uncertainties arising from the variations of the PDF set's eigenvalues. The expected yields are then rewritten as:

$$\begin{aligned}
N^{SM}_{\mathrm{gg},c}(\boldsymbol{\theta}^{gg}) &= N^{SM}_{\mathrm{gg},c}\exp(\sqrt{\log(1+\sigma^2_{gg_scale})}\theta_{gg_scale})(1+\sigma_{gg_PDF,gg}\theta_{gg_PDF}) \\
N^{SM}_{\mathrm{VBF},c}(\boldsymbol{\theta}^{VBF}) &= N^{SM}_{\mathrm{VBF},c}\exp(\sqrt{\log(1+\sigma^2_{VBF_scale})}\theta_{VBF_scale})(1+\sigma_{q\bar{q}_PDF,VBF}\theta_{q\bar{q}_PDF}) \\
N^{SM}_{\mathrm{WH},c}(\boldsymbol{\theta}^{WH}) &= N^{SM}_{\mathrm{WH},c}\exp(\sqrt{\log(1+\sigma^2_{WH_scale})}\theta_{WH_scale})(1+\sigma_{q\bar{q}_PDF,WH}\theta_{q\bar{q}_PDF}) \\
N^{SM}_{\mathrm{ZH},c}(\boldsymbol{\theta}^{ZH}) &= N^{SM}_{\mathrm{ZH},c}\exp(\sqrt{\log(1+\sigma^2_{ZH_scale})}\theta_{ZH_scale})(1+\sigma_{q\bar{q}_PDF,ZH}\theta_{q\bar{q}_PDF}) \\
N^{SM}_{\mathrm{ttH},c}(\boldsymbol{\theta}^{ttH}) &= N^{SM}_{\mathrm{ttH},c}\exp(\sqrt{\log(1+\sigma^2_{ttH_scale})}\theta_{ttH_scale})(1+\sigma_{gg_PDF,ttH}\theta_{gg_PDF}) \quad (4.21)
\end{aligned}$$

and the likelihood is multiplied by

$$G(\theta_{gg\_scale})G(\theta_{VBF\_scale})G(\theta_{WH\_scale})G(\theta_{ZH\_scale})G(\theta_{ttH\_scale})G(\theta_{gg\_PDF})G(\theta_{q\bar{q}\_PDF}) \quad (4.22)$$

The ten uncertainties (σ_{i_scale} and σ_{i_PDF}) are described by only 7 nuisance parameters because the PDF uncertainties for the gluon initiated processes, gluon-fusion and the $t\bar{t}H$, are correlated and shared the same nuisance parameter. Similarly, the VBF, WH and ZH processes originate from $q\bar{q}$ interactions and therefore their uncertainties are correlated and a single nuisance parameter $\theta_{q\bar{q}\_PDF}$ describes the PDF uncertainty on $N^{SM}_{\mathrm{VBF},c}$, $N^{SM}_{\mathrm{WH},c}$ and $N^{SM}_{\mathrm{ZH},c}$.

To take into account experimental systematic uncertainties, the expected signal yield (Equation 4.18) includes a factor

$$\begin{aligned}
f(\boldsymbol{\theta}_{\epsilon,BF}) = {} & \exp(\sqrt{\log(1+\sigma^2_{lumi})}\theta_{lumi}) \times \\
& \exp(\sqrt{\log(1+\sigma^2_{trig})}\theta_{trig}) \times \\
& \exp(\sqrt{\log(1+\sigma^2_{generator})}\theta_{generator}) \times \\
& \exp(\sqrt{\log(1+\sigma^2_{\gamma-ID})}\theta_{\gamma-ID}) \times \\
& \exp(\sqrt{\log(1+\sigma^2_{lepton-ID})}\theta_{lepton-ID}) \times \\
& \exp(\sqrt{\log(1+\sigma^2_{e\gamma-ES})}\theta_{e\gamma-ES}) \times \\
& \exp(\sqrt{\log(1+\sigma^2_{e\gamma-ISO})}\theta_{e\gamma-ISO}) \times \\
& \exp(\sqrt{\log(1+\sigma^2_{e\gamma-smear})}\theta_{e\gamma-smear}) \quad (4.23) \\
& \exp(\sqrt{\log(1+\sigma^2_{HpT-migration})}\theta_{HpT-migration}) \quad (4.24)
\end{aligned}$$

where the uncertainties σ_j are those described in Section 4.9.2 and summarized in Tables 4.6 and 4.7 of Section 4.9.1.

The spurious signal systematic uncertainty is included in the model by adding to the expected signal yield $N_{\mathrm{signal},c}(\mu, \boldsymbol{\theta}^{norm}_c)$ a term

$$\sigma_{spurious,c}\theta_{spurious,c}, \quad (4.25)$$

multiplying the likelihood by $G(\theta_{spurious,c})$ and profiling the nuisance parameter $\theta_{spurious,c}$.

As for the other ATLAS Higgs searches, all systematic uncertainties except the luminosity ones are considered fully correlated between 2011 and 2012.

4.10.4 Number of free parameters

In summary, the model includes 8 nuisance parameters describing theory uncertainties (5 for the scales, 2 for PDFs, 1 for the $H \to Z\gamma$ branching fraction), 14 for experimental uncertainties, and 2 for the spurious signal terms. Counting the background normalization parameters (10 parameters) and the background shape parameters (32 in total for the $m_{\ell\ell\gamma}$ fit), one gets a grand total of 64 nuisance parameters for the model. Together with the parameter of interest μ, they form the total set of free parameters in the fit.

4.11 Exclusion Limits and p-values

The compatibility between the data and the background-only hypothesis is tested by computing the p_0. The expected and observed p_0 values are shown in Figure 4.21 as a function of the Higgs boson mass. The expected p_0 ranges between 0.34 and 0.44 for $120 < m_H < 150$ GeV, corresponding to significances around 0.2 σ. The maximum observed p_0 is 0.05 (1.6 σ), for a mass of 141 GeV. The expected p_0 at $m_H = 125.5$ GeV is 0.42, corresponding to a significance of 0.2 σ, while the observed p_0 is 0.27 which corresponds to a significance of 0.6 σ. The observed p_0 values in the 10 cateogries are shown in Figure 4.22.

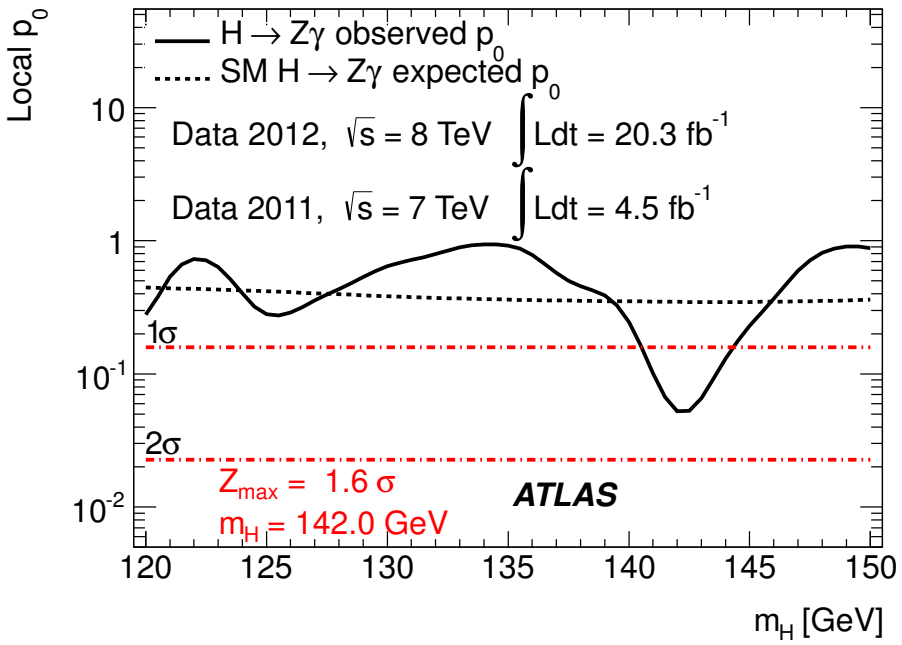

Figure 4.21 – Expected (dashed blue line) and observed (solid black line) p_0 (compatibility of the data with the background-only hypothesis) as a function of the Higgs boson mass, using 4.5 fb^{-1} of pp collisions at $\sqrt{s} = 7$ TeV and 20.3 fb^{-1} of pp collisions at $\sqrt{s} = 8$ TeV.

Since no significant signal is observed, upper limits are set on its measured production cross section, normalized to the SM expected one. The observed and median expected limit with 1σ and 2σ uncertainty bands are illustrated in Figure 4.23. The expected 95% CL limit ranges between 5.2 and 15.5 and the observed limit varies between 3.5 and 18.5 for a Higgs boson mass between 120 and 150 GeV. In particular, for a mass of 125.5 GeV, corresponding to the mass of the recently discovered Higgs boson-like particle,

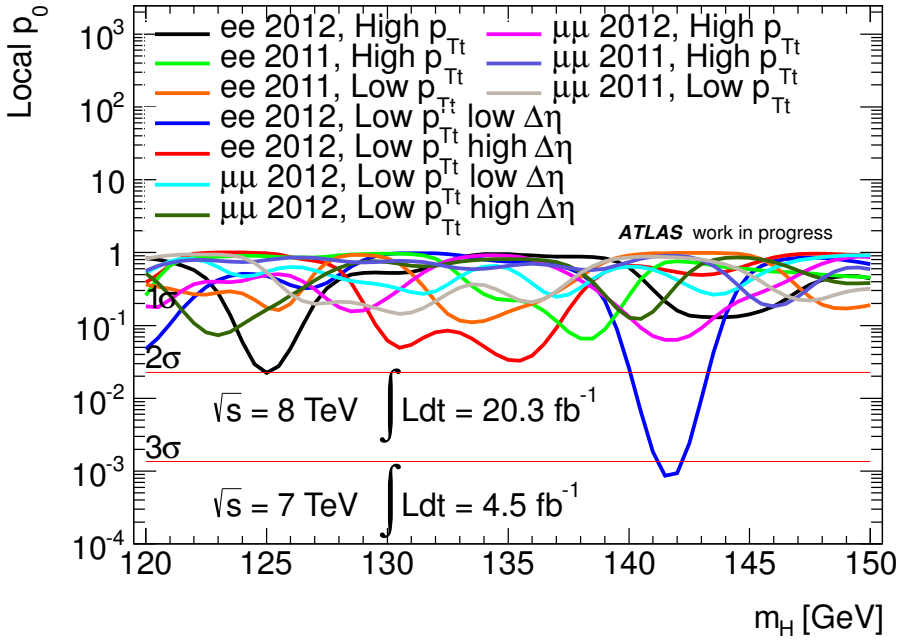

Figure 4.22 – Observed p_0 in 10 categories as a function of the Higgs boson mass, using 4.5 fb^{-1} of pp collisions at $\sqrt{s} = 7$ TeV and 20.3 fb^{-1} of pp collisions at $\sqrt{s} = 8$ TeV.

the expected and observed limits are 9.0 and 11.3 times the Standard Model prediction, respectively. The results are dominated by the statistical uncertainties: the expected limit when removing all the systematic uncertainties decreases by about half times the Standard Model cross section. The upper limit on Higgs production times branching ratio of H→ $Z\gamma$ are also set separately at $\sqrt{s} = 7$ TeV and 8 TeV with the theoretical uncertainty on the cross section and branching ratio excluded, as shown in Figure 4.24.

A compatible results were obtained from a similar study in the CMS experiment, using full run-I data set corresponding to integrated luminosities of 5.0 fb^{-1} at $\sqrt{s} = 7$ TeV and 19.6 fb^{-1} [117]. The limits are calculated in the 120−160 GeV mass range. The expected exclusion limits at 95% confidence level (CL) are between 5 and 16 times the SM cross section and the observed limit ranges between about 4 and 25 times the SM cross section. The observed and expected limits for $m_{\ell\ell\gamma}$ at 125 GeV are within one order of magnitude of the SM prediction.

We have also evaluated the expected p_0 and limit on the cross section using an Asimov dataset corresponding to a 1 times Standard Model signal injection at 125.5 GeV. They are shown in Figures 4.25 and 4.26. The expected upper limit at $m_H = 125.5$ GeV for $\mu = 1$ is 9.8 times the SM prediction.

4.12 Conclusions and Prospects

A search for a Higgs boson in the decay channel $H \to Z\gamma$, $Z \to \ell\ell$ ($\ell = e, \mu$), in the mass range 120–150 GeV, was performed using 4.5 fb^{-1} of proton–proton collisions at $\sqrt{s} = 7$ TeV and 20.3 fb^{-1} of proton–proton collisions at $\sqrt{s} = 8$ TeV recorded with the ATLAS detector at the LHC. No excess with respect to the background is found in the $\ell\ell\gamma$ invariant-mass distribution and 95% $C.L.$ upper limits on the cross section times branching ratio are derived. For $\sqrt{s} = 8$ TeV, the limit ranges between 0.13 and 0.5 pb;

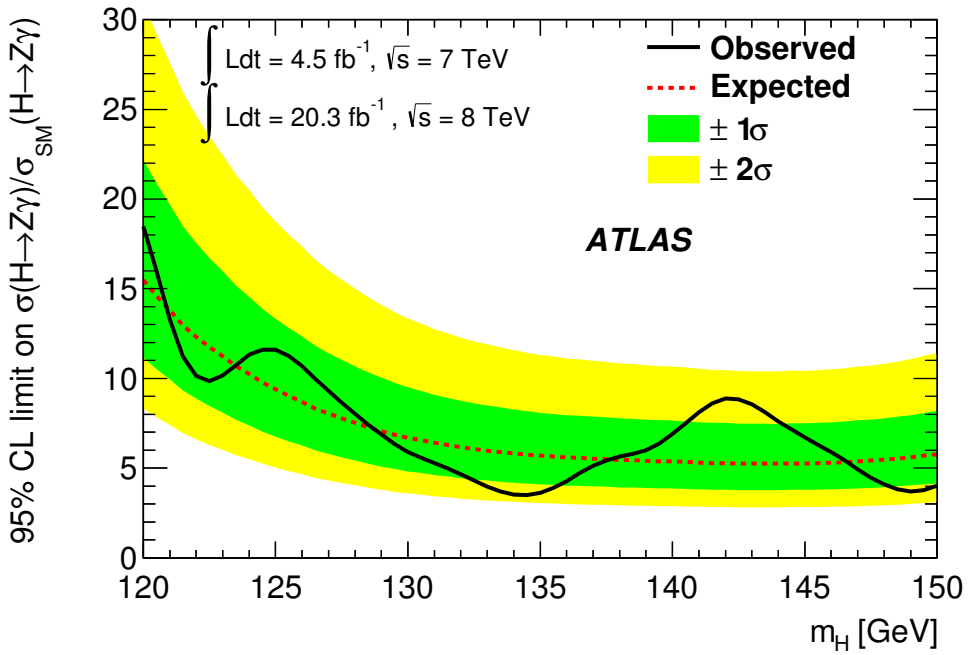

Figure 4.23 – Observed 95% *C.L.* limits (solid black line) on the production cross section of a SM Higgs boson decaying to $Z\gamma$ (normalized by SM expectation), as a function of the Higgs boson mass, using 4.5 fb^{-1} of pp collisions at $\sqrt{s} = 7$ TeV and 20.3 fb^{-1} of pp collisions at $\sqrt{s} = 8$ TeV. The median expected 95% *C.L.* exclusion limits (dashed red line) are also shown. The green and yellow bands correspond to the $\pm 1\sigma$ and $\pm 2\sigma$ intervals.

for $\sqrt{s} = 7$ TeV, the limit ranges between 0.2 and 0.8 pb. Combining $\sqrt{s} = 7$ and 8 TeV data after dividing the cross section by the Standard Model expectation, the limit ranges between 3.5 and 18.5. In particular, for a mass of 125.5 GeV, corresponding to the mass of the recently discovered Higgs boson-like particle, the expected and observed limits are 9.0 and 11.3 times the Standard Model prediction, respectively.

Based on the current analysis strategy, the prospects for the $H \to Z\gamma$ search have been studied, for an integrated luminosity of 3000 (300) fb^{-1} at $\sqrt{s} = 14$ TeV, assuming average pile-up corresponding to $\mu = 140$ ($\mu = 60$). The signals of the two main Higgs production processes (ggH, VBF) are generated with `POWHEG`, while the contributions from other processes (VH, ttH) are neglected. The $Z + \gamma$ background samples are generated at 14 TeV with `SHERPA`. The size of the background is evaluated by scaling the background from 8 TeV analysis by the $Z + \gamma$ continuum cross section ratio $\sigma^{Z\gamma}_{14\ TeV}/\sigma^{Z\gamma}_{8\ TeV} = 1.82$, and by factors to correct the difference of photon identification efficiency (63%), lepton identification efficiency (97%) and lepton trigger efficiency (97%) between the 14 TeV analysis and 8 TeV analysis. With 3000 fb^{-1} of integrated luminosity, for a mass of 125 GeV, the expected 95% *C.L.* limit on the production cross section times branching ratio is 0.52 times the SM expected one. The expected significance corresponds to 3.9 σ. The expected statistical (systematic) uncertainty on the signal strength is 0.26 (0.17), by assuming $\mu = 1$. With an integrated luminosity of 300 fb^{-1} at 14 TeV, the expected significance corresponds to 2.3 σ.

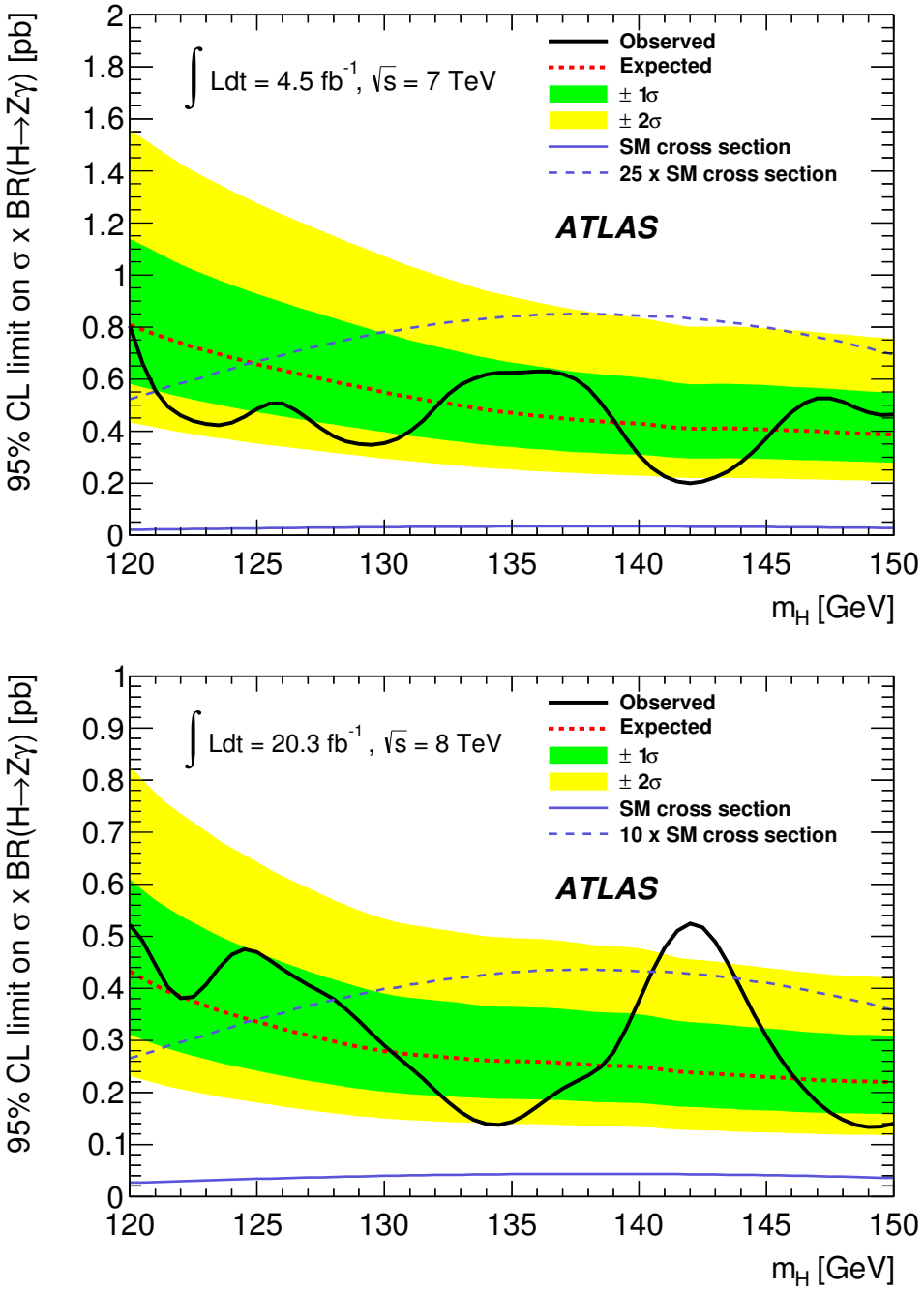

Figure 4.24 – Observed 95% *C.L.* limits (solid black line) on the production cross section of a Higgs boson decaying to $Z\gamma$, as a function of the Higgs boson mass, using 4.5 fb^{-1} of pp collisions at $\sqrt{s} = 7$ TeV (top) and 20.3 fb^{-1} of pp collisions at $\sqrt{s} = 8$ TeV (bottom). The median expected 95% *C.L.* exclusion limits (dashed red line) are also shown. The green and yellow bands correspond to the $\pm 1\sigma$ and $\pm 2\sigma$ intervals. The theoretical uncertainty on the cross section and branching ratio have been excluded.

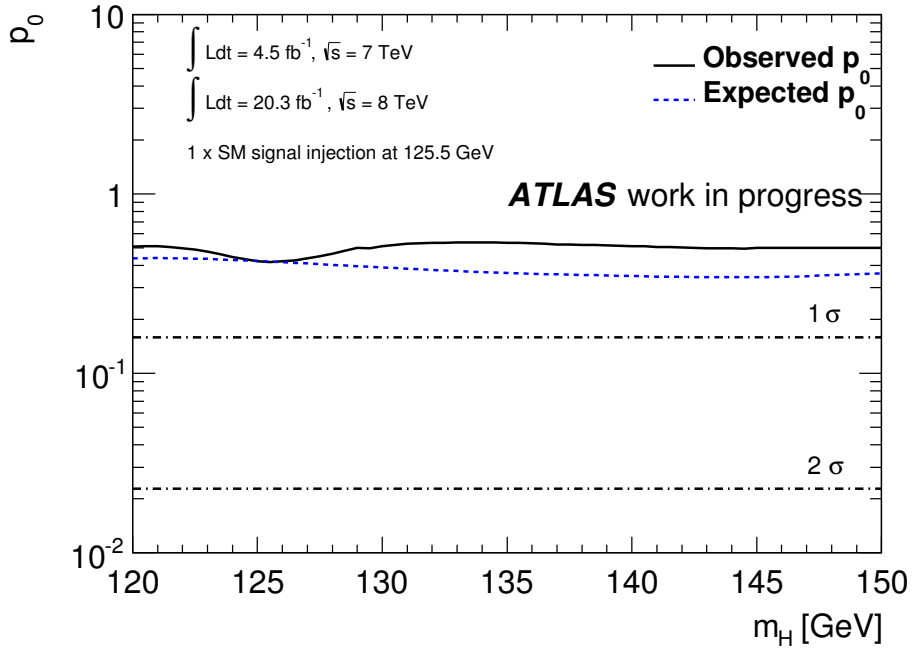

Figure 4.25 – Expected p_0 value with an Asimov dataset with $1\times$ SM signal injection for $m_H = 125.5$ GeV.

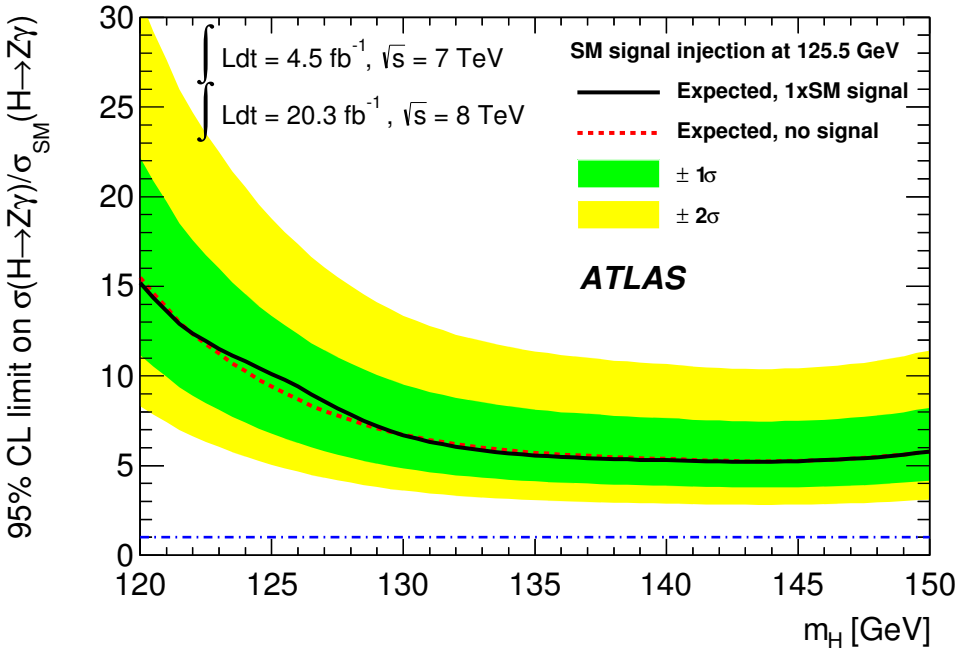

Figure 4.26 – Expected 95% CL limits on μ with $1\times$ SM signal injection for $m_H = 125.5$ GeV.

Chapter 5

Observation of the Higgs boson in $\gamma\gamma$ events

5.1 Introduction

The $H \to \gamma\gamma$ decay is one of the most important discovery channel for the Higgs boson search in the low mass range, $m_H < 150$ GeV. For $m_H = 125$ GeV, the SM $H \to \gamma\gamma$ production cross section times branching ratio is $\sigma \times BR = 39.56$ (50.45) fb at $\sqrt{s} =$ 7 TeV (8 TeV). The main backgrounds are expected to originate from $\gamma\gamma$ events from quark-antiquark annihilation ($q\bar{q} \to \gamma\gamma$), gluon fusion via a quark loop ($gg \to \gamma\gamma$), or parton-to-photon fragmentation in γ+jet events. Due to the misidentification of jets as photons, γ+jet, jet+γ and jet+jet events contribute to the background, too. They are suppressed by the photon identification and isolation requirements. Photons from $H \to \gamma\gamma$, with p_{T} of several tens of GeV and central pseudorapidity, can be reconstructed in the ATLAS detector with high efficiency and excellent energy resolution, and their invariant mass provides a powerful discriminate to separate the Higgs signal from the background remaining after the event selection.

The search for the Higgs boson decay to two photons is performed in ATLAS in the mass range between 110 GeV and 150 GeV. The first sensitivity studies on real data, based on 37 pb^{-1} of collisions collected at 7 TeV, were released in 2011 [118]. Based on the observed background level they predicted, for an integrated luminosity of 1 fb^{-1} at 7 TeV and a rather simple analysis, the possibility to exclude a Higgs boson produced with cross-sections at least 3.2–4.2 times larger than that of the SM in the 110-140 GeV mass range. During 2011 and 2012 the $H \to \gamma\gamma$ was continuously updated with the analysis of the additional data provided by the LHC and refinements to the selection strategy, better knowledge of the detector performance, and optimization of the signal-vs-background discrimination and classification [119, 120, 121, 122]. In May 2012, ATLAS had been able, using the $H \to \gamma\gamma$ channel, to reduce (at 95% confidence level) the allowed range for the mass of a SM Higgs boson to the intervals 117.5–118.5 GeV, 122.5–129.0 GeV and above 539 GeV [123]. On the 4th of July 2012, the ATLAS and CMS collaborations independently reported observations of a new particle that is compatible with the SM Higgs boson, using the data collected until the end of June 2012 [6, 7], through a combined analysis of the $H \to \gamma\gamma$, $H \to ZZ^* \to 4\ell$ and $H \to WW^* \to e\nu\mu\nu$ decays. In the $H \to \gamma\gamma$ channel only, an excess of events was observed by ATLAS with a local significance of 4.5 σ, based on 4.8 fb^{-1} of $\sqrt{s} = 7$ TeV and 5.9 fb^{-1} of $\sqrt{s} = 8$ TeV collision data [124].

The analysis shown in this chapter is obtained with the full run-I data set, with a combination of 4.8 fb^{-1} of data recorded at $\sqrt{s} = 7$ TeV and 20.7 fb^{-1} of data recorded

at $\sqrt{s} = 8$ TeV. The preliminary results were shown at the Moriond EW conference in February 2013 [125]. This chapter is organized as follows. Data and simulation samples are discussed in section 5.2. Event selection and categorization are discussed in section 5.3. The study of the data-driven background compositions is introduced in section 5.4. The modelling of the signal and background $m_{\gamma\gamma}$ distribution are reviewed in section 5.5. The systematic uncertainties are summarized in section 5.6. Finally, section 5.7 gives the results. The Higgs signal has been clearly observed and the observed event yield is compatible with the SM prediction.

5.2 Data and Simulation Samples

The data have been collected using the lowest-threshold unprescaled di-photon trigger, `g35_loose_g25_loose`. The leading (sub-leading) trigger object is required to have $p_{\mathrm{T}} >$ 35 (25) GeV and to pass loose criteria on three shower shape variables (R_{had}, $w_{\eta 2}$, R_{η}). This trigger has a signal efficiency above 99% for events passing all the other selection criteria. Data taken during periods when the detector is not fully operational are excluded.

To study the characteristics of the signal events, Monte Carlo samples are produced using various events generators. The details of the simulation samples have been introduced in section 4.2 in chapter 4. The Higgs boson cross sections, branching ratios and their uncertainties are given there, too.

5.3 Event Selection and Category

Events with good data quality and collected using the di-photon trigger have always at least one reconstructed primary vertex. A precise location of the di-photon production vertex is necessary, for the precise measurement of the di-photon invariant mass ($m_{\gamma\gamma}$), as well as for the computation of track-based quantities (e.g. track isolation, selection of jets associated to the hard interaction). The determination of this vertex is based on a global likelihood estimation combining the following elements: the directions of flight of the photons as determined by the measurements using the longitudinal segmentation of the calorimeter, the average beam spot position, and the $\sum p_{\mathrm{T}}^2$ of the tracks associated with each reconstructed vertex. In the case of the $\sqrt{s} = 7$ TeV, the conversion vertex is also used in the likelihood for converted photons with tracks containing silicon hits. As shown in Fig. 5.1 (left), the mass resolution calculated from the vertex determined using the likelihood technique is much better than the one using the maximum of $\sum p_{\mathrm{T}}^2$. Fig. 5.1 (right) shows the efficiency of finding the correct primary vertex as a function of the number of reconstructed vertices in the event using different methods. The likelihood approach gives higher efficiency for high pileup condition.

In the off-line event selection, at least two photon candidates are required to pass tight identification criteria based on photon shower shape information deposited in the EMC. The two highest p_{T} photons are tagged as leading and sub-leading photons, and are required to have $p_{\mathrm{T}} > 40$ GeV and 30 GeV, respectively. Both photons have to be within the fiducial calorimeter region of $|\eta| <$2.37, excluding the barrel/end-cap transition region 1.37$< |\eta| <$1.56. In addition to the identification criteria, both photons are also required to be isolated in both the inner tracker and the calorimeter. The first is the scalar sum of the transverse momenta of all tracks with $p_{\mathrm{T}} > 1$ GeV in a cone of size $\Delta R = \sqrt{(\Delta\eta)^2 + (\Delta\phi)^2} = 0.2$ around each photon, and is required to be less than 2.6 GeV. Only tracks consistent with originating from the di-photon production vertex are used, and tracks associated to converted photon candidates are excluded. The second

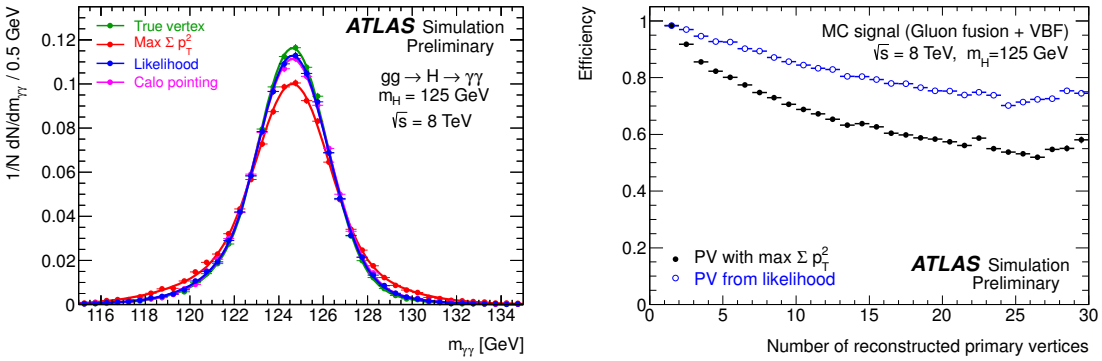

Figure 5.1 – Left: distribution of expected di-photon mas for $H \to \gamma\gamma$ signal events as a function of the algorithm used to determine the longitudinal vertex position of the hard-scattering event. Right: the dependence of the efficiency for selecting a reconstructed primary within Δz =0.2 mm of the true hard interaction vertex using two methods: the highest $\sum p_{\mathrm{T}}^2$ of all track assigned to a vertex (black) and from the likelihood as described in the text (blue).

variable is the transverse energy sum of positive-energy topological clusters [126] deposited in the calorimeter around each photon in a cone of $\Delta R = 0.4$, and is required to be less than 6 GeV. The energy sum excludes deposits in the core region of the photon shower, and corrections for the small estimated energy leakage outside this region are applied. The effects of the underlying event and of additional minimum bias interactions (pile-up) occurring in the same or neighbouring bunch crossings are corrected on an event-by-event basis [127, 128].

A total of 118893 (23788) collisions events at 8 TeV (7 TeV) are selected with di-photon invariant mass between 100 GeV and 160 GeV. To enhance the analysis sensitivity, the selected events are classified into categories with different invariant mass resolutions and different signal-to-background ratios.

5.3.1 Event categorisation at $\sqrt{s} = 7$ TeV

The selected events in 7 TeV data set are classified into 10 categories.

Firstly, a category of events enriched in VBF signal is selected exploiting the VBF signature, that consists of two forward jets, with little QCD radiation in the central region. These events are required to pass the following criteria:

- at least two hadronic jets with $|\eta^{\mathrm{jet}}| < 4.5$ and $p_{\mathrm{T}}^{\mathrm{jet}} > 25$ GeV. To suppress pile-up, jets in the tracker acceptance range ($|\eta| < 2.5$) are required to have a jet-vertex-fraction (JVF) of at least 0.75. The JVF is defined as the fraction of the sum of p_{T} carried by tracks in the jet and associated to the primary vertex selected with the likelihood method with respect to the total p_{T} carried by all the tracks associated to the jet [129]. The jets are required to pass jet quality cuts and to have a minimum distance $\Delta R = 0.4$ to any of the selected photons. Among the selected jets, the two jets with the highest p_{T} are considered as the tagging jets.
- The pseudorapidity difference between the tagging jets, $\Delta\eta_{jj}$, has to be larger than 2.8.
- The invariant mass of the tagging jets, m_{jj}, has to be larger than 400 GeV.

- The azimuthal angle difference $\Delta\phi$ between the di-photon system and the system of the two tagging jets has to be larger than 2.6.

For simulated VBF events, the efficiency of the 2-jets selection is 29%.

The remaining events are classified into 9 exclusive categories depending on the photon conversion status, pseudorapidity and the di-photon p_{Tt}. The 9 categories are the following:

- Unconverted central, low p_{Tt}: both photon candidates are reconstructed as unconverted photons and have $|\eta| < 0.75$. The di-photon system has $p_{\mathrm{Tt}} < 60$ GeV.
- Unconverted central, high p_{Tt}: both photon candidates are reconstructed as unconverted photons and have $|\eta| < 0.75$. The di-photon system has $p_{\mathrm{Tt}} > 60$ GeV.
- Unconverted rest, low p_{Tt}: both photon candidates are reconstructed as unconverted photons and at least one candidate has $|\eta| > 0.75$. The di-photon system has $p_{\mathrm{Tt}} < 60$ GeV.
- Unconverted rest, high p_{Tt}: both photon candidates are reconstructed as unconverted photons and at least one candidate has $|\eta| > 0.75$. The di-photon system has $p_{\mathrm{Tt}} > 60$ GeV.
- Converted central, low p_{Tt}: at least one photon candidate is reconstructed as converted photon and both photon candidates have $|\eta| < 0.75$. The di-photon system has $p_{\mathrm{Tt}} < 60$ GeV.
- Converted central, high p_{Tt}: at least one photon candidate is reconstructed as converted photon and both photon candidates have $|\eta| < 0.75$. The di-photon system has $p_{\mathrm{Tt}} > 60$ GeV.
- Converted rest, low p_{Tt}: at least one photon candidate is reconstructed as a converted photon and both photon candidates have $|\eta| < 1.3$ or $|\eta| > 1.75$, but at least one photon candidate has $|\eta| > 0.75$. The di-photon system has $p_{\mathrm{Tt}} < 60$ GeV.
- Converted rest, high p_{Tt}: at least one photon candidate is reconstructed as a converted photon and both photon candidates have $|\eta| < 1.3$ or $|\eta| > 1.75$, but at least one photon candidate has $|\eta| > 0.75$. The di-photon system has $p_{\mathrm{Tt}} > 60$ GeV.
- Converted transition: at least one photon candidate is reconstructed as a converted photon and at least one photon candidate is in the range $1.3 < |\eta| < 1.37$ or $1.52 < |\eta| < 1.75$.

5.3.2 Event categorisation at $\sqrt{s} = 8$ TeV

The higher statistics of the 8 TeV dataset allows us to increase the number of categories used in the event classification, with the addition of a few categories enhanced in VH signal, so that the signal strengths in gluon-fusion, VBF and associated-production modes can be fitted separately. The classification is based on the properties of the di-photon system as well as on the presence or absence of additional objects in the final states:

- Leptons: electrons with transverse energy greater than 15 GeV and $|\eta| < 2.47$, or muons with transverse momentum greater than 10 GeV and $|\eta| < 2.7$. Electrons must pass the identification criteria based on the electromagnetic shower shapes and track quality [40]. The track-isolation (in a cone size of 0.2) divided by the total muon p_{T} (electron E_{T}) is required to be less than 0.15 and the calorimetric isolation (in a cone size of 0.4) divided by the total muon p_{T} (electron E_{T}) is

required to be less than 0.2.

- Jets: jet candidates with transverse energy greater than 25 GeV (30 GeV) for $|\eta| < 2.4$ ($2.4 \leq |\eta| < 4.5$). The JVF is required to be greater than 0.25. To prevent potential double-counting, electrons overlapping with one of the two selected photons within a cone of $\Delta R(e,\gamma) = \sqrt{\Delta\eta^2 + \Delta\varphi^2} < 0.4$, jets within $\Delta R(\text{jet}, e) < 0.2$ or $\Delta R(\text{jet}, \gamma) < 0.4$, and muons within a cone of $\Delta R(\mu, \text{jet}) < 0.4$ or $\Delta R(\mu, \gamma) < 0.4$ are removed.
- Missing transverse energy: the E_{T}^{miss} significance, defined as $E_{\mathrm{T}}^{miss}/\sigma_{E_{\mathrm{T}}^{miss}}$, is used instead of a direct E_{T}^{miss} requirement in order to better reject multijet events where the E_{T}^{miss} arises from energy resolution effects, while still retaining high efficiency for signal events with E_{T}^{miss} coming from particles which do not interact with the detector.

The selected events in 8 TeV data are classified into 14 categories according to the order shown in Figure 5.2 and described here:

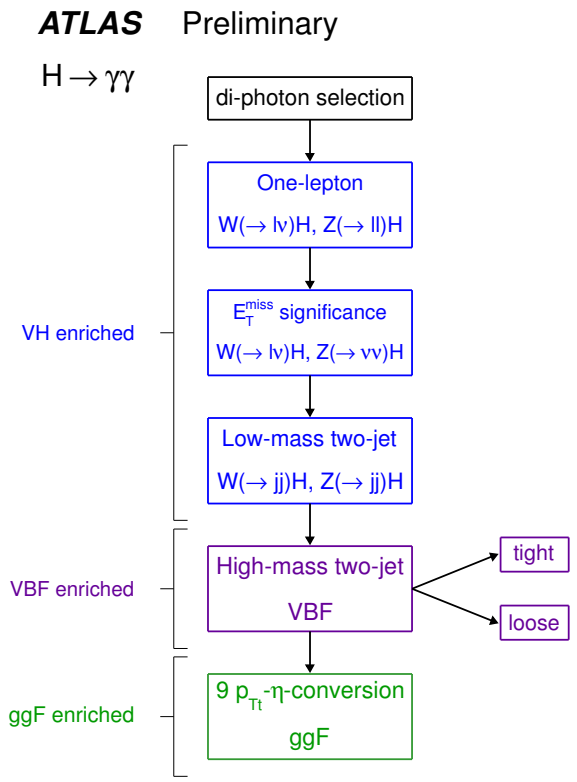

Figure 5.2 – Flow-chart of the event categorisation, giving the order of selection of the different categories.

- One-lepton category: events contain (at least) one lepton. These events are enriched in VH signal in which the vector boson V decays leptonically. To reduce the background from $Z(\rightarrow ee)\gamma$ where one of the two electrons is mis-identified as a photon, events having $84 < m_{\gamma e} < 94$ GeV are vetoed, where $m_{\gamma e}$ is the reconstructed invariant mass of the leading electron and one of the two photons.

Figure 5.3 shows the $m_{\gamma e}$ distributions from the VH processes and from data (background enriched). A significant $m_{\gamma e}$ peak in data from $Z(\to ee)\gamma$ events before the $m_{\gamma e}$ veto is observed. In addition, if one of the selected photons passes the electron identification requirements, the event is vetoed to reject the background from electroweak processes, like $W(\to e\nu)\gamma$, in which the electron is misidentified as a photon.

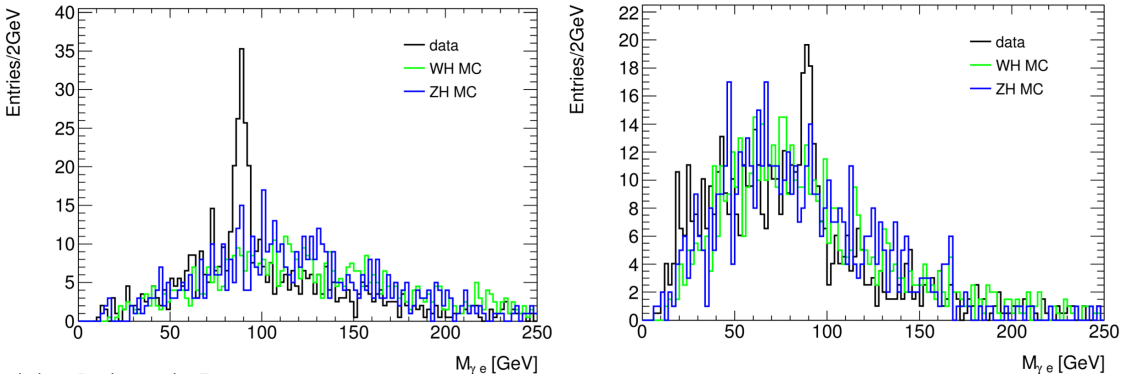

Figure 5.3 – $m_{\gamma e}$ distributions from the simulated VH processes and from the selected events in data (background enriched). Left: $m_{\gamma e}$ is reconstructed from the leading electron and the leading photon; Right: $m_{\gamma e}$ is reconstructed from the leading electron and the sub-leading photon.

- E_{T}^{miss} category: events must have an E_{T}^{miss} significance greater than 5. This corresponds to $E_{\mathrm{T}}^{miss} > 70$–$100$ GeV depending on $\sum E_{\mathrm{T}}$. This category is enriched in signal VH events in which the vector boson decays to final states with neutrinos ($Z \to \nu\nu$, or $W \to \ell\nu$ and the lepton does not pass the requirements of the lepton category). Events with at least one of the two photons passing the electron selection are vetoed to reject electroweak background.
- Low-mass two-jet category: events are required to contain two reconstructed jets with invariant mass in the range of 60–110 GeV and a pseudorapidity separation between the two jets of less than 3.5 units. The difference between the pseudorapidities of the di-photon and the di-jet systems has to be lower than 1. In addition, the p_{Tt} is required to be greater than 70 GeV. These events are enriched in VH signal with the vector boson decaying hadronically.
- High-mass two-jet categories: events enriched in VBF signal are selected based on the value of a multivariate discriminant exploiting the full event topology and the correlations of jets and photons kinematic quantities in VBF signal and in other signal production modes and backgrounds. The multivariate discriminant is a boosted-decision tree (BDT) [130], based on the following eight discriminating variables:
  — the invariant mass of the two leading jets m_{jj};
  — the two jets pseudorapidity η_{j1} and η_{j2};
  — the two jets pseudorapidity separation $\Delta\eta_{jj}$;
  — the p_{Tt} of the di-photon system;
  — the azimuthal angle difference between the di-photon and the di-jet systems $\Delta\phi_{\gamma\gamma,jj}$;
  — the di-photon system pseudorapidity with respect to the center of the two tag-

ging jet, defined as $\eta^* = \eta_{\gamma\gamma} - \frac{\eta_{j1}+\eta_{j2}}{2}$ [131];

— the minimal ΔR between one of the two photons and one of the two leading jets $\Delta R^{\gamma j}_{\rm min}$.

For the BDT training, we use simulated $\gamma\gamma$ events produced with the SHERPA generator, while γ + jet and jet + γ components are extracted in data sideband regions by reversing the sub-leading photon and leading photon isolation criteria. They are weighted according to the background composition fractions measured in data as described in the next section. Fig. 5.4 shows the validation of the BDT inputs in the left plot and the output of the BDT response in the right plot. Two categories are defined according to the BDT output value, leading to tight (BDT ≥ 0.74) and loose ($0.44 <$ BDT < 0.74) high-mass two-jet categories.

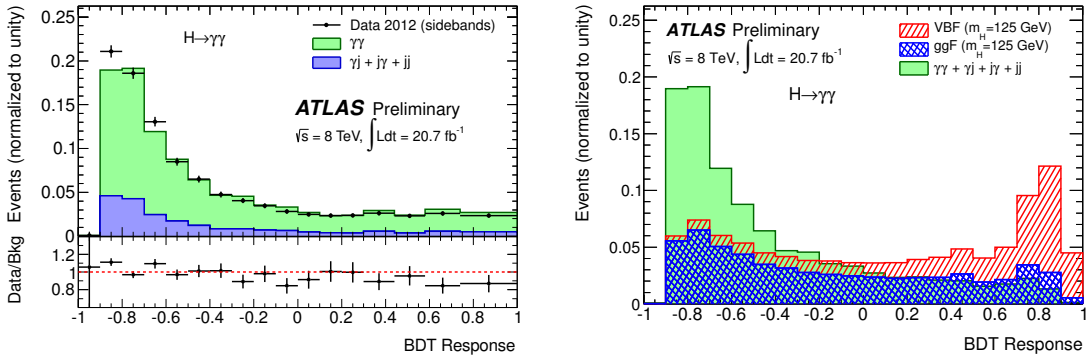

Figure 5.4 – Left: the response of the VBF BDT to the data in the signal sidebands, *i.e.* excluding events with $m_{\gamma\gamma}$ in the interval [120-130] GeV, and to the expected background after selection cuts, normalized to unity. Right: the response of the VBF BDT to the VBF signal sample, to the gluon-fusion signal sample, and to the expected background after selection cuts, normalized to unity.

- Other categories: the remaining events, enriched in signal produced by gluon fusion, are classified into 9 categories with different invariant mass resolution and S/B based on photon conversion status, calorimeter pseudorapidity and $p_{\rm Tt}$, similarly to the 7 TeV data.

The expected signal compositions from the various production processes for the 8 TeV categories at $m_H = 126.5$ GeV is illustrated in Fig. 5.5.

5.4 Data-driven Background Estimation

The main background in the $H \to \gamma\gamma$ search can be divided into two classes: irreducible background ($\gamma\gamma$) from QCD di-photon production, and reducible background (γ+jet, di-jet) in which one or two hadronic jets are misidentified as prompt photons. The reducible background has production cross-section significantly larger than the irreducible one ($\mathcal{O}(\alpha_s/\alpha)$ for γ+jet and $\mathcal{O}(\alpha_s^2/\alpha^2)$ for di-jet), but it is suppressed by the photon identification and isolation requirements. Finally, a small ($\approx 1\%$) contribution to the background arises from Drell-Yan production of an e^+e^- pair when both electrons are misidentified ad photons. Though the background composition is not an information used in the final fit to discriminate the signal from the background, the relative fractions of the different background sources are used in the optimization studies of the selection

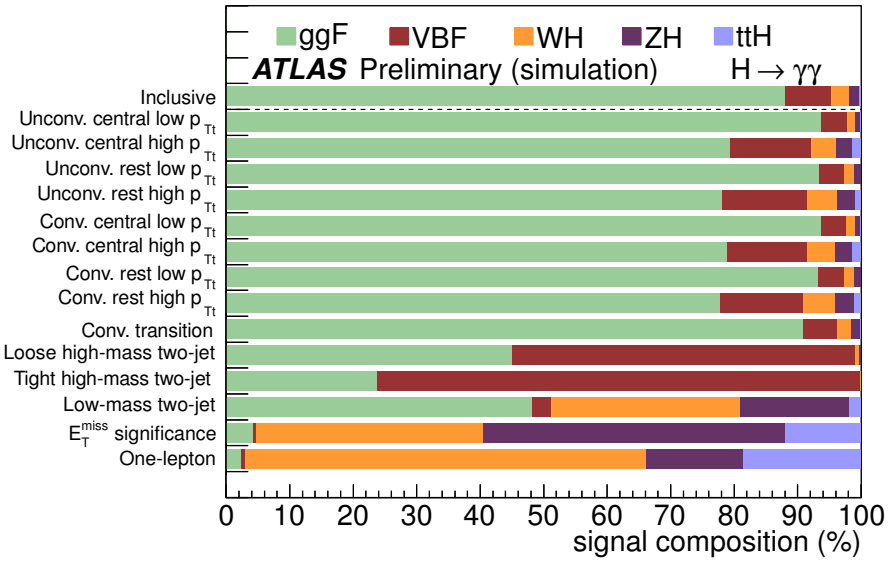

Figure 5.5 – Decompositions of the expected signal from various production processes for each category at $m_H = 126.5$GeV for $\sqrt{s} = 8$ TeV.

and of the BDT training for the VBF-enriched event categories, as well as in studies of the possible bias (spurious signal) on the fitted signal yield performed on background-only simulated samples. For these reasons it is important to have a precise knowledge of the background composition. Several data-driven methods, developed for the SM di-photon cross section measurements [132, 133], have been used to determine the composition of the selected data sample [134]. They yield consistent results within their uncertainties. The two-dimensional isolation fit method is described in the following.

The fractions of all components are extracted from an extended maximum likelihood fit to the two-dimensional transverse isolation energies ($E_{\mathrm{T},1}^{\mathrm{iso}}$, $E_{\mathrm{T},2}^{\mathrm{iso}}$) of the two photon candidates. The isolation template histograms are built in the [-5, 8] GeV isolation energy regions. The data distribution is fit with the sum of four components ($\gamma+\gamma$, γ+jet, jet+γ, jet+jet):

$$W_{\mathrm{tot}}^{\mathrm{TT}} F_{\mathrm{tot}}^{\mathrm{TT}} = W_{\gamma\gamma}^{\mathrm{TT}} F_{\gamma\gamma}^{\mathrm{TT}} + W_{\gamma j}^{\mathrm{TT}} F_{\gamma j}^{\mathrm{TT}} + W_{j\gamma}^{\mathrm{TT}} F_{j\gamma}^{\mathrm{TT}} + W_{jj}^{\mathrm{TT}} F_{jj}^{\mathrm{TT}}, \tag{5.1}$$

where $W_{\mathrm{tot}}^{\mathrm{TT}}$($W_{\gamma\gamma}^{\mathrm{TT}}$, $W_{\gamma j}^{\mathrm{TT}}$, $W_{j\gamma}^{\mathrm{TT}}$, W_{jj}^{TT}) represents the event yield and $F_{\mathrm{tot}}^{\mathrm{TT}}$ ($F_{\gamma\gamma}^{\mathrm{TT}}$, $F_{\gamma j}^{\mathrm{TT}}$, $F_{j\gamma}^{\mathrm{TT}}$, F_{jj}^{TT}) the probability density function (PDF) for all ($\gamma+\gamma$, γ+jet, jet+γ, jet+jet) events. The correlations between the isolation energies of the two photon candidates are checked in simulated events. They are found to be negligible for $\gamma+\gamma$, γ+jet, jet+γ events and thus their two-dimensional PDFs are factorized as a product of one-dimensional PDFs. For di-jet events, the correlation is not negligible and a two-dimensional isolation distribution is used. The fit function (5.1) is thus:

$$W_{\mathrm{tot}}^{\mathrm{TT}} F_{\mathrm{tot}}^{\mathrm{TT}} = W_{\gamma\gamma}^{\mathrm{TT}} F_{\gamma,1}^{T} F_{\gamma,2}^{T} + W_{\gamma j}^{\mathrm{TT}} F_{\gamma,1}^{T} F_{j,2}^{T} + W_{j\gamma}^{\mathrm{TT}} F_{j,1}^{T} F_{\gamma,2}^{T} + W_{jj}^{\mathrm{TT}} F_{jj}^{\mathrm{TT}} \tag{5.2}$$

where $F_{\gamma,1}^{T}$ and $F_{\gamma,2}^{T}$ are the one-dimensional leading and sub-leading photon isolation PDFs, and $F_{j,1}^{T}$ and $F_{j,2}^{T}$ are the one-dimensional leading and subleading jet isolation PDFs. The leading and subleading photon templates are extracted in simulated di-photon events. It is verified that the isolation distribution is similar for photons in $\gamma\gamma$ and γ+jet events.

The leading (sub-leading) jet template is extracted from the background control samples in data, from the leading (subleading) photon candidate passing the *loose'* identification criteria [1] but failing the tight criteria (denoted as $\tilde{\mathbf{T}}$) while the subleading (leading) photon candidate is required to pass the tight identification and isolation criteria (denoted as **TI**). The jet+jet two-dimensional PDF is extracted in data, by requiring both leading and subleading photon candidates to pass the loose' criteria but to fail the tight criteria. The signal leakage in the background control regions is taken into account in the following way. We use $F_{b,i}(i = 1, 2)$ and F_{bb} to denote the jet PDFs extracted from the background control sample. They can be written as functions of true jet and photon PDFs:

$$\begin{aligned} F_{b,i} &= (1-\alpha_i)F^T_{j,i} + \alpha_i F^T_{\gamma,i} && (5.3)\\ F_{bb} &= (1-\alpha'_1-\alpha'_2-\alpha'_3)F^{TT}_{jj} && (5.4)\\ &+ \alpha'_2 F^T_{\gamma,1}F^T_{j,2} \\ &+ \alpha'_1 F^T_{j,1}F^T_{\gamma,2} \\ &+ \alpha'_3 F^T_{\gamma,1}F^T_{\gamma,2} \end{aligned}$$

where α_1 (α_2) is the fraction of $\gamma\gamma$ events in the $\tilde{\mathbf{T}}\mathbf{TI}$ ($\mathbf{TI}\tilde{\mathbf{T}}$) sample. Similarly, α'_1 (α'_2, α'_3) is the fraction of jet+γ (jet+γ, $\gamma\gamma$) in the $\tilde{\mathbf{T}}\tilde{\mathbf{T}}$ sample. Using MC sample as input, the fractions read:

$$\alpha_1 = \frac{n^{\tilde{\mathbf{T}}\mathbf{TI}}_{\gamma\gamma,MC}}{n^{\mathbf{TT}}_{\gamma\gamma,MC}} \frac{W^{\mathbf{TT}}_{\gamma\gamma}}{n^{\tilde{\mathbf{T}}\mathbf{TI}}} \quad (5.5)$$

$$\alpha_2 = \frac{n^{\mathbf{TI}\tilde{\mathbf{T}}}_{\gamma\gamma,MC}}{n^{\mathbf{TT}}_{\gamma\gamma,MC}} \frac{W^{\mathbf{TT}}_{\gamma\gamma}}{n^{\mathbf{TI}\tilde{\mathbf{T}}}} \quad (5.6)$$

$$\alpha'_1 = \frac{n^{\tilde{\mathbf{T}}\tilde{\mathbf{T}}}_{\mathrm{j}\gamma,MC}}{n^{\mathbf{TT}}_{\mathrm{j}\gamma,MC}} \frac{W^{\mathbf{TT}}_{\mathrm{j}\gamma}}{n^{\tilde{\mathbf{T}}\tilde{\mathbf{T}}}} \quad (5.7)$$

$$\alpha'_2 = \frac{n^{\tilde{\mathbf{T}}\tilde{\mathbf{T}}}_{\gamma\mathrm{j},MC}}{n^{\mathbf{TT}}_{\gamma\mathrm{j},MC}} \frac{W^{\mathbf{TT}}_{\gamma\mathrm{j}}}{n^{\tilde{\mathbf{T}}\tilde{\mathbf{T}}}} \quad (5.8)$$

$$\alpha'_3 = \frac{n^{\tilde{\mathbf{T}}\tilde{\mathbf{T}}}_{\gamma\gamma,MC}}{n^{\mathbf{TT}}_{\gamma\gamma,MC}} \frac{W^{\mathbf{TT}}_{\gamma\gamma}}{n^{\tilde{\mathbf{T}}\tilde{\mathbf{T}}}} \quad (5.9)$$

$n^{XY}_{ij,MC}$ is the number of events of species ij in region $\mathbf{XY}$ as measured in the Monte Carlo, and $n^{\mathbf{XY}}$ is the number of events in region $\mathbf{XY}$ as measured in the data:

$$\begin{aligned} n^{\tilde{\mathbf{T}}\mathbf{TI}} &= \int F_{b,1}(E^{iso}_{T,1})dE^{iso}_{T,1} && (5.10)\\ n^{\mathbf{TI}\tilde{\mathbf{T}}} &= \int F_{b,2}(E^{iso}_{T,2})dE^{iso}_{T,2} && (5.11)\\ n^{\tilde{\mathbf{T}}\tilde{\mathbf{T}}} &= \int F_{bb}(E^{iso}_{T,1}, E^{iso}_{T,2})dE^{iso}_{T,1}dE^{iso}_{T,2} && (5.12) \end{aligned}$$

1. *loose'*: similar to the tight criteria but without F_{side}, $w_{\eta 1}$, ΔE and E_{ratio}

Finally, the w_{ij} coefficients can be written as a function of the event component yields:

$$
\begin{aligned}
w_{\gamma\gamma} &= W_{\gamma\gamma}^{\mathbf{TT}} \\
&\quad - \frac{\alpha'_3}{1-\alpha'_1-\alpha'_2-\alpha'_3} W_{jj}^{\mathbf{TT}} \\
&\quad - \frac{\alpha_2}{1-\alpha_2}\left(W_{\gamma \mathrm{j}}^{\mathbf{TT}} - \frac{\alpha'_2}{1-\alpha'_1-\alpha'_2-\alpha'_3} W_{jj}^{\mathbf{TT}}\right) \\
&\quad - \frac{\alpha_1}{1-\alpha_1}\left(W_{\mathrm{j}\gamma}^{\mathbf{TT}} - \frac{\alpha'_1}{1-\alpha'_1-\alpha'_2-\alpha'_3} W_{jj}^{\mathbf{TT}}\right) \qquad (5.13) \\
w_{\gamma \mathrm{j}} &= \frac{1}{1-\alpha_2}\left(W_{\gamma \mathrm{j}}^{\mathbf{TT}} - \frac{\alpha'_2}{1-\alpha'_1-\alpha'_2-\alpha'_3} W_{jj}^{\mathbf{TT}}\right) \\
w_{\mathrm{j}\gamma} &= \frac{1}{1-\alpha_1}\left(W_{\mathrm{j}\gamma}^{\mathbf{TT}} - \frac{\alpha'_1}{1-\alpha'_1-\alpha'_2-\alpha'_3} W_{jj}^{\mathbf{TT}}\right) \qquad (5.14) \\
w_{\mathrm{jj}} &= \frac{1}{1-\alpha'_1-\alpha'_2-\alpha'_3} W_{jj}^{\mathbf{TT}} \qquad (5.15)
\end{aligned}
$$

From the maximisation of the likelihood, one can directly extract the events of the four components ($W_{\gamma\gamma}^{\mathrm{TT}}, W_{\gamma \mathrm{j}}^{\mathrm{TT}}, W_{\mathrm{j}\gamma}^{\mathrm{TT}}, W_{jj}^{\mathrm{TT}}$) in the **TT** sample as well as – exploiting the knowledge of the partial integrals of the various PDFs in the isolation signal region – the events $W_{\gamma\gamma}^{\mathrm{TITI}}, W_{\gamma \mathrm{j}}^{\mathrm{TITI}}, W_{\mathrm{j}\gamma}^{\mathrm{TITI}}, W_{jj}^{\mathrm{TITI}}$ below the isolation cut (**TITI** sample).

The projections of the two-dimensional PDF fit for the leading and sub-leading photon candidates using 8 TeV data are shown in Fig. 5.6. The di-photon yield is then corrected to

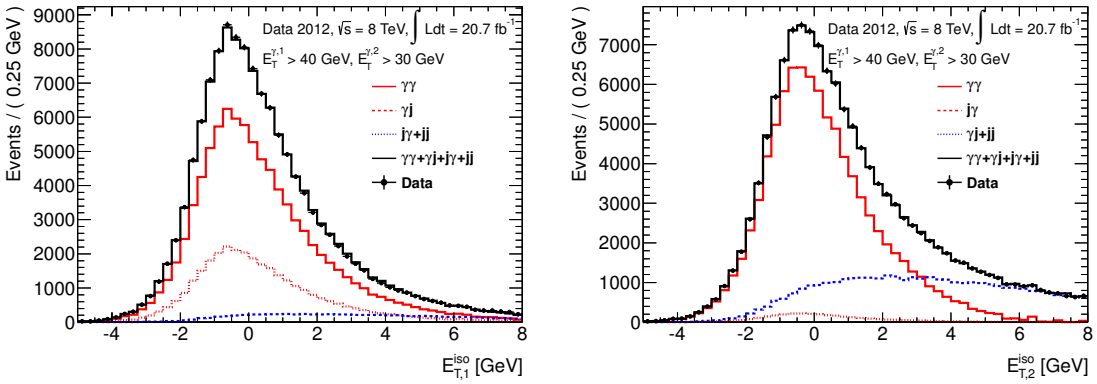

Figure 5.6 – Projections of the 2-dimensional PDF fit on transverse isolation energies of the two photon candidates: leading photon candidate (left) and sub-leading photon candidate (right).

subtract the small contribution from isolated electron pairs from Drell-Yan events, using the distribution of selected ee and $e\gamma$ events and the measured $e \to \gamma$ and $\gamma \to e$ fake rates. The resulting purity of di-photon events is found to be $(76^{+3}_{-4})\%$ ($(77^{+4}_{-3})\%$) for 8 TeV (7 TeV) data. Its uncertainty is estimated by repeating the template fit after changing the isolation range and using various loose' definitions to select the background-enriched regions in data (the default one is loose'-4). [2] [3] [4] [5].

2. loose'-2: similar to the tight criteria but without F_{side}, $w_{\eta 1}$
3. loose'-3: similar to the tight criteria but without F_{side}, $w_{\eta 1}$, ΔE
4. loose'-4: similar to the tight criteria but without F_{side}, $w_{\eta 1}$, ΔE, E_{ratio}
5. loose'-5: similar to the tight criteria but without F_{side}, $w_{\eta 1}$, ΔE, E_{ratio}, w_{tot1}

The background yields and fractions as a function of the reconstructed di-photon mass are estimated by repeating the isolation fit in 1 GeV-wide intervals of $m_{\gamma\gamma}$ between 100 and 160 GeV. The result is shown in Fig. 5.7.

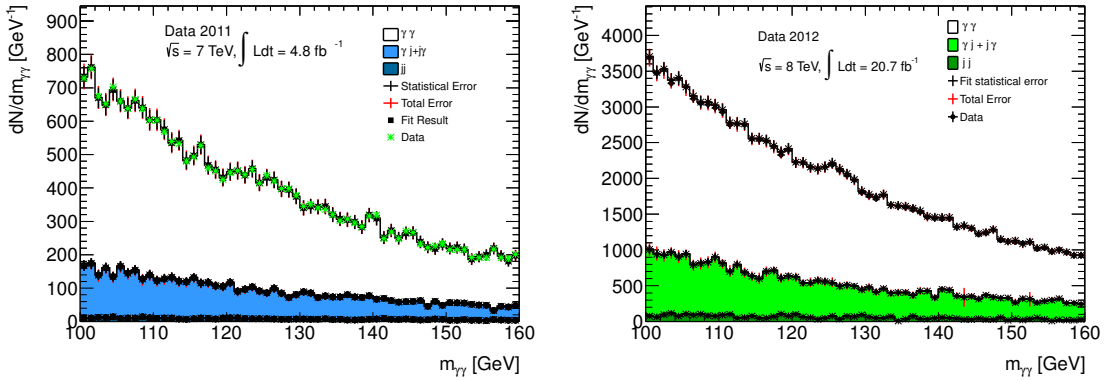

Figure 5.7 – Di-photon sample composition as a function of the invariant mass. Left: $\sqrt{s} = 7$ TeV. Right: $\sqrt{s} = 8$ TeV.

5.5 Signal and Background Modelling

The details of the Higgs boson signal sample simulation have been introduced in section 4.2 of Chapter 4. The Higgs boson production cross section, branching ratio as well as their uncertainties are also given there. The $H \to \gamma\gamma$ signal MC samples are generated in steps of 5 GeV for hypothetical Higgs boson masses between 100 and 150 GeV. A Crystal Ball plus a Gaussian function is used to describe the signal di-photon invariant mass distribution. The parameters of this function, as well as the signal yield, are parameterised as a function of hypothesised Higgs boson mass, and then a simultaneous fit to all signal MC samples is performed to interpolate the signal shape and signal yield for the intermediate mass points.

The background modelling is studied by performing a signal plus background fit to a background-only distribution. obtained by combining the γ-γ (`SHERPA`, `DIPHOX` [135], `MADGRAPH` [136]), γ-jet (`SHERPA`), jet-jet (`PYTHIA`) and Drell-Yan (`PYTHIA`) components according to their fractions determined from the data-driven background decomposition in section 5.4. A variety of functional forms are considered for the background parameterization. Parametrizations for which the estimated potential bias (called "spurious signal") is smaller than 20% of the uncertainty on the fitted signal yield or than 10% of the number of expected signal events for each tested Higgs boson mass are selected for further studies. Among these selected parametrizations, the one with the best expected sensitivity at $m_H = 125$ GeV is selected as the background parametrization. A summary of the chosen background models and of the expected signal and background yields in a small $m_{\gamma\gamma}$ interval in each of the 8 TeV categories for a Higgs boson mass of 126.5 GeV is given in Table 5.1.

The inclusive invariant mass distribution of the di-photon candidates for the combined $\sqrt{s} = 7$ TeV and $\sqrt{s} = 8$ TeV data sets is shown in Fig. 5.8 with overlaid signal-plus-background fit.

Table 5.1 – Signal mass resolution (σ_{CB}), number of observed events, number of expected signal events (N_S), number of expected background events (N_B) and signal to background ratio (N_S/N_B) in a mass window around $m_H = 126.5$ GeV containing 90% of the expected signal for each of the 14 categories of the 8 TeV data analysis. The numbers of background events are obtained from the background + signal fit to the $m_{\gamma\gamma}$ data distribution.

$\sqrt{s}$	8 TeV					
Category	$\sigma_{CB}(GeV)$	Observed	N_S	N_B	N_S/N_B	Background Model
Unconv. central, low p_{Tt}	1.50	911	46.6	881	0.05	Expo-pol 2
Unconv. central, high p_{Tt}	1.40	49	7.1	44	0.16	Exponential
Unconv. rest, low p_{Tt}	1.74	4611	97.1	4347	0.02	4th order pol.
Unconv. rest, high p_{Tt}	1.69	292	14.4	247	0.06	Exponential
Conv. central, low p_{Tt}	1.68	722	29.8	687	0.04	Expo-pol 2
Conv. central, high p_{Tt}	1.54	39	4.6	31	0.15	Exponential
Conv. rest, low p_{Tt}	2.01	4865	88.0	4657	0.02	4th order pol.
Conv. rest, high p_{Tt}	1.87	276	12.9	266	0.05	Exponential
Conv. transition	2.52	2554	36.1	2499	0.01	Expo-pol 2
Loose High-mass two-jet	1.71	40	4.8	28	0.17	Exponential
Tight High-mass two-jet	1.64	24	7.3	13	0.57	Exponential
Low-mass two-jet	1.62	21	3.0	21	0.14	Exponential
E_T^{miss} significance	1.74	8	1.1	4	0.24	Exponential
One-lepton	1.75	19	2.6	12	0.20	Exponential
Inclusive	1.77	14025	355.5	13280	0.03	4th order pol.

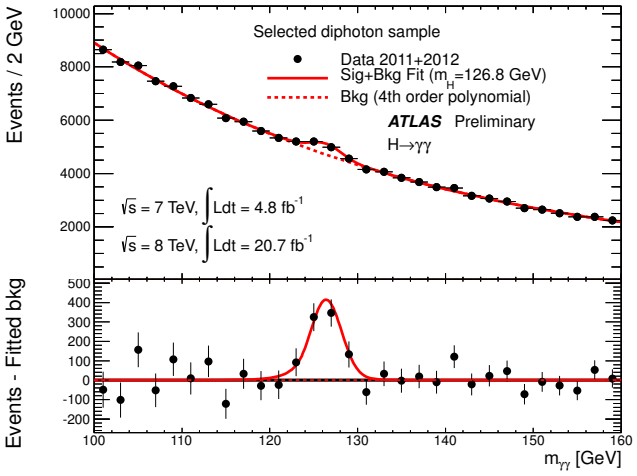

Figure 5.8 – Invariant mass distribution of di-photon candidates for the combined $\sqrt{s} = 7$ TeV and $\sqrt{s} = 8$ TeV data samples. The result of a fit to the data of the sum of a signal component fixed to $m_H = 126.8$ GeV and a background component described by a fourth-order polynomial is superimposed. The bottom inset displays the residuals of the data with respect to the fitted background component.

5.6 Systematic Uncertainties

Systematic uncertainties affect the expected signal yield, the signal resolution, the migration of events between categories and the signal mass measurement. All uncertainties are treated as fully correlated between 7 TeV and 8 TeV event categories except the one originating from the luminosity uncertainty.

5.6.1 Uncertainties on the signal yield

The following uncertainties affect signal yields of all event categories:

- The theoretical uncertainties of the Higgs boson production and branching ratio are provided in Ref. [76]. The theory uncertainties on the production cross section are given in Table 4.5. The uncertainty of $H \to \gamma\gamma$ branching ratio is 4.8% for $m_H = 126.5$ GeV.
- The uncertainty of the integrated luminosity is 3.6% (1.8%) for the 8 TeV (7 TeV) data.
- The uncertainty of the trigger photon efficiency is measured as described in section 3.1. It is 0.5% per event.
- The uncertainty of the off-line identification efficiency from the combination of the data-driven measurements described in section 3.3 is 2.4 % (8.4%) for the 8 TeV (7 TeV) data.
- The uncertainty on the isolation efficiency, estimated by comparing data and MC for $Z \to ee$ events, introduces an uncertainty of 1% on the event yield.
- The uncertainty of the photon energy scale leads to 0.25% uncertainty on the signal yield.

The theoretical uncertainty on the cross section of the $gg \to H$ production associated with two jets due to the missing higher order calculations has been determined based on the MCFM calculation [137, 138]. It leads to 48% and 28% uncertainty on the signal yield in the high-mass two-jet and low-mass two-jet category for 8 TeV data, respectively.

5.6.2 Uncertainties on the signal resolution

The uncertainties affecting the mass resolution are:

- The calorimeter energy resolution uncertainty together with the uncertainty arising from the extrapolation from the electron to photon response. It is found to be between 14% and 23% depending on the event category.
- Mis-modeling of the impact of pile-up on the resolution. It gives a 1.5% uncertainty.
- The uncertainty associated with the primary vertex selection is negligible (0.2%).

5.6.3 Events migration in categories

The following sources produce uncertainties in the fraction of events being classified in different categories (migration):

- The material mis-modelling: it produces a variation of -4% and $+3.5\%$ for unconverted and converted photon categories, respectively.

- Higgs boson kinematics: the uncertainties in the population of the p_{Tt} categories due to the modelling of the Higgs boson kinematics in the simulation amount to 1.1% in the low-p_{Tt} categories, 12.5% in the high-p_{Tt} categories, and 9% in the 2-jets category for 7 TeV data. For 8 TeV data, it has a 1.3% impact on the low-p_{Tt} categories, 10.2% on the high-p_{Tt} categories, 10.4%(8.5%) on the tight (loose) high-mass two-jet categories, 12.5% on the low-mass two-jet category, 2.0% on the E_{T}^{miss} category, and 4.0% on the one-lepton category.
- Jet energy scale and resolution: for 7 TeV data, the uncertainties of jet energy scale induce up to 19% uncertainty for the 2-jet category, and up to 4% for the other categories. For 8 TeV data, it induces an effect of up to 11.8% (10.7%) for the tight (loose) high-mass two-jet category, a 6.7% effect on the low-mass two-jet category and up to 0.7% for the other categories. The effect of jet energy resolution is found to be negligible for 7 TeV categories. At 8 TeV, its effect is at most 3.8% (3.4%) on the tight (loose) high-mass two-jet category, 3.4% on the low-mass two-jet category, and up to 0.9% on the other categories.
- Underlying event: the uncertainty due to the modelling of the underlying event is estimated by comparing simulations with and without multi-parton interaction (MPI). For the 2-jet category in 7 TeV data, it is at the level of 30% for gluon fusion and associated production processes, and around 6% for the vector-boson fusion process. For 8 TeV data, for the tight high-mass two-jet category, an 8.8% uncertainty is assigned to the ggF, VH and ttH processes and 2.0% to VBF process. For the loose high-mass two-jet category, these uncertainties are 12.8% and 3.3% respectively. For the low mass 2-jet category, the uncertainty is found to be 12% for the ggF, VH and ttH processes and 3.9% for VBF;
- The modelling of the $\Delta\phi_{\gamma\gamma,jj}$ and the η^* variables. For 8 TeV analysis, the uncertainties on the $\Delta\phi_{\gamma\gamma,jj}$ and η^* modelling lead to 12.1% (8.5%) and 7.6% (6.2%) uncertainties for the tight (loose) high-mass two-jet categories.
- Jet-vertex-fraction (JVF): an uncertainty on the choice of the JVF requirement gives a 0.3% (1.2%) uncertainty in the loose high-mass two-jet category for gluon fusion (VBF), and 2.3% (2.4%) in the low-mass two-jet category for gluon fusion (VBF) for 8 TeV data set. For the 7 TeV data set, it is found to be negligible.
- E_{T}^{miss} uncertainty: it is assessed by shifting the transverse energy of each of the input object used for calculating E_{T}^{miss} up and down by the uncertainties on their resolution and scale. The resulting uncertainty on the E_{T}^{miss} category is 66.4% for the gluon fusion production, 30.7% for the VBF production and 1.2% for the associated production.

5.6.4 Uncertainties on the mass measurement

The main sources of uncertainties on the mass measurement arise from the extrapolation of the photon energy scale from the $Z \to ee$ electron energy scale (0.3%), the material effects when extrapolating the electron energy scale to photons (0.3%) and the uncertainty of the presampler energy scale (0.1%). These systematic uncertainties amount to a total of 0.45% (0.6 GeV) on the mass peak position.

Dedicated cross checks have been performed on the mass measurement. The following additional uncertainties have been considered:

- The impact of possible small non-linearities of the EM calorimeter electronics has

been evaluated with $Z \to ee$ events to be at the level of 0.15%.

- The systematic uncertainty on the corrections for lateral energy leakage out of the cluster has been measured with radiative Z boson decays, and a 0.1% uncertainty is applied.
- The impact of the uncertainty on the fraction of converted photons has been evaluated. This uncertainty originates from wrong associations between EM clusters of unconverted photons and fake or valid conversion vertices or tracks. In such events, photons are miscalibrated and the measured mass could be biased. The agreement between the conversion fraction in data and MC is better than 10%, which leads to a very conservative upper bound on the uncertainty on the mass measurement of 0.13%.
- A systematic uncertainty on the relative calibration of the first and second sampling of the EMC is found to be at the level of 0.2%.
- The uncertainty from the photon direction measurement is evaluated by reconstructing the $Z \to ee$ mass using several primary vertex selection algorithms, namely the vertex pointing using only the longitudinal segmentation of the calorimeter, the primary vertex selected by maximising the sum of the squared momentum of tracks $\sum p_{\mathrm{T}}^2$, and the neural network. The uncertainty, taken as the spread of the data/MC ratio observed between different primary vertex selections, amounts to 0.03%. It has been checked that this additional uncertainty can cover effects on the calorimeter position, such as the calorimeter and tracker alignment and the η size of cells in the calorimeter barrel.
- The uncertainty arising from the background modelling choice is evaluated by generating pseudodatasets with alternative background models, and measuring the median deviation from the nominal value. The uncertainty is taken to be the maximum of the observed deviations (0.1%).

These additional uncertainties on the mass measurement amount to a total of 0.32% (0.4 GeV).

5.7 Results

We use the same likelihood-based statistical tests explained in section 4.10 to interpret our selected data samples in terms of a background plus the contribution of a Higgs boson decaying to $\gamma\gamma$. The signal strength μ, defined as the ratio of the measured number of signal events to the value expected in the Standard Model, is the parameter of interest of our model. The statistical tests are carried out for fixed values of m_H between 110 GeV and 150 GeV in steps of 0.5 GeV.

5.7.1 Observation of the Higgs particle

The expected and observed local p_0 values as a function of the Higgs boson mass, after the combination of 7 TeV and 8 TeV data, are shown in Fig. 5.9. We observe an excess at $m_H = 126.5$ GeV with a local significance of 7.4 σ, while the expected significance is 4.1 σ. As a cross check, an inclusive analysis (without any event categorization) is performed. The largest observed (expected) local significance is 6.1 (2.9) σ. The expected and observed local p_0 values as function of the the Higgs boson mass separately for 7 TeV and 8 TeV data are shown in Fig. 5.10. This provides evidence for a particle decaying to

photon pairs with a mass around 126.5 GeV. The mass m_H of this particle is determined by a profile likelihood ratio in which m_H is the parameter of interest, and the signal strength μ is treated as a nuisance parameter and profiled. The best-fit value is $m_H = 126.8 \pm 0.2(stat) \pm 0.7(syst)$ GeV. The dominant contribution to the systematic uncertainty comes from the uncertainties on the photon energy scale. At the best-fit value $m_H = 126.8$ GeV, the measured signal strength is $\mu = 1.65^{+0.24}_{-0.24}(stat)^{+0.25}_{-0.18}(syst)$. The excess with respect to the SM prediction is at the level of 2.3 standard deviations.

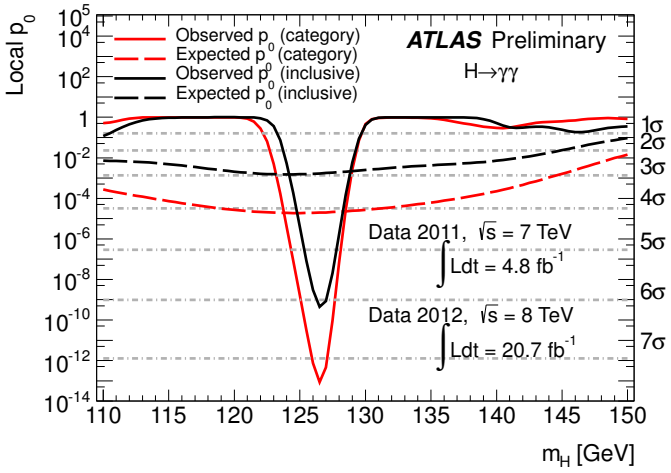

Figure 5.9 – The observed and expected local p_0 values as a function of Higgs boson mass m_H for the combination of $\sqrt{s} = 7$ TeV and $\sqrt{s} = 8$ TeV data for the inclusive case (black) and for the analysis using categories (red).

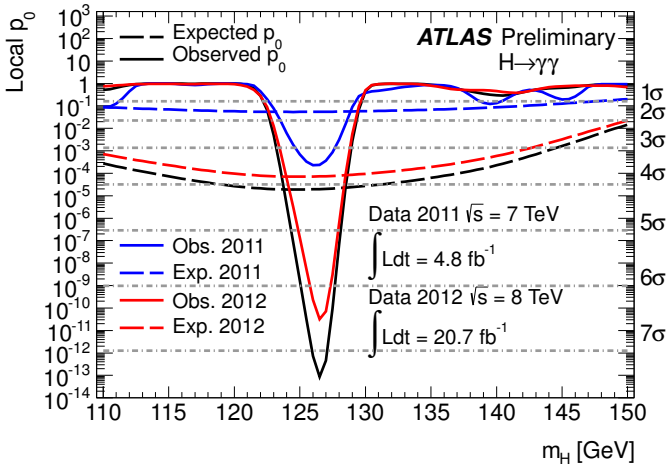

Figure 5.10 – The observed and expected local p_0 values as a function of Higgs boson mass m_H for the $\sqrt{s} = 7$ TeV data (blue), $\sqrt{s} = 8$ TeV data (red) and their combination (black).

5.7.2 Coupling Measurements

The introduction of event categories sensitive to the different Higgs boson production modes (gluon-fusion, VBF, VH) allows us to fit separately strength factors for different classes of production processes:

- $\mu_{ggH+ttH}$ is the strength factor for the gluon fusion and $t\bar{t}H$ production. Both processes are initiated by gluons and mediated by top quarks, so if the $t\bar{t}H$ coupling is different from the SM one, it should affect in the same way the gluon fusion and the $t\bar{t}H$ cross sections
- μ_{VBF+VH} is the strength factor for the VBF and VH production modes. Both are quark-initiated processes mediated by the HVV vertex, and modifications of the HVV coupling should lead to variations of both the VBF and VH cross sections.

The fitted contours of $\mu_{ggH+ttH} \times B/B_{SM}$ vs $\mu_{VBF+VH} \times B/B_{SM}$, where B/B_{SM} is the branching ratio for $H \to \gamma\gamma$ in data normalised to the SM expectation, are shown in Fig. 5.11. A simultaneous fit is also performed to determine the signal strengths of

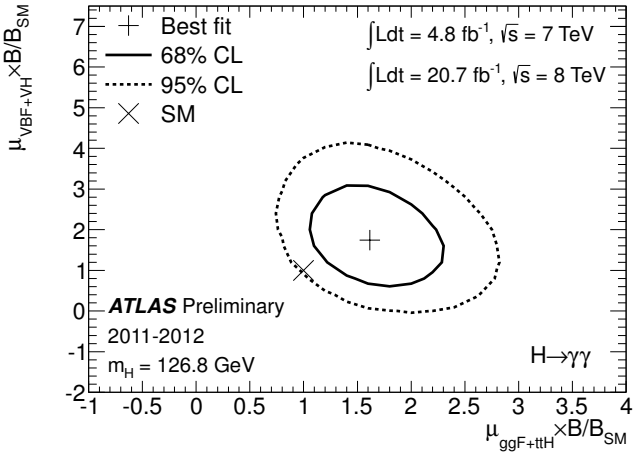

Figure 5.11 – The best-fit values (+) of $\mu_{ggF+ttH} \times B/B_{SM}$ and $\mu_{VBF+VH} \times B/B_{SM}$ from a simultaneous fit to the data and their 68% (solid) and 95% (dashed) CL contours. The expectation for a SM Higgs boson is also shown (×).

$\mu_{\mathrm{ggF+ttH}} \times B/B_{\mathrm{SM}}$, $\mu_{\mathrm{VBF}} \times B/B_{\mathrm{SM}}$, and $\mu_{\mathrm{VH}} \times B/B_{\mathrm{SM}}$, where the VBF and VH production modes are allowed to be rescaled by different scales, and the best-fit values are:

- $\mu_{\mathrm{ggF+ttH}} \times B/B_{\mathrm{SM}} = 1.6^{+0.3}_{-0.3}(\mathrm{stat})^{+0.3}_{-0.2}(\mathrm{syst})$;
- $\mu_{\mathrm{VBF}} \times B/B_{\mathrm{SM}} = 1.7^{+0.8}_{-0.8}(\mathrm{stat})^{+0.5}_{-0.4}(\mathrm{syst})$;
- $\mu_{\mathrm{VH}} \times B/B_{\mathrm{SM}} = 1.8^{+1.5}_{-1.3}(\mathrm{stat})^{+0.3}_{-0.3}(\mathrm{syst})$.

These results are also shown in Fig. 5.12. No statistically significant deviation from the SM expectation is found.

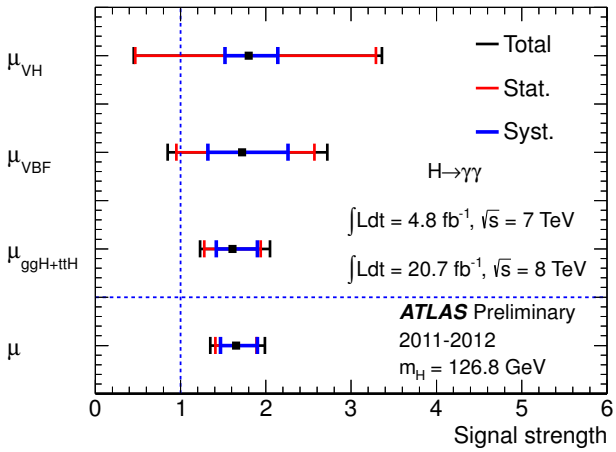

Figure 5.12 – Measured signal strengths $\mu_{ggF+ttH}$, μ_{VBF} and μ_{VH} for the different $H \to \gamma\gamma$ production modes, as well as overall strength μ.

5.8 The Higgs Boson Properties Measurements in Combined Channels

The Higgs boson properties measurements are also performed in channels of $H \to ZZ \to 4\ell$ [139], $H \to WW \to \ell\nu\ell\nu$ [139], and $H \to b\bar{b}$ [140] using full 2011 and 2012 pp collision data sample, and in channel of $H \to \tau\tau$ [141] using full 2012 pp collision data sample. The Higgs boson mass is measured in $H \to ZZ \to 4\ell$ channel which is $m_H = 124.3^{+0.6}_{-0.5}(\text{stat})^{+0.5}_{-0.3}(\text{sys})$ GeV [142]. The main sources of systematic uncertainty are the lepton energy and momentum scales. The consistency of fitted Higgs mass between $H \to \gamma\gamma$ channel ($m_H^{\gamma\gamma}$) and $H \to ZZ \to 4\ell$ channel (m_H^{ZZ}) is checked with the profile likelihood ratio ($\Lambda(\Delta m_H)$), where the parameter of interest is the mass difference $\Delta m_H = m_H^{\gamma\gamma} - m_H^{ZZ}$. The result is :

$$\Delta m_H = 2.3^{+0.6}_{-0.7}(stat) \pm 0.6(sys)\ GeV \tag{5.16}$$

which leads a deviation from $\Delta m_H = 0$ hypothesis with 2.5 σ significance. The combined Higgs mass from $m_H^{\gamma\gamma}$ and m_H^{ZZ} is :

$$m_H = 125.5 \pm 0.2(stat) \pm^{+0.5}_{-0.6}(sys)\ GeV \tag{5.17}$$

For a fixed mass hypothesis corresponding to the measured value of $m_H = 125.5$ GeV, the global signal strength parameter μ is measured in five individual channel respectively, as shown in Figure 5.13. The overall compatibility between the signal strengths measured in the five final states and the SM predictions is about 11%. They are combined in groups of three diboson channels ($\mu^{\gamma\gamma,ZZ^*,WW^*}$) and two fermion channels ($\mu^{bb,\tau\tau}$):

$$\begin{aligned} \mu^{\gamma\gamma,ZZ^*,WW^*} &= 1.35 \pm 0.14(stat) \pm 0.15(sys) \\ \mu^{bb,\tau\tau} &= 1.09 \pm 0.24(stat)^{+0.27}_{-0.21}(sys) \end{aligned} \tag{5.18}$$

Finally, the signal strength, obtained by combining all five channels, is

$$\mu = 1.30 \pm 0.12(stat)^{+0.14}_{-0.11}(sys). \tag{5.19}$$

The compatibility between this measurement and the SM Higgs boson expectation ($\mu = 1$) is about 7%. The data are fitted separating the VBF and VH processes from the ggF and ttH processes, using two signal strengths μ_{VBF+VH} and $\mu_{ggF+ttH}$. The $H \to b\bar{b}$ final state is not included, since the currently analysis is not sensitive to the ggF, VBF and VH processes. The results are shown in Figure 5.14. The 95% $C.L.$ contours of the measurements are consistent with the SM expectation.

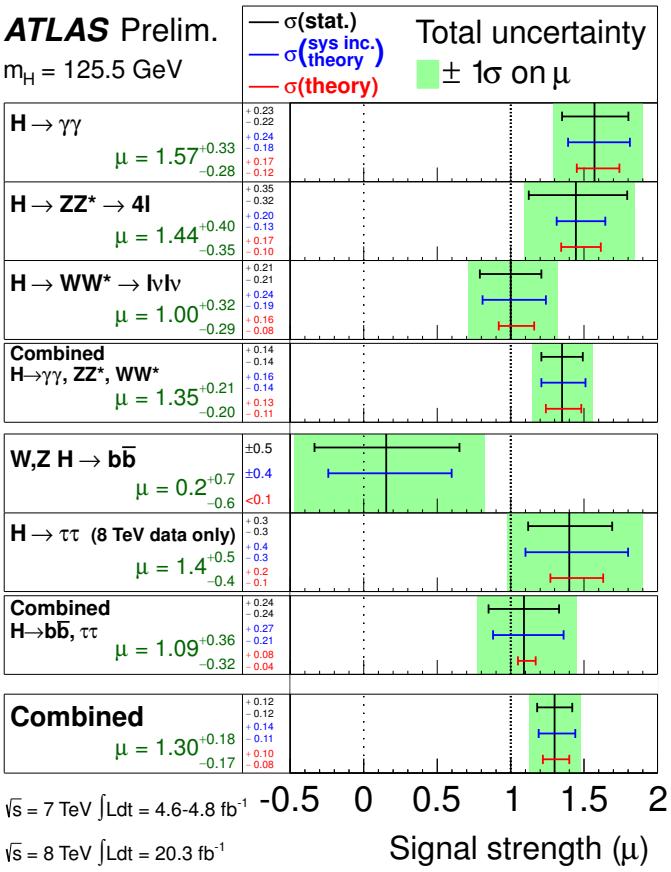

Figure 5.13 – The measured signal strengths for a Higgs boson of mass m_H =125.5 GeV, normalised to the SM expectations, for the individual final states and various combinations. The best-fit values are shown by the solid vertical lines. The total $\pm 1\sigma$ uncertainties are indicated by green shaded bands, with the individual contributions from the statistical uncertainty (top), the total (experimental and theoretical) systematic uncertainty (middle), and the theory uncertainty (bottom) on the signal strength (from QCD scale, PDF, and branching ratios) shown as superimposed error bars [139].

Studies of the spin and parity quantum numbers of the Higgs boson are performed using the Higgs boson decays $H \to \gamma\gamma$, $H \to ZZ^* \to 4\ell$ and $H \to WW^* \to e\nu\mu\nu/\mu\nu e\nu$, based on pp collision data corresponding to an integrated luminosity of 20.7 fb^{-1} collected at $\sqrt{s} = 8$ TeV [143]. For the $H \to ZZ^* \to 4\ell$ decay mode the dataset corresponding to an integrated luminosity of 4.6 fb^{-1} collected at $\sqrt{s} = 7$ TeV is added. The Standard Model spin-parity $J^P = 0^+$ hypothesis for the Higgs boson has been compared to alternative spin-parity hypotheses. In the $H \to \gamma\gamma$ channel, the $J^P = 0^+, 2^+$ hypotheses are tested, using the absolute value of the cosine of the polar angle θ^* of the photons as the discriminating variable. Since the Landau-Yang theorem forbids the direct decay of an on-shell spin-1 particle into a pair of photons [144, 145], the spin-1 hypoth-

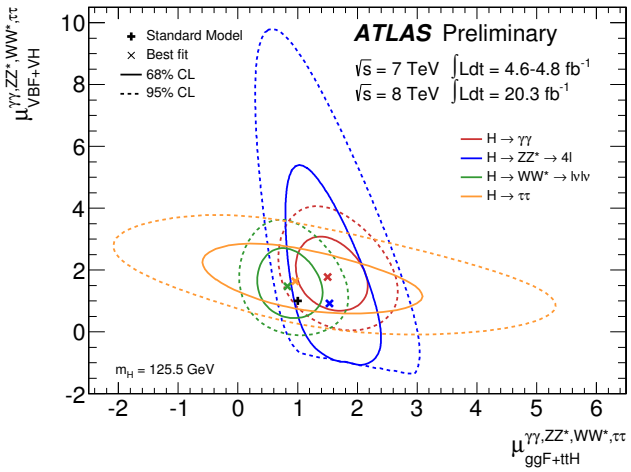

Figure 5.14 – Likelihood contours in the ($\mu_{ggF+ttH}$, μ_{VBF+VH}) plane for the channels $H \to \gamma\gamma$, $H \to ZZ \to 4\ell$, $H \to WW \to \ell\nu\ell\nu$, and $H \to b\bar{b}$ and a Higgs boson mass m_H = 125.5 GeV. The best-fit values to the data (×) and the 68% (full) and 95% (dashed) *C.L.* contours are indicated, as well as the SM expectations (+) [139].

esis is therefore strongly disfavoured by the observation of the $H \to \gamma\gamma$ decay. In the $H \to ZZ^* \to 4\ell$ channel, a MVA-based technique is performed on the reconstructed mass of the two Z boson candidates and five production and decay angles (see section 7 in the reference [146]), to separate the $J^P = 0^+$ hypothesis from $J^P = 0^-, 1^\pm$ and 2^+ hypotheses. In the $H \to WW^* \to e\nu\mu\nu/\mu\nu e\nu$ channel, the $J^P = 0^+$ hypothesis is studied against to $J^P = 1^\pm, 2^+$, using the dilepton invariant mass ($m_{\ell\ell}$) and the azimuthal separation of the two leptons ($\Delta\phi_{\ell\ell}$) as discriminating variables. Their combination results are summarized in Figure 5.15. The data favours the SM quantum numbers of $J^P = 0^+$. The 0^- hypothesis is rejected at 97.8% *C.L.* by using the $H \to ZZ^* \to 4\ell$ channel alone. The $1^\pm$ hypotheses are rejected with a *C.L.* of at least 99.7% by combining the $H \to ZZ^* \to 4\ell$ and $H \to WW^* \to e\nu\mu\nu/\mu\nu e\nu$ channels. Finally, the $J^P = 2^+$ hypothesis is rejected at more than 99.9% *C.L.* by combining above three diboson channels.

5.9 The Higgs Boson Properties Measurements in $H \to \gamma\gamma$ Channel with the CMS Detector

The studies of searching for a Higgs boson also been performed in the two photon decay channel with 5.1 (19.6) fb^{-1} of pp collisions at $\sqrt{s}$ = 7 (8) TeV with the CMS detector [147, 148]. Two kinds of analysis are performed: MVA-based analysis and cut-based analysis. The most sensitive, MVA-based analysis observes an excess of events at m_H = 125 GeV, with a local significance of 3.2 σ, where a local significance of 4.2σ is expected. The best-fit signal strength μ is 0.78 ± 0.27 at m_H = 125 GeV. The mass is fitted to be $125 \pm 0.5(stat) \pm 0.6(syst)$. The cut-based analysis observes a corresponding excess with a local significance of 3.9 σ (3.5 σ expected), and the fitted $\mu = 1.11 \pm 0.31$ at m_H =124.5 GeV. All measurements are compatible among themselves and with a Higgs boson with a mass of 125.4 GeV. The natural width of the new state is found to be $<$ 6.9 GeV (expected $<$ 5.9 GeV) at 95% C.L. The SM spin-0 hypothesis is compared to a graviton like spin-2 hypothesis with minimal couplings using 8 TeV data set only. This particular spin-2 model cannot be ruled out. The observed data is found to be compatible

with the SM with a χ^2 $p-$value of 0.68.

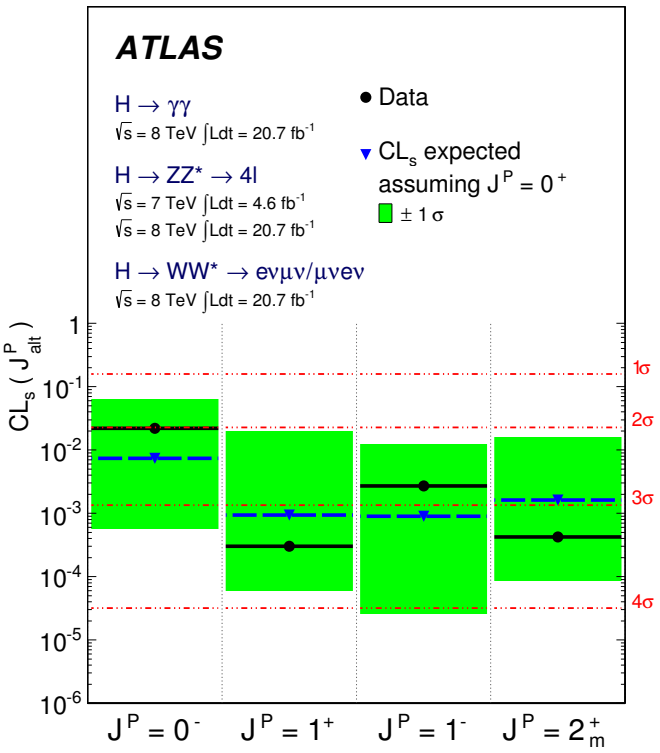

Figure 5.15 – Expected (blue triangles/dashed lines) and observed (black circles/solid lines) confidence level CL_s for alternative spin-parity hypotheses assuming a 0^+ signal. The green band represents the 68% CL_s (J^P_{alt}) expected exclusion range for a signal with assumed 0^+. For the spin-2 hypothesis, the results for the specific 2^+_m model, are shown. On the right y-axis, the corresponding numbers of Gaussian standard deviations are given, using the one-sided convention [143].

Conclusion

After 25 years of planning, R&D and construction, the LHC machine has started to deliver *pp* collisions at the end of 2009. During the first run of the LHC in the years 2010-2012 the ATLAS detector has collected about 25 fb^{-1} data at $\sqrt{s} = 7$ TeV and $\sqrt{s} = 8$ TeV. These data have led to a good understanding of the detector performances, thanks to the large control samples accumulated, and to precise measurements of the cross sections of many Standard Model processes, which have been found in good agreement with the theoretical calculations, increasing the confidence in the knowledge gained of the detector performance. Furthermore, the analysis of such data, exploiting some of the techniques developped for the SM cross section measurements and the most accurate detector calibrations and efficiency measurements, as well as sophisticated statistical techniques, has led to the discovery of a particle whose properties are consistent with those of the Standard Model Higgs boson with a mass near 125 GeV. The work performed for this thesis in the past three years gave a significant contribution to such measurements.

I started to work on the photon identification efficiency measurement using collision data in 2011, in order to improve its precision. At that time, the photon identification efficiency was estimated from the simulation with rather large uncertainties. I was the first in ATLAS to develop both a matrix method and the selection of a $Z \to \ell\ell\gamma$ control sample to measure the efficiency of the photon identification criteria directly from the data. These methods were applied to both the 7 TeV and 8 TeV data, leading to a reduction of the uncertainty on the efficiency for $H \to \gamma\gamma$ candidates from $\sim$11% to 2.4%. The same results have been used by all the other measurements of SM photon cross-sections and searches for exotic di-photon and photon-jet resonances. The pure photon samples selected in data from radiative Z decays by this analysis have also been reused for many other photon performance studies, including photon energy calibration, photon conversion fraction studies, optimization of neural networks for photon identifiation at low transverse momentum, and photon trigger efficiency studies.

Before the 2012 data taking, expecting more significant pile-up effects due to increased instantaneous luminosity, I proposed a new photon trigger that could be efficient and at the same time satisfy the stringent requirements on the output rate and limited dependence on the number of pile-up collisions per bunch crossing. Compared to the previous triggers, the rate for the new di-photon trigger was reduced by a factor of 2, while the efficiency for events passing the offline selection is still as high as 99%. For the $H \to \gamma\gamma$ analysis, the new trigger was used in 2012 as a backup trigger and validated against the previous one, and it will be the default di-photon trigger for the run-II data taking. Using radiative Z decays I also measured the trigger efficiency and its uncertainty for $H \to \gamma\gamma$ analysis. The uncertainty was reduced to < 0.5 %.

Once the photon performance of the ATLAS detector were well understood, searches for the Higgs boson in the $H \to \gamma\gamma$ channel have been performed. The first limit on the production cross section with 7 TeV data was published in June 2011, and then updated

as more data and better detector calibrations and improved physics object reconstruction and selections become available. On July 4^{th}, 2012, a new particle was observed in the search for a SM Higgs boson, in the combination of the diboson channels $H \to \gamma\gamma$, $H \to ZZ^* \to 4\ell$, $H \to WW^* \to \ell\nu\ell\nu$ and the fermion channels $H \to b\bar{b}$ and $H \to \tau^+\tau^-$. I personally contributed to the search of the Higgs boson in the $H \to \gamma\gamma$ channel. In this thesis the results of this work using full run-I data set are discussed. We observe a signal in the $H \to \gamma\gamma$ channel only, with a significance greater than 7 σ, at a mass $m_H = 126.8 \pm 0.2(stat) \pm 0.7(syst)$ GeV, with a production cross-section times branching ratio, normalised to the Standard Model Higgs boson expectation, $\mu = 1.65^{+0.24}_{-0.24}(stat)^{+0.25}_{-0.18}(syst)$.

After the Higgs boson discovery, it has become of primary importance to measure precisely its properties, like mass, spin, coupling to other particles. This program includes the measurement of the branching ratios to various final states, even rare channels like $H \to Z\gamma$ which, being induced at loop-level in the SM, are expected to be particularly sensitive to the presence of new physics beyond the SM. In this thesis I described the search of the $H \to Z\gamma$ decays that I have performed using the full run-I data set and recently published. No excess with respect to background is observed and, for a Higgs boson mass at 125.5 GeV, we set an upper limit on the production cross section times $H \to Z\gamma$ branching ratio of 11 times the SM prediction, at 95% confidence level. More collision data from run-II is needed to draw interesting conlusions on this rare channel.

Bibliography

[1] S. L. Glashow, *Partial Symmetries of Weak Interactions*, Nucl. Phys. **B 22** (1961) 579.

[2] J. Beringer et al., *2012 Review of Particle Physics - Gauge and Higgs Bosons*, Phys. Rev. D **86** 1.

[3] D. B. Chitwood and others MuLan Collaboration, *Improved Measurement of the Positive-Muon Lifetime and Determination of the Fermi Constant*, Phys. Rev. Lett. **99** (2007) 032001.

[4] B. Lee, C. Quigg, and H. Thacker, *Weak Interactions at Very High-Energies: The Role of the Higgs Boson Mass*, Phys. Rev. D **16** (1977) 1519.

[5] B. Lee, C. Quigg, and H. Thacker, *The Strength of Weak Interactions at Very High-Energies and the Higgs Boson Mass*, Phys. Rev. Lett. **38** (1977) 883–885.

[6] The ATLAS Collaboration, *Observation of a new particle in the search for the Standard Model Higgs boson with the ATLAS detector at the LHC*, Phys. Lett. B **716** (2012) 1–29.

[7] CMS Collaboration, *Observation of a new boson at a mass of 125 GeV with the CMS experiment at the LHC*, Phys. Lett. B **716** (2012) 30.

[8] The CDF Collaboration, the D0 Collaboration, the Tevatron New Physics, Higgs Working Group, *Updated Combination of CDF and D0 Searches for Standard Model Higgs Boson Production with up to 10.0 fb^{-1} of Data*, arXiv:1207.0449 [hep-ph].

[9] M. Baak et al., *The electroweak fit of the standard model after the discovery of a new boson at the LHC*, Eur. Phys. J. C **72** (2012) 2205.

[10] LHC Higgs Cross Section Working Group, S. Dittmaier, C. Mariotti, G. Passarino, and R. Tanaka (Eds.), *Handbook of LHC Higgs Cross Sections: 1. Inclusive Observables*, .

[11] LHC Higgs Cross Section Working Group, S. Dittmaier, C. Mariotti, G. Passarino, and R. Tanaka (Eds.), *Handbook of LHC Higgs Cross Sections: 2. Differential Distributions*, .

[12] G. Passarino, C. Sturm, and S. Uccirati, *Higgs Pseudo-Observables, Second Riemann Sheet and All That*, Nucl.Phys.B **834** (2010) 77–115.

[13] C. Anastasiou, S. Buehler, F. Herzog, and A. Lazopoulos, *Inclusive Higgs boson cross-section for the LHC at 8 TeV*, .

[14] CMS Collaboration, *Constraints on the Higgs boson width from off-shell production and decay to ZZ to $\ell\ell\ell\ell$ and $\ell\ell\nu\nu$*, CMS-PAS-HIG-14-002 (2014) . https://cds.cern.ch/record/1670066.

[15] A. Djouadi and P. Gambino, *QCD corrections to Higgs boson self-energies and fermionic decay widths*, Phys. Rev. D **51** (1995) 218.

[16] R. N. Cahn, M. S. Chanowitz, and N. Fleishon, *Higgs particle production by $Z \to H\gamma$*, Phys. Lett. B **82** (1978) 113–116.

[17] D. A. Dicus and S. S. D. Willenbrock, *Photon pair production and the intermediate-mass Higgs boson*, Phys. Rev. D **37** (1988) 1801.

[18] L. Dixon and M. S. Siu, *Resonance-continuum interference in the di-photon Higgs signal at the LHC*, Phys. Rev. Lett. **90** (2003) 252001.

[19] S. P. Martin, *Shift in the LHC Higgs diphoton mass peak from interference with background*, Phys. Rev. D **86** (2012) 073016.

[20] S. Y. Choi, M. M. Muhlleitner, and P. M. Zerwas, *Theoretical Basis of Higgs-Spin Analysis in $H \to \gamma\gamma$ and $Z\gamma$ Decays*, Phys. Lett. B **718** (2012) 1031–1035.

[21] M. E. Rose, *Elementary Theory of Angular Momentum*, Dover Publications (1995) .

[22] D. Boer, W. J. den Dunnen, C. Pisano, and M. Schlegel, *Determining the Higgs spin and parity in the diphoton decay channel*, Phys. Rev. Lett. **111** (2013) 032002.

[23] I. Low, J. Lykken, and G. Shaughnessy, *Singlet scalars as Higgs boson imposters at the Large Hadron Collider*, Phys. Rev. D **84** (2011) 035027.

[24] N. O. Nobuhito Maru, *Diphoton and Z photon Decays of Higgs Boson in Gauge-Higgs Unification: A Snowmass white paper*, .

[25] C. Han, N. Liu, L. Wu, J. M. Yang, and Y. Zhang, *Two Higgs doublet model with a color triplet scalar a joint explanation for top quark forward backward asymmetry and Higgs decay to diphoton*, Eur. Phys. J. C **73** (2013) 2664.

[26] A. Azatov, R. Contino, A. D. Iura, and J. Galloway, *New Prospects for Higgs Compositeness in $h \to Z\gamma$*, Phys. Rev. D **88** (2013) 075019.

[27] B. Swiezewska and M. Krawczyk, *Diphoton rate in the Inert Doublet Model with a 125 GeV Higgs boson*, Phys. Rev. D **88** (2013) 035019.

[28] *LEP Design Report, Vol1: The LEP Injector Chain*, CERN-LEP/TH/83-29 (1983) .

[29] *LEP Design Report, Vol1: The LEP Main Ring*, CERN-LEP-84-01 (1984) .

[30] *ATLAS public website*, . http://home.web.cern.ch/about/experiments/atlas.

[31] *CMS public website*, . http://home.web.cern.ch/about/experiments/cms.

[32] *ALICE public website*, . http://home.web.cern.ch/about/experiments/alice.

[33] *LHCb public website*, . http://home.web.cern.ch/about/experiments/lhcb.

[34] ATLAS Collaboration, *The ATLAS Experiment at the CERN Large Hadron Collider*, JINST **3** (2008) 117–119.

[35] ATLAS Collaboration, *Electron and photon reconstruction and identification in ATLAS: expected performance at high energy and results at 900 GeV*, ATLAS-CONF-2010-005 (2010) . https://cds.cern.ch/record/1273197.

[36] ATLAS Collaboration, *Electron and Photon calibration for the LHC Run1*, ATL-COM-PHYS-2013-1652 (2013) . https://cds.cern.ch/record/1637529.

[37] ATLAS Collaboration, *Electron performance measurements with the ATLAS detector using the 2010 LHC proton-proton collision data*, Eur. Phys. J. C **72** (2012) 1909.

[38] ATLAS Collaboration, *Electron energy response stability with pile-up in 2012 data with 13 fb^{-1}*, ATL-COM-PHYS-2012-1668 (2012) . https://atlas.web.cern.ch/Atlas/GROUPS/PHYSICS/EGAMMA/PublicPlots/20121129/ATL-COM-PHYS-2012-1668/index.html.

[39] ATLAS Collaboration, *Improved electron reconstruction in ATLAS using the Gaussian Sum Filter-based model for bremsstrahlung*, ATLAS-CONF-2012-047 (2012) . http://cds.cern.ch/record/1449796.

[40] ATLAS Collaboration, *Electron reconstruction and identification efficiency measurements with the ATLAS detector using the 2011 LHC proton-proton collision data*, The European Physical Journal C (2014) , arXiv:1404.2240 [hep-ex].

[41] ATLAS Collaboration, *Electron Efficiency Measurements for 2012 and 2011 Data*, ATL-COM-PHYS-2013-1287 (2013) . https://atlas.web.cern.ch/Atlas/GROUPS/PHYSICS/EGAMMA/PublicPlots/20130926/ATL-COM-PHYS-2013-1287/index.html.

[42] ATLAS Collaboration, *Expected electron performance in the ATLAS experiment*, ATL-PHYS-PUB-2011-006 . http://cdsweb.cern.ch/record/1345327.

[43] ATLAS Collaboration, *Preliminary results on the muon reconstruction efficiency, momentum resolution, and momentum scale in ATLAS 2012 pp collision data*, ATLAS-CONF-2013-088 (2013) . https://cds.cern.ch/record/1580207.

[44] M. Cacciari, G. P. Salam, and G. Soyez, *The anti-k_t jet clustering algorithm*, JHEP **0804** (2008) 063.

[45] M. Cacciari and G. P. Salam, *Dispelling the N^3 myth for the k_t jet-finder*, Phys. Lett. B **6411** (2006) 57–61.

[46] ATLAS Collaboration, *Jet energy measurement with the ATLAS detector in proton-proton collisions at sqrt(s) = 7 TeV*, Eur. Phys. J. C **73-3** (2013) 2304.

[47] ATLAS Collaboration, *Performance of Missing Transverse Momentum Reconstruction in ATLAS studied in Proton-Proton Collisions recorded in 2012 at 8 TeV*, ATLAS-CONF-2013-082 (2013) . https://cds.cern.ch/record/1570993.

[48] ATLAS Collaboration, *Performance of the ATLAS Electron and Photon Triggers in p-p Collisions at $\sqrt{s}$=8 TeV in 2012*, ATL-COM-DAQ-2013-121 (2013) . https://cds.cern.ch/record/1609629?

[49] Saxon, J and Williams, H H, *Neural Networks for Photon Identification in $H \to \gamma\gamma$*, ATL-COM-PHYS-2013-305 (2013) . https://cds.cern.ch/record/1524081.

[50] K. Liu and G. Marchiori and Y. Liu and E. Soldatov, *Measurement of the identification efficiency of isolated prompt photons using radiative $Z \to \ell\ell\gamma$ decays in 4.9 fb^{-1} of ATLAS data*, ATL-COM-PHYS-2012-382 (2012) . https://cds.cern.ch/record/1437004?

[51] Jimenez, M and Tackmann, K , *Photon identification efficiency extrapolated from electrons in $Z \to e^+e^-$ decays*, ATL-COM-PHYS-2012-241 (2012) . https://cds.cern.ch/record/1428906.

[52] K. Liu and G. Marchiori and Y. Liu, *Measurement of the identification efficiency of isolated prompt photons using the matrix method and 4.9 fb^{-1} of ATLAS data*, ATL-COM-PHYS-2012-242 (2012) . https://cds.cern.ch/record/1428909?

[53] L. Devroye, *Non-Uniform Random Variate Generation*, New York: Springer-Verlag.

[54] W. M. Yao et al., *Review of Particle Physics*, J. Phys. G: Nucl. Part. Phys. **33** (2012) 1–1232.

[55] D. G. L. Lyons and P. Clifford, *How to combine correlated estimates of a single physical quantity*, Nucl. Instrum. Meth **A270** (1988) 110.

[56] P. Avery, *Combining measurements with correlated errors*, CBX (1996) 95–55.

[57] A. Valassi, *Combining correlated measurements of several different physical quantities*, Nucl. Instrum. Meth **A500** (2003) 391.

[58] J. Saxon, *egamma meeting of may 16th 2012*, . https://indico.cern.ch/event/163469/contribution/5/material/0/0.pdf.

[59] ATLAS Collaboration, *Measurements of the photon identification efficiency with the ATLAS detector using 4.9 fb^{-1}1 of pp collision data collected in 2011*, ATLAS-CONF-2012-123 (2012) . https://cds.cern.ch/record/1473426.

[60] K. Liu and G. Marchiori and Y. Liu and E. Soldatov, *Measurement of the identification efficiency of isolated prompt photons using radiative $Z \to \ell\ell\gamma$ decays in 20.3 fb^{-1} of ATLAS data*, ATL-COM-PHYS-2013-1639 (2013) . https://cds.cern.ch/record/1636404.

[61] K. Liu and G. Marchiori and Y. Liu and M. Kuna and M. Pitt, *Measurement of the identification efficiency of isolated prompt photons using the matrix method and 20.3 fb^{-1} of ATLAS data*, ATL-COM-PHYS-2013-1628 (2013) . https://cds.cern.ch/record/1635964.

[62] ATLAS Collaboration, *Search for the Standard Model Higgs boson in the $H \to Z\gamma$ decay mode with pp collisions a $\sqrt{s}$ = 7 and 8 TeV*, ATLAS-COM-CONF-2013-014 (2013) . https://cds.cern.ch/record/1516924?

[63] ATLAS Collaboration, *Search for Higgs boson decays to a photon and a Z boson in pp collisions at $\sqrt{s}$=7 and 8 TeV with the ATLAS detector*, Phys. Lett. **B732** (2014) 8–27, arXiv:1402.3051 [hep-ex].

[64] ATLAS Collaboration, *Luminosity Determination in pp Collisions at $\sqrt{s} = 7$ TeV Using the ATLAS Detector at the LHC*, Eur. Phys. J. C **71** (2011) 1630, arXiv:1101.2185 [hep-ex].

[65] ATLAS Collaboration Collaboration, ATLAS Collaboration, *Improved luminosity determination in pp collisions at $\sqrt{s} = 7$ TeV using the ATLAS detector at the LHC*, arXiv:1302.4393 [hep-ex].

[66] GEANT4 Collaboration, S. Agostinelli et al., *GEANT4 - a simulation toolkit*, Nucl. Instrum. Methods A **506** (2003) 250.

[67] ATLAS Collaboration, *The ATLAS Simulation Infrastructure*, Eur. Phys. J. C **70** (2010) 823–874, arXiv:1005.4568 [physics.ins-det].

[68] S. Alioli, P. Nason, C. Oleari and E. Re, *NLO Higgs boson production via gluon fusion matched with shower in POWHEG*, JHEP **04** (2009) 002, arXiv:0812.0578 [hep-ph].

[69] P. Nason and C. Oleari, *NLO Higgs boson production via vector-boson fusion matched with shower in POWHEG*, JHEP **02** (2010) 037, arXiv:0911.5299 [hep-ph].

[70] T. Sjöstrand, S. Mrenna, P. Skands, *A brief introduction to PYTHIA 8.1*, Comput.Phys.Commun. **178** (2008) 852–867, arXiv:0710.3820 [hep-ph].

[71] H.-L. Lai, M. Guzzi, J. Huston, Z. Li, P. M. Nadolsky, et al., *New parton distributions for collider physics*, Phys. Rev. D **82** (2010) 074024, arXiv:1007.2241 [hep-ph].

[72] J. Pumplin et al., *New generation of parton distributions with uncertainties from global QCD analysis*, JHEP **07** (2002) 012.

[73] A. Djouadi, J. Kalinowski, and M. Spira, *HDECAY: A program for Higgs boson decays in the standard model and its supersymmetric extension*, Comput. Phys. Commun. **108** (1998) 56–74, arXiv:hep-ph/9704448.

[74] A. Bredenstein, A. Denner, S. Dittmaier, and M. M. Weber, *Precise predictions for the Higgs-boson decay $H \to WW/ZZ \to 4$leptons*, Phys. Rev. **D 74** (2006) 013004, arXiv:hep-ph/0604011.

[75] S. Actis, G. Passarino, C. Sturm, and S. Uccirati, *NNLO Computational Techniques: the Cases $H \to \gamma\gamma$ and $H \to gg$*, Nucl. Phys. **B 811** (2009) 182–273, arXiv:0809.3667 [hep-ph].

[76] LHC Higgs Cross Section Working Group, S. Dittmaier, C. Mariotti, G. Passarino, and R. Tanaka (Eds.), *Handbook of LHC Higgs cross sections: 1. Inclusive observables*, arXiv:1101.0593 [hep-ph]. CERN-2011-002.

[77] LHC Higgs Cross Section Working Group, S. Dittmaier, C. Mariotti, G. Passarino, and R. Tanaka (Eds.), *Handbook of LHC Higgs Cross Sections: 2. Differential distributions*, arXiv:1201.3084 [hep-ph].

[78] A. Djouadi, M. Spira, and P. M. Zerwas, *Production of Higgs bosons in proton colliders: QCD corrections*, Phys. Lett. **B 264** (1991) 440–446.

[79] S. Dawson, *Radiative corrections to Higgs boson production*, Nucl. Phys. **B 359** (1991) 283–300.

[80] M. Spira, A. Djouadi, D. Graudenz, and P. M. Zerwas, *Higgs boson production at the LHC*, Nucl. Phys. **B 453** (1995) 17–82, arXiv:hep-ph/9504378.

[81] R. V. Harlander and W. B. Kilgore, *Next-to-next-to-leading order Higgs production at hadron colliders*, Phys. Rev. Lett. **88** (2002) 201801, arXiv:hep-ph/0201206.

[82] C. Anastasiou and K. Melnikov, *Higgs boson production at hadron colliders in NNLO QCD*, Nucl. Phys. **B 646** (2002) 220–256, arXiv:hep-ph/0207004.

[83] V. Ravindran, J. Smith, and W. L. van Neerven, *NNLO corrections to the total cross section for Higgs boson production in hadron hadron collisions*, Nucl. Phys. **B 665** (2003) 325–366, arXiv:hep-ph/0302135.

[84] U. Aglietti, R. Bonciani, G. Degrassi, and A. Vicini, *Two-loop light fermion contribution to Higgs production and decays*, Phys. Lett. **B 595** (2004) 432–441, arXiv:hep-ph/0404071.

[85] S. Actis, G. Passarino, C. Sturm, and S. Uccirati, *NLO Electroweak Corrections to Higgs Boson Production at Hadron Colliders*, Phys. Lett. **B 670** (2008) 12–17, arXiv:0809.1301 [hep-ph].

[86] D. de Florian and M. Grazzini, *Higgs production at the LHC: updated cross sections at $\sqrt{s} = 8$ TeV*, Phys. Lett. **B718** (2012) 117–120, arXiv:1206.4133 [hep-ph].

[87] C. Anastasiou, S. Buehler, F. Herzog, and A. Lazopoulos, *Inclusive Higgs boson cross-section for the LHC at 8 TeV*, JHEP **1204** (2012) 004, arXiv:1202.3638 [hep-ph].

[88] J. Baglio and A. Djouadi, *Higgs production at the lHC*, JHEP **03** (2011) 055.

[89] M. Ciccolini, A. Denner, and S. Dittmaier, *Strong and electroweak corrections to the production of Higgs+2jets via weak interactions at the LHC*, Phys. Rev. Lett. **99** (2007) 161803, arXiv:0707.0381 [hep-ph].

[90] M. Ciccolini, A. Denner, and S. Dittmaier, *Electroweak and QCD corrections to Higgs production via vector-boson fusion at the LHC*, Phys. Rev. **D 77** (2008) 013002, arXiv:0710.4749 [hep-ph].

[91] K. Arnold et al., *VBFNLO: A parton level Monte Carlo for processes with electroweak bosons*, Comput. Phys. Commun. **180** (2009) 1661–1670, arXiv:0811.4559 [hep-ph].

[92] P. Bolzoni, F. Maltoni, S.-O. Moch, and M. Zaro, *Higgs production via vector-boson fusion at NNLO in QCD*, Phys. Rev. Lett. **105** (2010) 011801, arXiv:1003.4451 [hep-ph].

[93] T. Han and S. Willenbrock, *QCD correction to the $p\ p \to W\ H$ and $Z\ H$ total cross- sections*, Phys. Lett. **B 273** (1991) 167–172.

[94] O. Brein, A. Djouadi, and R. Harlander, *NNLO QCD corrections to the Higgs-strahlung processes at hadron colliders*, Phys. Lett. **B 579** (2004) 149, arXiv:hep-ph/0307206.

[95] M. L. Ciccolini, S. Dittmaier, and M. Kramer, *Electroweak radiative corrections to associated WH and ZH production at hadron colliders*, Phys. Rev. **D 68** (2003) 073003, arXiv:hep-ph/0306234.

[96] W. Beenakker, S. Dittmaier, M. Kramer, B. Plumper, M. Spira, et al., *Higgs radiation off top quarks at the Tevatron and the LHC*, Phys. Rev. Lett. **87** (2001) 201805, arXiv:hep-ph/0107081 [hep-ph].

[97] W. Beenakker et al., *NLO QCD corrections to t anti-t H production in hadron collisions.* , Nucl. Phys. **B 653** (2003) 151–203, arXiv:hep-ph/0211352.

[98] S. Dawson, L. Orr, L. Reina, and D. Wackeroth, *Next-to-leading order QCD corrections to $pp \to t\bar{t}h$ at the CERN Large Hadron Collider*, Phys. Rev. **D67** (2003) 071503, arXiv:hep-ph/0211438 [hep-ph].

[99] S. Dawson, C. Jackson, L. H. Orr, L. Reina, and D. Wackeroth, *Associated Higgs production with top quarks at the Large Hadron Collider: NLO QCD corrections*, Phys. Rev. **D 68** (2003) 034022, arXiv:hep-ph/0305087.

[100] T. Gleisberg, S. Hoche, F. Krauss, A. Schalicke, S. Schumann, and J. Winter, *SHERPA 1.alpha, a proof-of-concept version*, JHEP **02** (2004) 056, arXiv:hep-ph/0311263 [hep-ph].

[101] T. Gleisberg et al., *Event generation with SHERPA 1.1*, JHEP **02** (2009) 007, arXiv:0811.4622 [hep-ph].

[102] S. Hoeche, S. Schumann, and F. Siegert, *Hard photon production and matrix-element parton-shower merging*, Phys. Rev. D **81** (2010) 034026, arXiv:0912.3501 [hep-ph].

[103] M. L. Mangano et al., *ALPGEN, a generator for hard multiparton processes in hadronic collisions*, JHEP **07** (2003) 001, arXiv:hep-ph/0206293.

[104] G. Corcella et al., *HERWIG 6: an event generator for hadron emission reactions with interfering gluons (including super-symmetric processes)* , JHEP **01** (2001) 010.

[105] J. M. Butterworth, J. R. Forshaw, and M. H. Seymour, *Multiparton interactions in photoproduction at HERA*, Z. Phys. **C 72** (1996) 637–646, arXiv:hep-ph/9601371.

[106] ATLAS Collaboration, *New ATLAS event generator tunes to 2010 data*, ATL-PHYS-PUB-2011-008 (2011) . http://cds.cern.ch/record/1345343.

[107] P. Golonka and Z. Was, *PHOTOS Monte Carlo: A Precision tool for QED corrections in Z and W decays*, Eur. Phys. J. **C 45** (2006) 97–107, arXiv:hep-ph/0506026.

[108] D. de Florian, G. Ferrera, M. Grazzini, and D. Tommasini, *Higgs boson production at the LHC: transverse momentum resummation effects in the $H \to 2\gamma$, $H \to WW \to l\nu l\nu$ and $H \to ZZ \to 4l$ decay modes*, JHEP **1206** (2012) 132, arXiv:1203.6321 [hep-ph].

[109] M. Grazzini and H. Sargsyan, *Heavy-quark mass effects in Higgs boson production at the LHC*, JHEP **1309** (2013) 129, arXiv:1306.4581 [hep-ph].

[110] S. Dittmaier, C. Mariotti, G. Passarino, R. Tanaka, et al., *Handbook of LHC Higgs Cross Sections: 2. Differential Distributions*, arXiv:1201.3084 [hep-ph].

[111] *Reconstruction of collinear final-state-radiation photons in Z decays to muons in sqrts=7 TeV proton-proton collisions.*, .

[112] T. Vesterinen, *A Novel Technique for Studying the Z Boson Transverse Momentum Distribution at Hadron Colliders*, Nucl.Instrum.Meth **A602** (2009) 432–437, arXiv:0807.4956v1 [hep-ph].

[113] ATLAS Collaboration, *Measurement of the inclusive isolated photon cross section in pp collisions at $\sqrt{s} = 7TeV$ with the ATLAS detector*, Phys. Rev. D **83** (2011) 052005, arXiv:1012.4389 [hep-ex].

[114] A. Dicus, C. Kao, and W. Repko, *Comparison of $H \to \ell\bar{\ell}$ and $H \to \gamma Z, Z \to \ell\bar{\ell}$ including the ATLAS cuts*, Phys.Rev.D **89** (2014) 033013.

[115] A. L. Read, *Presentation of search results: The CL(s) technique*, J. Phys. G **28** (2002) 2693–2704.

[116] G. Cowan, K. Cranmer, E. Gross, and O. Vitells, *Asymptotic formulae for likelihood-based tests of new physics*, Eur. Phys. J. **C 71** (2011) 1554, arXiv:1007.1727.

[117] CMS Collaboration, *Search for a Higgs boson decaying into a Z and a photon in pp collisions at $\sqrt{s} = 7$ and 8 TeV*, Phys. Lett. B **726** (2013) 587, arXiv:1307.5515 [hep-ex].

[118] ATLAS Collaboration, *Measurement of the backgrounds to the $H \to \gamma\gamma$ search and reappraisal of its sensitivity with 37 pb^{-1} of data recorded by the ATLAS detector*, ATLAS-CONF-2011-004 (2011) . http://cds.cern.ch/record/1327196.

[119] ATLAS Collaboration, *Search for the Higgs boson in the diphoton final state with 38 pb^{-1} of data recorded by the ATLAS detector in proton-proton collisions at $\sqrt{s}$=7 TeV*, ATLAS-CONF-2011-025 (2011) . http://cds.cern.ch/record/1336758.

[120] ATLAS Collaboration, *Search for the Higgs Boson in the Diphoton Channel with the ATLAS Detector using 209 pb^{-1} of 7 TeV Data taken in 2011*, ATLAS-CONF-2011-085 (2011) . http://cds.cern.ch/record/1356193.

[121] ATLAS Collaboration, *Search for the Standard Model Higgs boson in the two photon decay channel with the ATLAS detector at the LHC*, Physics Letters B **705** (2011) 452–470.

[122] ATLAS Collaboration, *Search for the Standard Model Higgs boson in the diphoton decay channel with 4.9 fb^{-1} of pp collisions at $\sqrt{s}$=7 TeV with ATLAS*, Phys. Rev. Lett. **108** (2012) 111803.

[123] ATLAS Collaboration, *An update to the combined search for the Standard Model Higgs boson with the ATLAS detector at the LHC using up to 4.9 fb^{-1} of pp collision data a $\sqrt{s}$ = 7 TeV*, ATLAS-CONF-2012-019 (2012) . http://cds.cern.ch/record/1430033.

[124] ATLAS Collaboration, *Observation of an excess of events in the search for the Standard Model Higgs boson in the gamma-gamma channel with the ATLAS detector*, ATLAS-CONF-2012-091 (2012) . http://cds.cern.ch/record/1460410.

[125] ATLAS Collaboration, *Measurements of the properties of the Higgs-like boson in the two photon decay channel with the ATLAS detector using 25 fb^{-1} of proton-proton collision data*, ATLAS-CONF-2013-012 (2013) . http://cds.cern.ch/record/1523698.

[126] W. Lampl, S. Laplace, D. Lelas, P. Loch, H. Ma, S. Menke, S. Rajagopalan, D. Rousseau, S. Snyder, and G. Unal, *Calorimeter clustering algorithms: description and performance*, ATL-LARG-PUB-2008-002 (2008) .

[127] S. Laplace and J. De Vivie, *Calorimeter isolation and pile-up*, . https://cds.cern.ch/record/1444890?

[128] M. Cacciari and G. P. Salam, *Pileup subtraction using jet areas*, Physics Letters B **659** (2008) 119.

[129] ATLAS Collaboration, *Pile-up subtraction and suppression for jets in ATLAS*, ATLAS-CONF-2013-083 (2013) . http://cds.cern.ch/record/1570994.

[130] A. Hoecker, P. Speckmayer, J. Stelzer, J. Therhaag, E. von Toerne, and H. Voss, *TMVA 4 (Toolkit for multivariate data analysis with ROOT) Users Guide*. 2009.

[131] D. Rainwater, R. Szalapski, and D. Zeppenfeld, *Probing color-singlet exchange in Z + 2-jet events at the CERN LHC*, Phys. Rev. D **54** (1996) 6680.

[132] ATLAS Collaboration, *Measurement of the isolated diphoton cross-section in pp collisions at $\sqrt{s}$ = 7 TeV with the ATLAS detector*, Phys. Rev. D **85** (2012) 012003.

[133] ATLAS Collaboration, *Measurement of isolated-photon pair production in pp collisions at $\sqrt{s}$ = 7 TeV with the ATLAS detector*, JHEP **01** (2013) 086.

[134] K. Liu et al., *Background determination in photon samples*, . https://indico.cern.ch/event/219420/session/11/contribution/39/material/slides/0.pdf.

[135] T. Binoth, J. Guillet, E. Pilon, and M. Werlen, *A full next-to-leading order study of direct photon pair production in hadronic collisions*, Eur. Phys. J **C16** (2000) 311.

[136] J. Alwall, M. Herquet, F. Maltoni, O. Mattelaer, and T. Stelzer, *MadGraph 5 : Going Beyond*, JHEP **1106** (2011) 128, arXiv:1106.0522 [hep-ph].

[137] S. Gangal and F. J. Tackmann, *NLO Uncertainties in Higgs + 2 jets from Gluon Fusion*, arXiv:1302.5437 [hep-ph].

[138] J. M. Campbell and R. Ellis, *MCFM for the Tevatron and the LHC*, Nucl.Phys.Proc.Suppl. **205-206** (2010) 10–15, arXiv:1007.3492 [hep-ph].

[139] ATLAS Collaboration, *Updated coupling measurements of the Higgs boson with the ATLAS detector using up to 25 fb^{-1} of proton-proton collision data*, ATLAS-CONF-2014-009 (2014) . http://cds.cern.ch/record/1670012.

[140] ATLAS Collaboration, *Search for the bb decay of the Standard Model Higgs boson in associated W/ZH production with the ATLAS detector*, ATLAS-CONF-2013-079 (2013) . http://cds.cern.ch/record/1563235.

[141] ATLAS Collaboration, *Evidence for Higgs Boson Decays to the $\tau\tau$ Final State with the ATLAS Detector*, ATLAS-CONF-2013-108 (2013) . http://cds.cern.ch/record/1632191.

[142] ATLAS Collaboration, *Measurements of Higgs boson production and couplings in diboson final states with the ATLAS detector at the LHC*, Phys. Lett. B **726** (2013) 88, arXiv:1307.1427 [hep-ex].

[143] ATLAS Collaboration, *Evidence for the spin-0 nature of the Higgs boson using ATLAS data*, Phys. Lett. B **726** (2013) 120–144, arXiv:1307.1432 [hep-ex].

[144] L. D. Landau, *On the angular momentum of a two-photon system*, Dokl. Akad. Nauk Ser. Fiz. **60** (1948) 207.

[145] C.-N. Yang, *Selection Rules for the Dematerialization of a Particle Into Two Photons*, Phys. Rev. **77** (1950) 242.

[146] ATLAS Collaboration, *Measurements of the properties of the Higgs-like boson in the four lepton decay channel with the ATLAS detector using 25 fb^{-1} of proton-proton collision data*, ATLAS-CONF-2013-013 (2013) . https://cds.cern.ch/record/1523699.

[147] CMS Collaboration, *Updated measurements of the Higgs boson at 125 GeV in the two photon decay channel*, CMS-PAS-HIG-13-001 (2013) . http://cds.cern.ch/record/1530524.

[148] CMS Collaboration, *Properties of the observed Higgs-like resonance using the diphoton channel*, CMS-PAS-HIG-13-016 (2013) . http://cds.cern.ch/record/1558930.